On the Clinical Potential of Ion Computed Tomography with Different Detector Systems and Ion Species

Sebastian Meyer

München 2019

On the Clinical Potential of Ion Computed Tomography with Different Detector Systems and Ion Species

Sebastian Meyer

Dissertation
an der Fakultät für Physik
der Ludwig–Maximilians–Universität
München

vorgelegt von
Sebastian Meyer
aus Dachau

München, den 21. Juni 2019

Erstgutachter: Prof. Dr. Katia Parodi
Zweitgutachter: Prof. Dr. Otmar Biebel
Tag der mündlichen Prüfung: 01. August 2019

Contents

Abbreviations and Acronyms

2D Two-Dimensional. 2, 41, 44, 54, 60, 63, 75, 132, 147, 154

3D Three-Dimensional. 16, 40, 48, 50, 57, 59, 64, 67, 72, 73, 88, 97, 98, 105, 120, 147

BAMS Beam Application and Monitoring System. 50, 51, 72, 74, 75

BPD Bragg Peak Decomposition. xiv, xvii, 71, 80–83, 88–90, 92, 93, 151, 152

CBCT Cone Beam Computed Tomography. 36, 135, 147

cCT Carbon Computed Tomography. xiv, 43, 82, 83, 85–89, 91, 92, 95, 99, 101, 102, 105–107, 121–126, 152, 153

CNR Contrast-to-Noise Ratio. xv, 137, 144, 145, 148

cRAD Carbon Radiography. 83–86, 90, 91

CSDA Continuous Slowing-Down Approximation. 10, 11, 49, 57, 124, 147

CSP Cubic Spline Path. xiv, 53, 57, 58, 65, 69, 98–100, 105, 106, 109, 138, 139, 144, 146

CT Computed Tomography. xiii, 30, 36, 148

DECT Dual Energy Computed Tomography. 30, 32–34, 97, 107, 109, 148

DSB Double-Strand Break. xiv, xvii, 18, 111–115, 117, 119–121, 123, 125–127

ESF Edge Spread Function. xiii, 67, 68, 136, 140, 141

FBP Filtered Back Projection. 58, 65, 144

FWHM Full Width at Half Maximum. 13, 17, 91, 108, 136

GNP Gold-Nanoparticle. 137, 148, 149, 154

heCT Helium Computed Tomography. xiv, 82, 83, 85–87, 95, 99, 101, 102, 107, 121–124, 126, 152, 153

heRAD Helium Radiography. 83–86, 90, 91

HIT Heidelberg Ion-Beam Therapy Center. xiii, 11, 50–53, 69, 72, 73, 75, 81, 83, 88, 96, 98, 100, 108, 151

HU Hounsfield Unit. xiii–xv, 28, 30, 31, 33, 34, 52, 53, 67, 77, 97, 101–103, 107, 109, 144, 146, 152

iCT Ion Computed Tomography. xiii, xiv, xvii, xix–xxi, 5–10, 17, 24, 34, 38–40, 42–48, 53, 55, 58, 62, 64, 67–69, 72, 75, 82, 85, 86, 92, 95–97, 101–111, 120–123, 125–127, 135, 137, 151–154

IMPT Intensity-Modulated Particle Therapy. xiv, 25, 27, 29, 97, 98, 103, 105, 106, 109

iRAD Ion Radiography. xiv, 67, 75, 83–86, 90, 152

LET Linear Energy Transfer. xiii, 18–21, 111, 114, 115, 117, 121, 123, 125, 126

LQ Linear-Quadratic. 19, 20, 112, 114, 117, 119, 125

MC Monte Carlo. xiv, xix–xxi, 6, 10, 11, 13–17, 28, 29, 34, 46–48, 52, 53, 56, 57, 64, 66–69, 77, 78, 80, 83, 86, 87, 90, 92, 96–101, 108, 111, 116, 118–120, 123, 124, 129, 133, 134, 137, 138, 140, 141, 146, 149, 153, 154

MCDS Monte Carlo Damage Simulation. xiv, xvii, 111, 115, 116, 118, 120, 121, 123, 126, 153

MCS Multiple Coulomb Scattering. 12, 15, 21, 29, 34, 38, 41–44, 46, 49, 53, 54, 56, 65, 69, 82, 88, 91, 92, 95, 99, 105, 107, 109, 133, 138, 146, 147, 149, 151, 152

MLP Most Likely Path. xiv, 53, 54, 56–58, 65, 69, 98–100, 105, 106

MTF Modulation Transfer Function. 67, 68, 140, 141

OAR Organ At Risk. 28, 34, 37, 96, 98, 103

OS-SART Ordered Subset Simultaneous Algebraic Reconstruction Technique. xiii, 60, 63, 64, 66, 69, 99

pCT Proton Computed Tomography. xv, 4–6, 41, 42, 48, 52, 53, 82, 83, 95, 99, 101–103, 107–109, 121–124, 126, 129, 131, 133–137, 140, 141, 143–149, 151–154

PET Positron Emission Tomography. 16, 28, 130, 131, 136

PMMA Poly(Methyl Methacrylate). xiv, 73–75, 77–83, 87, 91

PPIC Parallel-Plate Ionization Chamber. 73–75, 77, 78, 80, 81, 92

pRAD Proton Radiography. 83–86, 91

PTV Planning Target Volume. 36, 96, 98, 102, 104

RBE Relative Biological Effectiveness. xiii, xiv, xvii, 20–22, 111, 114, 115, 117, 120–123, 125, 126, 153

RMF Repair-Misrepair Fixation. xiv, xvii, 6, 21, 111, 112, 114, 115, 117–121, 123, 125, 127, 153

RMS Root Mean Square. xiv, xv, 57, 79, 99, 100, 138–140, 147

ROI Region of Interest. 66, 136, 137, 140, 141

RP Raster Point. 50, 51, 66, 74, 75, 77, 80–83, 85, 88, 89, 92, 93, 96, 101, 120, 152

RPTC Rinecker Proton Therapy Center. 52, 69

RSP Relative Stopping Power. xiv, xv, xvii, xix–xxi, 28, 30–34, 38–40, 43, 46, 53, 58, 59, 65–67, 75–79, 82, 83, 86–92, 95, 97–99, 101, 102, 106–110, 123, 129, 135–137, 141, 143–148, 151–153

SART Simultaneous Algebraic Reconstruction Technique. 61, 63, 64, 66

SFUD Single Field Uniform Dose. xiv, 27, 97, 102, 107, 109

SIRMIO Small animal proton Irradiator for Research In Molecular Image-guided radiation-Oncology. xiv, xv, 6, 129–131, 134, 135, 149, 154

SLP Straight Line Path. xiv, 53, 65, 66, 69, 99, 100, 105, 106, 138, 139, 144, 147

SOBP Spread Out Bragg Peak. xiv, 3, 27, 120, 121

TPC Time-Projection-Chamber. xv, 129, 133, 134, 140–144, 146, 147, 153, 154

TPS Treatment Planning System. 29, 30, 46, 95, 97, 154

TVS Total Variation Superiorization. xiii, 63, 64, 66, 69, 99, 106

WEPL Water-Equivalent Path Length. xv, 40–44, 46, 49, 57–59, 64–66, 96, 108, 109, 133, 136, 138, 140–143, 147, 154

WET Water-Equivalent Thickness. xvii, 27, 58, 66, 67, 73–75, 77, 79–82, 84–88, 90–93, 139, 151, 152

xCT X-ray Computed Tomography. xv, 5, 6, 28, 30–34, 36, 38, 39, 46, 49, 52, 65, 67, 77, 88, 92, 95–97, 102–107, 109, 110, 117, 119, 121, 125, 136, 146–148, 153

List of Figures

List of Tables

Über das klinische Potenzial von Ionen Computertomographie mit verschiedenen Detektor Konfigurationen und Ionentypen

Zusammenfassung

Strahlentherapie mit schweren energetischen Ionen ist eine sich schnell entwickelnde Form der Krebstherapie, denn Ionenstrahlen ermöglichen aufgrund ihrer endlichen Eindringtiefe eine sehr konforme Anpassung der abgegebenen Dosis an das Tumorvolumen. Die Ausschöpfung des vollen Potenzials der Ionentherapie ist jedoch nach wie vor durch eine erhöhte Anfälligkeit für Unsicherheiten in der geschätzten Ionenstrahl-Reichweite eingeschränkt. Eine der Hauptquellen für diese Unsicherheit, die der aktuellen Form der Bestrahlungsplanung innewohnt, ist die semiempirische Umrechnung von Röntgen-Computertomographie Informationen in das relative (bezüglich Wasser) Bremsvermögen (RSP) der Ionen. Die Ionen Computertomographie (iCT) eliminiert potenziell diese Ungenauigkeit durch eine direkte Rekonstruktion der RSP-Verteilung innerhalb eines Patienten aus einer Reihe von Ionenradiographien. Dies könnte letztlich die Verbesserung des klinischen Ergebnisses für Patienten, die Ionentherapie erhalten, ermöglichen und neue Wege für adaptive Behandlungskonzepte eröffnen.

Diese Arbeit zielte darauf ab, das Potenzial und die Auswirkungen von iCT mit verschiedenen Ionenarten und zwei Detektor-Konfigurationen, einem kostengünstigen und einem komplexen hochmodernen System, für klinische Anwendungen zu untersuchen. Dazu wurde eine entsprechende FLUKA Monte Carlo (MC) Simulationsumgebung entwickelt, welche eine akkurate Beschreibung der aktiven Dosisapplikation und der Strahleigenschaften von klinischen Therapiezentren beinhaltet. Darüber hinaus wurden verschiedene Methoden der iterativen tomographischen Bildrekonstruktion untersucht. Basierend auf einem Prototyp eines am Heidelberger Ionenstrahl-Therapiezentrum untersuchten Detektor-Systems wurden die Möglichkeiten des Integrationsmodus untersucht, welcher potenziell eine leichtere klinische Umsetzung erlaubt. Insbesondere Kohlenstoff-iCT ermöglichte eine durchschnittliche RSP-Genauigkeit von besser als 1% in experimentellen und simulierten Phantomstudien. Die entwickelte Signalverarbeitungsmethode erzielte eine erhebliche Verbesserung der Bildqualität. Allerdings wurde das begrenzte räumliche Auflösungsvermögen aufgrund von intrinsischen Ungenauigkeiten durch Reichweitenvermischung als wesentliche Einschränkung für eine Anwendung in der klinischen Bestrahlungsplanung identifiziert. Einzelteilchen-iCT erzielte unter idealen Bedingungen eine bessere Bildqualität bei geringerer physikalischer Strahlenexposition im Vergleich zum Integrationsmodus, insbesondere Helium-iCT. Das klinische Potenzial von iCT wurde quantitativ an Hand der Genauigkeit der Dosisberechnung bewertet. Dabei konnte aufgezeigt werden, dass generell verringerte Reichweitenunsicherheiten in der Protonentherapie-Bestrahlungsplanung im Vergleich zur aktuellen klinisch angewandten Methode erzielt werden können. Um eine erste detaillierte Abschätzung der biologischen Auswirkungen klinisch relevanter iCT-Aufnahmebedingungen zu ermöglichen, wurde das mechanistische 'repair-misrepair-fixation' Modell und der 'Monte Carlo damage simulation' Algorithmus in die FLUKA

MC-Simulation integriert. Die Ergebnisse zeigten, dass iCT im Vergleich zu diagnostischen Röntgenspektren, welche für die Bestrahlungsplanung verwendet werden, potenziell reduzierte biologische DNA Schädigungen hervorruft. Um die Lücke zur klinischen Umsetzung der Ionenbildgebung zu schließen, wurde ein zur Bildgebung von Kleintieren bestimmtes Protonen-iCT System untersucht und optimiert. Basierend auf MC-Simulationen der optimierte Detektor Konfiguration wurde ein räumliches Auflösungsvermögen von rund $3\,\mathrm{mm}^{-1}$ und ein RSP Genauigkeit von besser als 0.5% erreicht. Dies erlaubt eine präzisere Bildgebung als derzeitige Röntgen-Computertomographie für die Bestrahlungsplanung in der präklinischen Forschung.

On the Clinical Potential of Ion Computed Tomography with Different Detector Systems and Ion Species

Abstract

External beam radiotherapy with energetic heavy charged particles is a rapidly emerging form of cancer therapy. Ion beams enable a highly conformal shaping of the delivered dose to the tumor volume due to their finite penetration depth. However, exploiting the full potential of ion beam therapy is still constrained by an increased sensitivity to potential uncertainties in the estimated ion beam range. One major source of uncertainty inherent in the current clinical practice of ion therapy treatment planning is the semi-empirical conversion of X-ray CT information to ion Relative Stopping Power (RSP) (with respect to water). Ion Computed Tomography (iCT) potentially eliminates this inaccuracy by enabling a direct reconstruction of patients' RSP distributions from a series of ion radiographies. This could ultimately improve the clinical outcome of patients receiving ion therapy and open new pathways for in-room adaptive treatment concepts.

This thesis aims at investigating the potential and implications of iCT for clinical applications with different ion species and two detector configurations: cost-effective integration-mode and state-of-the-art single-particle tracking. Therefore, a customized FLUKA Monte Carlo (MC) simulation framework is developed to mimic the scanned ion beam delivery and beam characteristics of clinical facilities. Moreover, different methodologies of iterative tomographic image reconstruction are explored. Based on a prototype detector system under investigation at the Heidelberg Ion-Beam Therapy Center, the capabilities of an integration-mode instrumentation, which potentially enables an easier translation into clinical realization, are examined. In particular, carbon iCT enables an average RSP accuracy better than 1% in experimental and simulation-based phantom studies. The developed signal-processing strategy demonstrates a substantial gain in image quality. However, the limited spatial resolution due intrinsic range mixing effects is identified as a major constraint for an imaging application in treatment planning. Single-particle tracking iCT, particularly helium iCT, yields superior image quality at lower physical dose exposure for an ideal detector compared to integration-mode. The clinical potential of single-particle tracking iCT is quantitatively evaluated by assessing the dose calculation accuracy, demonstrating reduced range uncertainties in proton therapy treatment planning with respect to current clinical practice. In order to provide first detailed estimations on the radiobiological implications related to clinical-like iCT acquisition conditions, the FLUKA MC code is coupled to the mechanistic repair-misrepair-fixation model and the Monte Carlo damage simulation algorithm. Findings indicate that iCT potentially causes reduced biological DNA damage compared to diagnostic X-ray CT spectra used for treatment planning imaging. To bridge the gap toward the potential clinical realization of ion imaging, a proton iCT scanner dedicated to small animal imaging is characterized and optimized. Based on MC simulations for the proposed layout improvements, a spatial resolution of around $3\,\mathrm{mm}^{-1}$ and sub-0.5% RSP accuracy is obtained for phantom reconstructions. The system enables accurate imaging capabilities for treatment planning in pre-clinical research, which is expected to provide superior range accuracy compared to the current state-of-the-art.

"It is not possible to be a scientist unless you believe that it is good to learn. It is not good to be a scientist, and it is not possible, unless you think that it is of the highest value to share your knowledge, to share it with anyone who is interested. It is not possible to be a scientist unless you believe that the knowledge of the world, and the power which this gives, is a thing which is of intrinsic value to humanity, and that you are using it to help in the spread of knowledge, and are willing to take the consequences."

J. Robert Oppenheimer

"The saddest aspect of life right now is that science gathers knowledge faster than society gathers wisdom."

Isaac Asimov

1 Introduction

1.1 Radiation Therapy: from X-rays to Particle Beams

In cancerous cells the orderly process of cell division and death fails, resulting in uncontrolled proliferation. This can cause severe damage to adjacent tissue and organs, or spread to other body parts with life threatening consequences for the patient. Nowadays, cancer is the second leading cause of death globally, and incidence and mortality are rapidly growing, accounting for around 9.6 million deaths in 2018 as estimated by the WHO [2014]. The reasons for this trend are complex but reflect the inevitable population aging, as well as changes in the prevalence and distribution of the main risk factors [Bray et al., 2018]. The earliest written reference to cancer[1] is the ancient Egyptian Edwin Smith Papyrus, written approximately 3000 B.C. [Hajdu, 2011]. Even though the author concluded at this time that *'there is no treatment'* [Breasted, 1930], nowadays modern medicine offers various patient-tailored treatment forms. These encompass among others chemotherapy, surgery, immunotherapy and radiation therapy. The latter has become a standard for most cases and is received by around two-thirds of cancer patients [Durante and Paganetti, 2016].

[1] The word cancer was not explicitly mentioned since it dates back to the Greek physician Hippocrates at around 400 B.C.

The foundation of the field of radiation science dates back to the discovery of X-rays by Wilhelm Conrad Röntgen in 1895, the natural radioactivity by Henri Becquerel in 1896, and the isolation of radium and polonium by Marie and Pierre Curie in 1898. Those transformative moments made modern radiation oncology possible so it could benefit mankind [Das and Paganetti, 2015]. More than 100 years of experience established radiation therapy as one of the main treatment modalities in oncology. Technological advances like computerized treatment planning, the introduction of non-coplanar mega-voltage X-rays and dynamic geometrical field shaping significantly improved the therapeutic effectiveness of electromagnetic radiation. However, due to its physical and radiobiological properties the application of conventional photon irradiation is intrinsically constrained, especially for radio-resistant tumors.

The use of energetic charged particles like protons or carbon ions to overcome aforementioned limitations of conventional radiation was first outlined in a seminal article by Robert Wilson [1946]. The favorable depth-dose distribution is characterized by a steep increase close to the end of the range, the so-called Bragg peak (cf. figure 1.1), which can be exploited to obtain highly conformal dose distributions. Additionally, heavy ions experience reduced lateral and longitudinal scattering, complemented with a beneficial differential biological effect [Amaldi and Kraft, 2005]. Those properties can be exploited to achieve an excellent conformation of the dose to the distal and lateral side of the target. Wilson's idea was picked up few years later by Cornelius A. Tobias at the Lawrence Berkeley Laboratory, California, pioneering the medical use of accelerated particle beams in first biology experiments and clinical trials [Tobias et al., 1952, 1958]. In the next decades ion therapy development continued in various research facilities worldwide like the Gustav Werner Institute, Sweden [Larsson, 1961], the Harvard Cyclotron Laboratory in Cambridge, Massachusetts [Kjellberg et al., 1962] or the National Institute of Radiological Sciences, Japan [Kanai et al., 1980]. With the first dedicated hospital-based particle therapy facility starting operation in 1990 at the Loma Linda Medical Center [Slater et al., 1992], particle therapy finally moved from nuclear physics laboratories into health care environment. This was a crucial step since dedicated patient care within a hospital-based ion therapy center is a prerequisite for the treatment of pediatric patients requiring anesthetics [Goitein et al., 2002]. Nowadays, the use of Two-Dimensional (2D) intensity-modulated raster scanning [Haberer et al., 1993] with active energy variation allows dose conformity to the tumor with a spatial precision never observed until then [Debus et al., 2000]. By December 2018 around 70 proton and 11 carbon ion therapy centers are operational in 17 countries with

many more under construction or in planning stage [PTCOG], demonstrating the emerging role of ion therapy in modern radiation oncology. However, its undeniable potential comes at the burden of an increased sensitivity to any source of uncertainty between planned and delivered dose application (cf. figure 1.1, red lines).

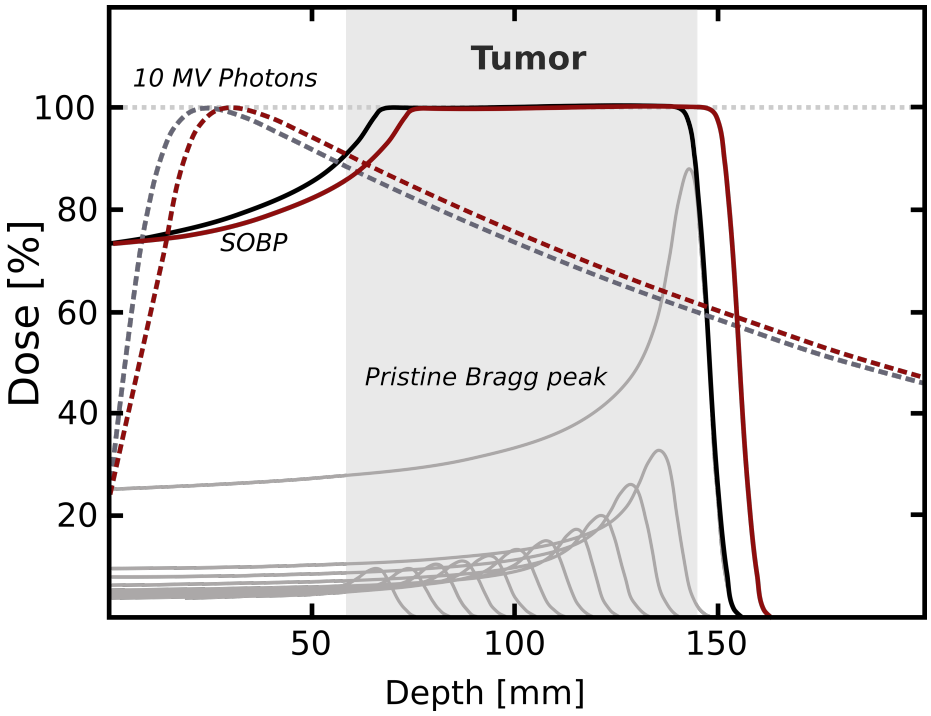

Figure 1.1: Depth-dose distribution for a Spread Out Bragg Peak (SOBP) (black solid), its constitute pristine Bragg peaks (gray solid), and a 10 MV photon beam (gray dashed). The individual pristine Bragg peaks are modulated in energy to match the tumor extent in depth. Longitudinal shifts in the dose distributions (red) can be caused by unaccounted uncertainties or anatomical variations along the beam path.

1.2 Imaging with Ion Beams

The use of ion beams for imaging is not a new idea, it dates back almost sixty years. The theoretical conception was A.M. Cormack's work on the *'Representation of a Function by Its Line Integrals, with Some Radiological Applications'* [Cormack, 1963, 1964]. The noble laureate already recognized that his method has strong potential for proton imaging and proton therapy treatment planning in order to *'produce the high ionization at just the right place'*. The surprising fact that exactly this problem is still a remaining challenge in modern particle therapy, demonstrates that it is highly non-trivial.

The experimental landmark studies were conducted by A.M. Koehler [1968] at the Cyclotron Laboratory of Harvard university, obtaining the very first proton radiography (cf. figure 1.2a). Steward and Koehler [1973] demonstrated that proton radiography provides superior visualization of the internal structures and tumors within specimens compared to X-ray imaging. The first to apply charged particles to tomographic imaging was Goitein [1972] based on projection data measured using an alpha particle beam. His work demonstrated the potential of iterative image reconstruction algorithms and evaluated in detail image resolution and artifacts. Conceptual and experimental advances were achieved by the pioneering work of Hanson et al. [1981] (cf. figure 1.2b) at Los Alamos Laboratory, as nowadays state-of-the-art single-particle tracking approach [Hanson et al., 1982].

The use of heavy ions was explored at the Bevatron accelerator at Lawrence Berkeley Laboratory [Benton et al., 1973]. Tobias et al. [1977] showed the elimination of motion artifacts and the detection of tissue stopping power differences as small as 0.2% for the use of carbon ion beams. Those studies were supported by findings of Sommer et al. [1978], demonstrating superior density resolution of ion imaging for tumors in pathological specimens compared with X-rays even at low radiation dose.

Due to technical limitations at that time, for example the sparse availability of dedicated particle accelerators, ion-based imaging could not keep up with the rapid development of X-ray imaging. However, the up-rise of proton therapy as a new treatment modality in the 1990s also revived the interest in ion imaging. The work of Schneider and Pedroni [1995] at the Paul Scherrer institute in Switzerland demonstrated the potential of proton radiography for range verification. They also acquired images of a living animal patient [Schneider et al., 2004] and later on established the usefulness of proton imaging as a tool for patient-specific quality control of ion therapy treatment plans [Schneider et al., 2005]. Recent developments in detector and accelerator technology together with the clinical need for improved range accuracy initiated the foundation of the Proton Computed Tomography (pCT) collaboration in 2003 [Schulte and Wroe, 2012]. Even though ion imaging has not yet reach clinical application the topic is gaining increased attention from the medical physics research community.

From a technological point of view, experimental limitations of the complex detector systems are still challenging a clinical realization. This initiated the revived interest in simplified integration-mode systems, especially for carbon ions [Telsemeyer et al., 2012; Rinaldi et al., 2013]. Furthermore, promising results for helium ions [Gehrke et al., 2018b; Piersimoni et al., 2018] have been recently published, once again indicating that the chosen

ion type has strong impact on the final image quality. However, a significant gain in treatment planning quality relative to single and dual energy X-ray Computed Tomography (xCT) still needs to be demonstrated [Johnson, 2018].

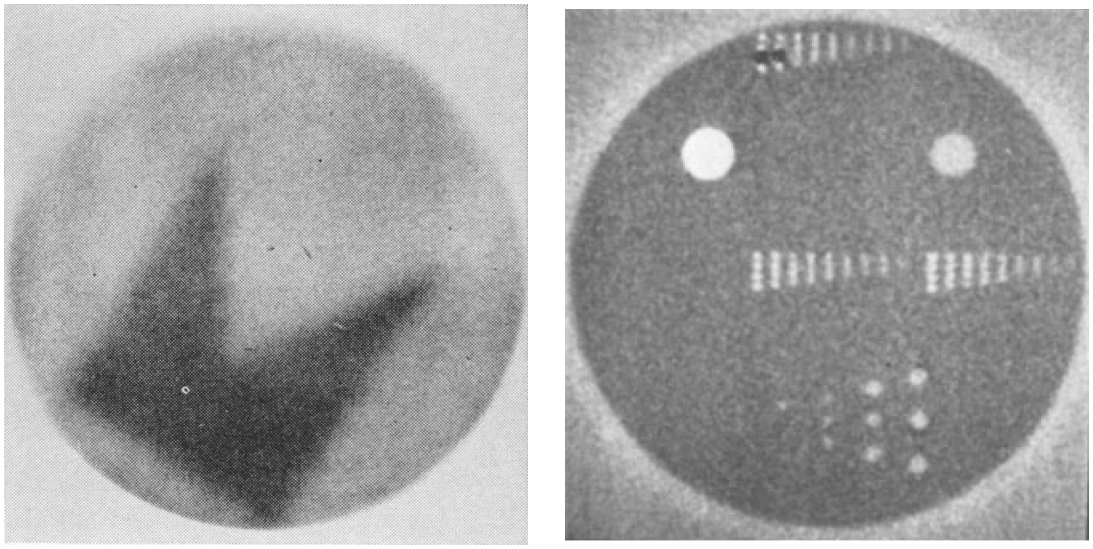

(a) (b)

Figure 1.2: (a) First published proton radiography by Koehler [1968]. (b) pCT image of a 29.5 cm diameter polyethylene phantom by Hanson et al. [1981].

1.3 Aim and Outline of this Thesis

This thesis contributes to the development of ion imaging in the following topics:

- Performance comparison of different ion species for integrating and single-particle tracking detector systems.
- Demonstration of a gain in treatment plan quality compared to xCT.
- First insights on radiobiological implications of ion imaging irradiation scenarios.
- Development and optimization of a pre-clinical pCT setup for small-animal imaging.

The aim is to compare and further improve ion imaging for different detector systems and ion species in order to demonstrate a gain in treatment planning quality without exceeding dosimetric constraints, ultimately bringing Ion Computed Tomography (iCT) closer to a clinical realization.

The first part contributes to the ongoing search for the ideal iCT detector system and particle species with the final goal of improving the treatment plan quality. Hence, the second part aims at demonstrating the gain in range accuracy for proton therapy treatment planning associated with iCT for realistic clinical cases in direct comparison to xCT. Since future patient applications put forward dosimetric constraints, the third part provides the first dedicated investigation of the biological implications related to high-energy low-dose iCT irradiation scenarios. While various phantom investigations have been performed, the final piece for bringing ion imaging into the clinical environment might be the demonstration of its capabilities in pre-clinical applications. Therefore, the last part of this work reports on the optimization and performance of a dedicated pCT system for pre-clinical research currently under development at our department within the European Research Council funded Small animal proton Irradiator for Research In Molecular Image-guided radiation-Oncology (SIRMIO) project.

This thesis is organized as follows. In chapter two a comprehensive overview on the main physical and radiobiological aspects of ion beam interactions with tissue is given. Chapter three introduces the principles of ion-based transmission imaging within the context of ion therapy, emphasizing the peril and origins of range uncertainties. Chapter four presents the necessary techniques of iCT simulation and reconstruction required for the following investigations. The fifth chapter contains an experimental and simulation-based investigation of a cost-effective integration-mode detector system, encompassing advanced post-processing and potential detector upgrades. Chapter six presents the evidence that iCT can reduce range uncertainties in proton therapy treatment planning for cranial cases. Chapter seven introduces the results for estimating the radiobiological implications of typical iCT irradiation scenarios using a coupling between the FLUKA Monte Carlo (MC) code and the Repair-Misrepair Fixation (RMF) model. The eighth chapter describes the development and optimization of a pCT system for pre-clinical research within the SIRMIO project. Finally, conclusions and future perspectives are summarized in the last chapter.

"No one any longer pays attention to - if I may call it - the spirit of physics, the idea of discovery, the idea of understanding. I think it's difficult to make clear to the non-physicist the beauty of how it fits together, of how you can build a world picture, and the beauty that the laws of physics are immutable."

Hans Bethe

2

Basic Principles of Ion Beam Interaction with Matter

The treatment of deep-seated tumors with 15-30 cm penetration depth requires mildly-relativistic (up to $\beta \approx 0.6 - 0.7$) ion beams with initial energies of around 150-430 AMeV (A - mass number) [Durante and Paganetti, 2016]. However, the clinical implementation typically demands precision in the order of a few millimeters, which requires accurate knowledge of all involved physical and biological processes. Therefore, this chapter features the description of the most important interaction mechanisms of charged particles with matter. The differences arising for proton, helium and carbon ion beams will be highlighted and the consequences for the clinical implementation of ion therapy are outlined, ultimately constituting the rationale of iCT.

2.1 Physical Properties of Ion Beams

In order to understand the capabilities and limitations of ion-based transmission imaging, it is necessary to review the basic physics principles of charged particle interaction with

matter. Ions quasi-continuously *slow down* (and finally come to rest) by a very large number of Coulomb (or electromagnetic) interactions with atomic electrons. Charged particles can also be *scattered* and deflected by multiple Coulomb interactions with atomic nuclei. Additionally, they can undergo *nuclear reactions* causing the production of secondary particles. Schematics of the interaction mechanisms are shown in figure 2.1 for the case of protons. These three distinct processes, *stopping*, *scattering* and *nuclear reactions*, primarily determine the characteristics of the different ion species for iCT and strongly influence design concepts of detector systems.

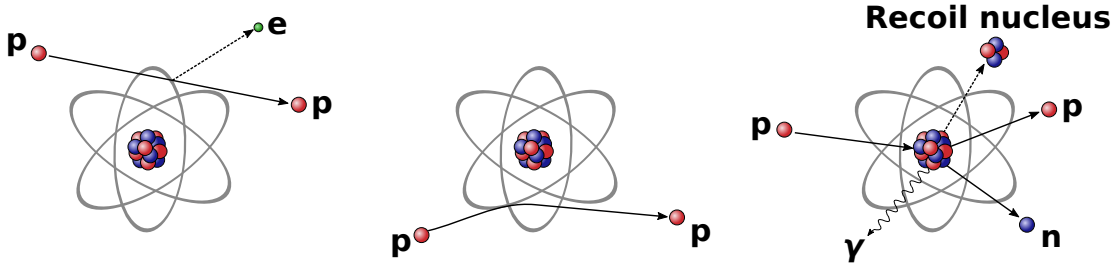

Figure 2.1: Schematics of the main interaction processes of charged particles with matter in the case of protons: Coulomb interaction with atomic electrons (a) and nuclei (b), nuclear interaction with atomic nuclei (c). Figure redrawn from Newhauser and Zhang [2015].

2.1.1 The Stopping of Ions

The dominant energy loss mechanism for ions in the therapeutic energy regime[1] is excitation and ionization of atomic orbital electrons via inelastic Coulomb interaction (cf. figure 2.1a). Intuitively, the amount of energy loss depends on the interaction time, hence, the energy loss rate of ions is expected to increase gradually in the process of slowing down. Above 1 AMeV the average rate of kinetic energy loss $\mathrm{d}E$ per unit path length $\mathrm{d}x$, called stopping power S, can be described by an analytic expression derived by Bethe [1930] and Bloch [1933a]. The first-order relativistic version of this so-called Bethe-Bloch equation is

$$S = -\left\langle \frac{\mathrm{d}E}{\mathrm{d}x} \right\rangle = 4\pi\, r_e^2\, m_e c^2\, \rho_e\, \frac{Z^2}{\beta^2} \left[\ln\left(\frac{2\, m_e c^2\, \beta^2}{1-\beta^2} \right) - \beta^2 - \frac{C}{Z_t} - \ln\langle I \rangle - \frac{\delta}{2} \right], \qquad (2.1)$$

where r_e and m_e are the classical electron radius and rest mass, respectively, Z and $\beta = v/c$ are the charge and velocity (relative to the speed of light) of the incident particle, respec-

[1] The energy regime of interest in ion therapy is around 3-300 MeV for protons [Gottschalk, 2012], corresponding to approximately 0.01-51.45 cm penetration depth in water [Berger et al., 2005].

tively. ρ_e and $\langle I \rangle$ are the electron density and mean excitation energy of the traversed material with atomic number Z_t, respectively. The *shell correction* C [Fano, 1963] accounts for the invalid assumption that the orbital electrons of the absorber are at rest (relative to the projectile), being a prerequisite of the Bethe-Bloch theory. This effect can be up to 6% for protons in the energy regime of 1-100 MeV [Ziegler, 1999]. The *density correction* δ includes the stopping power reduction due to polarization effects in the medium, which reaches the 1% level only above 500 MeV [Berger et al., 1993].

At energies of around 10 AMeV the projectile velocity becomes comparable to the orbital electron velocity ($\approx 0.008\,c$). This causes a mean charge state reduction due to a dynamic interplay of energy loss and recombination effects. Thus, the projectile charge Z in equation (2.1) must be replaced by an effective charge Z_{eff}, which can be calculated from the empirical formula of Barkas [1963]:

$$Z_{\text{eff}} = Z\left(1 - e^{-125\,\beta\,Z^{-\frac{2}{3}}}\right) . \tag{2.2}$$

Higher-order Born corrections terms (i.e., Barkas et al. [1963] and Bloch [1933b] corrections) are generally of minor importance for therapeutic energies and can be safely neglected for protons above 100 keV [Emfietzoglou et al., 2009]. While equation (2.1) describes only interactions with atomic electrons (the so-called electronic stopping power), it is permissible to neglect contributions from interactions with atomic nuclei or inelastic radiative interactions (Bremsstrahlung) in the clinically relevant energy regime. The specific energy loss of ^{1}H, ^{4}He and ^{12}C ions in water is compared in figure 2.2, exemplifying the substantial increment in stopping power for heavier particles.

From the perspective of the material traversed by a charged particle beam, two important quantities are of substantial impact for the stopping power: the electron density ρ_e and the mean ionization potential $\langle I \rangle$. Since equation (2.1) primarily determines how an ion beam will dissipate its energy, the knowledge of those parameters is fundamental for properly planning tumor therapy with ion beams. Section 3.2 will review how this is typically performed in current clinical practice and discuss the associated uncertainties.

It should be kept in mind that the concept of stopping power as presented in equation (2.1) expresses the *mean* energy loss for a large number of particles of identical energy. Nonetheless, each individual ion will experience a slightly different energy loss throughout the slowing down process due to the stochastic nature of the interaction. This phenomenon is called *energy loss straggling* and will be of considerable importance for iCT, representing an intrinsic accuracy limitation as it will be outlined in detail in section 3.4.3.

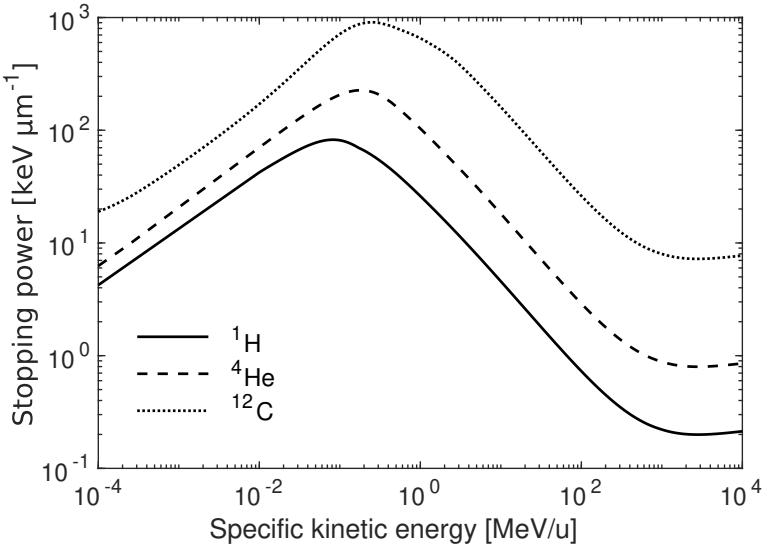

Figure 2.2: Total (unrestricted) stopping power for ^{1}H, ^{4}He and ^{12}C ions in a water target. Data obtained from the FLUKA [Ferrari et al., 2005; Böhlen et al., 2014] MC code.

Within the central limit theorem (i.e., for many collision events), energy loss fluctuations can be described by a Gaussian probability density function for which only the first two moments are non-zero. Using the theory of Bohr [1915, 1948], the variance of the energy loss distribution for particles of atomic number Z and initial energy E_0 passing through material of thickness x is represented by [Scheidenberger et al., 1996]:

$$\sigma_E^2(x) = 4\pi\, Z^2\, \rho_e \left(\frac{e^2}{4\pi\,\epsilon_0}\right)^2 \int_0^x \frac{1 - \frac{1}{2}\,\beta^2(E(E_0, x'))}{1 - \beta^2(E(E_0, x'))}\,\mathrm{d}x'\,, \tag{2.3}$$

where ϵ_0 is the vacuum permittivity. For energy losses exceeding 20% of the original beam energy, Bohr's theory becomes inaccurate since higher order moments can have substantial contributions causing a skewed non-Gaussian distribution. In this case, representing also the iCT scenario, a more accurate description is given by the theory of Tschalär and Maccabee [1970], as it was demonstrated by Schulte et al. [2005].

As a consequence of energy straggling, particles of the same initial energy will have a slightly different penetration depth or range, called *range straggling*. To estimate this distribution of path lengths, *'range'* needs to be defined. While there is not a general concept of range, most commonly one refers to the so-called Continuous Slowing-Down

Approximation (CSDA) range, which is defined for an ion of initial energy E_0 by:

$$R_{\mathrm{CSDA}}(E_0) = \int_{E_0}^{0} \left(\frac{dE}{dx}\right)^{-1} dE = -\int_{E_0}^{0} \frac{dE}{S}\,, \tag{2.4}$$

where S is the stopping power of the traversed material according to equation (2.1). Therefore, the range of charged particles in a certain medium is determined by the initial beam energy as it is shown in figure 2.3. One should keep in mind that R_{CSDA} does not necessarily represent the penetration depth in beam direction, since equation (2.4) solely takes into account the energy loss while neglecting deflection due to scattering. However, for protons and especially heavier ions of clinically relevant energies, the ratio between projected and CSDA range (also known as *detour factor*) is close to 1.

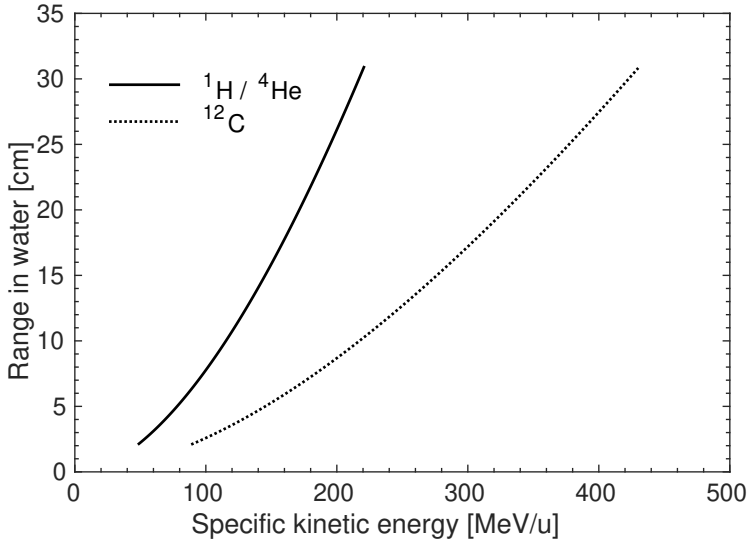

Figure 2.3: Range of ^{1}H, ^{4}He and ^{12}C ion pencil beams in a water target. Data obtained from dedicated FLUKA [Ferrari et al., 2005; Böhlen et al., 2014] MC simulations to reproduce the beam line of the Heidelberg Ion-Beam Therapy Center (HIT) [Bauer et al., 2014].

The range straggling variance σ_R^2 can be computed from the energy loss straggling by [Schardt et al., 2010]

$$\sigma_R^2 = \int_0^{E_0} \left(\frac{\mathrm{d}\sigma_E}{\mathrm{d}x}\right) \left(\frac{\mathrm{d}E}{\mathrm{d}x}\right)^{-3} \mathrm{d}E\,, \tag{2.5}$$

which leads to the following dependency of the straggling width σ_R on the beam range R:

$$\sigma_R = \frac{R}{\sqrt{m}}\; f\left(\frac{E}{mc^2}\right)\,, \tag{2.6}$$

where m and E are the projectile mass and energy, respectively, and f is a slowly varying absorber specific function [Rossi, 1952].

According to equation (2.6), range straggling is reduced for heavier ions. Experimental measurements by Tessonnier et al. [2017] demonstrated that protons and helium ions exhibit a 3.3 and 1.7 times larger straggling than carbon ions in water, respectively, which is only slightly inferior to the $1/\sqrt{m}$ scaling. In tissue range straggling corresponds to around 1.1% of the mean range for protons, while being only 0.5% and 0.3% for helium and carbon ions, respectively [Linz, 2012].

2.1.2 Multiple Coulomb Scattering

When passing through material, ions will be deflected laterally (cf. figure 2.1b). This is mainly caused by a large number of elastic and semi-elastic Coulomb interactions with atomic nuclei causing an accumulated effect called Multiple Coulomb Scattering (MCS).

The most comprehensive theoretical approach to MCS was developed by Moliére [1948]. Since the rigorous calculation can be algebraically complex and cumbersome, Fermi and Eyges [Eyges, 1948] developed a Gaussian theory for the transport of particles in matter. A very practical formula for the scattering angle standard deviation θ_0 after traversing a material slab of thickness x has been proposed by Highland [1975][2]:

$$\theta_0 = 14.1\,\mathrm{MeV}\,\frac{Z}{p\,v}\sqrt{\frac{x}{X_0}}\left[1+\frac{1}{9}\log_{10}\left(\frac{x}{X_0}\right)\right], \tag{2.7}$$

where X_0 is the radiation length of the material and p and v are momentum and velocity of the projectile with atomic charge number Z, respectively.

From the $\theta_0 \propto Z/(p\,v)$ proportionality in equation (2.7) conclusions can be drawn about the scattering behavior of different ion species. Considering the same range, the angular spread of protons and helium ions is around 3.6 and 1.8 times larger than pertains to carbon ions [Gehrke et al., 2018a], being in good agreement with experimental measurements by Tessonnier et al. [2017]. The lateral spread of ion pencil beams due to MCS in water can be seen in figure 2.4.

The original Highland formalism has been generalized by Gottschalk et al. [1993] for thick targets and when using the refinements proposed by Lynch and Dahl [1991] one obtains the following expression for the moments $A_n(x_1, x_2)$ $(n = 0, 1, 2)$ of the projected

[2]The exact energy constant from Highland's original publication is $17.5\ \mathrm{MeV} \times 1.125/\sqrt{2} = 13.92\,\mathrm{MeV}$. However, nowadays 14.1 MeV is normally used as standard.

angular-spatial distribution at depth x_2, assuming an entry depth x_1:

$$A_n(x_1, x_2) = E_0^2 \left[1 + 0.038 \ln\left(\frac{x_2 - x_1}{X_0}\right)\right]^2 \times \int_{x_1}^{x_2} \left(\frac{Z}{p\,v}\right)^2 \frac{(x_1 - x')^n}{X_0}\,\mathrm{d}x' \,, \tag{2.8}$$

where $E_0 = 14.1\,\mathrm{MeV}$ is an empirical energy constant (cf. equation 2.7).

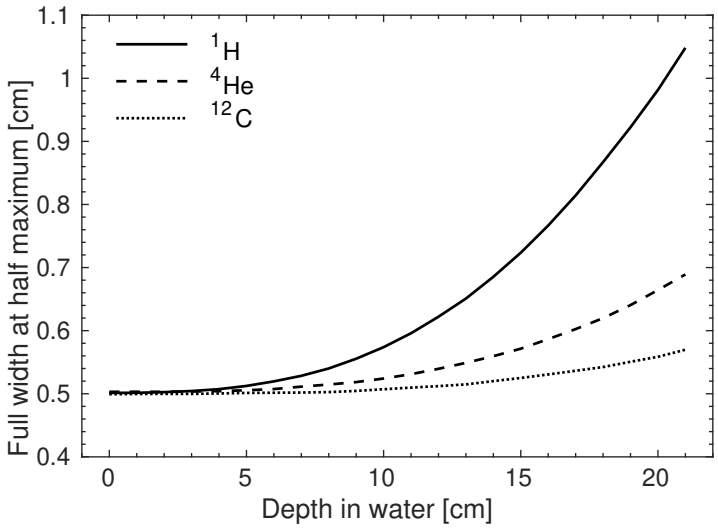

Figure 2.4: Lateral scattering of ^{1}H, ^{4}He and ^{12}C ion pencil beams in a water target. The initial beam spot size is 0.5 cm Full Width at Half Maximum (FWHM). Data obtained from FLUKA [Ferrari et al., 2005; Böhlen et al., 2014] MC simulations.

2.1.3 Nuclear Reactions

In addition to electromagnetic processes, there is a finite probability that charged particles directly interact via the nuclear force (cf. figure 2.1c). These interactions can be *elastic* (kinetic energy is conserved and internal states of target nucleus and projectile are unchanged) or *inelastic* (kinetic energy is not conserved and nuclei may undergo fragmentation). Nuclear reactions of helium/carbon ions (nucleus-nucleus) and protons (nucleon-nucleus) are conceptually different since the incoming nucleons are not free [Kraan, 2015].

Nucleus-nucleus collision reactions can be described by the two-step abrasion-ablation model [Hüfner et al., 1975] illustrated in figure 2.5. In the rapid ($\sim 10^{-22} - 10^{-21}\,\mathrm{s}$) abrasion stage, nucleons are striped off in the overlapping reaction zone (*fireball*) forming pre-fragments. During the ablation stage, which proceeds on a much slower time scale ($\sim 10^{-18} - 10^{-16}\,\mathrm{s}$), remaining fragments decay by evaporation into the observed stable

nuclei under emission of γ-rays, neutrons, protons, leptons or light fragments. Concluding, reactions at several hundreds of MeV can cause a complete disintegration of projectile and target. A description of the nuclear interaction models implemented within the FLUKA MC code is presented in section 4.1.1.

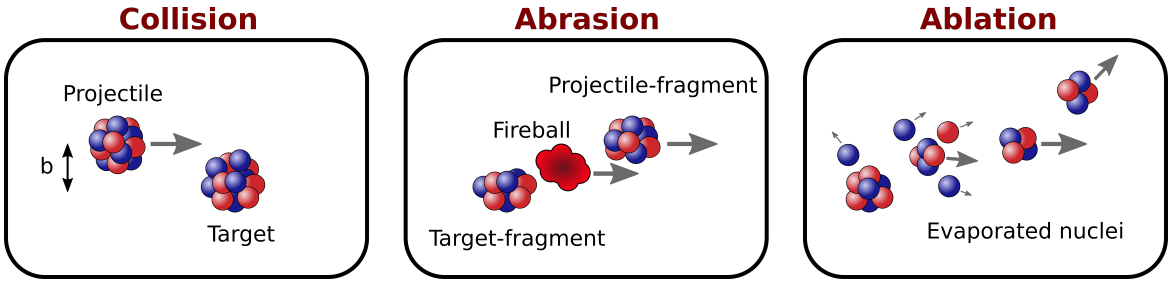

Figure 2.5: Illustration of the abrasion-ablation model for a peripheral nucleus-nucleus collision with overlap factor b. A fireball is formed in the central region by partial particle removal (*abrasion stage*). Afterwards, the created fragments and the fireball will de-excite (*ablation stage*). Figure adapted from Gunzert-Marx et al. [2008] and Durante and Paganetti [2016].

The nucleus-nucleus reaction cross-section σ_R exhibits a strong energy dependence below 20 AMeV [Parodi, 2004] causing distinct maxima. However, for higher energies the dependence vanishes and geometrical factors become decisive since peripheral collisions prevail. The cross-section can be parameterized by the energy-independent Bradt-Peters formula [Bradt and Peters, 1950]:

$$\sigma_R = \pi\, r_0^2 \left(A_p^{1/3} + A_t^{1/3} - b \right)^2 , \tag{2.9}$$

where A_p and A_t are mass number of projectile and target, respectively, b is the overlap or transparency factor (cf. figure 2.5) and r_0 the nucleon radius. Nuclear reactions have important practical consequences, affecting ion therapy and ion imaging. First, the primary particle fluence Φ decreases exponentially as a function of depth x inside the target:

$$\Phi(x) = \Phi_0\, e^{-\mathcal{N}\sigma x} , \tag{2.10}$$

where $\mathcal{N}$ is the atomic density of target nuclei in the material, σ is the total reaction cross-section and Φ_0 is the initial fluence. Accordingly, approximately 20% of all protons in a typical treatment scenario will undergo inelastic nuclear interactions [Durante and Paganetti, 2016] and only around 50% of all ^{12}C ions actually reach the designated depth. A comparison of the primary particle fluence reduction for protons, helium and carbon ions is shown in figure 2.6 for the case of a water target.

For protons, only target fragmentation can occur. While the contribution of nuclear recoils is mostly negligible since they remain approximately at rest at the interaction point [Paganetti, 2002], the spatial pattern of energy deposition is considerably affected [Parodi, 2004]. This is predominantly due to the liberation of secondary protons and neutrons, since light nuclei do not undergo fission. Additionally, the neutron contamination has a non-negligible biological impact causing an increased risk for radiogenic late effects [Newhauser and Zhang, 2015]. Interestingly, neutron contributions inevitably produced inside a patient are comparable for carbon ion and proton therapy at the same treatment dose [Schardt et al., 2010]. The reduced number of ^{12}C ions required for the same energy deposition compensates for the higher neutron yield per primary ion. Projectile fragmentation is one of the major reasons why ions beyond oxygen are no longer considered for particle therapy.

For helium and carbon ions projectile fragmentation is the dominant contribution to secondary particle build-up along the penetration depth (cf. figure 2.7). Fragments are mostly forward emitted in the laboratory frame with nearly the original velocity [Greiner et al., 1975], creating a mixed radiation field. Light fragments with $Z < Z_p$ travel beyond the initial primary range due to the A/Z^2 range dependence at the same velocity (cf. equation (2.4)), causing an energy deposition tail. Additionally, the energy deposition is deteriorated by an enhanced lateral spread compared to MCS [Schardt et al., 2010].

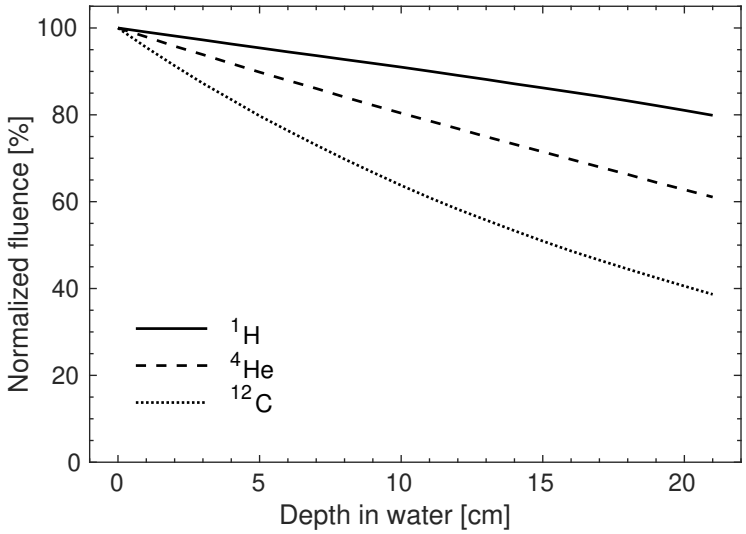

Figure 2.6: Fluence attenuation of ^{1}H, ^{4}He and ^{12}C ion pencil beams in a water target. Data obtained from FLUKA [Ferrari et al., 2005; Böhlen et al., 2014] MC simulations.

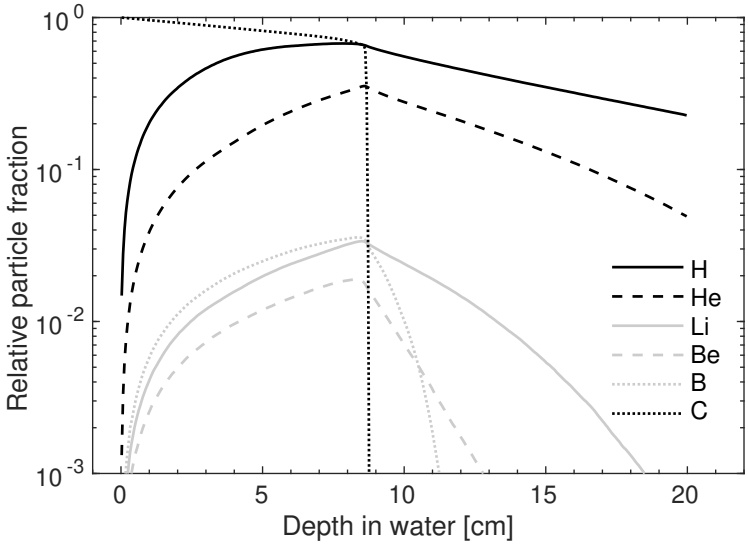

Figure 2.7: Attenuation of 200 MeV/u ^{12}C ions and build-up of secondary fragments in a water target. Data obtained from FLUKA [Ferrari et al., 2005; Böhlen et al., 2014] MC simulations.

Secondary particles and photons originating from nuclear interactions inside the irradiation target can be exploited for image-guidance by means of Positron Emission Tomography (PET) [Parodi et al., 2008], prompt gamma imaging [Polf et al., 2009] or interaction vertex imaging [Henriquet et al., 2012]. Thereby, the ion beam range can in principle be inferred *in vivo* [Parodi and Polf, 2018].

2.2 The Depth-Dose Distribution of Ion Beams

In the previous sections, the energy loss mechanisms of ions were described. However, the most important physical quantity in radiation therapy is dose [Schardt et al., 2010]. Following the ICRU [2011] report, *absorbed dose* is defined as the ratio of the mean energy $\mathrm{d}\epsilon$ imparted by ionizing radiation to matter of mass $\mathrm{d}m$ and has the unit Gray (Gy). For a mono-energetic ion beam of fluence Φ, the absorbed dose D in a thin slice of absorbing material with mass density ρ is related to the stopping power S by:

$$D\,[\mathrm{Gy}] = 1.6 \times 10^{-9} \times S\left[\frac{\mathrm{keV}}{\mu\mathrm{m}}\right] \times \Phi\left[\frac{1}{\mathrm{cm}^2}\right] \times \frac{1}{\rho}\left[\frac{\mathrm{cm}^3}{\mathrm{g}}\right] . \tag{2.11}$$

The final Three-Dimensional (3D) dose distribution of charged particle beams results from a combination of the different physical interaction mechanisms (i.e., *stopping*, *scatter-*

ing and *nuclear reactions*). The main characteristic feature is a steep dose increase toward the end of the ion beam range (cf. $S \propto \beta^{-2}$ in equation (2.1)), the so-called *Bragg peak* [Bragg and Kleeman, 1905], since the energy loss increases as the ions slow down. The longitudinal and lateral spread is enhanced for lighter ions (cf. $\sigma_R \propto 1/\sqrt{m}$ in equation (2.6) and $\theta_0 \propto Z/(pv)$ in equation (2.7)). For heavier ions a dose tail due to light nuclear fragments appears beyond the Bragg peak as shown in figure 2.8.

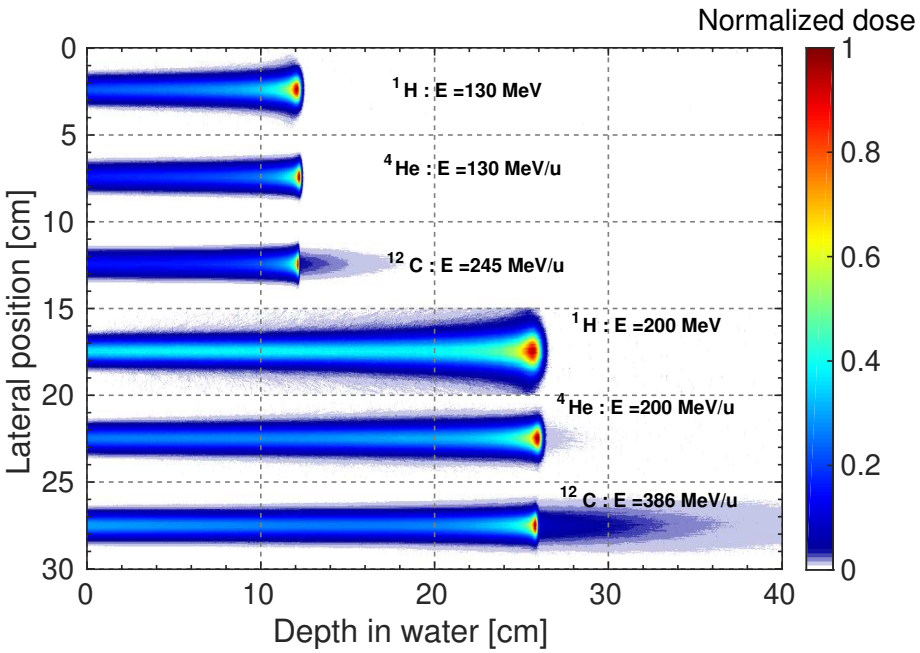

Figure 2.8: Dose distributions of ^{1}H, ^{4}He and ^{12}C ion pencil beams in a water target. The beams have approximately the same range and an initial Gaussian beam spot size of 1 cm FWHM. Data obtained from FLUKA [Ferrari et al., 2005; Böhlen et al., 2014] MC simulations.

2.3 Biological Aspects of Ionizing Radiation

In addition to the aforementioned enticing physical properties originating from the depth-dose distribution, the use of ions for tumor therapy can relate to more favorable biological effects than it pertains to sparsely ionizing radiation[3]. In contrast, this advantage can potentially cause undesired side effects for iCT, which might constrain the tolerable imaging dose, ultimately limiting the achievable image quality.

[3]Photons (i.e., X-rays or γ-rays) are generally considered sparsely ionizing radiation.

2.3.1 Response of Cells to Radiation

The discrete energy depositions associated with charged particles can cause radio-toxic damage sites within cellular structures. The most deleterious lesion is thought to be the Double-Strand Break (DSB), a break in the backbone of each of the opposite DNA strands causing high cytotoxicity [Lomax et al., 2013]. Differences in the biological response between different radiation qualities mainly reflect variations in the microscopic spatial distribution (clustering) of damage along the radiation track. Since the proximity of DNA lesions relates to the damage severity, clustering may be considered as a signature of ionizing radiation in contrast with endogenously induced lesions [Lomax et al., 2013].

Coulomb interactions of heavy charged particles liberate electrons of sufficient energy to generate further ionization, so-called δ-electrons. Consequently, a radial dose distribution is created around the primary ion track. The concept of Linear Energy Transfer (LET) was introduced to quantify the local concentration of energy deposition, taking into account the residual range spectrum of secondary electrons. The ICRU [2011] defines LET as the mean energy lost by charged particles due to electronic interactions in traversing a distance $\mathrm{d}x$ excluding the kinetic energies of all electrons released by charged particles above Δ (not excluding the binding energy):

$$\mathrm{LET} = \frac{\mathrm{d}E_{\Delta}}{\mathrm{d}x}\,, \tag{2.12}$$

becoming numerically equal to stopping power in the limit of $\Delta \to \infty$ and is conventionally used in radiobiology. Hence, the LET is correlated with the ionization density along a particle track for a certain ion. However, different ions of the same LET have different ionization density due to the energy dependence of the track diameter [Fokas et al., 2009].

Low energy ions create a dense emission pattern of slow δ-electrons below 100 eV [Krämer and Durante, 2010], as illustrated in figure 2.9. Those electrons have a mean free path of a few nm, bearing a high probability for ionization events in each of the 2 nm separated DNA strands. High-LET radiation enhances the complexity of clustered damage sites, which have reduced repairability, since lesions are increasingly concentrated in space. By contrast, the energy of secondary electrons from photon beams is much higher than for ions [Paganetti, 2015]. Therefore, high-LET radiation gives rise to a substantially larger number and higher complexity of aberrations compared to low-LET radiation, even for the same number of ionization events per cell [Nikjoo et al., 1998]. Due to the energy dependence, the LET at the end of the particle range is much larger than in the entrance channel creating a differential effect which is compelling for ion therapy.

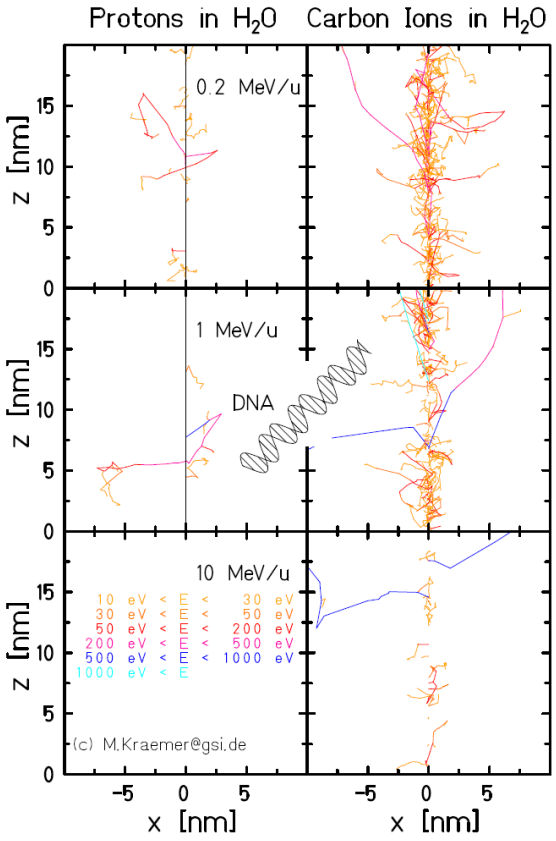

Figure 2.9: TRAX (http://bio.gsi.de/DOCS/trax.html) [Krämer] simulations of δ-electrons from ^{1}H and ^{12}C ions of various energies. Adapted from Krämer and Durante [2010].

Generally, the interaction of radiation with living cells is a complex sequence involving physical, biochemical and physiological processes [Paganetti, 2012a]. A simplified schematic of the biological manifestation of DNA damage is shown in figure 2.10. The secondary electrons liberated by the primary radiation can either directly create DNA damage or indirectly via the formation of highly reactive radicals. The contribution of direct damage increases for high-LET radiation. DNA lesions can be chemically repaired under hypoxia but can also become permanently fixated (i.e., being lethal) by oxygen radicals [Carlson, 2006]. Additionally, damage can be repaired by the cells to their original state via enzymatic repair. Unrepaired or misrepaired cells will either die or form mutations.

2.3.2 The Relative Biological Effectiveness

The repair capability of a cellular system can be parameterized by a linear-quadratic relationship. According to the Linear-Quadratic (LQ) model [Kellerer and Rossi, 1978] the

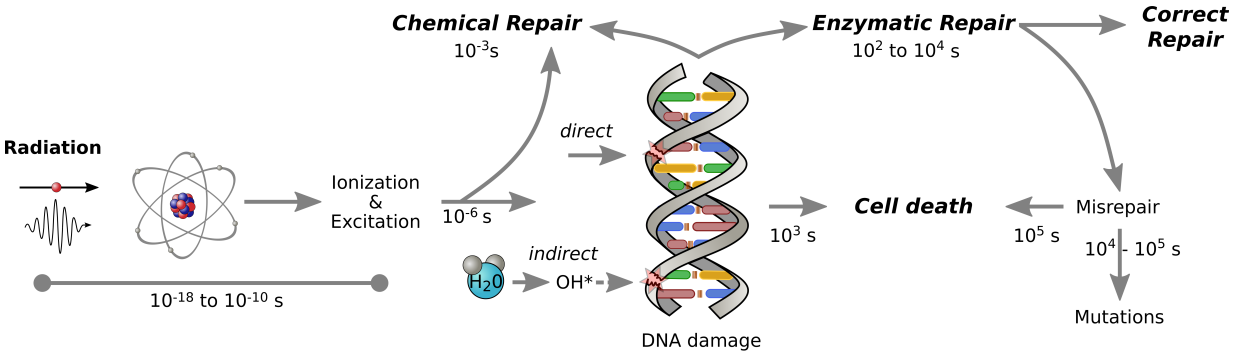

Figure 2.10: Schematic illustrating the biological manifestation of DNA damage and the corresponding time scales. Redrawn from Frese [2011].

cell survival S following the exposure of a dose D is expressed through

$$-\ln S = \alpha\, D + \beta\, D^2\,, \tag{2.13}$$

where α and β are damage coefficients for lethal lesions made by one-track and two-track action, respectively. Both depend on cell type, biological endpoint and radiation quality.

As discussed in the previous section, ion beams have a drastically different biological response compare to photons. This is quantified by the Relative Biological Effectiveness (RBE), which is defined as the ratio of the low-LET reference radiation dose D_X (typically MV X-rays or γ-rays from ^{60}Co) and the charged particle radiation dose D_{ion} required to generate the same biological effect. The RBE is a versatile weighting factor, depending among others on the reference radiation quality, the radiosensitivity of the irradiated cell line or tissue (i.e., α and β), the level of biological effect (i.e., the biological endpoint) and dose (cf. figure 2.11a) as well as the LET and particle type (cf. figure 2.11b).

Within the framework of the LQ model the RBE for reproductive cell death due to the particle irradiation of dose D_{ion} is given by

$$\text{RBE}_{\text{LQ}}\left(\alpha_X, \beta_X, \alpha_{\text{ion}}, \beta_{\text{ion}}, D_{\text{ion}}\right) = \frac{\sqrt{\alpha_X^2 + 4\beta_X D_{\text{ion}}(\alpha_{\text{ion}} + \beta_{\text{ion}} D_{\text{ion}})} - \alpha_X}{2\beta_X D_{\text{ion}}}\,, \tag{2.14}$$

where α_X/β_X and $\alpha_{\text{ion}}/\beta_{\text{ion}}$ are the tissue radiosensitivity parameters for the reference radiation and the considered (particle) radiation, respectively.

In order to calculate the RBE for a specific irradiation scenario, biophysical models are required. Those models aim at relating the biological effect of ionizing radiation to the physical properties of the incident radiation field.

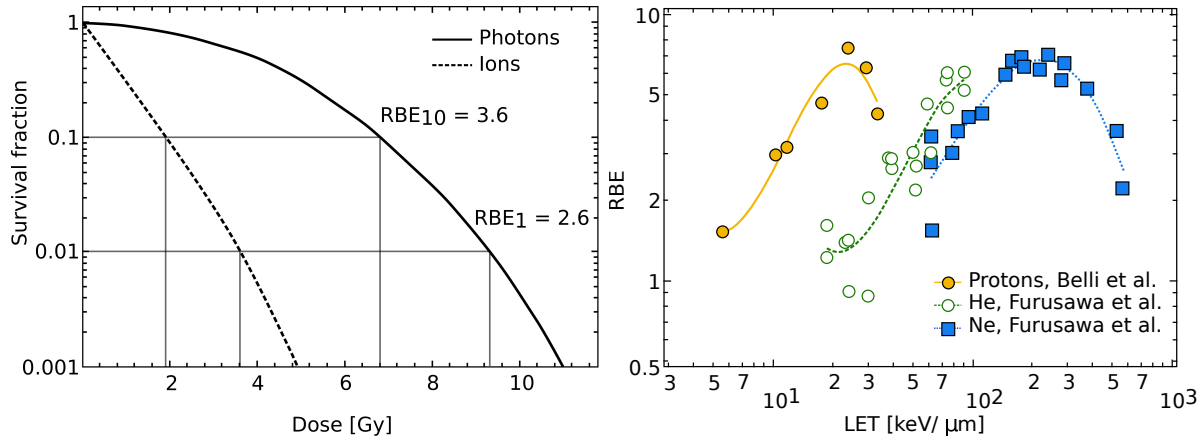

Figure 2.11: (a) Schematic of the RBE definition for the endpoint of 10% and 1% cell survival. (b) Dependence of the RBE on LET for ^{1}H, ^{4}He and ^{20}Ne ion beams. Experimental data from Belli et al. [1992] and Furusawa et al. [2000]. Redrawn from Schardt et al. [2010].

For protons simplified LET-based models can be used, since the relevant proton LET range is low enough to show a linear relationship with dose-response parameters [Paganetti et al., 2015]. However, in clinical practice a single value of 1.1 is widely used. Even though there is strong evidence that the RBE is not constant, clinical data can neither indicate that a generic value of 1.1 is unreasonable, nor that it is correct [Paganetti, 2012a]. For heavier ions, modeling radiation action mechanistically is complicated because the radiation field can be complex due to nuclear fragmentation reactions (cf. section 2.1.3).

Various phenomenological [Wilkens and Oelfke, 2004; Cárabe-Fernández et al., 2007; Wedenberg et al., 2013] and mechanistic [Hawkins, 1998; Friedrich et al., 2012] biophysical models have been proposed by several groups worldwide. The selected approach in this thesis is the RMF model [Carlson et al., 2008], which will be presented in chapter 7.1.

2.4 Conclusions

This chapter provided the basic macroscopic quantities relevant for the physical description of ion therapy and particle imaging. The interaction mechanisms (stopping, scattering and nuclear reactions) of heavy charged particles with matter determine the depth-dose distribution, characterized by a steep gradient at the end of the particle range, the Bragg peak. While ions heavier than protons are benefiting from reduced MCS and range straggling, they also deliver an increased physical dose per particle and suffer from an elevated loss of

primaries in depth due to nuclear fragmentation.

From a radiobiological point of view, ionization processes causing DNA lesions are responsible for cell killing. The DNA damage response pathway is a complex multistep process involving various mechanisms like damage recognition, cell cycle regulation and the activation of appropriate repair systems [Karger and Peschke, 2018]. The biological impact is quantified by the RBE, which is a multivariate weighting factor being typically larger for heavier ions than for protons. Furthermore, the biological dose computation requires sophisticated biophysical models.

"We must not forget that when radium was discovered no one knew that it would prove useful in hospitals. The work was one of pure science. And this is a proof that scientific work must not be considered from the point of view of the direct usefulness of it. It must be done for itself, for the beauty of science, and then there is always the chance that a scientific discovery may become like the radium a benefit for humanity."

Marie Curie

3

Ion Imaging in the Context of Tumor Therapy with Charged Particles

The aim of radiation therapy, in conjunction with other treatment modalities, is to deprive cancer cells of their uncontrolled proliferation potential and ideally kill all cancer cells while avoiding damage to healthy tissue. Since the discovery of X-rays by W. C. Röntgen in 1895, this lead to a quest for the *'magic bullet'* [Durante and Paganetti, 2016] to cure cancer. Through their favorable physical and biological properties outlined in chapter 2, ion beams are generally a promising candidate. On paper the superiority of ions over X-rays is uncontroversial. Especially heavy ions could enable better biological dose to the tumor, improved sparing of healthy tissue and allow to overcome anatomical constraints due to adjacent sensitive structures as illustrated in figure 3.1. However, reality is different and some argue that this superiority is solely *'theoretical'* [Zietman, 2015].

Putting aside the cost ratio of 4.8 and 3.2 for a combined (i.e., carbon ion and proton) and proton-only facility compared to photons, respectively [Peeters et al., 2010], a main allegation is the absence of clear evidence for the magnitude of clinical benefit. A general consensus however is the usefulness for the treatment of pediatric cases because the risk for

secondary malignancies is expected to be lower due the reduced integral dose. Nevertheless, most proton therapy treatments for example in the United States are not pediatric but for prostate cancer, which showed very small benefit, if there is any, over photons [Schulz-Ertner and Tsujii, 2007]. However, there is an expectation that a meaningful clinical superiority of ion beam therapy will be demonstrated on the long term for many indications via controlled clinical trials and large patient cohorts [Zietman, 2015].

A more immanent issue is the susceptibility of ion therapy to range uncertainties and its impact, which is intrinsically related to the implemented ion therapy workflow in clinical practice. This currently imposes a major constraint in exploiting the full potential of ion therapy. In order to understand these limitations, the next two sections will outline the ion therapy workflow with a dedicated focus on the appearing uncertainties, the current clinical solutions and how modern imaging technology like iCT can contribute.

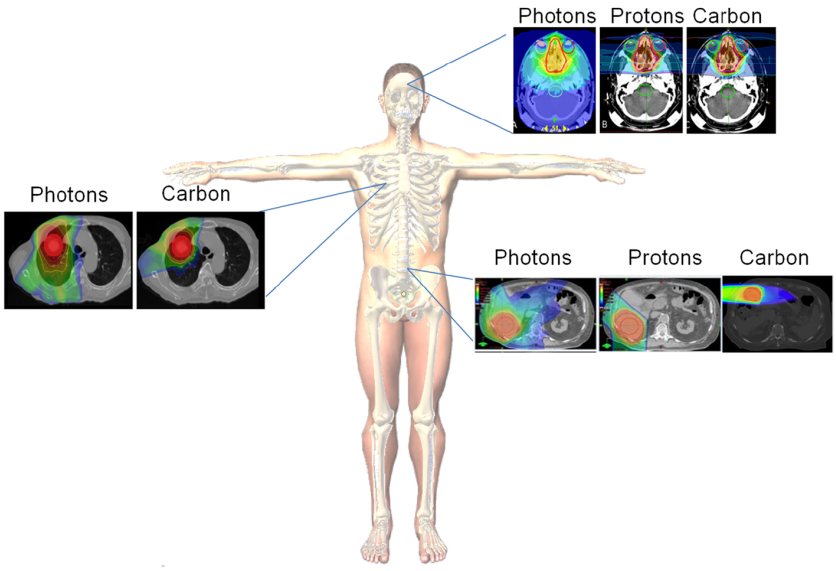

Figure 3.1: Comparison of photon, proton and carbon ion treatment plans for the same histology at different sites such as glioblastoma multiforme (intracranial), lung (thoracic region), and rectal carcinoma (abdominal/pelvic). Extracted from Schlaff et al. [2014].

3.1 Clinical Implementation of Ion Beam Delivery

Producing ion beams of energies up to 430 AMeV requires a powerful and dedicated accelerator, the *'engine'* of a treatment facility [Goitein, 2008]. Nowadays, synchrotron and cyclotron are the two types of commercially available particle accelerators. A cyclotron

is a fixed energy machine with a variable-thickness degrader (typically made of carbon or beryllium) downstream for adjusting the beam energy. Conventional cyclotrons are until now only used for protons since carbon ions exhibit a three times larger magnetic rigidity making the machine excessively large [Schippers, 2009]. In contrast, synchrotrons are typically used for heavier ions and allow the generation of a variable energy by extracting the increasingly accelerated beam at the right moment. An important consequence is the intrinsically bunched macroscopic beam structure (with gaps of few seconds).

The generated unmodified beam is typically not confined to the extent of the target region. Hence, the dose spread of the particle beam, laterally and in depth, has to be modified while being transported toward the patient, ideally from an arbitrary direction using a rotating gantry. A gantry is a mechanical system that rotates the magnets of the last part of the beam line system around the patient [Schippers, 2015]. Generally one distinguishes two different approaches of beam delivery: passive scattering and active pencil beam scanning. The description will be restricted to the latter since all studies presented within this thesis use the state-of-the-art scanning technique.

3.1.1 Pencil Beam Scanning

In pencil beam scanning, ion beams are magnetically displaced using two sets of fast dipoles located several meters upstream the isocenter in order to control the lateral position and scan the target region. This can be performed as discrete step-and-shoot approach (spot scanning) or in continuous fashion (raster scanning). In order to obtain a reasonable treatment duration, the ion beam is deflected with a velocity of approximately 1 cm/ms at the isocenter [Schippers, 2009]. Furthermore, the depth (i.e., the Bragg peak location) is dynamically modulated by varying the beam energy. The basic principle of pencil beam scanning is indicated in figure 3.2.

This technique enables to *'paint'* basically any arbitrary dose distribution, enabling excellent dosimetric conformity even for complex geometries. In addition, ions are used more efficiently with only few being lost during the delivery and no patient-specific hardware like apertures or compensators are required (except for shallow tumors). Consequently, the secondary neutron background is substantially reduced [Goitein, 2008]. The scanning technique also allows the irradiation of a relatively large field of view of up to around $40 \times 40\,\mathrm{cm}^2$ [Smith, 2009]. Certainly, the most important advantage of active beam delivery lies in the possibility to simultaneously modulate the cross-field fluence and the depth-dose curve of the radiation. This so-called Intensity-Modulated Particle Therapy

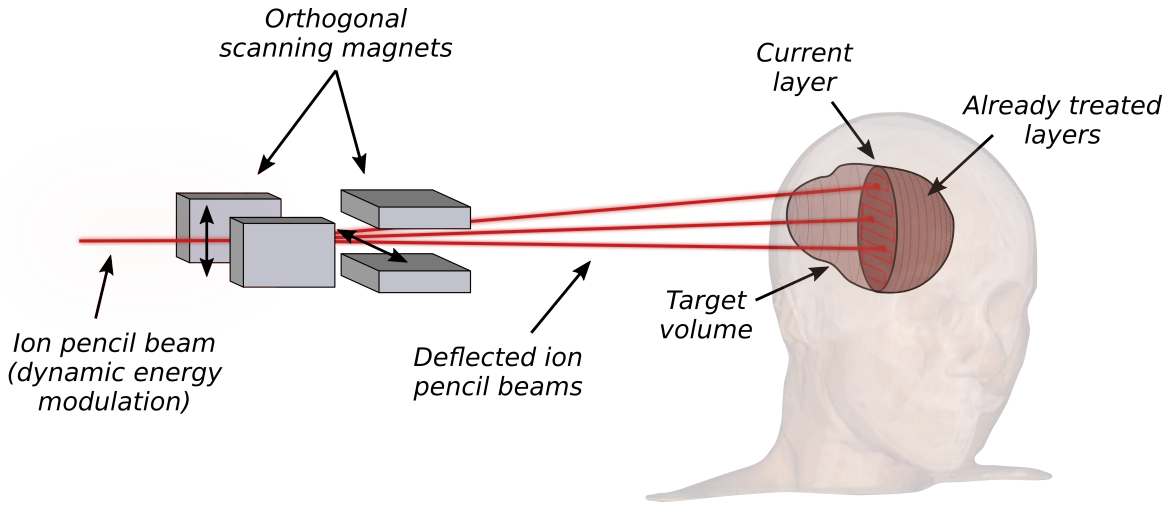

Figure 3.2: Basic principle of active pencil beam scanning: the accelerated ion beam is deflected by two sets of dipole magnets in order to scan a layer of the target region. By dynamically varying the beam energy the Bragg peaks can be located at variable depths. Furthermore, the beam intensity can be individually adjusted to allow full degrees of freedom in modulation.

(IMPT) is the true equivalent of intensity-modulated radiotherapy with photons [Lomax et al., 2015] and provides additional degrees of freedom for treatment planning.

Among the disadvantages of this technique are interplay effects induced by organ and tumor motion [Schippers and Lomax, 2011]. This increased sensitivity demands complex safety mechanisms to accurately control the beam intensity since the parameter values can be time-driven for raster scanning [Schippers, 2009].

3.1.2 Discrepancies Between Planned and Delivered Dose Distribution

An obviously crucial task is the accurate application of the dose distribution to the patient. However, there are several sources for uncertainties solely from the dose delivery itself, i.e., independent of dose calculation or treatment planning.

These uncertainties are for example related to the measurement uncertainty for commissioning in water and the beam reproducibility [Paganetti, 2012b]. Another major source of uncertainties are geometric changes due to patient-tissue variability. Two factors contribute to range degradation in patients [Palta and Yeung, 2012]. First, the patient setup inside the treatment room. Any discrepancy in the patient alignment relative to the planned beam direction is directly translated into range degradation, which can be up to several millimeters [Liebl et al., 2014]. This can be caused by tissue heterogeneities, high-Z re-

gions or air cavities which can shift tangential to the patient surface. Nevertheless, even for perfect external patient setup the internal structures can change due to inter-fractional anatomic variations like tumor shrinkage, weight gain/loss or filling up of sinuses.

Finally, any material present in the beam potentially represents an additional source of errors. The impact of materials in terms of their Water-Equivalent Thickness (WET) needs to be determined precisely. Non-uniformity of accessories like immobilization masks or tabletops can introduce uncertainties in the energy loss [Palta and Yeung, 2012]. This becomes even more important for compensator and apertures used in passive (but occasionally also in active) beam delivery. Additional issues arise for respiration and other intra-fractional motions, which demand dedicated strategies like rescanning, gating or a combination thereof as reviewed by Mori et al. [2018].

3.2 Treatment Planning for Ion Beam Therapy

Treatment planning describes the process of designing a patient-specific plan of the beam arrangement by tweaking various beam-specific and treatment plan-specific parameters. The final goal of a treatment plan is to fulfill the clinical goals set by the radiation oncologist while providing the best trade-off between tumor coverage and sparing of sensitive healthy tissue. The decision about the plan goodness is based on the inspection and quantitative evaluation (e.g., using dose-volume histograms) of the predicted dose distribution that will be (ideally) delivered to the patient during the treatment.

Three different treatment planning concepts can be distinguished: for the Single Field Uniform Dose (SFUD) method, each individual beam angle is optimized in a way to deliver the prescribed homogeneous dose to the target by using Spread Out Bragg Peaks (SOBPs). In contrast, for field patching each single patch field covers only partially the tumor with the distal end of one or more fields being directly abutted against the lateral edge of another field to obtain a nearly uniform dose profile along the junction [Goitein et al., 2002]. The aforementioned IMPT method delivers individually inhomogeneous dose distributions from various directions to yield the desired homogeneous combined dose [Trofimov et al., 2007].

3.2.1 Calculation of an Optimized Patient Dose Distribution

A prerequisite for treatment planning is clinical information in terms of a collection of imaging data along with the experience and expertise of a radiation oncologist. The three main roles of treatment planning are [Lomax et al., 2015]: (1) identification and delin-

eation of the target volume and critical Organs At Risk (OARs), (2) treatment design and (3) definition of machine control data.

The first task is typically supported by various co-registered complementary imaging modalities (e.g., contrast enhanced xCT, magnetic resonance imaging or PET). The treatment design requires imaging data providing information about the expected ion beam energy loss within the patient. However, during the facility commissioning, dosimetric basic data (i.e., laterally integrated depth-dose distributions, fragment spectra (for heavier ions) and lateral dose parametrization) are only measured in water for different beam energies, supported by dedicated MC simulations [Parodi et al., 2012]. Since a patient is made up of various different tissues, the ion beam range must be scaled according to the Relative Stopping Power (RSP) of the traversed materials. The RSP is defined as the ratio of the electronic stopping power for the specific material and water. Using the Bethe-Bloch equation (cf. equation (2.1)) without correction terms, one obtains for a material m:

$$\mathrm{RSP} = \eta_e \times \frac{\ln\left(2\,m_e c^2\,\beta^2 / \langle I_m\rangle\,(1-\beta^2)\right) - \beta^2}{\ln\left(2\,m_e c^2\,\beta^2 / \langle I_w\rangle\,(1-\beta^2)\right) - \beta^2} = \eta_e \times K\,, \tag{3.1}$$

where $\eta_e = \rho_{e,m}/\rho_{e,w}$ is the relative electron density (with respect to water), $c\beta$ is the particle velocity, m_e is the electron mass and $\langle I_m\rangle$ and $\langle I_w\rangle$ are the mean ionization energies for material m and water, respectively. Schneider et al. [1996] investigated different tissue substitutes and found that the parameter K varies between 0.975 and 1.025, but is rather insensitive to the value of $\langle I\rangle$. This demonstrates that relative electron density and RSP are closely related but neither is the ratio unity nor is it constant [Langen et al., 2015]. In current clinical practice, the RSP map of a patient is derived via a semi-empirical conversion from the Hounsfield Unit (HU) values of a (single energy) xCT.

In order to make judicious decisions about a treatment plan, one needs to accurately predict the dose distribution finally received by the patient. For this calculation two fundamentally different computational approaches exist: semi-empirical analytical dose calculation algorithms and MC-based techniques.

Analytical algorithms for particle therapy treatment planning were first developed by Chen et al. [1979] using a broad-beam ray casting technique and are now universally used in routine practice. They are considerably faster than MC methods by making numerous simplifying approximations; nevertheless, they are still accurate enough in most cases. However, particularly simple ray-casting methods have limited capabilities in modeling the disturbance of the dose distribution behind complex heterogeneities causing a change

of the energy spectrum (so-called range dilution). This is incorporated in more advanced analytical pencil beam methods [Schaffner et al., 1999]. Here, the beam is modeled as a superposition of various individual narrow beamlets, referred to as pencil beams, with weights directly proportional to the particle fluence. This conceptual assumption is suitable since narrow ion beams are pencil beams by themselves, but with an extended phase space. Simply speaking, the general formalism for calculating the energy released within the patient is a convolution of the modeled fluence along the pencil beam axis with a lateral energy diffusion kernel [Clasie et al., 2012]. However, the accuracy of the implementation highly depends on the mathematical description of the involved physical interactions. Advances of the original concept, especially for the use in IMPT were provided by the algorithm of Soukup et al. [2005] introducing beamlet decomposition into sub-spots to better account for the finite extent of lateral heterogeneities and an accurate incorporation of the nuclear beam halo. All these improvements are very important for active scanning beam delivery since small discrepancies significantly accumulate for several thousands of beamlets. An example for analytical pencil beam algorithms is the dose engine of the Treatment Planning System (TPS) RayStation (*RaySearch Laboratories, Stockholm, Sweden*), which was used for the work presented in chapter 6.

MC transport techniques are still considered as gold standard for dose calculation since they are more accurate than analytical models in that they take into account the physical interaction processes during the transport [Newhauser and Zhang, 2015]. MC methods employ repeated random sampling of the interaction probability density function to mathematically create the particle transport. The general concept of this technique for particle interaction simulation will be outlined in chapter 4.1. The main dosimetric difference compared to analytic algorithms is the adequate handling of MCS, which becomes particularly important at high-density gradients in the beam direction like tissue-lung interfaces [Paganetti et al., 2015]. A drawback of MC methods is the long computational time, since the statistical uncertainty of the dose calculation depends on the number of simulated particle histories. While this is currently limiting the use in clinical routine [Knopf and Lomax, 2013], recently developed GPU-based MC approaches have already demonstrated a significant gain in speed [Jia et al., 2014].

A crucial step in treatment planning is the optimization of the plan itself, aiming at the best possible treatment plan for the patient. For the case of active scanning, this requires to determine the pencil beam intensities that result in a dose distribution as close as possible to the desired one. *Forward* planning or *'manual optimization'* (even though in a strict

mathematical sense it can not be termed optimization since it neither involves an iterative adjustment nor is it systematic [Trofimov et al., 2012]) is normally too complicated if the irradiation scenario allows for several degrees of freedom. Hence, the optimization problem is mathematically formulated as an *inverse* problem within the TPS solved by minimizing or maximizing an objective function while satisfying a set of constraints. This represents a typical large-scale optimization problem, particularly if convex objectives and constraints are used [Unkelbach et al., 2015]. Commercial systems typically solve the treatment plan optimization problem with a single-criterion approach [Trofimov et al., 2012], i.e., using a composite objective function as overall estimate of the plan quality.

One should keep in mind the importance of the underlying imaging data of the patient. Independent of the selected planning strategy, dose calculation engine or optimization algorithm, any variations between the planning data and the actual patient will cause changes in the dose distribution delivered to the patient.

3.2.2 Range Calculation Uncertainties

Range calculation uncertainties can be divided in two groups: those from the patient model based on volumetric Computed Tomography (CT) data and those from the dose calculation algorithm itself. Since most uncertainties do actually depend on the beam energy or range it is appropriate to give uncertainties in % rather than mm [Paganetti, 2012b].

As previously mentioned, the image data plays a crucial role since it defines the ions' energy loss assumed by the TPS, consequently defining the dose distribution. Current clinical practice in treatment planning relies on the use of tomographic images obtained with X-rays. Here one has to distinguish between two approaches, since they provide different accuracy in estimating the required RSP. Single energy xCT (normally simply referred to as xCT) is the commonly used system. In contrast, Dual Energy Computed Tomography (DECT) is a modern approach; however, already being commercially available.

Single energy xCT

Single energy xCT images contain information on the photon attenuation coefficient μ relative to water expressed in the HU scale:

$$\mathrm{HU} = \frac{\mu_m - \mu_w}{\mu_w} \times 1000 = \left(\frac{\mu_m}{\mu_w} - 1\right) \times 1000\,, \tag{3.2}$$

where μ_m and μ_w are the attenuation coefficients for the specific material m and water,

respectively. Since there is no functional relationship between the measured HU values and the required RSP because photons and ions interact in a substantially different way, semi-empirical calibration methods are commonly employed. In the most straightforward approach called *'tissue substitute'* calibration, tissue substitutes of known density and chemical composition are imaged [Chen et al., 1979]. Afterwards a direct calibration of the HU values is performed by either calculating or measuring the corresponding RSP values and assuming a bi-linear relationship.

The *stoichiometric* calibration proposed by Schneider et al. [1996] allows a more precise conversion and is widely adopted in the ion therapy community. This method is based on the dependence of the photon attenuation on the electron density ρ_e:

$$\mu = \rho_e \left(\sigma^{\mathrm{pe}} + \sigma^{\mathrm{coh}} + \sigma^{\mathrm{incoh}}\right) , \tag{3.3}$$

where σ^{pe}, σ^{coh} and σ^{incoh} are the cross sections (per electron) for the photo electric effect, coherent (Rayleigh) and incoherent (Compton) scattering, respectively. For a polyenergetic X-ray beam with a peak energy less than 1.02 MeV, the cross sections can be parametrized by their dependence on the effective atomic number:

$$\mu = \rho_e \left(K^{\mathrm{pe}} \tilde{Z}^{3.62} + K^{\mathrm{coh}} \hat{Z}^{1.86} + K^{\mathrm{KN}}\right) , \tag{3.4}$$

where K^{pe}, K^{coh} and K^{KN} are constants which characterize the relative contribution of photoelectric interaction, coherent and incoherent scattering for the used xCT energy spectrum, respectively. $\tilde{Z}$ and $\hat{Z}$ are the effective atomic numbers for composite materials, calculated according to Jackson and Hawkes [1981].

Using the parametrization of equation (3.4) for water and a certain material m, equation (3.2) becomes a function of three scanner-specific parameters (K^{pe}, K^{coh} and K^{KN}) and three object-related parameters ($\rho_{e,m}$, $\tilde{Z}_m$ and $\hat{Z}_m$):

$$\frac{\mathrm{HU}}{1000} + 1 = \eta_e \frac{\left[K^{\mathrm{pe}} \tilde{Z}_m^{3.62} + K^{\mathrm{coh}} \hat{Z}_m^{1.86} + K^{\mathrm{KN}}\right]}{\left[K^{\mathrm{pe}} \tilde{Z}_w^{3.62} + K^{\mathrm{coh}} \hat{Z}_w^{1.86} + K^{\mathrm{KN}}\right]} . \tag{3.5}$$

The stoichiometric calibration procedure can be separated into four steps [Yang et al., 2012]: (1) imaging of tissue substitutes of known density and elemental composition using the treatment planning xCT scanner; (2) calculation of the scanner-specific K parameters using the measurements of step 1; (3) calculation of *'virtual'* (i.e., theoretical) HU/RSP

pairs for typical human tissues based on the density and elemental composition recommended in the literature using equations (3.1) and (3.5); (4) derivation of the calibration curve using a linear regression within each tissue group and connecting them piece-wise.

An exemplary stoichiometric calibration curve is shown in figure 3.3. The range uncertainties related to the RSP estimation with this method were comprehensively reviewed by Yang et al. [2012], who separated the following uncertainty categories:

- Uncertainties inherent to the xCT imaging of the patient (e.g., scatter conditions and beam-hardening effects).
- Uncertainties in the parametrization of the stoichiometric formula (i.e., parameters K^{pe}, K^{coh} and K^{KN} in equation (3.4)).
- Uncertainties due to the use of ICRU standard tissues, which do not reflect tissue variations of individual patients (e.g., due to age or health).
- Uncertainties in the mean excitation energies.
- Uncertainties from the assumption of an energy-independence of the RSP by the dose calculation algorithm.

The composite range uncertainty (95^{th} percentile) for different treatment sites was $3.0 - 3.4\%$ due to the large abundance of soft tissue [Yang et al., 2012].

Dual energy xCT

DECT exploits, in contrast to single energy xCT, scans at two different photon energy spectra (typically 100 kVp and 140 kVp). This is currently implemented in several different ways in commercial scanners [Siegel et al., 2016; Albrecht et al., 2018]: Source-based solutions include dual-source (two X-ray tubes and two corresponding detector rows), dual-spin (one X-ray tube acquiring two consecutive spiral scans at different kVp), rapid kVp switching (alternation between different kVp energies within the same gantry rotation), and twin-beam (one X-ray spectrum that is separated in two energy spectra by using a split-filter). Detector-based DECT solutions include dual-layer *'sandwich'* detectors (two-layered detector separating the high- and low-energy photons) and photon counting xCT.

The additional information gathered by a DECT system can be used to separate the material contributions of the measured attenuation coefficient. Using the material decomposition approach, the material of every voxel imaged can be separated into its constituent elements expressed in terms of two basis materials (e.g., soft tissue and calcium). Alternatively, and more important for RSP estimation, the spectral decomposition enables

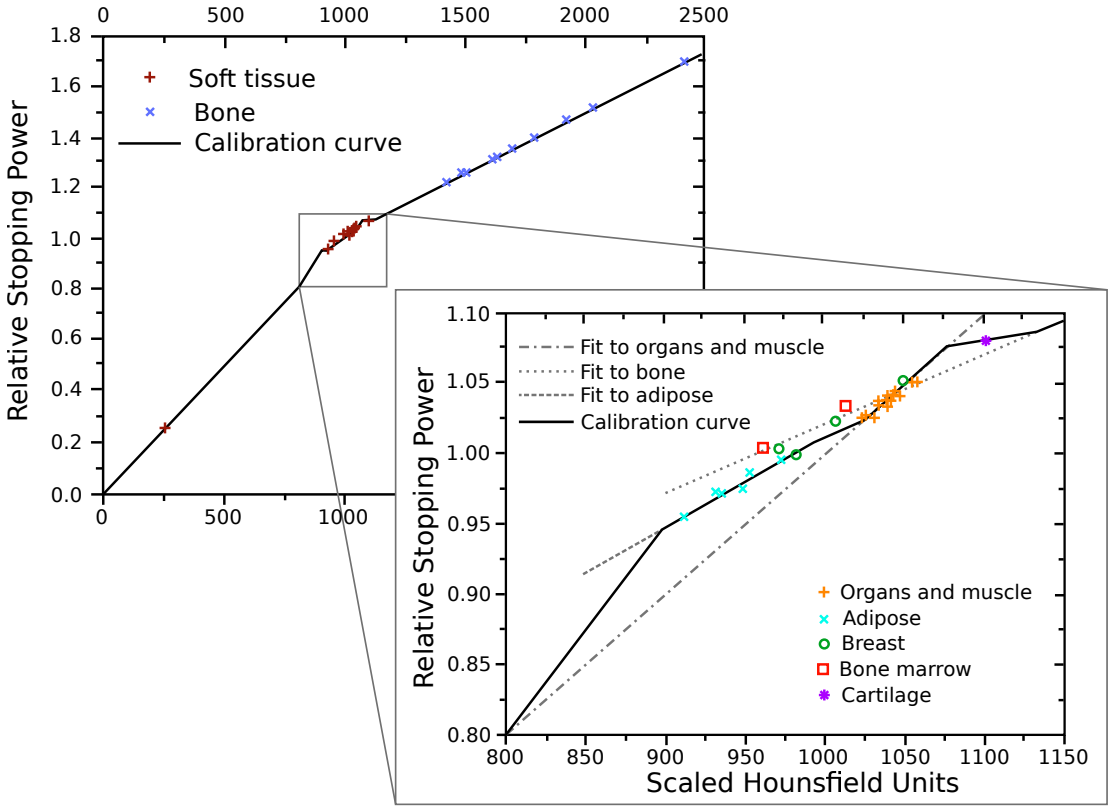

Figure 3.3: Stoichiometric calibration curve and calculated HU-RSP pairs for various biological tissues. Image redrawn from Schaffner and Pedroni [1998].

a transformation of the attenuation maps into relative (to water) electron density (η_e) and effective atomic number (Z_{eff}). In contrast to the stoichiometric parametrization, not the relative contribution of the different interactions mechanisms (i.e., the K parameters) have to be determined, but their energy dependency using measurements with two different photon spectra. Various methods [Alvarez and Macovski, 1976; Heismann et al., 2003; Saito, 2012; Landry et al., 2013] have been proposed for spectral decomposition either in projection-domain (i.e., in pre-reconstruction space) or in image-domain (i.e., in post-reconstruction space).

Yang et al. [2010] first proposed the use of DECT for reducing RSP uncertainties with respect to the stoichiometric calibration for single energy xCT. They found an empirical linear relationship between the logarithm of the mean excitation energy and the effective atomic number of human tissues. Hence, DECT provides basically by design the possibility to calculate RSP directly from equation (3.1), which makes the DECT method more robust against tissue variations in density and elemental composition [Langen et al., 2015].

Theoretical RSP improvements of up to 2% were observed for selected materials using DECT images for proton range calculation in MC simulations [Hünemohr et al., 2014]. Hudobivnik et al. [2016] and a retrospective clinical study by Wohlfahrt et al. [2017] demonstrated the improved range accuracy for DECT-based treatment planning. Water-equivalent range variations with respect to single energy xCT were mostly 1.5% for cranial tumors, putting forward some design goals for iCT as it will be discussed in chapter 6.

Besides the HU-RSP conversion, the HU values themselves have intrinsic uncertainties arising from noise, beam-hardening and the tomographic image reconstruction (e.g., partial volume effects from density heterogeneities).

Furthermore, non-organic high-Z materials like dental fillings, hip prosthesis or orthopedic hardware cause extremely high X-ray absorption outside the HU range of clinical scanners. Direct beam paths through implants can create range underestimation of up to 77% [Jäkel, 2006], which can be significantly reduced by using empirical range relations [Jäkel et al., 2001]. Furthermore, the strong attenuation causes *'streak artifacts'* during the tomographic reconstruction that can severely deteriorate the image quality and cause large uncertainties in the ion beam range [Jäkel and Reiss, 2007].

Regarding the dose calculation, density heterogeneities can be difficult to handle correctly by pencil beam algorithms (predominantly for protons, depending on the distribution of the inhomogeneities relative to the treatment field [Bauer et al., 2014]). This is mainly caused by range degradation effects due to MCS. For small fields, analytical calculations in patients might misevaluate the dose in the target volume by several percent when the ion beam is traversing a highly inhomogeneous region [Bueno et al., 2013].

3.3 Managing Range Uncertainties in Clinical Practice

Particle therapy can be considered a double-edged sword. On the one hand it allows a potentially high dose conformity to the target region being one key benefit. However, on the other hand, this also entails the peril of inflicting severe damage to undesired locations if the particle range is not precisely known and accurately delivered. This is schematically illustrated in figure 3.4. The depth-dose distribution of protons (and ions in general) is more susceptible to range uncertainties than for photons. This can cause a considerable dose to an OAR (e.g., the brainstem) behind the target. Consequently, exploiting the full potential of particle therapy is challenged by uncertainties appearing in just about every link of the radiotherapy chain [Mohan et al., 2015], as outlined in previous sections.

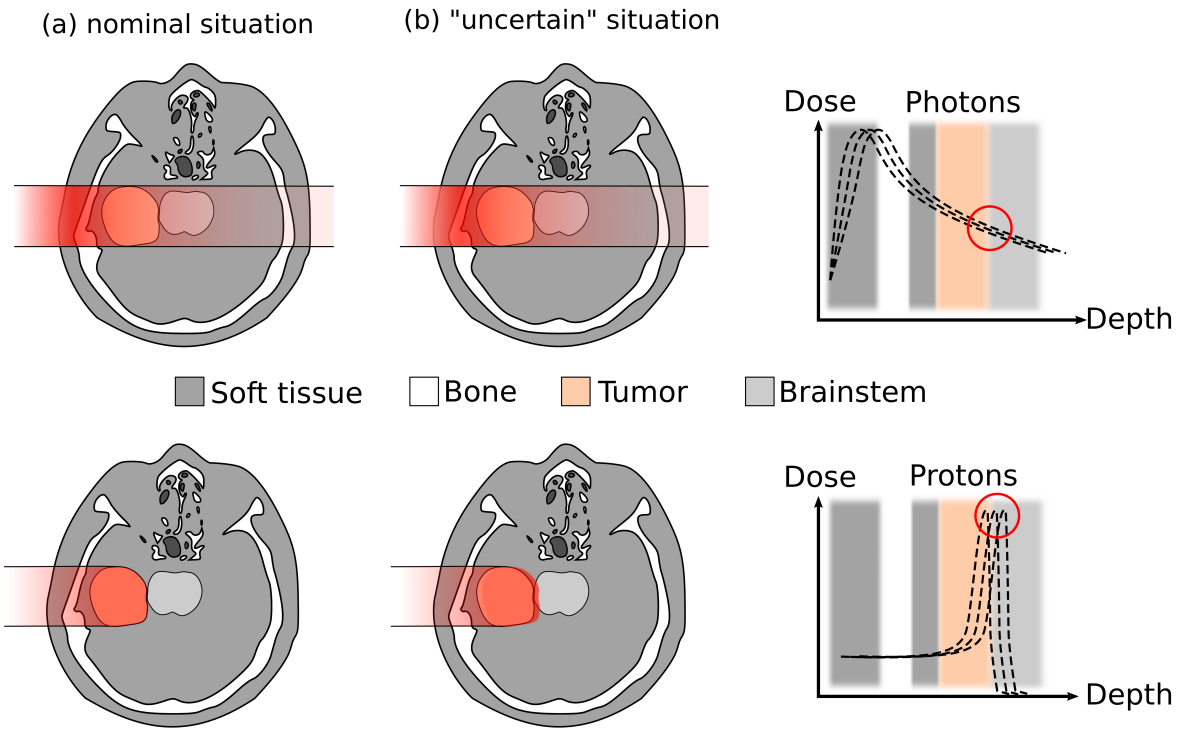

Figure 3.4: Potential dosimetric benefit of a treatment with protons compared to photons and the impact of range uncertainties on the depth-dose distribution. Idea of the illustration adapted from Knopf and Lomax [2013].

There are several sources of evidence that those uncertainties can affect the clinical outcome. An investigation of the effective dose level by Herring and Compton [1971] concluded that a therapeutic dose should be administered with a precision of 3.5% expressed as one relative standard deviation in the combined uncertainty, which resulted in the nowadays accepted standard of 5% (as a 1.5 standard deviation) [Mijnheer et al., 1987]. This corroborates that uncertainties have to be adequately considered in the treatment planning and delivery stage for mitigating complications. In order to manage range uncertainties in clinical practice, the following general strategy is adopted [Mohan et al., 2015]: one tries to minimize uncertainties as much as possible and residual uncertainties need to be incorporate in the planning and delivery process.

Minimize range uncertainties

Reducing geometric uncertainties requires special care and adequate immobilization during the treatment process. This is necessary to ensure stability of the patient's external contour throughout the treatment and hence a reproducible water-equivalent target depth

to minimize inter-fractional variations [Wroe et al., 2015]. For head and neck or CNS (central nervous system) tumors, fiberplast masks, bite blocks and stereotactic frames can be used to guarantee a consistent patient pose. The use of those devices requires accurate characterization and incorporation into the treatment plan. Furthermore, they have to undergo regular quality assurance checks to verify variations with respect to the initial commissioning, for example from mishandling or aging. In addition to external anatomy uncertainties, also inter- and intra-fractional variations of internal structures should be minimized. For prostate cancer treatments for example, endorectal balloons or spacer gels can be utilized to hold the prostate gland against the bony pelvic anatomy [Kruse, 2015].

In order to guarantee a precise positioning of the immobilized patient with respect to the isocentric treatment room coordinate system, image guidance is required. One common solution is the alignment of orthogonal kV setup images with planned digitally reconstructed radiographs relative to skeletal features or implanted fiducials. Recent commercially available Cone Beam Computed Tomography (CBCT) or xCT on rails opened the door to volumetric and even time-resolved in-room imaging in ion therapy (but not always at the treatment isocenter) [Landry and Hua, 2018]. However, the use of CBCT brings technological and workflow challenges. Low image quality due to spatially varying artifacts from increased scattering and truncation impedes the use for treatment planning. Using dedicated correction methods [Landry et al., 2015; Park et al., 2015], CBCT represents the first step toward implementing adaptive ion therapy.

Generally, it would be desirable to acquire a new treatment planning CT if image guidance reveals anatomical changes and adaptation is deemed necessary. However, this needs to be balanced against the additional imaging dose [Mohan et al., 2015].

In order to cope with metal artifacts, software-based correction methods have been proposed and are on the verge of becoming commonly available in clinical practice [Schwarz, 2011]. However, studies on their actual usefulness in clinical proton therapy treatment planning are scarce [Langen et al., 2015].

Incorporating residual uncertainties

It is crucial to maintain the designated dose level within the whole target region for a treatment to be effective. Thus, the radiation oncologist will delineate the visible tumor tissue (the so-called gross tumor volume) and based on his/her experience generally expand it to the clinical target volume to account for the suspected invisible spread of the tumor [Engelsmann and Bert, 2012]. Finally, in a similar manner to photon therapy, systematical and random errors are combined into an additional margin, defining the Planning Target Vol-

ume (PTV). This margin is typically around 3.5% of the prescribed range plus a constant setup uncertainty, which turns out to be relatively conservative [Paganetti, 2012b].

It might appear tempting to aim an ion beam directly against a critical OAR as indicated in figure 3.5(a). However, this is typically avoided in clinical practice due to range uncertainties and potential complications. Hence, intrinsically robust treatment plans are desired, for instance by applying fields tangentially to the OAR (cf. figure 3.5(b) and (c)). Yet this comes at the cost of compromising the dosimetric conformity, since the lateral edge is less sharp than the distal falloff (in particular for proton beams).

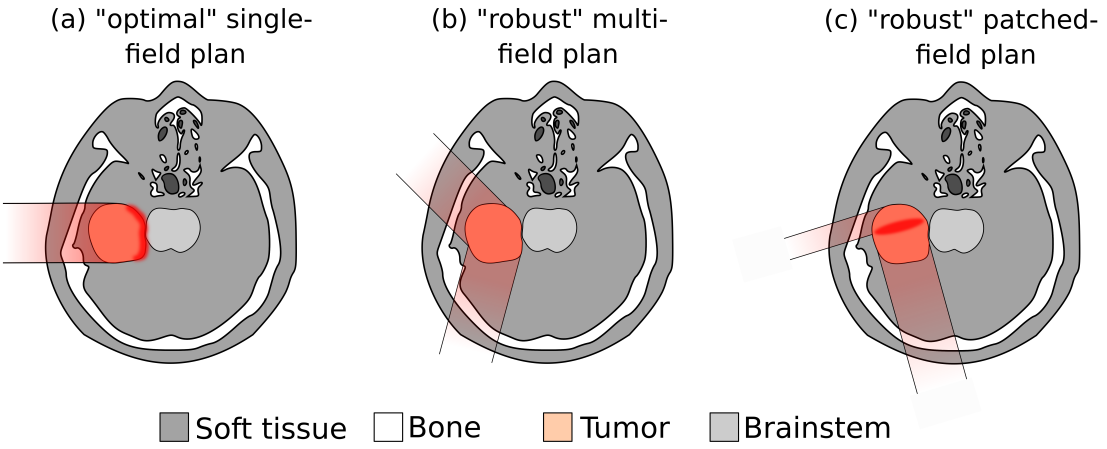

Figure 3.5: Different ion therapy planning strategies and their potential sensitivity to uncertainties in the ion beam range. Idea of the illustration adapted from Knopf and Lomax [2013].

Additionally, the plan robustness can be included in the plan optimization procedure by integrating various uncertainty scenarios in the objective function. Thereby, potential dosimetric effects of delivery and positioning uncertainties can be directly considered, for instance by finding a treatment plan which is as good as possible for the worst case scenario [Trofimov et al., 2012]. Ideally, the optimization should automatically yield a solution to the planning problem, which is intrinsically robust to the considered uncertainties. However, if one tries to ensure adequate target coverage under all likely uncertainties, it will inevitably lead to unwanted over irradiation of neighboring normal tissues [Lomax, 2018]. Thus, it is desirable to interactively explore different trade-off scenario, for instance by using multi-criteria optimization techniques like Pareto surface navigation [Wedenberg et al., 2018].

The quantitative impact of remaining uncertainties on the ion beam range inside the patient was evaluated in the exceptional articles by Paganetti [2012b] and Yang et al. [2012].

3.4 Medical Imaging with Ion Beams

Despite extensive efforts to reduce the origins and consequences of range uncertainties, the clinical implementation of ion beam therapy still faces limitations from remaining uncertainties. It was shown that imaging plays a crucial role for obtaining the patient's RSP map, accurate positioning and to establish an adaptive workflow. Since the current X-ray imaging technology has its limitations in physics and implementation, one might ask: Why not image the patient with the radiation quality available in any treatment room, i.e., the ion beam itself? In contrast to therapeutic applications, ion imaging requires higher energies capable of fully traversing the patient in order to measure changes in the transmitted ion range. It turns out that iCT indeed represents an intuitive solution to significantly reduce or rule out most sources of range uncertainties.

The basic idea of transmission imaging is to infer the internal structure of an imaged object from changes in the transmitted radiation quality due to physical interactions within the object itself. In this sense iCT and xCT are the same. However, there are fundamental differences between the use of X-rays and ion beams. Neutral particles will either interact with the traversed tissue or not and consequently the number of X-rays exponentially decreases, providing information about the photon attenuation within the imaged object. In contrast, charged particles will interact in various substantially different ways as reviewed in chapter 2. This allows to distinguish four different ways of using ions for imaging depending on the selected observable [Bopp et al., 2013].

The commonly used **energy loss iCT** exploits the residual energy or range of particles, which can be related to the RSP as it will be discussed in detail in the following section. Since mono-energetic particles undergo various interactions within the imaged object, statistical fluctuations cause an energy loss dispersion. Consequently, the outgoing particles are characterized by an energy distribution (cf. equation (2.3)), which could be exploited in the reconstruction of **energy straggling (or range dilution) iCT**. Furthermore, particles passing through an object undergo attenuation[1] in much the same way as X-rays, except that the underlying mechanism is nuclear interaction, as discussed in section 2.1.3. In **attenuation iCT** the measured fluence reduction can be related to the inelastic nuclear cross section [Quinones, 2016]. In a similar manner as energy loss, ions experience an increase in deflection with depth due to MCS as explain in section 2.1.2.

[1] It should be noted that there is some inconsistency in the literature about attenuation and scattering imaging, since there is a certain interplay between both mechanisms.

The total mean-square angular deflection of exiting ions after traversing the imaged object can be used to reconstruct the relative scattering power in the so-called **scattering iCT** [Taylor et al., 2016].

The work of this thesis will solely focus on energy loss iCT, referred to as simply iCT from now on, since the reconstructed RSP represents the most important quantity for ion therapy treatment planning.

3.4.1 Motivation and Rationale

The main rationale for pursuing the development of ion transmission imaging is established by four key advantages over xCT:

- Reduced physical dose exposure to the patient [Schulte et al., 2005].
- Improved ion therapy treatment plan accuracy due to reduced RSP uncertainties.
- Absence of artifacts from high-Z materials appearing during the tomographic image reconstruction [Oancea et al., 2018].
- Iso-centric imaging within the treatment room enables new pathways in image-guided and adaptive ion therapy [Landry and Hua, 2018].

Not all points have been equally addressed in the literature so far, especially the second one. Hence, the treatment planning accuracy will be subject of this thesis.

The reduced RSP uncertainty is a consequence of iCT facilitating a direct RSP reconstruction. Following the Bethe-Bloch equation (cf. equation (2.1)), the energy loss rate (or stopping power) can be express as:

$$-\frac{\mathrm{d}E}{\mathrm{d}x}(\mathbf{r}) = S\left(I(\mathbf{r}), E(\mathbf{r})\right) = \eta_e(\mathbf{r})\, F(I(\mathbf{r}), E(\mathbf{r}))\,, \tag{3.6}$$

where η_e is the relative electron density. F is a function of the mean excitation energy (I) and particle energy (E) for an ion of charge Z:

$$F(I(\mathbf{r}), E(\mathbf{r})) = C\frac{Z^2}{\beta^2(E)}\left[\ln\left(\frac{2m_e c^2}{I(\mathbf{r})}\frac{\beta^2(E)}{1-\beta^2(E)}\right) - \beta^2(E)\right]\,, \tag{3.7}$$

where $C = 4\pi\, r_e^2\, m_e c^2\, \rho_{e,w} \approx 0.170\,\mathrm{MeV/cm}$ combines various physical constants, m_e is the electron mass and β is the ion velocity relative to the speed of light. The dependence on $\mathbf{r}$

indicates that all quantities are varying with the position inside the patient. In addition, F is also energy dependent; hence, the differential equation (3.6) does not represent a variable separable form. Dividing equation (3.6) by the stopping power of water (S_w) and rearranging the terms one obtains

$$-\frac{1}{S_w(I_w, E)}\,\mathrm{d}E = \frac{S(I(\mathbf{r}), E)}{S_w(I_w, E)}\,\mathrm{d}x\,, \tag{3.8}$$

where the right-hand side contains the RSP. Under the assumption that RSP is energy-independent, which holds within 0.7 % for tissue-equivalent materials in the energy range of 80 MeV to 300 MeV [Arbor et al., 2015], the energy and position dependent variables can be separated. This allows to perform the integration along the 3D ion trajectory $\mathbf{\Gamma}$ of length L. The left-hand side yields the amount of water corresponding to the measured energy loss, also called Water-Equivalent Path Length (WEPL):

$$\mathrm{WEPL} = -\int_{E_\mathrm{in}}^{E_\mathrm{out}} \frac{\mathrm{d}E}{S_w(I_w, E)} \approx \int_L \mathrm{RSP}\left(\mathbf{\Gamma}(l)\right)\mathrm{d}\mathbf{\Gamma}(l)\,. \tag{3.9}$$

Mathematically, equation (3.9) describes a Radon transform, representing the basis for reconstructing tomographic images. Hence, iCT allows to directly relate the required RSP to measured WEPL values, which are either calculated from the energy loss (requiring knowledge of I_w) or obtained by calibrating the detector response to material of known RSP and thickness [Bashkirov et al., 2016]. It should also be noted that the use of equation (3.9) demands an estimation of the ion path $\mathbf{\Gamma}$ through the object.

3.4.2 Principle of Ion-Based Transmission Imaging and Contemporary Instrumentation Designs

After the mathematical and theoretical foundation of ion imaging, this section discusses the implemented imaging procedures and state-of-the-art systems. Most systems currently under development by various groups worldwide are focused on proton imaging due to the sparse availability of heavy ion accelerators. iCT systems have to be distinguished in two conceptually different approaches: *single-particle tracking* and *integration-mode*.

Single-particle tracking

State-of-the-art single-particle tracking requires tracking of individual ions through the imaged object and a measurement of the associated residual energy or range. The typical imaging system as illustrated in figure 3.6 contains two pairs of 2D position-sensitive tracking detectors before and behind the patient, providing information on the ion position and direction required for the path integral in equation (3.9). Additionally, this enable to take into account the MCS inevitably occurring during the passage through the imaged object. The second component of the detector is a calorimeter or range telescope (or a hybrid system) to measure the residual energy or range of ions, respectively, which can be correlated with the required WEPL information.

The most complete ion imaging system is the phase-II scanner of the US pCT collaboration. Each tracker module consists of two paired 0.4 mm thick silicon strip detectors with a strip pitch of 0.228 mm [Giacometti et al., 2017]. The residual energy is obtained from a fast polystyrene-based scintillator divided in five stages to reduce requirements on the energy resolution [Bashkirov et al., 2016]. With the detection rate of the current system a full scan of half of a human head can be completed in less than 10 minutes [Johnson et al., 2016].

The British PRaVDA (Proton Radiotherapy Verification and Dosimetry Applications) consortium initiated a project to develop the first fully solid-state imaging system for pCT. Their tracker system, composed of silicon strip detectors originally developed for the ATLAS experiment at CERN, provides an active area of around $10 \times 10\,\mathrm{cm}^2$ and a strip pitch of 90.8 µm [Taylor et al., 2016]. The unique feature of this system is to use a stack of the same silicon strip detectors interleaved with absorbers for the range telescope, working as range counter. This allows to cope with an extremely high proton fluence of 2×10^8 protons/second [Esposito et al., 2018]. Recently, a research collaboration in Norway proposed a similar high granularity digital tracking calorimeter based on CMOS active pixel sensors [Pettersen, 2018].

The iMPACT (innovative Medical Protons Achromatic Calorimeter & Tracker) project has the ambitious goal of achieving a global proton rate of 1 GHz [Mattiazzo et al., 2018], thereby reducing the scanning time to a few seconds. CMOS active pixel sensors embedding an innovative compression readout scheme are foreseen for the tracking system [Giubilato et al., 2015]. For the WEPL information a range calorimeter is proposed, which is assembled of up to 64 detection planes segmented into 16 fast (decay time <2 ns) plastic scintillating fingers arranged in orthogonal layers [Mattiazzo et al., 2017].

A rather different approach is pursued by a group at the German Cancer Research Center in Heidelberg for helium ions; however, currently only in radiography domain. They employ a setup of three parallel Timepix detectors downstream of the imaged object [Gehrke et al., 2018b]. These semiconductor pixel detectors can be operated either in time mode for tracking or in energy mode to obtain the image contrast (based on the deposited energy). Information from an additional pair of tracking detectors upstream of the imaged object allows to calculate more sophisticated trajectory models [Gehrke et al., 2018a].

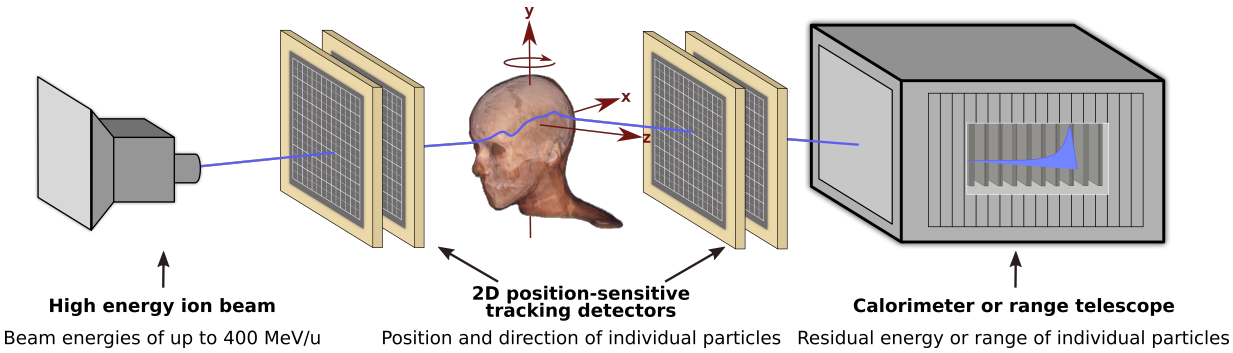

Figure 3.6: Schematic of a single-particle tracking iCT detector system. Position and direction of individual particles from a highly energetic ion beam are measured before and behind the object of interest. The residual range or energy is obtained from a range telescope or calorimeter.

Integration-mode

Integration-mode systems use the accumulated signal from a finite number of particles downstream of the imaged object. Hence, no position-sensitive tracking detectors are in principle required. This enables simplified and cost-effective configurations with easier operation and reduced technological requirements. Consequently, a variety of detector instrumentation designs have been demonstrated for integration-mode, being especially suitable for heavier ions, since they benefit from a smaller beam spot size and reduced MCS. However, for the currently available technology and computational methodology the dose exposure is typically several orders of magnitude larger than for single-particle tracking, thus, potentially restricting the application to radiographic imaging.

At Massachusetts General Hospital Zygmanski et al. [2000] developed a pCT system using a scattered broad beam, modulated in energy, irradiating a Gd_2O_2S:Tb intensifying screen viewed by a cooled CCD camera. The measured intensity was calibrated to WEPL based on a correlation between detector response and beam penetration depth by placing absorbers of various thicknesses. Despite the implementation of a dedicated correction strategy, reconstructed pCT images were severely degraded by MCS edge artifacts.

A similar system was employed for Carbon Computed Tomography (cCT) at the National Institute for Radiological Sciences in Japan [Abe et al., 2002]. Their experiments demonstrated that the reduced MCS of heavier ions significantly improves blurring effects [Muraishi et al., 2009]. An upgraded instrumentation which was extended to human head sized objects achieved a spatial resolution of 1 mm [Muraishi et al., 2016].

Telsemeyer [2012] investigated the suitability of a commercial amorphous silicon flat-panel detector with $800 \times 800\,\mu m^2$ pixel size for cCT. The WEPL information was obtained from a repeated irradiation sequence with pencil beams of different energies. This commercial system enabled a promising RSP accuracy of 0.01; however, the clinical realization was still constrained by an excessive imaging dose of 8 Gy [Telsemeyer et al., 2012].

Additionally, the energy modulation technique has been proposed in the context of passively scatted proton beams degraded by a range modulator wheel [Testa et al., 2013]. Due to the time-controlled irradiation with known time-energy relationship, a time-resolved dose measurement is encrypting the WEPL information of the traversed tissue. Proton radiographies acquired with this technique for an amorphous silicon flat panel detector with 0.388 mm pixel pitch demonstrated a WEPL accuracy of better than 1% [Zhang et al., 2018]. For state-of-the-art active pencil beam scanning, energy-resolved dose functions have been proposed as an alternative [Bentefour et al., 2016].

An advancement in order to reduce the dose required with aforementioned single-detector systems is a multi-layer approach providing an immediate residual range measurement without active (or passive) energy variation. Rinaldi et al. [2013] and Magallanes [2017] investigated a multi-layer ionization chamber for carbon ion transmission imaging. A detailed explanation of this system will be given in chapter 5. For protons, this approach has been pursued with a commercial quality assurance detector [Farace et al., 2016; Krah et al., 2018b]. Besides imaging applications, such instrumentation has also been investigated in the context of patient positioning verification [Hammi et al., 2018].

3.4.3 Physical Limitations and Technological Challenges

The quality of an iCT image predominantly depends on equation (3.9), i.e., the accuracy of the WEPL measurement and path estimation, both being intrinsically limited by the physical interaction processes taking place. The RSP accuracy is mainly constrained by the WEPL resolution of the residual range/energy detector. However, since particles traversing material encounter statistical energy loss fluctuations a certain residual energy distribution occurs even for mono-energetic particles passing trough the same material. Thus the

achievable WEPL resolution is intrinsically constrained by range straggling according to equation (2.6). This corresponds to around 2.8 mm for 200 MeV protons and represents an important design criteria for new detector instrumentation [Bashkirov et al., 2016]. An additional uncertainty originates from the energy spread of the accelerator since no energy measurement is performed upstream of the imaged object.

The ion path estimation precision strongly determines the spatial resolution of the reconstructed image. For single-particle tracking, the accuracy is limited by the statistical uncertainty of the used mathematical path model which will be discussed in section 4.2. Furthermore, the accuracy depends on the tracker system characteristics [Bopp et al., 2014]: (1) the spatial resolution of the position-sensitive trackers; (2) the material budget of the innermost (i.e., closest to the imaged object) tracker half due to MCS in the material; (3) the spacing between the two tracker halves and (4) the distance between object and tracker causing an amplification of uncertainties in position and direction estimation. Integration-mode systems are limited by the absence of direct position information since neither trackers are typically employed nor can the integrated signal be correlated with a single trajectory. Range dilution effects from lateral tissue heterogeneities can cause signal ambiguities of difficult interpretation due to the finite dimension of ion beams [Meyer et al., 2017]. Impact and potential solutions for this problem are investigated in chapter 5.

From a technological point of view, it is very demanding to develop detector instrumentation operating close to the aforementioned intrinsic accuracy limits. In particular, it is not straightforward to achieve the required energy resolution of 1% (for 200 MeV protons) over the whole range of expected residual energy using a direct residual energy calorimeter [Bashkirov et al., 2016]. Hence, hybrid detector systems [Giacometti et al., 2017] potentially offer better WEPL resolution, but at the cost of a more complex instrumentation. In general, it is very crucial to achieve excellent detector efficiency for a system involving a set of measurements for each individual ion, since a single failure will cause the event to be completely lost or at least substantially compromised [Johnson, 2018].

At high particle rates strip-based detectors can cause pattern-ambiguities due to the one-dimensional segmentation. Furthermore, the good spatial resolution of the double-layer design comes at the cost of an increased material budget. An alternative are pixel matrix detectors providing 2D position information from a single sensor approach [Mattiazzo et al., 2017]; however, further increasing the complexity of the system.

Keeping in mind the foreseen clinical application, a potential iCT system needs to work at sufficient detection rate to achieve a reasonable acquisition time. This is important for

economical advantages and patient comfort. Scan times of around six minutes have been already demonstrated with current prototypes [Johnson et al., 2016] being close to the design specification for the data acquisition of less than five minutes originally proposed by Schulte et al. [2004a].

Another issue is that modern ion therapy systems are not designed for ion imaging applications. Typical beam intensities are several orders of magnitude larger than the MHz acquisition rate of current detector system. Nonetheless, manually reducing the beam current using the beam line's research-mode typically causes the intensity to drop below the sensitivity threshold of beam monitoring systems, implemented in the nozzle of therapeutic ion therapy beam lines [Langen et al., 2015]. This can create system interlocks or compromise the beam steering accuracy of the scanning delivery.

Furthermore, the maximum beam energy provided by current accelerator technology typically corresponds to around 30 cm of water, except for the synchrotron-based Radiance 330 proton therapy system (*ProTom International, Inc., Flower Mound, TX, USA*) which enables up to 330 MeV (i.e., around 60 cm range in water) [Owen et al., 2016]. While this allows imaging for cranial locations and upper abdominal regions, it is insufficient to fully penetrate the hip region of a typical adult from all directions, and far short of the shoulder-to-shoulder distance through a human male [Johnson, 2018].

As mentioned previously, time is a crucial aspect for clinical realization. This does not only affect the acquisition itself but also the whole treatment planning workflow. A gantry for rotating the ion beam around the patient to acquire the projection images, as well as modern GPU implementations for dose calculation [Jia et al., 2012] and tomographic image reconstruction [Schultze et al., 2018] are required to perform the whole treatment workflow (i.e., imaging, treatment planning and delivery) inside the treatment room without repositioning of the patient or additional imaging technology.

Last, and maybe most importantly there is the question about the price. Systems fulfilling all aforementioned criteria typically employ detector instrumentation (especially semiconductor technology) from high-energy physics laboratories making them rather expensive. Thus, future clinical systems need to be affordable in order to avoid that ultimately economical limitations prevent iCT to be an option for healthcare providers.

3.5 Conclusions

Ion beam therapy has reached the stage of a widely adopted clinical tool. It has moved from the laboratory to the clinic, and from an obscure activity to a real possibility for healthcare professionals [Goitein et al., 2002]. The particular benefit of ion therapy is still partially limited by uncertainties which are an inevitable part of the planning and delivery stages. Understanding and managing uncertainties are of extreme importance in order to obtain good tumor control and reduce complications [Palta and Yeung, 2012].

Modern analytic dose calculation engines contain an accurate and realistic description of the physical processes undergone by ion beams within the patient. Nonetheless, MC dose calculation is expected to provide a significant accuracy gain in complex geometries where local range uncertainties due to MCS limit analytic algorithms, especially for light ions. Independent of the dose calculation engine, the underlying imaging data impose limitations on the accuracy of TPS predictions. The current clinical practice of deriving the RSP maps of patients from single energy xCT information via stoichiometric or empirical calibration introduces range uncertainties of around 3%. Practically speaking, this means that *'what you see in the treatment plan is not what you get in the patient'* [Palta and Yeung, 2012].

This intrinsic uncertainty when relying on xCT motivates the perspective use of iCT to enable a direct reconstruction of RSP maps from measured WEPL information, thereby eliminating range uncertainties inherent in the aforementioned calibration procedure. This is expected to enhance the treatment planning accuracy, allowing a reduction of the related safety margins for improving clinical outcome of patients receiving ion therapy.

However, currently no iCT system is commercially available or has been integrated into the clinical environment for patient applications. The optimal configuration, in terms of detector instrumentation and particle type, is still under investigation. Besides technological obstacles, the integrability into clinical practice with a dedicated and adjusted workflow still has to be addressed. Nevertheless, iCT has strong potential to be a imaging paradigm shift in ion therapy, facilitating an image-guided and adaptive treatment workflow.

"There is also hope that even in these days of increasing specialization there is a unity in the human experience."

Allan McLeod Cormack

4

Computational Methods for Ion Imaging Investigations

As already indicated by the name *'computed tomography'*, computational methods are an integral part of iCT. This does not only concern the tomographic image reconstruction problem, but also the trajectory simulation and estimation. A key concept for the following iCT studies are MC methods. The FLUKA MC code [Böhlen et al., 2014; Ferrari et al., 2005] was used to benchmark and support the experimental investigations, study the image quality for clinical scenarios under controlled conditions and provide insight on radiobiological aspects at iCT acquisition scenarios. This chapter will introduce the most important concepts of the implemented simulation framework, trajectory estimation and tomographic image reconstruction methods.

4.1 Monte Carlo Simulations

MC techniques are a broad class of computational methods used to determine the average or probable behavior of a system based on the outcome of a large number of trials of

processes that simulate physical events. Each trial is simulated according to a sequence of random (or pseudo-random) numbers based on the known probability distribution of the underlying phenomenon. Due to the statistical sampling, these methods are eminently suitable for the stochastic process of radiation transport [Hendricks, 1994].

MC simulations have been used for a variety of applications in particle therapy, including the calculation of irradiation-induced positron emitter distributions for clinical cases [Parodi et al., 2007], biological dose calculation [Mairani et al., 2010] or treatment planning [Mairani et al., 2013]. Furthermore, MC simulations offer valuable and flexible support for the start-up and clinical operation of particle therapy facilities [Parodi et al., 2012] and the development and optimization of pCT systems [Giacometti et al., 2017].

Compared to traditional analytical methods [Gianoli et al., 2019], MC simulations have the advantage of considering the detailed structure and elemental composition of the human body [Parodi et al., 2007]. Moreover, they fully account for the 3D particle fluence spread and complexity of the mixed radiation field [Böhlen et al., 2010].

In the context of iCT, MC simulations play an important role in understanding the intrinsic limitations of the technique itself, for optimizing the system performance and to test new reconstruction algorithms or data processing methods. This is of particular interest for aspects that are difficult (or even impossible) to address experimentally.

4.1.1 The FLUKA Monte Carlo Code

FLUKA (`www.fluka.org`), which stands for FLUktuierende KAskade, is a FORTRAN-based fully integrated general purpose MC code for the calculation of particle transport and interaction with matter. In the scope of medical physics research it has been applied to various aspects related to particle therapy [Battistoni et al., 2016]. The code is jointly developed and distributed by the European Organization for Nuclear Research (CERN) and the Italian National Institute for Nuclear Physics (INFN).

FLUKA includes a combinatorial geometry package, which allows to model complex geometries, for example, detector systems and objects of interest. The user input files for FLUKA are standard ASCII files containing a sequence of options (often called cards for historical reasons). This is used to tailor the simulation to the need of the user, offering a huge variety of standardized options without requiring programming from the user. However, for more complex or unusual problems not covered by the standard settings, users can further interface the simulation with self-written *'user routines'*. Different templates are already available in the FLUKA library, but have to be modified according to the problem

and the user needs. A graphical user interface called FLAIR (www.fluka.org/flair/) [Vlachoudis, 2009] facilitates the preparation, error-free editing and debugging of simulation input files. Furthermore, it contains an advanced geometry editor and an interface for importing DICOM files, which is important for simulations based on clinical xCT data.

FLUKA can handle transport and interaction calculations for around 60 different particles plus heavy ions in an energy range from few keV up to cosmic ray energies. The charged particle transport is performed through an original MCS algorithm based on Molière's theory [Ferrari et al., 1992], supplemented by an optional single scattering method.

At energies relevant for particle therapy and ion imaging, hadron-nucleus reaction mechanisms are provided by the PEANUT (Pre-Equilibrium Approach to NUclear Thermalization) interaction environment [Ferrari and Sala, 1993]. This model includes a sophisticated Generalized Intra-Nuclear Cascade (GINC) stage, coupled to an exiton based pre-equilibrium and equilibrium particle emission phase. For higher energies, the multiple collisions within the nuclear constituents are considered by means of Gribov-Glauber calculus within a less refined GINC [Fassò et al., 1995].

Nucleus-nucleus interactions from few GeV/u down to around 0.1 GeV/u are handled in FLUKA via an interface to a modified version of the Relativistic Quantum Molecular Dynamics model (RQMD-2.4) [Sorge et al., 1989]. At lower energies, FLUKA switches gradually to an event generator based on the Boltzmann Master Equation (BME) theory [Cavinato et al., 1996; Battistoni et al., 2016]. Above the clinically relevant energies (>5 GeV/u) the DPMJET-III (Dual Parton Model and JETs) [Roesler et al., 2000] event generator is used, which is based on the two component dual parton model in connection with the Glauber formalism [Mairani, 2007].

Within this work the standard FLUKA version 2011.2c with pre-defined 'HADROTHErapy' defaults was used, setting the thresholds for particle transport at 100 keV and for MCS at the minimum allowed energy. In order to reduce the computational time a CSDA without explicit δ-ray production by charged hadrons was employed. For several reasons it is desirable to implement a realistic description of the beam parameters (i.e., energy and momentum distribution, shape and divergence) as produced by a clinical accelerator. First, this is mandatory to ensure good agreement with experimental measurements. Second, the accelerator's energy spread imposes an additional intrinsic limitation on the achievable WEPL resolution. And third, the beam shape is of major importance for the overall integration-mode performance, especially at lateral heterogeneities.

4.1.2 Simulation Model for the HIT Beam Line

An accurate beam model would require a detailed geometrical description of all beam line elements. However, due to confidentiality issues concerning proprietary details of the exact nozzle geometry, this information is not available for external users' applications at HIT. For this reason, Tessonnier et al. [2016] developed phase-space files providing accurate models of the different HIT particle beams without disclosing confidential components of the beam line. A phase-space characterizes the beam by scoring the beam properties of each individual particle crossing a plane perpendicular to the beam direction at a certain location. In this case, the phase-space files contain information on charge, mass, energy, generation (i.e., primary or secondary), coordinates and direction cosines of each particle at the exit of the Beam Application and Monitoring System (BAMS), i.e., downstream of the last element of the HIT beam line about 112 cm before the isocenter.

Tessonnier et al. [2016] used an original narrow-beam approach by simulating the propagation of a central infinitely narrow (*'zero-width'*) beam through the beam line. Therefore, this model can be adapted to any desired beam focus (i.e., beam size in air at isocenter) by convolving it with the estimated beam size in vacuum before entering the beam line. For each energy and particle type ten million primaries were simulated, resulting in phase-space files of around 500 MB, split in primary and secondary particles.

The initial beam generation performed through particle-by-particle sampling of primaries and secondaries from the phase-space files is fully implemented within the *source.f* user routine. Briefly, the primary beam generation works in the following way. Prior to the simulation, the user needs to define an irradiation plan with the desired beam parameters like ion type, energy and focus number, and the locations to be irradiated, the so-called Raster Points (RPs). The selected beam characteristics are specified according to the LIBC (List of Ion Beam Characteristics), which contains the different available initial beam energies (E1-255), foci (F1-6) and intensities (I1-15).

During the initialization phase, the beam plan is read and the first requested phase-space file is loaded. Subsequently, the simulation loops over all requested primaries for the given irradiation position. In this process, a deflection of individual pencil beams is implemented to mimic the active raster scanning technique [Marcelos, 2014]. According to the required deflection angle θ for the selected RP location, the position and direction vector of each particle have to be adjusted individually. For the 3D rotation of the direction

cosine vectors $\mathbf{d} \in \mathbb{R}^3$ the rotation formula of Rodrigues [1840] is implemented:

$$\mathbf{d}' = \mathbf{d}\cos(\theta) + (\mathbf{k} \times \mathbf{d}) + \mathbf{k}\,(\mathbf{k} \cdot \mathbf{d})\,(1 - \cos(\theta)) \;, \tag{4.1}$$

where $\mathbf{k} \in \mathbb{R}^3$ is a unity vector describing the axis of rotation and $\mathbf{d}' \in \mathbb{R}^3$ is the direction cosine rotated by an angle θ being handed to FLUKA, as sketched in figure 4.1. The starting position for the particle transport simulation is derived by adding the individual particle position (randomly sampled from the phase-space file and adjusted according to the selected focus) to the requested RP location (specified at isocenter) at BAMS level, obtained by back-projection along the deflected beam. Once all requested particles for the desired RP are delivered, the beam location and deflection angle will be automatically updated. If necessary, the simulation will loop over all requested energies.

This phase-space approach demonstrated excellent accuracy for several cases (e.g., depth-dose distributions and lateral dose profiles) [Tessonnier et al., 2016] and has been used in various publications in literature [Meyer et al., 2017; Kelleter et al., 2017; Gehrke et al., 2018a]. The results presented in chapters 5, 6 and 7 rely on this beam model and all use the smallest available beam focus (F1).

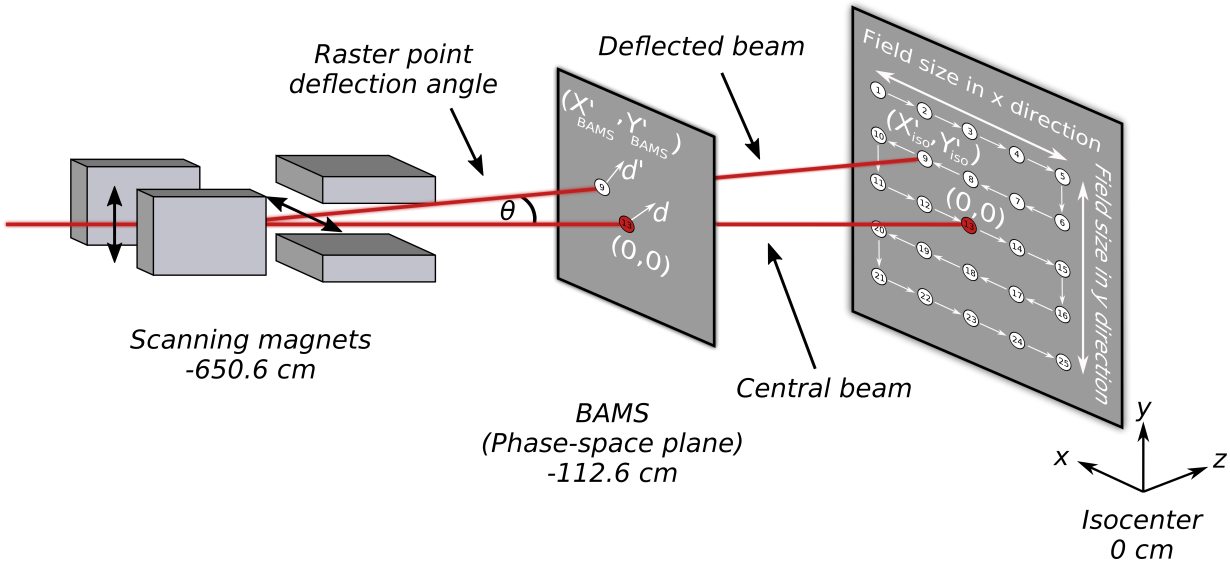

Figure 4.1: The principle of simulating active raster scanning at HIT using phase-space files [Tessonnier et al., 2016]. Cosine director and position at the BAMS level are sampled from the phase-space and adjusted according to the deflection angle of the requested RP and a random spread reflecting the finite beam size.

4.1.3 Simulation Model for the RPTC Beam Line

The pCT system developed and optimized in chapter 8 is foreseen to be experimentally investigated at a ProBeam® beam line (*Varian Medical Systems, Inc., Palo Alto, CA, USA*) based on an example of the Rinecker Proton Therapy Center (RPTC) in Munich.

Consequently, the beam characteristics were implemented following the approach previously developed by Englbrecht [2014]. The initial beam momentum spread and virtual source extension were independently adjusted in an iterative trial and error procedure to best reproduce measured dose distributions. The optimal parameters are stored in a database, which is read during the initialization phase of the simulation to obtain the ideal source parameters for the requested beam energy.

In contrast to the HIT beam line, geometrical dimensions and material compositions of treatment nozzle elements were provided by the vendor. Hence, the simulation model explicitly contains the beam line nozzle including vacuum window, multi-strip and transmission ionization chamber. Particle sampling and active scanning are implemented in a similar manner as for the aforementioned HIT phase-space file approach [Würl, 2014]. Excellent agreement was found between measured dose distributions and MC simulation results also for extended target volumes [Würl et al., 2016].

4.1.4 Implementation of Phantom Geometries

In order to benchmark the achievable image quality, phantoms of different geometry and complexity are required. The *in silico* object geometries were modeled directly within FLUKA according to the known physical dimensions. This is done by using the combinatorial geometry feature, which allows to create complex geometries by combining basic convex shapes using Boolean operations (i.e., union, intersection and subtraction). All material properties were implemented according to the manufacturer specifications.

4.1.5 Implementation of Clinical and Pre-Clinical Data

In order to import clinical and pre-clinical xCT data, voxelized geometries are available in FLUKA, which can be created via an interface in FLAIR. Since it is neither memory- nor CPU-efficient to implement separate materials for each HU value, ranges of HUs are grouped into intervals (also called organs) via the *'MATERIAL'* and *'COMPOUND'* cards. The HU scale is segmented into 24 different materials of defined elemental composition and nominal mean density (i.e., mass density corresponding to the HU value at the center of

the considered interval), based on the work of Schneider et al. [2000] and an extrapolation to include metallic implants of titanium (i.e., HU $\geq$ 3060) [Parodi et al., 2007].

However, the real mass density, influencing nuclear and electromagnetic interaction processes, continuously varies with the HU values within each material sharing a single nominal mean density in the MC simulation. In order to account for this, HU dependent scaling correction factors are applied for each interval [Parodi et al., 2007], as originally proposed by Jiang and Paganetti [2004]. Nuclear processes are adjusted only using the ratio between the mass density and the nominal mean density. In addition, electromagnetic processes are also rescaled to match a bijective clinical-like HU-RSP conversion curve, reproducing a similar curve as implemented at HIT for cranial applications.

In contrast to real patient scenarios, MC simulations enable an ideal HU-RSP conversion curve, since uncertainties due to the stoichiometric calibration are not present. Thus, the ground truth RSP distribution of the patient anatomy, for which the iCT acquisition is simulated, is precisely known. The only remaining uncertainty in the presented approach originates from the energy dependency of RSP, which is negligible for the used energies [Meyer et al., 2019].

4.2 Trajectory Estimation

As a consequence of MCS, ion trajectories are not straight lines. Many small-angle deflections when passing through material cause stochastic path variations. Hence, a curved path has to be implemented in single-particle tracking image reconstruction to avoid substantial degradation of the spatial resolution in iCT images, predominantly for protons. Two mathematical concepts have been established in the ion imaging community: the Most Likely Path and the Cubic Spline Path.

4.2.1 Most Likely Path Formalism

The Most Likely Path (MLP) concept was originally introduced by Schneider and Pedroni [1994]. They developed a formalism to calculate the most probable proton trajectory through an object based on the generalized Fermi-Eyges theory of MCS. Williams [2004] derived a more convenient closed-form representation assuming knowledge of entry and exit position and exit direction by using $\mathcal{X}^2$ statistics. The superior spatial resolution in pCT obtained by Williams's MLP method compared to a Straight Line Path (SLP) was demonstrated by Li et al. [2006].

The MLP expressions of aforementioned articles require the computation of complicated ratios of polynomials. More recently, Schulte et al. [2008] proposed a more elegant and compact matrix-based MLP formalism employing Bayesian statistics to calculate the intermediate positions and directions of maximum likelihood along an ion path. The description of the MLP calculation presented in this section will follow this formalism.

Without loss of generality the MLP derivation will be restricted to a single plane (e.g., the $z-y$ plane) since MCS in lateral and vertical direction can be treated as two independent statistical processes. Let Y_1 be the parameter vector at a certain depth z_1:

$$Y_1 = \begin{pmatrix} y_1 \\ \theta_1 \end{pmatrix} , \tag{4.2}$$

where y_1 and θ_1 are the corresponding coordinate and direction angle at the given depth, respectively. In the same way one can define the 2D parameter vector at entrance (Y_0) and exit point (Y_2) of the traversed object of interest.

Simply speaking, the MLP formalism aims at determining the most probable state vector of a particle at any depth using a Bayesian framework, given the measured information at entry and exit location. In Bayesian statistics, the posterior likelihood that a particle at depth z_1 had a state vector Y_1 for the obtained exit information, $\mathcal{L}\left(Y_1|\text{exit data}\right)$, is related to the prior probability of finding the particle at depth z_1 in the state Y_1 given knowledge on its initial state Y_0, $\mathcal{L}\left(Y_1|\text{entry data}\right)$, and the likelihood of observing the particle with the exit information given Y_1 at depth z_1, $\mathcal{L}\left(\text{exit data}|Y_1\right)$:

$$\mathcal{L}\left(Y_1|\text{exit data}\right) = \mathcal{L}\left(\text{exit data}|Y_1\right)\mathcal{L}\left(Y_1|\text{entry data}\right) . \tag{4.3}$$

In the following, the Gaussian approximation of the generalized Fermi-Eyges theory for MCS (cf. equation (2.8)) will be used to describe the scattering process. Since the object composition is typically unknown, a common approach consists in assuming scattering in homogeneous water. Hence, the likelihood functions will be expressed by bi-variate Gaussian distributions. For instance, the prior likelihood for a particle with zero displacement and angle, can be written in the following compact matrix notation:

$$\mathcal{L}\left(Y_1|Y_0 = \begin{pmatrix} 0 \\ 0 \end{pmatrix}\right) = \exp\left(-\frac{1}{2}Y_1^T\Sigma_1^{-1}Y_1\right) , \tag{4.4}$$

where the scattering matrix Σ_1 contains the variances and covariances acquired between

z_0 and z_1, given by the first three Eyges moments (cf. equation (2.8)):

$$\Sigma_1 = \begin{pmatrix} A_2(z_0, z_1) & A_1(z_0, z_1) \\ A_1(z_0, z_1) & A_0(z_0, z_1) \end{pmatrix} . \tag{4.5}$$

In order to calculate the likelihood, the measurement point must be directed toward the reconstruction point at depth z_1, i.e., one needs to change the local coordinate system of the particle. Since angles in typical iCT scenarios are relatively small, i.e., limited to a few degrees, it is reasonable to apply a small-angle approximation ($\sin\theta \approx \theta$). Therefore, the propagation matrix is defined as

$$R_0 = \begin{pmatrix} 1 & z_1 - z_0 \\ 0 & 1 \end{pmatrix} , \tag{4.6}$$

which directs the probability originating from Y_0 along its path without changing the initial angle. This yields the following notation for the prior probability of obtaining Y_1 given Y_0:

$$\mathcal{L}(Y_1|Y_0) = \exp\left(-\frac{1}{2}\left(Y_1^T - Y_0^T R_0^T\right)\Sigma_1^{-1}\left(Y_1 - R_0 Y_0\right)\right) . \tag{4.7}$$

Following the same procedure, one can define the likelihood of the exit parameter vector Y_2 at depth z_2 given the measurement of Y_1 at depth z_1 as

$$\mathcal{L}(Y_2|Y_1) = \exp\left(-\frac{1}{2}\left(Y_2^T - Y_1^T R_1^T\right)\Sigma_2^{-1}\left(Y_2 - R_1 Y_1\right)\right) , \tag{4.8}$$

where the scattering matrix Σ_2 and propagation matrix R_1 for the transition from z_1 to z_2 are defined analogous to equation (4.5) and (4.6):

$$\Sigma_2 = \begin{pmatrix} A_2(z_1, z_2) & A_1(z_1, z_2) \\ A_1(z_1, z_2) & A_0(z_1, z_2) \end{pmatrix} \quad \text{and} \quad R_1 = \begin{pmatrix} 1 & z_2 - z_1 \\ 0 & 1 \end{pmatrix} . \tag{4.9}$$

By combing equation (4.7) and (4.8) according to equation (4.3), the posterior likelihood becomes

$$\begin{aligned} \mathcal{L}(Y_1|Y_2) &= \exp\left(-\frac{1}{2}\left(\left(Y_1^T - Y_0^T R_0^T\right)\Sigma_1^{-1}\left(Y_1 - R_0 Y_0\right) + \left(Y_2^T - Y_1^T R_1^T\right)\Sigma_2^{-1}\left(Y_2 - R_1 Y_1\right)\right)\right) \\ &\equiv \exp\left(-\mathcal{X}^2\right) . \end{aligned} \tag{4.10}$$

In order to derive the MLP one needs to maximize the likelihood, which corresponds to minimizing $\mathcal{X}^2$. Carrying out the differentiation with respect to z_1 and θ_1 yields

$$\nabla\mathcal{X}^2 = \left(\Sigma_1^{-1} + R_1^T\Sigma_2^{-1}R_1\right)Y_1 - \Sigma_1^{-1}R_0Y_0 - R_1^T\Sigma_2^{-1}Y_2\,. \tag{4.11}$$

Setting this equal to zero and solving for Y_1 results in the following expression for the MLP:

$$Y_{MLP} = \left(\Sigma_1^{-1} + R_1^T\Sigma_2^{-1}R_1\right)^{-1}\left(\Sigma_1R_0Y_0 + R_1^T\Sigma_2^{-1}Y_2\right)\,, \tag{4.12}$$

which can be understood as an average path of the projection of the entry and exit position, weighted by the scattering to the point of interest [Collins-Fekete, 2017].

Since the distribution of possible trajectories is known due to the Gaussian approximation of MCS, the error matrix can be calculated as the inverse of the curvature matrix:

$$\varepsilon_{y_1,\theta_1} = 2\left(\Sigma_1^{-1} + R_1^T\Sigma_2^{-1}R_1\right)^{-1}\,, \tag{4.13}$$

where the element in the first row and first column returns the variance of the lateral displacement at depth z_1.

Based on strict Bayesian theory, Collins-Fekete et al. [2017b] demonstrated that the MLP framework is usable for every ion in the same way, i.e., independent of the ion mass and charge. However, the Gaussian standard deviation of the statistical error envelope (cf. equation (4.13)) has to be scaled by the factor $(Z/A)^2$.

For calculating the MLP according to equation (4.12) one needs to evaluate the scattering matrix, whose elements require knowledge on the ions energy loss within the object (i.e., $1/\beta(z_1)^2p(z_1)^2$ in equation (2.8)). A common approach is an approximation by a fifth-degree polynomial using MC simulations to obtain the necessary fitting parameters [Williams, 2004]. For the MLP results presented in this work the term was directly calculated from a numerical integration of the Bethe-Bloch formula using the measured energy at the tracking detectors before and behind the imaged object.

Finally, it should be noted that the MLP calculation assumes an object of homogeneous water rather than the real patient/phantom. Theoretically, the concept can be extended to heterogeneous objects based on prior knowledge on the local particle energy and material radiation length. However, this drastically increases the complexity of the calculation and showed only little improvement in the path estimation error [Collins-Fekete et al., 2017a].

4.2.2 Cubic Spline Path Formalism

The MLP calculation is mathematically complex and computationally demanding. Given four variables, i.e., data on entry and exit position and direction, the highest degree polynomial with a unique solution is the cubic spline. Li et al. [2006] first introduced the Cubic Spline Path (CSP) concept for estimating proton trajectories. The CSP between a given entry ($\mathbf{X}_0$) and exit ($\mathbf{X}_1$) position is represented by

$$\mathbf{X}(t) = (2t^3 - 3t^2 + 1)\,\mathbf{X}_0 + (t^3 - 2t^2 + t)\,\mathbf{P}_0 + (-2t^3 + 3t^2)\,\mathbf{X}_1 + (t^3 - t^2)\,\mathbf{P}_1\,, \tag{4.14}$$

where $\mathbf{X}(t)$ represents the 3D position vector at a given depth defined by the temporal parameter $t \in [0, 1]$, representing the fraction of crossed CSP. $\mathbf{P}_0$ and $\mathbf{P}_1$ are the entrance and exit direction vectors (i.e., at $t = 0$ and $t = 1$ respectively).

While the particle angle sets the initial CSP direction, the magnitude of the direction vector defines how strongly the curve converges to a straight line. Hansen et al. [2014] applied a scaling according to the physical thickness between exit and entry position:

$$\mathbf{P}_{\{0,1\}} = \hat{\mathbf{P}}_{\{0,1\}} \cdot |\mathbf{X}_1 - \mathbf{X}_0|\,. \tag{4.15}$$

Collins-Fekete et al. [2015] proposed a more sophisticated phenomenological approach to accurately define the direction vector magnitude based on energy loss information. Here, they introduced two scaling factors $\Lambda_{\{0,1\}}$ aiming at minimizing the Root Mean Square (RMS) error of the path estimation:

$$\mathbf{P}_{\{0,1\}} = \hat{\mathbf{P}}_{\{0,1\}} \cdot \Lambda_{\{0,1\}} \cdot |\mathbf{X}_1 - \mathbf{X}_0|\,. \tag{4.16}$$

The Λ factors are parameterized by the ratio of WEPL over CSDA range in water. In order to obtain the optimal parameters, MC simulations were performed over a wide range of energy values and for different materials (cf. figure 4.2). Fitting the data with a quadratic law yielded the following relationships:

$$\Lambda_0 = 1.01 + 0.43\left(\frac{\mathrm{WEPL}}{R_{\mathrm{CSDA}}}\right)^2 \quad \text{and} \quad \Lambda_1 = 0.99 - 0.46\left(\frac{\mathrm{WEPL}}{R_{\mathrm{CSDA}}}\right)^2\,. \tag{4.17}$$

Based on a rigorous Bayesian formalism Collins-Fekete et al. [2017b] found that the phenomenological approximation and the theoretical model agree well within uncertainties. While CSP and MLP appear to be two completely different approaches, recent work showed

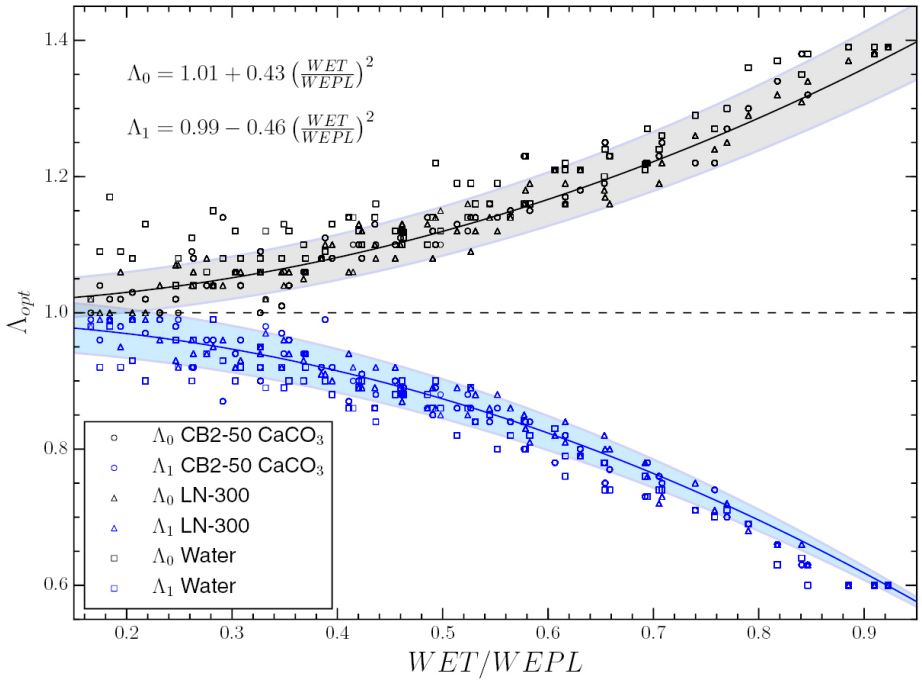

Figure 4.2: Optimal Λ factors minimizing the path estimation error. Shaded areas represent the standard deviation between the fit and the data. Please note that WET and WEPL in the notation of Collins-Fekete et al. [2015] correspond to WEPL and R_{CSDA} in the notation used in this work, respectively. Extracted from Collins-Fekete et al. [2015].

that there is certain connection between both formalism and that the phenomenological model can be described theoretically [Rädler, 2017; Collins-Fekete et al., 2017b]. Using the optimized scaling factors, CSP and MLP yield the same path estimation accuracy. Hence, the CSP is assumed to provide the best compromise between an accurate estimate of ion trajectories and reasonable calculation time [Collins-Fekete et al., 2015]. Finally, it should be noted that the CSP formalism is also independent of the ion type.

4.3 Tomographic Image Reconstruction for Ion CT

The task of tomographic image reconstruction is to obtain information about the nature of material occupying exact positions inside an object based on specific cross section measurements [Herman, 2009]. For the case of iCT this means solving the inverse problem of equation (3.9) in order to obtain the RSP distribution from measured RSP line integrals.

Analytic methods, like the widely-used Filtered Back Projection (FBP) employ continuous mathematical models of the inverse problem which are solved with integral transforms.

In contrast, iterative algorithms follow a fully-discretized modeling approach wherein both the object and the external source distribution are discretized at the beginning, which leads to finite-dimensional vector space formulations [Penfold and Censor, 2015].

4.3.1 The Concept of Iterative Image Reconstruction

Iterative reconstruction methods involve three iteratively repeated steps [Beister et al., 2012]: (1) forward projection of the current object estimate to obtain artificial raw data; (2) comparison of estimated artificial and measured projection data to obtain a correction term; (3) backprojection of the correction term into image domain.

Recalling equation (3.9), the measured WEPL is given by the line integral through the 3D RSP distribution of the object along the ion trajectory:

$$\int_L \mathrm{RSP}\left(\mathbf{\Gamma}(l)\right) \mathrm{d}\mathbf{\Gamma}(l) = \mathrm{WEPL}\,. \tag{4.18}$$

For iterative reconstruction algorithms, the continuous model is transformed into a fully-discretized representation, typically written in compact matrix notation:

$$\mathbf{A}x = b\,, \tag{4.19}$$

where the system matrix $\mathbf{A}$ is an $N \times M$ matrix containing the length of intersection (or chord length) $\{a_j^i\}$ of the i^{th} particle history with the j^{th} voxel of the image space as schematically indicated in figure 4.3 for the case of a straight trajectory. $b = \{b_1, b_2, ..., b_N\}$ is an N-dimensional vector whose elements b_i represent the WEPL measured for the i^{th} particle and $x = \{x_1, x_2, ..., x_M\}$ is the M-dimensional image vector of unknown RSP values, which needs to be determined. The system of equations represented by equation (4.19) will be inconsistent and very large; however, the matrix $\mathbf{A}$ is rather sparse.

In order to efficiently compute the matrix elements $\{a_j^i\}$, a CPU-based raytracing algorithm was implemented [Siddon, 1985; Jacobs et al., 1998]. Since ions do not follow straight trajectories, discrete points were sampled along the estimated curved path (cf. section 4.2) and joined with straight line segments. In order to minimize inaccuracies, the step size was set equal to half the voxel size of the reconstruction space. Penfold et al. [2009] proposed the use of an effective chord length assigned to all pixels intersected by a certain particle in order to reduce the raytracing time. Since the computational cost was not of major importance in this study this simplified approach was not pursued.

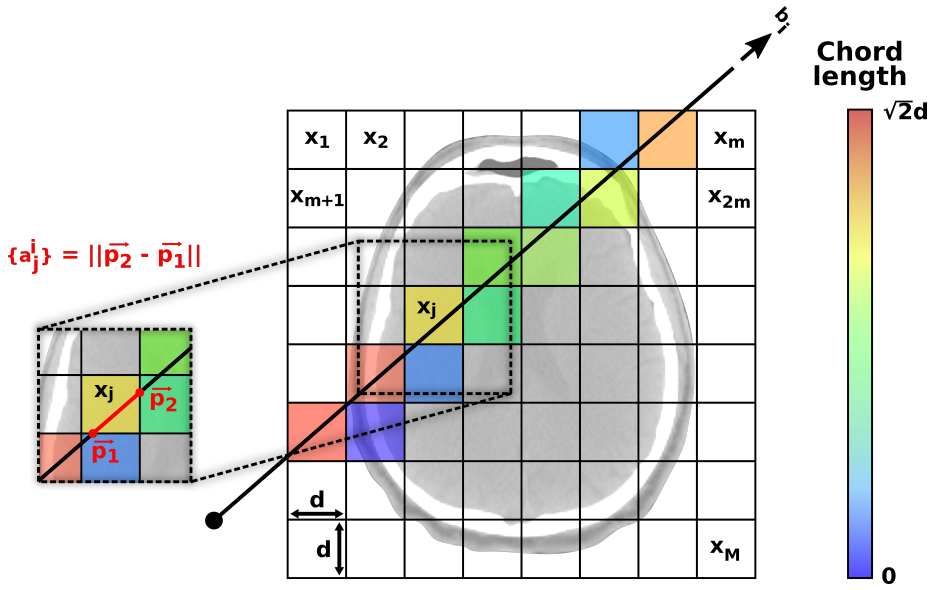

Figure 4.3: System matrix definition for a straight trajectory in 2D using a pixel basis representation. The color-coded chord length qualitatively indicates the values obtained from the raytracing algorithm. The individual matrix elements can be calculated by the euclidean norm as indicated in the zoom-in view.

4.3.2 Ordered Subset Simultaneous Algebraic Reconstruction Technique

Solving equation (4.19) is not straightforward since the problem is ill-posed and the measured projections contain noise. Mathematically, the individual linear equations describe hyperplanes in an M-dimensional Euclidean space, i.e., they represent convex sets. Hence, the modeling approach leads to the *convex feasibility problem* of finding a point in the non-empty intersection of a family of closed convex sets [Censor et al., 2012].

A common approach for solving feasibility-seeking problems are iterative projection methods. These algorithms offer computational advantages and can handle huge-sized problems of dimensions beyond which more sophisticated methods cease to be efficient or even applicable due to memory requirements [Censor et al., 2010]. In order obtain the subsequent iterate x^{k+1} from a given image estimate x^k, the algorithm's update step can be simply written as

$$x^{k+1} = \mathbf{P}_Q \, x^k \,, \tag{4.20}$$

where $\mathbf{P}_Q$ is the projection operator of the chosen algorithm. In this work, the Ordered Subset Simultaneous Algebraic Reconstruction Technique (OS-SART) algorithm [Wang

and Jiang, 2004] was employed, which has a block-iterative projection algorithmic scheme:

$$x^{k+1} = x^k + \lambda_k \left(\frac{1}{\sum_{i \in B_{t(k)}} a_j^i} \right) \sum_{i \in B_{t(k)}} \frac{b_i - \left\langle a^i, x^k \right\rangle}{\sum_{l=1}^{M} a_l^i} a_j^i \,, \tag{4.21}$$

where $\left\langle a^i, x^k \right\rangle$ is the inner product of the i^{th} column vector of $\mathbf{A}^T$ (i.e., the transpose of $\mathbf{A}$) with the current image estimate. Here, iterations are only performed with respect to the constraints set by indices i in a certain block $B_{t(k)}$ (also called subset), obtained by partitioning the data into K blocks. The algorithm selects blocks according to a control sequence $(t\,(k))_{t=0}^{\infty}$, which is cyclic in this work, i.e., $t(k) = k \mod K+1$. For the case of a single subset, which means that the image update considers all equations simultaneously, the algorithm simplifies to the standard Simultaneous Algebraic Reconstruction Technique (SART) algorithm of Andersen and Kak [1984].

The iterative image update procedure is schematically illustrated in figure 4.4. First, the current image estimate x^k is projected onto all hyperplanes representing the current subset. The consecutive image x^{k+1} is obtained by forming a convex combination of those projections. This already indicates that the construction of the subsets, i.e., the angles between the hyperplanes considerably influence the convergence rate toward the solution [Kak and Slaney., 1988]. In order to obtain an efficient convergence, this work used 36 blocks consisting of an equal number of events randomly selected from all projections.

It is important to notice that the (mathematically) optimal solution of equation (4.19) might actually not be desired because it does not represent the true data of interest due to noise and inconsistent projection data. Hence, the algorithm was stopped if a certain number of iteration cycles was completed or the change of the data fidelity per iteration number k was below an user-defined threshold ε [Meyer et al., 2017], which is expressed as

$$\left| \frac{\partial D\left(x^k\right)}{\partial k} \right| < \varepsilon \,, \tag{4.22}$$

using the following formulation for the data fidelity from Bian et al. [2014]:

$$D\left(x^k\right) = \|\mathbf{A}x^k - b\|/N \,. \tag{4.23}$$

The value of ε depends on the accepted data inconsistency which is influenced by the noise condition, system configuration and data quality [Sidky and Pan, 2008]. Hence, it has to be adjusted accordingly to achieve proper convergence without noise break-up.

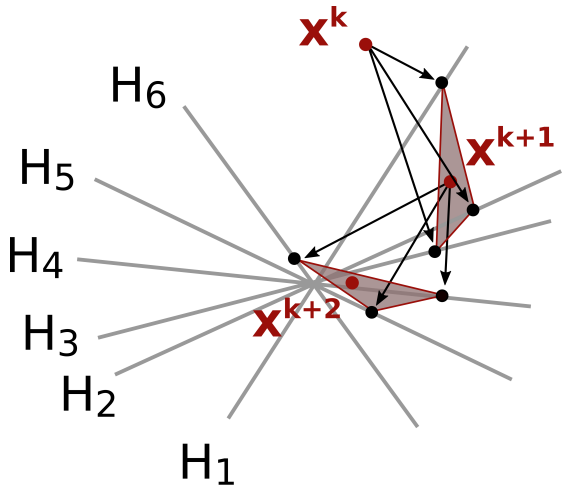

Figure 4.4: Iterative image update from projection algorithms of block-iterative structure. The consecutive image x^{k+1} is estimated by projecting the current estimate x^k onto all hyperplanes H of the current subset and forming a convex combination. Adapted from Penfold [2010].

4.3.3 Total Variation Superiorization

The projection algorithms introduced in the previous section can be computationally efficient and less demanding methods for solving convex feasibility problems. The reason is that projections onto the individual sets are easier to perform than projections onto other sets (e.g., the intersection of the sets) that are derived from the given individual sets [Davidi et al., 2009]. It is important to notice that feasibility-seeking is fundamentally different from optimization (as for example used in treatment planning), which aims at finding the best possible solution by minimizing an objective function while satisfying a set of typically convex constraints. However, in iCT reconstruction the minimum of the cost function is often not the best representative of the true data, due to inconsistencies in the acquired data [Penfold, 2010].

The novel idea of superiorization conceptually lies in between feasibility-seeking for the constraints and full-fledged constrained minimization of the objective function subject to these constraints. This means, one aims at a solution that is not only constraints-compatible, but is also desirable according to a specified optimization criterion. This is done by proactively interlacing perturbations into the original algorithm in order to reduce (not necessarily minimize) a given merit function.

The key to superiorization lies in the *'bounded perturbation resilience'* of the original algorithm, meaning that certain kinds of changes (i.e., perturbations) in each iterative step of the algorithm still lead to a constraints-compatible solution [Herman et al., 2012]. It was

proven by Davidi et al. [2009] that the general class of block-iterative projection methods is indeed resilient to bounded perturbations.

A very popular merit function is total variation, since the image solution is assumed to be piece-wise constant. To this end, the Total Variation Superiorization (TVS) scheme proposed by Penfold et al. [2010][1] was implemented. Briefly, the proposed algorithm works in the following way. Compared to the original projection algorithm (cf. equation (4.20)), the current image iteration is proactively perturbed by a bounded perturbation $\beta_k v^k$ in a way that the algorithm is steered toward a feasible solution encompassed with a reduced value of the target/merit function:

$$x^{k+1} = \mathbf{P}_Q \left(x^k + \beta_k v^k \right) , \tag{4.24}$$

where *'bounded perturbation'* means that β_k are real non-negative numbers such that $\sum_{k=0}^{\infty} \beta_k < \infty$ and the sequence $\left(v^k\right)_{k=0}^{\infty}$ is bounded [Penfold et al., 2010]. As merit function Φ, which needs to be reduced during the reconstruction, the total variation was used. For a 2D image represented by a $J \times J$ pixel array, the total variation is defined as

$$\Phi(p^k) = \sum_{g=1}^{J-1} \sum_{l=1}^{J-1} \sqrt{\left(p^k_{g+1,l} - p^k_{g,l}\right)^2 + \left(p^k_{g,l+1} - p^k_{g,l}\right)^2} , \tag{4.25}$$

where p^k is the 2D image representation of the image vector x^k. The normalized non-ascending perturbation vector v^k is calculated as the negative of the normalized sub-gradient s^k of the total variation for the current image estimate x^k:

$$v^k = \begin{cases} -\dfrac{s^k}{\|s^k\|}, & \text{if } s^k \neq 0, \\ 0, & \text{otherwise,} \end{cases} \tag{4.26}$$

where the subgradient is computed according to the method of Combettes and Luo [2002]. A pseudocode definition of the TVS scheme implemented in MATLAB® (*MathWorks, Inc., Natick, Massachusetts, USA*) is written as:

[1] The chosen algorithm was originally denoted as *'TVS2-DROP*'* in the publication of Penfold et al. [2010]. In this thesis, the superiorization scheme was implemented for the OS-SART/SART algorithm.

set $k = 0$, $l = 0$, $\beta_k = 1$;
while *repeat for each subset over the requested number of cycles* **do**
  if $\|s^k\| \geq 0$ **then**
    $v^k = -\frac{s^k}{\|s^k\|}$;
  else
    $v^k = s^k$;
  end
  while *loop* **do**
    set $y^k = x^k + \beta_k v^k$;
    if $\Phi(y^k) \leq \Phi(x^k)$ **then**
      $x^k = y^k$;
      set $loop = false$;
    end
    $\beta_k = \beta_k / 2$;
  end
  $x^{k+1} = \mathbf{P}_Q x^k$;
  $k = k + 1$;
end

Figure 4.5: TVS scheme for the block-iterative OS-SART/SART algorithm.

4.4 Image Reconstruction Workflow

The main methodologies of image reconstruction have been introduced in the previous sections. Here, an overview is given on how the different parts are implemented in the combined workflow for tomographic iCT reconstruction. The complete process for single-particle tracking and integration-mode reads as follows:

Single-particle tracking

1) Data import

In the first step, the binary output data obtained from the MC simulation are read. These data entail kinetic energy, upstream and downstream 3D position and direction, along with the projection angle for each particle history. Relying on the scored data, the individual WEPL values are derived. Those are either computed from the Bethe-Bloch formula using the recorded kinetic energy loss between front and rear tracker (chapter 6) or are directly obtained from the detector signal (chapter 8)

2) Spatial filter

For reducing the computational cost, particles missing the reconstruction volume are sorted out *a priori* by assuming a straight line connection between the simulated entry and exit coordinates.

3) Data binning

Next, the particle histories are grouped into parallel-ray projection bins. To this end, the remaining events from step *2* are projected onto the reconstruction volume using a straight path along the recorded entry and exit directions. This is reasonable, since particles will scatter far less per unit length in the surrounding air compared to the actual object of interest. Then, the derived intersection points are joined via a straight line. The angle with respect to the beam-axis (i.e., z-direction) defines the detector rotation bin whereas the intersection with the central reconstruction plane containing the axis of rotation defines the lateral and vertical displacement bins.

4) Statistical 3σ-filter

For each bin, a statistical 3σ-filter originally proposed by Schulte et al. [2008] was applied in order to minimize the effects of nuclear reactions and large-angle MCS events. Particles with a relative exit angle (i.e., difference between exit and entry angle) or WEPL outside 3σ around the mean value of the corresponding bin are not further processed.

5) Initial FBP reconstruction

The binned data derived in step *3* are converted into a conventional (parallel-ray) WEPL sinogram representation. An analytical FBP reconstruction is employed to obtain an initial image estimation. A Ram-Lak filter was applied to avoid a degradation of the edges, since the image is solely used for the patient contour estimation.

6) Object boundary estimation

Based on the initial FBP estimate, the object mask is derived by thresholding the reconstructed RSP map (i.e., RSP>0.2). To avoid ambiguities, a convex hull of the mask is derived. Alternatively, the mask can be directly obtained from prior information, e.g., the xCT used for treatment panning (as performed in chapter 6).

7) Path and system matrix computation

Each individual particle is forward- and backprojected onto the object boundary (of step *6*) based on the measured entry and exit position and direction. The ion path calculation according to the selected path model (i.e., either SLP, CSP or MLP) is bound by the intersection points with the contour. By performing a piece-wise raytracing the individual chord lengths are computed and stored in the system matrix.

8) Iterative TVS OS-SART reconstruction

In the last step, the large scale inverse problem is iteratively solved by a TVS OS-SART algorithm (cf. equation (4.21) and scheme 4.5) using the system matrix derived in step *7* and the WEPL values calculated in step *1*.

Integration-mode

1) Data import

First, the binary output data of the MC simulation are read. These data contain the integrated detector information for each specific pencil beam and the corresponding RP location according to the irradiation plan. From the obtained residual range signal of the particle ensemble, the most probable WEPL value (which is more commonly termed WET in the context of integration-mode, where no individual ion trajectory can be computed) can be directly derived based on dedicated calibrations (cf. chapter 5).

2) Sinogram binning

Next, the WET information is binned into a sinogram representation based on the object rotation angle (angular bin) and the RP location (projection displacement bin).

3) System matrix computation

The system matrix is generated by applying a SLP raytracing based on the geometrical information from step *1*. This procedure is performed along the central beam axis, since it represents the most probably path of the finite-width pencil beam.

4) Iterative TVS SART reconstruction

In the last step, the TVS SART algorithm is employed to iteratively solve the inverse problem, using the system matrix of step *3* and the WET values obtained in step *1*.

4.5 Quantitative Image Quality Evaluation

4.5.1 Image Accuracy and Noise

The WET or RSP accuracy and noise were evaluated for homogeneous regions within the investigated objects. For this assessment, a Region of Interest (ROI) of reduced size with respect to the original region within the phantom was applied to avoid inaccuracies originating from range mixing and partial volume effects at the material borders. The accuracy was calculated by the mean value of the relative error distribution based on the known ground truth reference images. The noise within the same region was evaluated in terms of the corresponding standard deviation.

In order to quantify the overall Ion Radiography (iRAD) and iCT image quality with respect to the known ground truth, the RSP/WET (total image) relative error ε_{rel} [Penfold, 2010] was employed, which is defined as

$$\varepsilon_{\text{rel}} = \frac{\sum_i |x'_i - x_i|}{\sum_i x'_i} \,, \tag{4.27}$$

where x_i and x'_i are the RSP/WET values of the i-th voxel of the obtained and ground truth image, respectively. Voxels only containing air according to the ground truth image were excluded from the quantification. For reconstructed 3D RSP maps of clinical and pre-clinical data sets, the relative error was evaluated on a slice-by-slice basis and the RSP ground truth was obtained from the ground truth patient anatomy of the xCT and the HU-RSP conversion of the MC simulation. Furthermore, the joint histogram of the reconstructed iCT and the corresponding ground truth HU values enabled the calculation of the RSP precision as a measure of noise of the iCT images [Meyer et al., 2019].

4.5.2 Spatial Resolution

In this work, the Modulation Transfer Function (MTF) was used to characterize the loss of spatial resolution for a certain imaging system due to the attenuation of high spatial frequencies. This degradation is mainly due to uncertainties in the estimated ion path employed in the tomographic system matrix, the tomographic image reconstruction algorithm and the finite discretization of the image volume. In order to determine the MTF in tomographic image domain, the *'slanted-edge method'* of Mori and Machida [2009] was implemented. A high-density block phantom was placed at a small angle ($\sim 2°$) with respect to the vertical and horizontal axis of the image reconstruction grid. The angle does not have to be precisely known but should be sufficiently small in order to reduce blurring from the spread of the edge position within the pixel pitch. Different profiles crossing the edge will provide a sampling at varying intervals, as schematically indicated in figure 4.6. By recombining the individual profiles with the proper phase alignment [Fujita et al., 1992] (cf. figure 4.6) a composite high-resolution oversampled Edge Spread Function (ESF) is produced, which provides the ability to overcome the Nyquist limitation imposed by the pixel dimension within the reconstructed image.

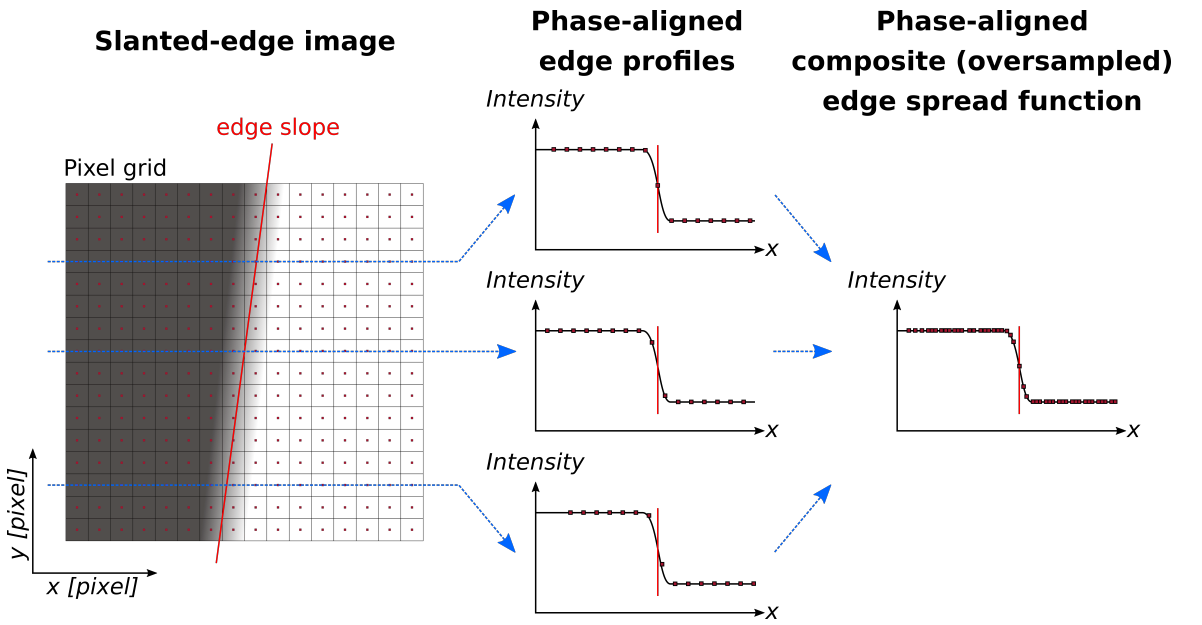

Figure 4.6: Generation of a composite oversampled ESF from a slanted-edge image. The phase alignment of the individual profiles is performed using the method of Fujita et al. [1992]. The composite ESF exhibits a high resolution, which is beyond the original pixel resolution.

The line spread function (LSF) is derived by analytical differentiation of the ESF:

$$\mathrm{LSF} = \frac{\mathrm{dESF}(x)}{\mathrm{d}x}\,, \tag{4.28}$$

where x is the position along the edge profile. Finally, the MTF is obtained by performing the Fourier transform of the blurring-corrected line spread function:

$$\mathrm{MTF} = \mathcal{F}\left(\mathrm{LSF}(x)\right)\,. \tag{4.29}$$

In this work, the absolute spatial resolution limit of the reconstructed image for a certain system is given by the frequency where the MTF is reduced to 10% intensity ($\mathrm{MTF}_{10\%}$). This is a common choice to represent the limit of visual detail.

4.6 Conclusions

In this chapter the computational methods required for the iCT investigations presented in this thesis have been reviewed: MC simulations and tomographic image reconstruction for curved ion paths with iterative methods.

MC simulations are an extremely useful tool to investigate the performance of detector systems and imaging applications. The implemented MC simulation framework was based on the FLUKA code. This platform included experimentally validated beam models for two particle therapy centers, HIT and RPTC, in order to accurately reproduce real beam properties, ensuring a reliable comparison with experimental measurement.

Due to the inevitable MCS of ions experienced while traversing matter, their trajectories are not straight. For single-particle tracking the CSP and MLP have been proposed to provide an analytic approximation to the MCS deflected path. While the Bayesian formalism of the MLP can be extended by additional prior information, e.g., about the actual composition of the object [Collins-Fekete et al., 2017a], the CSP has computational advantages. First, it provides both lateral displacements simultaneously and second it is rapidly adjustable for different energies. It is important to keep in mind that both models are calculated in water and consequently do not consider heterogeneities encountered in a real patient. For this work, the presented image reconstruction workflow for the SLP [Siddon, 1985; Jacobs et al., 1998], CSP [Collins-Fekete et al., 2015] and MLP [Schulte et al., 2008] has been implemented in MATLAB®.

Due to advances in modern computing technology, limitations of iterative reconstruction algorithms like computational time and memory usage are becoming less and less a concern for the application in clinical scenarios. Hence, a state-of-the-art OS-SART algorithm coupled with a TVS scheme was implemented. The superiorization methodology enables improved results with approximately the same computational cost as the unperturbed version. This can be achieved if the original algorithm is useful for the applied problem and computationally efficient perturbation steps are implemented [Censor, 2015]. While one might intuitively assume that TVS causes a degraded spatial resolution due to the intrinsic smoothing, the algorithm actually yields equal or even better spatial resolution. This is attributed to the possibility of performing a greater number of iteration cycles before reaching the noise break-up limit [Penfold et al., 2010].

It should be noted that also analytical image reconstruction methods, like the *distance-driven binning* approach of Rit et al. [2013] or the *backprojection-then-filtering* method from Poludniowski et al. [2014], have been applied in iCT. Those techniques require considerably less computing power but do not offer the flexibility of iterative methods. Future work should compare the different reconstruction algorithms used within the iCT community regarding image quality and computational time.

"It doesn't matter how beautiful your theory is, it doesn't matter how smart you are. If it doesn't agree with experiment, it's wrong."

Richard P. Feynman

5

Integration-Mode Ion Imaging Using Active Beam Delivery

In this chapter, a comparative study of ion imaging with different ion beams using an integration-mode range telescope prototype is presented. Compared to previous preliminary work, the novelty lies in the rigorous comparison of proton, helium and carbon ions for various indications using a realistic simulation model. Integration-mode detection allows ion imaging with relatively cost-effective systems which are easy to operate; however, the absence of direct position information can cause signal ambiguities due to range mixing effects. In order to make the most of the investigated integration-mode system, a dedicated post-processing method, called Bragg Peak Decomposition, was developed. The methodology and application to experimental and simulated data is presented. Furthermore, a performance comparison between the integration-mode functionality with the currently available prototype and potential improvements resulting from an envisioned detector upgrade in terms of improved range resolution (using thinner absorbers) is carried out. In the last part, the imaging capabilities for clinical-like data are investigated. Parts of this chapter have been published in Meyer et al. [2016, 2017] and recently submitted for publication in another manuscript Magallanes et al. [2019].

5.1 Experimental Setup

This section will review the necessary iCT system constituents and how they have to work in synchronization to generate accurate experimental ion images with the prototype integration-mode range telescope.

5.1.1 The Heidelberg Ion-Beam Therapy Center

HIT is a state-of-the-art 119-million euro multi-ion particle therapy facility located in Heidelberg, Germany. Building upon the initial experience of the pilot project at the GSI Helmholzzentrum für Schwerionenforschung (GSI, Darmstadt, Germany) the active clinical operation began in November 2009. HIT is the first hospital-based combined particle therapy center for protons and heavier ions in Europe and the worldwide first for heavy ions with entirely active beam delivery and a rotating gantry [Haberer et al., 2004].

The ions are extracted from three dedicated ECR (electron cyclotron resonance) ion sources and pre-accelerated in a two stage LINAC (linear accelerator) before being injected into the synchrotron ring. The beam energy can be varied between 48 MeV/u and 430 MeV/u in 255 discrete steps, corresponding to a range in water of 2-30 cm[1] [Ondreka and Weinrich, 2008]. 3D intensity-modulated active raster scanning [Haberer et al., 1993], combined with the world's first 360° heavy ion gantry, enables dose conformity to the tumor with extremely high spatial selectivity. The facility itself was designed for the therapeutic irradiation with proton, helium, carbon and oxygen ions, even though only protons and carbon ions are currently used clinically for patient treatment.

All those technological aspects make HIT ideally suited for ion imaging investigations. An essential device for ion therapy (but also for the presented imaging application) is the BAMS, a beam-verification system consisting of three ionization and two multi-wire proportional chambers. It is mounted in the nozzle at the exit of the vacuum beam line and continuously monitors (with a minimum sampling time of 1.7 ms [Magallanes, 2017]) important beam properties (e.g., position, size and fluence). This is required to verify the accurate application of the irradiation plan in order to achieve the prescribed dose distribution. A sketch of the HIT accelerator complex including the main components of the beam line is shown in figure 5.1.

[1] The corresponding maximum penetration depth in water for oxygen ions is around 20 cm.

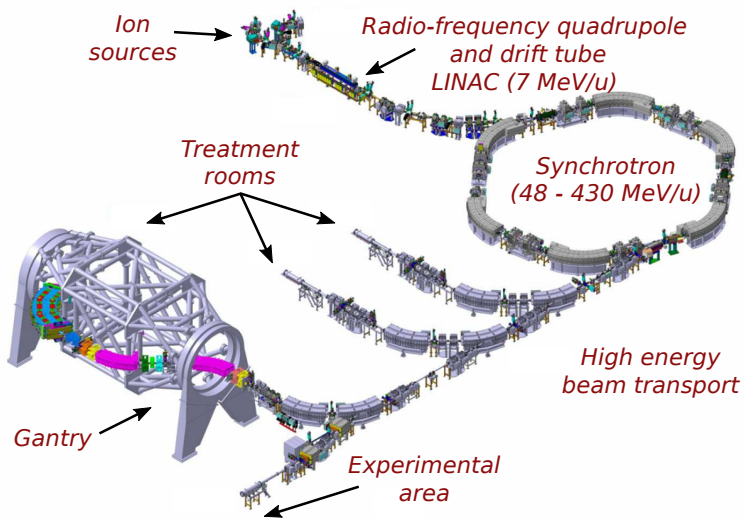

Figure 5.1: Overview of the HIT accelerator complex. Ions extracted from ion sources are pre-accelerated in the linear accelerator (LINAC) before being injected into the synchrotron ring. The high energy beam transport line guides the ions to the two horizontal treatment rooms, the gantry or the experimental area. Adapted from Schoemers et al. [2015].

5.1.2 Multi-Layer Ionization Chamber

The used prototype detector has been originally developed at the GSI Helmholzzentrum für Schwerionenforschung (GSI, Darmstadt, Germany) [Voss et al., 2010] and the feasibility of such a system for the 3D reconstruction of relative depth-dose distributions has been demonstrated by Brusasco et al. [2000]. The proof-of-principle studies of carbon ion imaging with this prototype were performed by Rinaldi et al. [2014]; however, at rather high doses [Rinaldi, 2011]. More recently, Magallanes [2017] characterized the system for low-dose irradiation schemes, i.e., below 2 mGy per full radiography.

Only a brief review on the working principle of the detector configuration will be given. For more detailed information the reader is referred to Magallanes [2017]. The residual range detector, as it can be seen in figure 5.2, is assembled from 61 Parallel-Plate Ionization Chambers (PPICs) interleaved with Poly(Methyl Methacrylate) (PMMA) absorber plates. Due to the large active area of $30 \times 30\,\mathrm{cm}^2$ the whole isocentric scanning field of $20 \times 20\,\mathrm{cm}^2$ available at HIT can be exploited for imaging. The active volume of the individual PPICs is filled with air and has a thickness of 6 mm. This yields essentially the same performance as other gases (e.g., N_2), but at easier operation conditions [Brusasco et al., 2000]. The PMMA slabs have a thickness of 3 mm. This granularity sets the WET resolution of the detector system to approximately 3 mm and the dynamic range to around 21 cm WET.

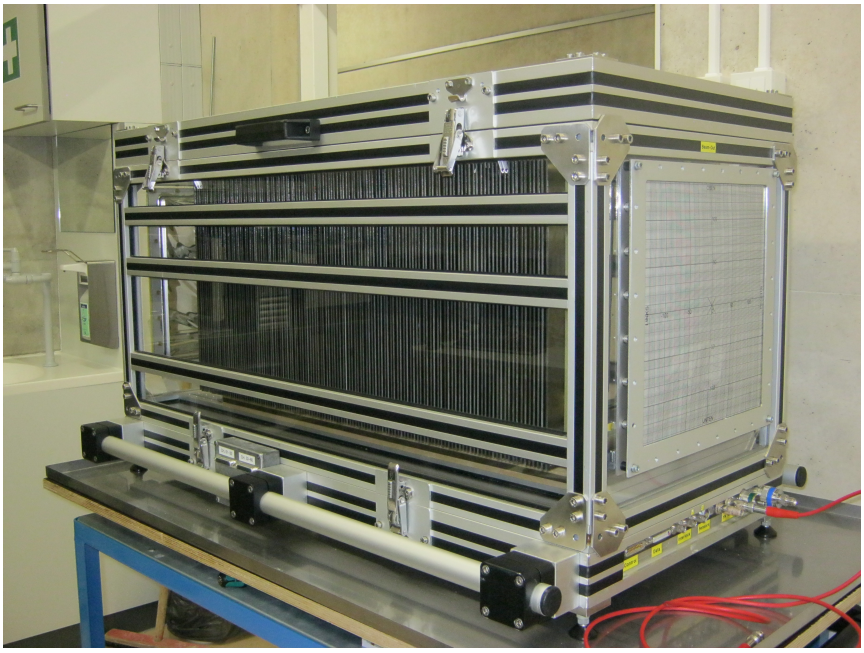

Figure 5.2: Range telescope detector without shielding box. The individual channels (consisting of a PMMA absorber and a PPIC) can be seen. The beam is entering from the right-hand side.

In the application of ion-based transmission imaging, the detector functions as a range telescope, meaning that the integrated signal is represented by the measured PPIC charge within each channel. This results in a discretized Bragg curve for each individual RP. Furthermore, the absolute value of PPIC charge is irrelevant, while the maximum signal conveying the WET information of the traversed material can be clearly identified.

For the image acquisition process it is essential that the detector readout electronics acquire and stream the integrated charge measured by the PPICs in synchronization with the active beam delivery, as schematically indicated in figure 5.3. To this end, the detector system is equipped with a I128 multi-channel electrometer (*Pyramid Technical Consultants, Inc., Lexington, MA, USA*). The Siemens therapy control system provides a transistor-transistor logic signal, the so-called *Next-Point trigger*, indicating the irradiation of a successive RP within the scanning sequence monitored by the BAMS. This prompts a second trigger in the electrometer, initializing the charge integration within all PPICs simultaneously. It should be noted that the current system only accommodates fixed integration periods, which have to be matched to the minimal irradiation time between RPs in order to avoid missing scanning steps. However, this restriction heavily compromises the detection efficiency and signal quality since the dwell time of the beam varies by around 0.3 ms (as $1\,\sigma$), due to beam intensity fluctuations [Magallanes, 2017].

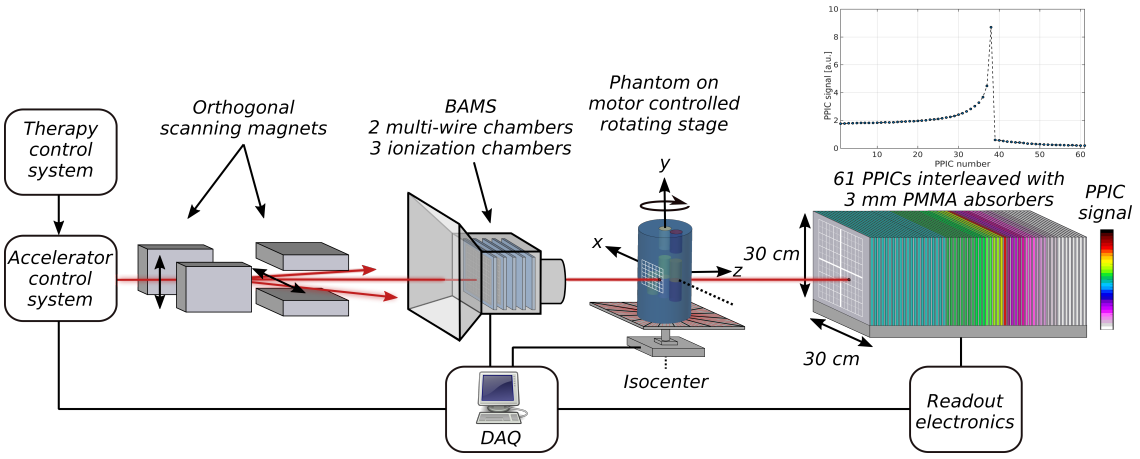

Figure 5.3: Schematic of the ion transmission imaging setup located at HIT. A high-energy ion beam coming from the accelerator leaves the beam line through the BAMS, fully penetrates a phantom located at isocenter on a motor controlled rotating stage and is stopped inside the range telescope. Each PPIC measures the charge due to the energy deposition after the beam is degraded by the upstream 3 mm PMMA. The colorbar indicates the amount of energy deposition in each PPIC and the integrated signal for a single RP is shown above the detector. A 2D ion radiography is obtained by scanning the beam across the object using the active beam delivery.

5.1.3 Phantoms

In this study, three phantoms (shown in figure 5.4) have been adopted to investigate different geometries: A *'slab phantom'* consisting of six plates of tissue-like materials (*Gammex, Inc., Middleton, WI, USA*), a PMMA *'rod phantom'* using seven cylindrical inserts of tissue-equivalent materials (*CIRS, Inc., Norfolk, VA, USA*) and a *'stepped wedge phantom'* machined from PMMA. Table 5.1 lists the properties of all investigated tissue-equivalent materials. The RSP of the individual materials was experimentally determined at HIT from carbon ion beam range measurements with a precision of 10 µm and an accuracy of 100 µm, using an adjustable water column system named Peakfinder (*PTW, Freiburg, Germany*). The exact procedure is outlined in Parodi et al. [2012] and the associated RSP measurement uncertainty was 0.2%. The rod phantom was exploited to investigate iCT, whereas the slab and stepped wedge phantom were only used for iRAD studies, since the present high spatial frequencies along specific dimensions represent a worst-case (and clinically unrealistic) scenario for tomographic image reconstruction. As indicated in figure 5.4, the slab phantom iRADs were acquired by irradiating parallel to the long slab interfaces. The stepped wedge phantom was irradiated from the side (configuration 1; as shown in figure 5.4) to produce an image of the step-like shape and also from behind (configuration 2) to obtain WET images of the thicknesses of the individual PMMA steps.

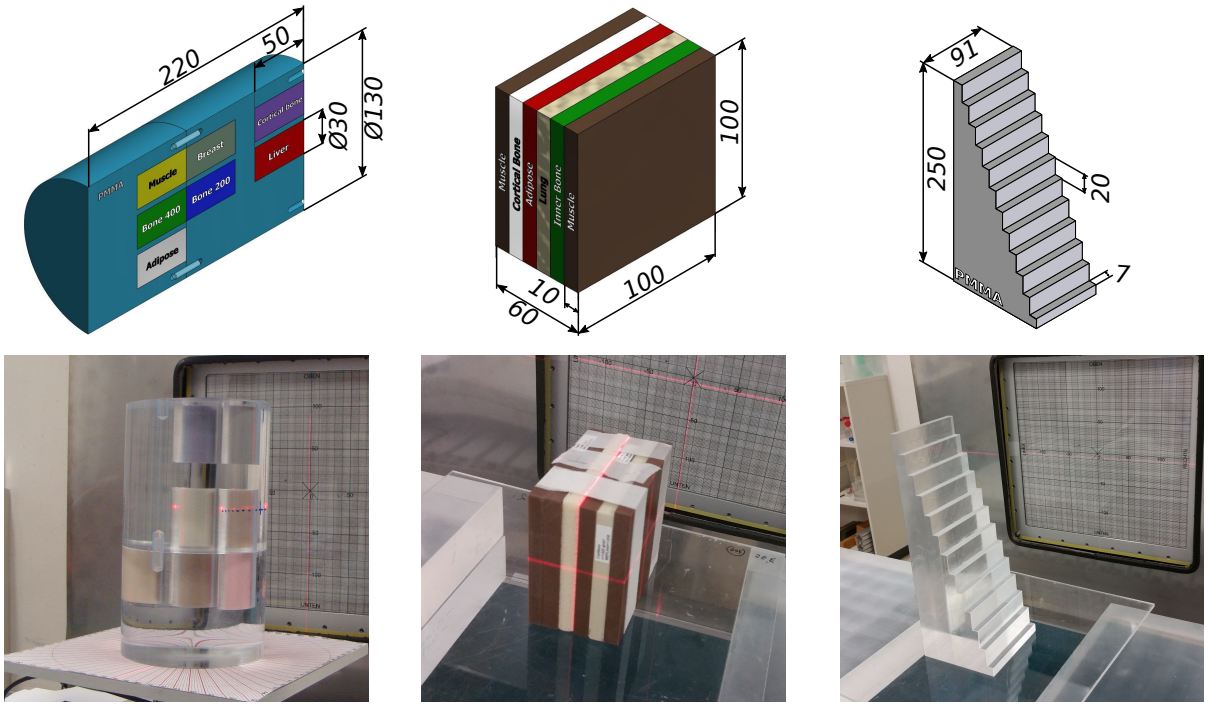

Figure 5.4: Physical dimensions [mm], geometry and insert arrangement for the rod (left), slab (middle) and stepped wedge phantom (right). In the pictures the phantoms can be seen in the irradiation position in front of the range telescope. The rod phantom is located on a motor controlled rotating stage for tomographic acquisition.

Material	Manufacturer	Density [g/cm^3]	RSP	Elemental Composition [%]										
				H	C	N	O	Mg	Si	P	S	Cl	Ca	Ba
Muscle	CIRS	1.062	1.057	9.1	69.7	2.1	16.8	0	0	0	0	0.1	2.2	0
Bone 400		1.260	1.215	8.1	57.63	1.28	18.87	0	0	4.32	0.08	0.04	9.31	0.35
Adipose		0.960	0.970	10	71.3	1.8	16.4	0	0	0	0	0.2	0.3	0
Breast 50/50		0.991	0.989	9.6	70.3	1.9	17	0	0	0	0	0.2	0.9	0
Trabecular bone 200		1.161	1.117	7	56.3	2	22.7	0	0	3.3	0	0.2	8.5	0
Cortical bone		1.910	1.688	3.3	25.37	0.91	35.28	3.36	0	8.82	0	0.03	22.91	0
Liver		1.072	1.064	9.0	69.4	2.1	17.1	0	0	0	0	0.1	2.2	0
Muscle	Gammex	1.049	1.036	8.1	67.17	2.42	19.85	0	0	0	0	0.14	2.32	0
Cortical bone		1.834	1.618	3.41	31.41	1.84	36.50	0	0	0	0	0.04	26.81	0
Adipose		0.946	0.948	9.06	72.30	2.25	16.27	0	0	0	0	0.13	0	0
Lung		0.282	0.284	8.46	59.38	1.96	18.14	11.19	0.78	0	0	0	0.10	0
Inner Bone		1.152	1.104	6.67	55.64	1.96	23.52	0	0	3.23	0	0.11	8.86	0

Table 5.1: Mass density and elemental composition of the Gammex and CIRS phantom materials used in this work. The RSP was experimentally measured using the Peakfinder (*PTW, Freiburg, Germany*) water column system [Parodi et al., 2012].

5.2 Monte Carlo Model

The detector geometry was modeled by alternating homogeneous PMMA blocks of 3 mm thickness with 6 mm air regions; thus, neglecting the electrodes compared to the actual range telescope configuration. Hence, the density of the absorber material was tuned to 1.216 g/cm^3 in order to match the experimentally determined RSP value of 1.192 [Meyer et al., 2017]. The detector signal, i.e., the energy deposition in each air region resembling the active volume, was scored using the *mgdraw.f* routine[2]. As in the experimental scenario, the energy depositions were accumulated in each detector channel (i.e., air regions) for all (primary and secondary) particles belonging to the pencil beam of the corresponding RP.

The *in silico* phantom geometries were directly modeled in FLUKA, as explained in section 4.1.4. In addition, the ionization potentials of the individual compounds, calculated by FLUKA according to the Bragg additivity rule, were manually adjusted in a trial and error procedure to ensure an agreement with the experimentally measured RSP of better than 0.3%. For evaluating the imaging performance in more realistic scenarios, the DICOM xCT data of a left frontobasal anaplastic astrocytoma case were imported in FLUKA as voxel geometry. The conversion of HUs into RSP was embedded by forcing the MC code to follow a bijective and error-free clinical-like HU-RSP conversion curve (cf. section 4.1.5).

5.3 Data Processing

The detector signal for every RP is given by a Bragg curve discretized into the 61 PPICs carrying information on the energy loss of the particles within the material traversed before impinging on the detector. The WET of the imaged object is encoded in the location of the largest PPIC signal and can be directly obtained by means of dedicated detector calibrations, as explained in the following.

5.3.1 Formation of Projection Data

In order to correlate the location of maximum signal with the traversed WET, the peak-signal position has to be parametrized as a function of the initial beam energy and

[2] In previous work [Meyer, 2015; Meyer et al., 2017] the scoring was implemented in the *comscw.f* routine. The applied change makes the implementation more convenient without influencing the result. *mgdraw.f* provides a general event interface to the whole FLUKA particle transport process, which allows to directly access for example energy deposition, boundary crossing or trajectory drawing. *comscw.f* allows to interface and weight the energy/stars/residual nuclei obtained via the standard FLUKA scoring cards.

the thickness of a material with known RSP [Rinaldi et al., 2013]. Without any object inside the beam path, the location of the maximum signal exclusively depends on the initial beam energy, i.e., higher energetic ion beams will be stopped in a more distal part of the range telescope. For the first calibration, the peak position of the detector signal was determined for a series of experimentally validated MC simulations with varying initial beam energy. The results are shown in figure 5.5. In order to improve the accuracy for very low (<100 MeV/u) and high (>350 MeV/u) energies a 2$^{\text{nd}}$-degree polynomial fit was employed instead of the semi-empirical Bragg-Kleeman rule applied in a previous study [Rinaldi et al., 2013]. Hence, the parametrization of the peak location N^0_{max} in dependence of the initial beam energy is given by

$$N^0_{\text{max}}(E) = a_1 \cdot E^2 + a_2 \cdot E + a_3 \,. \tag{5.1}$$

Here, a_1, a_2 and a_3 are ion-dependent fitting parameters listed in table 5.2, E is the initial beam energy in MeV/u and the superscript ^{0} denotes that no material was placed within the beam path.

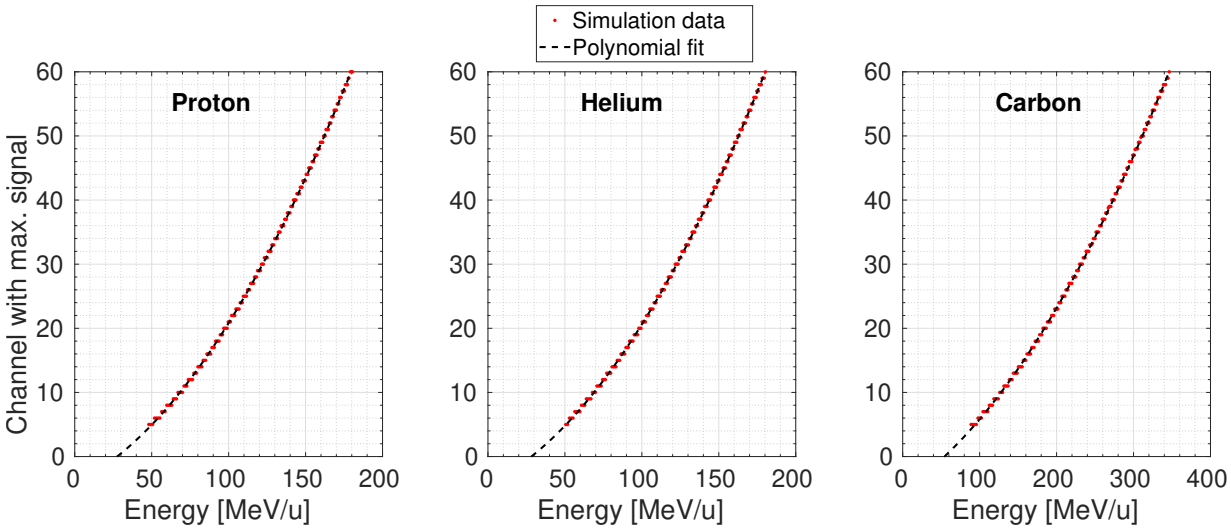

Figure 5.5: Energy calibration curves using a 2$^{\text{nd}}$-degree polynomial fit for simulated ^{1}H, ^{4}He and ^{12}C ion beams. The corresponding fit parameters are listed in table 5.2.

In a second step, the location of the maximum PPIC signal for a certain amount of material traversed by the beam (N_{max}) was parametrized as a function of known PMMA

Particle	Fit parameter		
	a_1 [(MeV/u)$^{-2}$]	a_2 [(MeV/u)$^{-1}$]	a_3
^{1}H	0.001348	0.1154	-4.197
^{4}He	0.001341	0.1151	-4.310
^{12}C	0.000311	0.0805	-5.488

Table 5.2: Parameters of the 2$^{\text{nd}}$-degree polynomial fit for the channel-to-WET conversion. In all cases R^2 values and RMS errors were better than 0.999 and 0.33, respectively.

absorber thickness for a fixed beam energy E. This yields a linear relationship of the form

$$N_{\text{max}}(E, \Delta x_{\text{object}}) = -c\ \Delta x_{\text{object}} + N^0_{\text{max}}(E)\,, \tag{5.2}$$

where Δx_{object} is the absorber thickness placed in front of the detector and c is a fitting parameter. Since the used absorbers were of the same material as the absorber slabs of the detector, c represents the inverse absorber plate thickness, i.e., $c = 1/3\,\text{mm}^{-1}$. This was confirmed with an accuracy of 0.25% by simulations for different absorber thicknesses. By substituting $N^0_{\text{max}}(E)$ in equation (5.2) with expression (5.1) and using $\Delta x_{\text{object}} = \text{WET}/1.192$, where 1.192 is the experimentally determined RSP of the PMMA absorbers, one obtains

$$N_{\text{max}}(E, \text{WET}) = -\frac{1}{3}\,\frac{\text{WET}}{1.192} + a_1 \cdot E^2 + a_2 \cdot E + a_3\,. \tag{5.3}$$

Finally, the WET (given in mm) of an unknown object imaged with an ion beam of initial energy E (given in MeV/u) can be derived by rearranging equation (5.3), which yields the following channel-to-WET conversion formula:

$$\text{WET} = 1.192 \cdot 3 \cdot \left(a_1 \cdot E^2 + a_2 \cdot E + a_3 - N_{\text{max}}\right)\,. \tag{5.4}$$

In order to further validate the simulation model, the same parametrization as in Rinaldi et al. [2013] was tested in addition. Only minor variations in the deduced fitting parameters and consequently the reconstructed WET values were observed.

5.3.2 Bragg Peak Decomposition

In presence of material interfaces or inhomogeneities perpendicular to the pencil beam axis, the detector signal contains distinct multiple WET information due to range mixing effects. As a consequence, the maximum signal location may not always coincide with the most relevant WET contribution [Krah et al., 2015]. The integrated detector signal is therefore described as a linear combination of different pristine Bragg peaks. Accordingly, a RP-wise decomposition strategy called Bragg Peak Decomposition (BPD) was implemented to disentangle each individual component of the mixed Bragg curve and identify the main WET contribution [Meyer et al., 2017].

The method relies on a MC-based lookup-table $\mathbf{BC}_{\mathrm{LUT}}$ of pristine Bragg curve signals, shown in figure 5.6. This energy dependent database was created by simulating PMMA absorbers of varying thicknesses in steps of 0.1 mm in front of the detector. A thickness sampling finer than the intrinsic WET resolution of the detector was chosen for two reasons. First, to account for possible peak shape changes of the detected signal, which depends on the actual Bragg peak position relative to the PPIC. And second, to increase the degree of freedom of the purely mathematical optimization [Meyer et al., 2017].

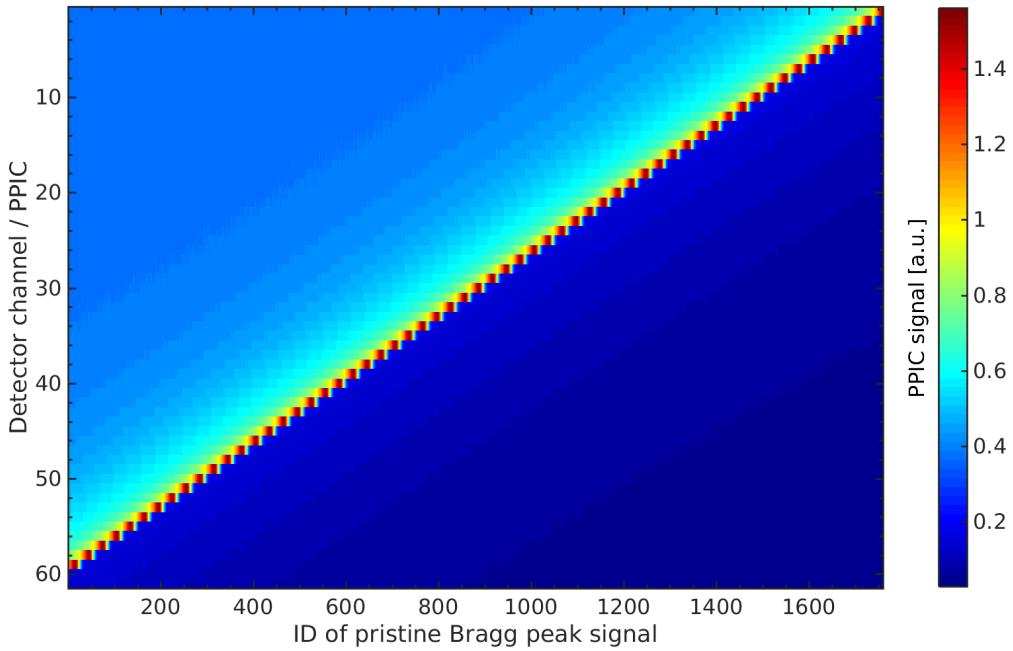

Figure 5.6: MC-based lookup-table (for a ^{12}C ion beam of 344.94 MeV/u initial energy) displaying the vertically organized pristine Bragg peak signals for various PMMA absorber thicknesses.

The signal component weights are derived from the following linear least-squares problem with bound constraints, solved by means of Euclidean distance minimization:

$$\min_{\mathbf{w}} \frac{1}{2}\|\mathbf{BC}_{\mathrm{LUT}} \cdot w - BC\|_2^2 \;\text{ for }\; 0 \leq w_i \leq 1 \;\; \forall i\,, \tag{5.5}$$

where BC is a vector containing the 61 PPIC signals for the specific RP and w is the weight-coefficient vector to be determined. $\mathbf{BC}_{\mathrm{LUT}}$ is the lookup-table matrix including the column-wise organized detector signals for pristine Bragg peaks, while the individual columns represent cases of various different absorber thicknesses (cf. figure 5.6).

To ultimately derive the WET information by applying equation (5.4), the obtained weight-coefficient vector was re-binned to the actual detector resolution by adding up the weights of all pristine Bragg peaks having the same maximum location. The most dominant component, i.e., the channel of largest weight, is identified as N_{max} for the specific RP.

5.3.3 Tomographic Image Reconstruction

The tomographic image reconstruction is implemented as explained in section 4.4, using a geometrical system matrix considering parallel integration-lines. This is justified by the quasi-parallel beam geometry due to the large distance of around 6.5 m between the scanning magnets and isocenter at HIT, resulting in a divergence of less than 1 mrad for typical irradiation scenarios [Parodi et al., 2012].

5.4 Results

5.4.1 Impact of Data Post-Processing

This section investigates the impact of the proposed BPD method on the overall integration-mode imaging performance. Figure 5.7 exemplary shows the BPD application for the signal of a RP located beside the rod phantom, however, still close to the air-PMMA interface. The broad peak signal component originates from the rounded boundary of the cylinder, whereas the more narrow peak at channel 50 corresponds to ^{12}C ions not intersecting the phantom. This *'double peak'* causes ambiguities in the WET conversion since the largest signal is found at channel 36, while the RP is geometrically located next to the phantom, i.e., channel 50 would be correct for the employed parallel-beam system matrix. Using the developed BPD method resolves this issue and correctly determines the weights

of the individual Bragg peak components within the integrated signal.

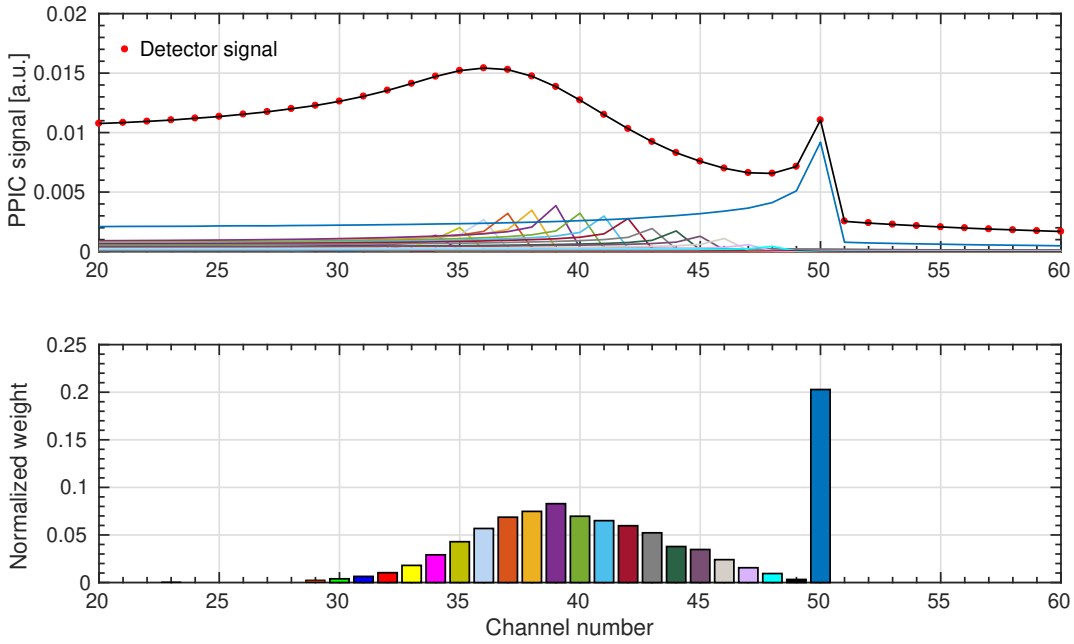

Figure 5.7: BPD for the signal of a RP close to the air-PMMA interface occurring at the boarder of the rod phantom. The top panel shows the detector signal (red dots), the individual weighted signal components (colored) obtained from the BPD and their summation (black). The lower panel shows the weights assigned to the corresponding pristine Bragg peak signal, which are drawn in the same color.

Additional simulation studies indicated that the increase in RSP accuracy from full (360°) angular coverage is relatively small compared to a partial tomographic coverage of 180° and does not justify the double dose exposure. This is expected due to the linearity of WET combinations, causing a redundant sampling of the same information in the second half [Meyer et al., 2017]. The only difference is ascribed to MCS and nuclear interaction processes. Hence, in the following only 180° angular coverage will be considered for iCT. In order to quantitatively assess the impact of the BPD on the RSP accuracy, a pCT, Helium Computed Tomography (heCT) and cCT of the rod phantom were simulated with 10000 ^{1}H, 2500 ^{4}He and 500 ^{12}C ions per RP and 1 mm spacing, yielding a comparable dose of ∼190 mGy for the 200 radiographic projections. The selected number of simulated primaries was sufficient to obtain a stable detector signal for each RP without substantially altering the image quality. A value of $\varepsilon = 5 \times 10^{-4}$ was selected as stopping criteria for all iCT reconstructions (cf. equation (4.22)). The obtained RSP accuracy for the individual

phantom inserts is summarized in table 5.3. Applying the developed BPD method improved the RSP accuracy substantially for almost all materials, predominantly for pCT. The average RSP relative error reduction was 3.93%, 2.74% and 1.72% for pCT, heCT and cCT, respectively. Based on this outcome, all following results presented in this chapter use the BPD method.

	Bottom insert row			Middle insert row			Top insert row		
	Adipose	Bone400	Muscle	Breast	Bone200	PMMA	Cort. bone	Liver	PMMA
Proton CT									
Without BPD	-3.47%	-10.52%	-4.28%	-2.95%	-11.54%	-4.82%	-10.09%	-6.93%	-4.93%
With BPD	3.15%	-1.06%	2.87%	3.80%	-2.89%	3.44 %	2.54%	1.18%	3.31%
Helium CT									
Without BPD	-2.45%	-5.29%	-3.02%	-2.50%	-6.42%	-3.82%	-7.79%	-1.07%	-3.83%
With BPD	2.05%	0.31%	1.11%	1.87%	-0.30%	0.34%	-1.20%	4.11%	0.27%
Carbon CT									
Without BPD	-1.77%	-2.94%	-2.07%	-1.97%	-0.87%	-2.34%	-5.05%	-4.71%	-2.24%
With BPD	0.42%	-1.16%	-0.10%	0.15%	0.82%	-0.47%	-2.41%	-2.59%	-0.39%

Table 5.3: Mean RSP relative errors of the individual insert materials and PMMA for the simulated rod phantom pCT, heCT and cCT with or without applying the BPD method.

5.4.2 Experimental Phantom Investigations

Experimental Proton Radiographies (pRADs), Helium Radiographies (heRADs) and Carbon Radiographies (cRADs) were acquired for the slab and stepped wedge phantom [Kopp, 2017]. For all acquisitions, the phantoms were set up manually in the HIT experimental room using the in-room isocentric positioning laser system. Moreover, the images were acquired on the same day and in succession to each other without repositioning the phantoms in order to enable a consistent comparison between the different iRADs.

In order to obtain approximately the same imaging dose of around 9.5 mGy for all iRADs (estimated from MC simulations), the delivered number of particles per RP was scaled accordingly. Thus, 100000 protons, 25000 helium ions and 4000 carbon ions were irradiated per RP, all using the nominal beam energy E152 which corresponds to a range in water of around 17.2 cm. For comparison purposes, MC simulations [Kopp, 2017] were performed for this setup, however, using only 50% of the actually delivered particles due

to computational reasons. Nevertheless, the statistics were sufficient to yield a stable (simulated) detector signal, considering the limited particle collection efficiency of the experimental prototype.

The experimentally acquired and simulated iRADs for the slab phantom are shown in figure 5.8. Qualitatively all images accurately resemble the phantom geometry and the correct WET of the individual slabs. However, the pRADs exhibit an increased sensitivity to signal fluctuations at material interfaces compared to heavier ions. The WET of most materials in the experimental images was retrieved with an accuracy of better than 2.1% for all ions, demonstrating good agreement with simulation results. Only the relative error for lung exceeded 5% for the pRAD and heRAD. The relative error for the complete radiographic image (cf. equation (4.27)) was 13.8%, 7.1%, and 4.2% for the experimentally acquired pRAD, heRAD and cRAD, respectively.

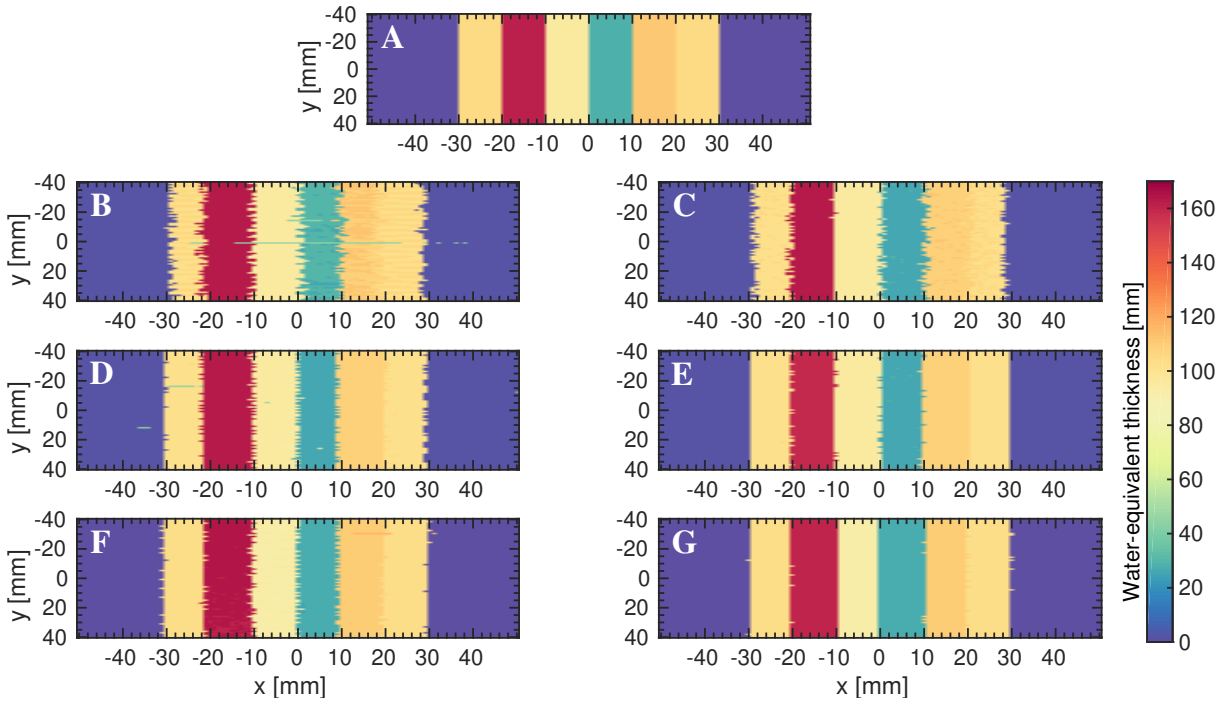

Figure 5.8: Comparison of experimental and simulated integration-mode iRADs for the slab phantom. The ground truth (A) is shown along with the experimental (left column) and simulated (right column) pRADs (B & C), heRADs (D & E) and cRADs (F & G).

Figure 5.9 displays the experimental and simulated iRADs for the stepped wedge phantom in configuration 1. As for the slab phantom, all images demonstrate very good agreement with the ground truth. At the physically straight sides of the phantom rounded artifacts in between the steps are visible, predominantly for protons and helium ions.

However, in all images the individual steps are sharply resolved. The overall relative error for the experimental images was 5.9% for the pRAD, 4.3% for the heRAD and 4.1% for the cRAD. The simulated data exhibited similar image quality as the experimental acquisitions with corresponding relative errors of 4.4%, 3.4% and 2.7%.

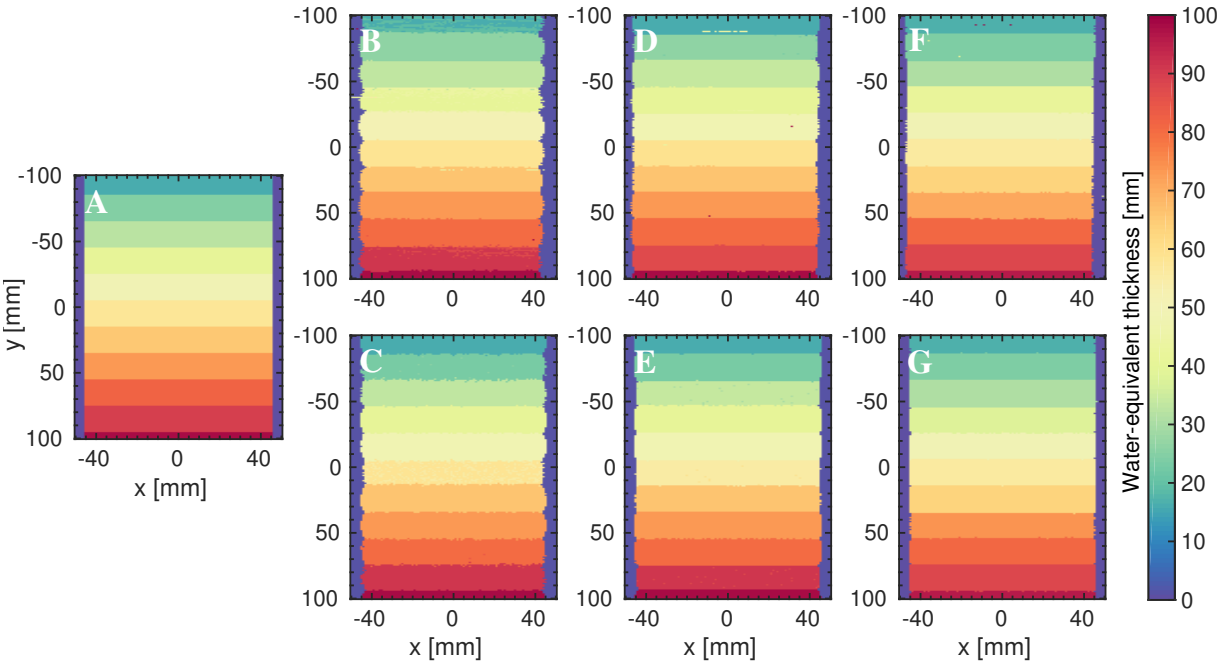

Figure 5.9: Comparison of experimental and simulated integration-mode iRADs for the stepped wedge phantom (configuration 1). The ground truth (A) is shown along with the experimental (top row) and simulated (bottom row) pRADs (B & C), heRADs (D & E) and cRADs (F & G).

Experimental and simulated iRADs for the stepped wedge phantom (configuration 2) are shown in figure 5.10, again demonstrating good visual agreement with the ground truth WET image. However, the step-like shape appears blurred for the heRADs, while for the pRADs the individual steps are barely visible. This is reflected in the overall image relative error, which was 5.5% for the experimental pRAD, 2.4% for the heRAD and 3.7% for the cRAD. The corresponding errors for the simulated iRADs were 2.2%, 1.3% and 0.8%.

In addition, full iCTs were performed for the rod phantom. Due to the inferior quality already observed for the acquired pRADs, only a heCT and cCT were acquired. In contrast to the radiography study, both tomographies were not acquired consecutively, since a single iCT acquisition takes several hours with the current systems. A total of 25000 helium ions and 5000 carbon ions were delivered per RP at 163.25 MeV and 310.58 MeV respectively (nominal beam energy E162), which corresponds to a range in water of around 18.2 cm. The resulting full tomography dose for 200 projections with 1 mm isotropic RP spacing was

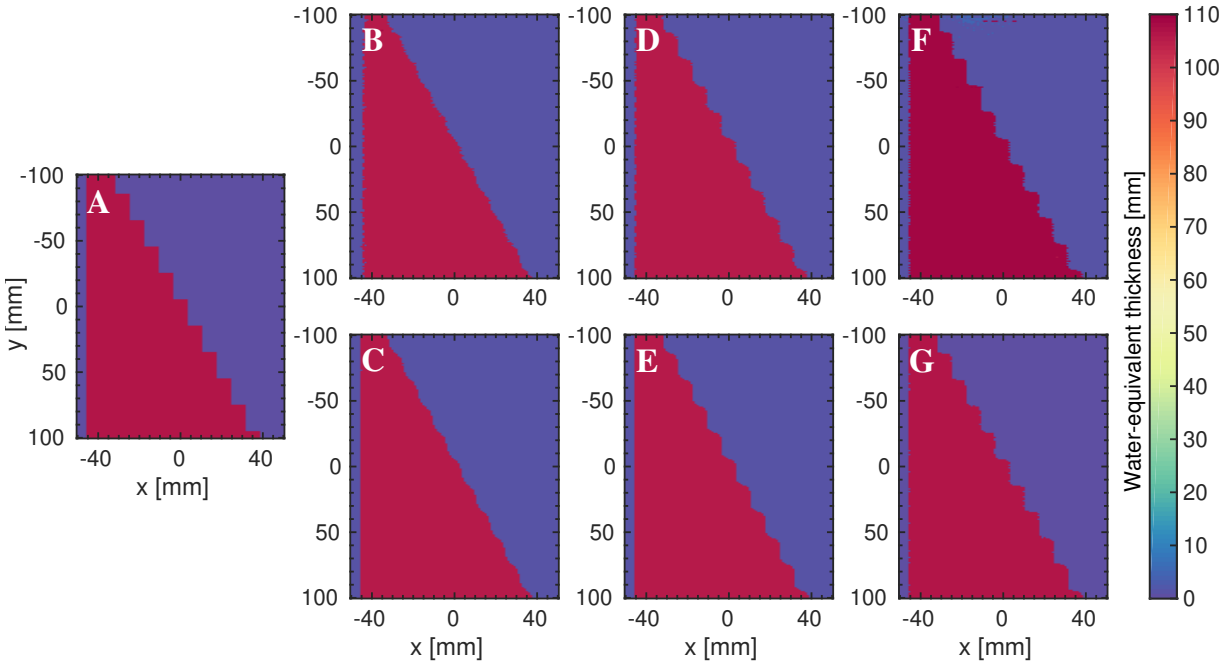

Figure 5.10: Comparison of experimental and simulated integration-mode iRADs for the stepped wedge phantom (configuration 2). The ground truth (A) is shown along with the experimental (top row) and simulated (bottom row) pRADs (B & C), heRADs (D & E) and cRADs (F & G).

around 1.9 Gy. Since the noise conditions in the experimental campaigns were comparable, $\varepsilon = 5 \times 10^{-4}$ (cf. equation (4.22)) was chosen for the stopping criterion in both cases.

Exemplary reconstructed transaxial slices are shown in figure 5.11. Due to the malfunction (i.e., under-response or extreme sensitivity to noise) of detector channels relevant to large WET values in the considered experimental run, slices reconstructed for the upper part of the phantom suffered from substantial artifacts and distortions, making those images not usable for RSP accuracy assessment. Visually, all displayed images exhibit relatively similar image quality, whereas ring artifacts are slightly more pronounced in the heCT reconstructions. The RSP relative error distributions for both iCTs are displayed as box plots in figure 5.12. Strong ring artifacts extending into the insert locations within the heCT image caused the considerably large RSP error for bone200 and bone400, which are placed in the center of the phantom. The average RSP relative error for the cCT was $(0.34 \pm 1.44)\%$, being marginally better than for the heCT, which yielded $(2.15 \pm 1.85)\%$. In agreement with the qualitative evaluation, the noise for both acquisitions is comparable. The corresponding results from MC simulations (for 10% of the original primaries) were $(0.50 \pm 1.41)\%$ and $(0.89 \pm 1.02)\%$.

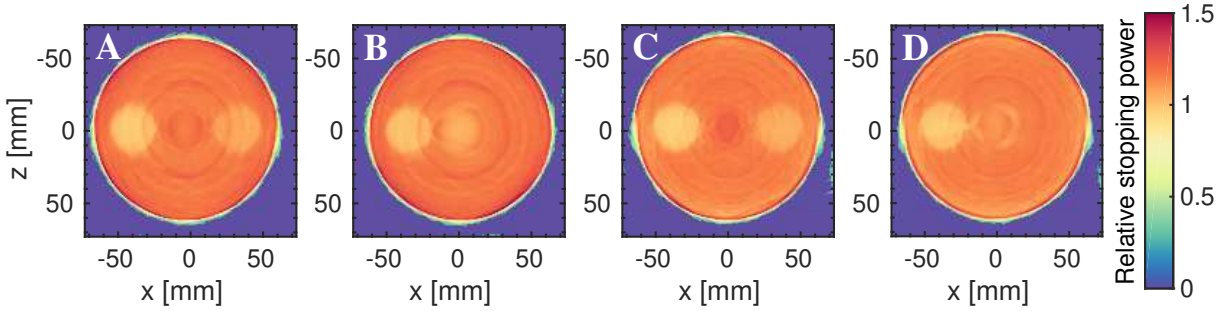

Figure 5.11: Reconstructed experimental transaxial integration-mode heCT (A & B) and cCT (C & D) slices for the bottom (A & C) and middle (B & D) insert row of the rod phantom.

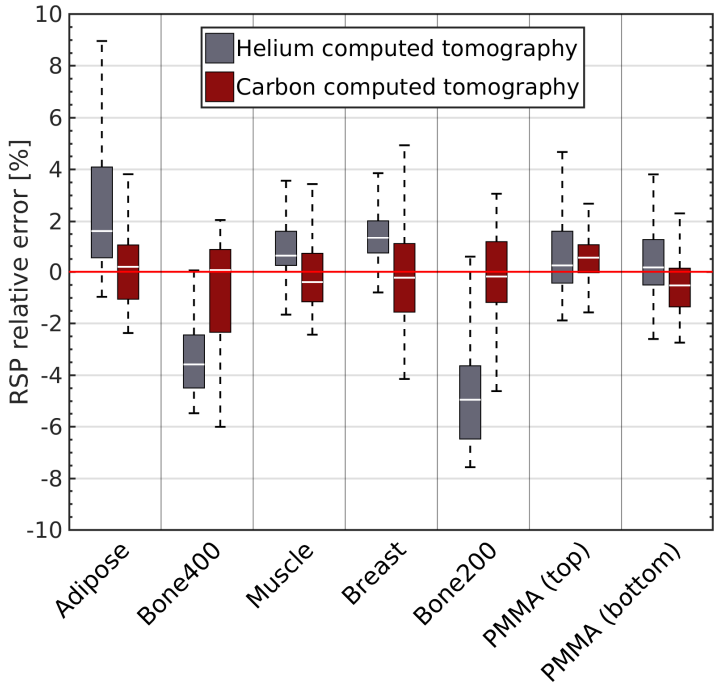

Figure 5.12: Box plot comparison of the RSP relative error distributions obtained for the experimental heCT and cCT acquisitions of the rod phantom. The median of the distribution is represented by the central white line, the box corresponds to the 25^{th} and 75^{th} percentiles, and whiskers indicate the last point within 25^{th}-1.5×(75^{th}-25^{th}) and 75^{th}+1.5×(75^{th}-25^{th}).

5.4.3 Potential Detector Upgrades

Besides efficiency shortcomings and noise issues related to the electronics, the current system performance is limited by the coarse range detector segmentation due to the 3 mm PMMA tiles. In order to improve the WET resolution, an upgraded system with reduced absorber thickness of 1 mm was proposed and investigated using MC simulations. For

this setting new fitting parameters of the channel-to-WET conversion (cf. equation (5.4)) were derived: $a_1 = 0.0009489\,(\mathrm{MeV/u})^{-2}$, $a_2 = 0.2321\,(\mathrm{MeV/u})^{-1}$, $a_3 = -14.59$ and $c = 1\,\mathrm{mm}^{-1}$. Moreover, a dedicated lookup-table for the BPD method was created.

This investigation solely focused on cCT since it is most suited for integration-mode imaging due to reduced MCS as demonstrated in the previous sections. Furthermore, carbon ions are more sensitive to an improved WET resolution compared to lighter ions, due to the reduced range straggling (cf. equation (2.6)). Acquisitions of 500 ^{12}C/RP, 2 mm RP spacing and 1.5° angular sampling were simulated. This configuration demonstrated substantial dose reduction (by a factor of ~ 67 compared to the experimental cCT scenario using the current prototype) with only slightly degraded RSP accuracy [Meyer et al., 2017]. Exemplary slices of the three different insert rows are shown in figure 5.13 for the current and the upgraded system. The reduced absorber thickness visually improves the homogeneity of the circular inserts and reduces ring artifacts. Figure 5.14 displays a box plot comparison of the RSP relative error distributions for both detector configurations. The reduced absorber thickness enhanced the RSP accuracy for most materials, showing improvements in the RSP relative error of up to 2.17%. While the average error reduction was only 0.36%, the standard deviation of the inserts RSP relative error distributions was substantially improved by 0.95%.

5.4.4 Imaging of Clinical-Like Data

Based on the aforementioned results, the potential of integration-mode imaging for clinical-like data was investigated for carbon ions using an upgraded range telescope with 1 mm absorber thickness. To this end, DICOM xCT data were imported in FLUKA as outlined in section 5.2. Nevertheless, the expected range of WET values across all projections exceeded the dynamic range of the detector. In order to artificially enhance the dynamic range by limiting the residual range of carbon ions, an algorithm was developed to derive a multi-energy irradiation plan based on prior knowledge of the digitally reconstructed WET radiographs and the initial beam shape (neglecting MCS). For anatomical regions of large WET carbon ions of 399.04 MeV/u (HIT nominal beam energy E232) were selected, whereas all other RPs were simulated with a nominal energy of 344.94 MeV/u (HIT nominal beam energy E194). Furthermore, the large irradiated field of view of up to 15 cm pencil beam deflection in the isocenter plane caused image reconstruction artifacts, since the original assumption of a parallel-beam geometry is not fully valid anymore. Hence, a 3D cone-beam geometry system matrix was implemented by straight line raytracing from

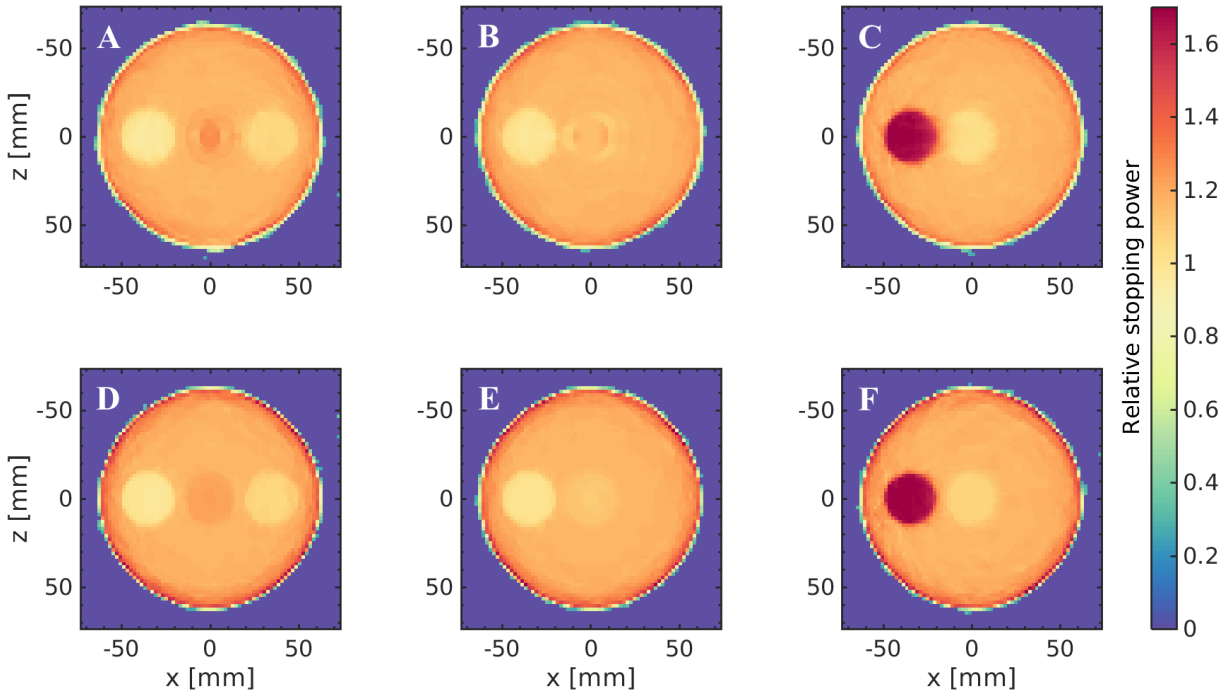

Figure 5.13: Reconstructed transaxial cCT slices for the rod phantom using a simulated integration-mode detector with 3 mm (A, B and C) and 1 mm (D, E and F) absorber thickness. Left, middle and right column correspond to the bottom, middle and top insert rows, respectively.

the position of the scanning magnet (0 cm, 0 cm, -650.6 cm) through the individual RP locations. A value of $\varepsilon = 5 \times 10^{-5}$ (cf. equation (4.22)) was selected as stopping criterion and the physical imaging dose (mean ± standard deviation) to the patient scored in FLUKA was (51 ± 2) mGy.

Two exemplary slices of the reconstructed cCT are displayed in figure 5.15a in comparison with the ground truth images. While the overall anatomical geometry is retrieved, the images suffer from substantial distortion artifacts, which strongly degrade the image quality. In particular, structures within the homogeneous brain tissue are not visible, due to the deteriorated contrast. Furthermore, the limited spatial resolution does not allow to reconstruct small-sized details, e.g., in the nasal cavities. Figure 5.15b shows the corresponding RSP relative errors for all reconstructed slices, being on average $(4.64 \pm 1.38)\%$.

5.5 Discussion

The developed BPD method demonstrated a clear benefit for the image quality achievable with the considered integration-mode range telescope by resolving ambiguities in the

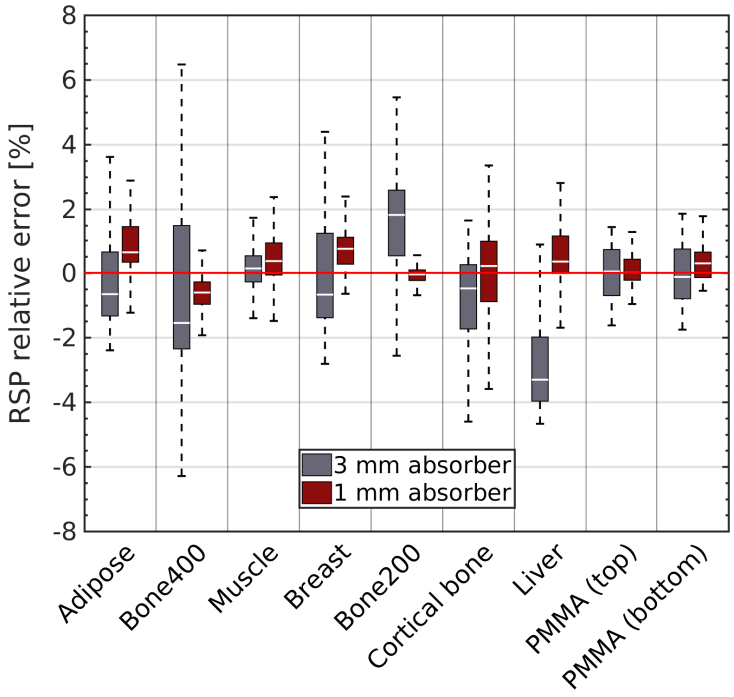

Figure 5.14: Box plot comparison of the RSP relative error distributions obtained with a simulated detector configuration (integration-mode) of 3 mm and 1 mm absorber thickness for the rod phantom. The same representation as in figure 5.12 is used.

maximum signal identification in tissue heterogeneities and interfaces [Meyer et al., 2017]. Without post-processing, lateral interfaces increase the integrated detector signal of more proximal channels due to an overlap of the signal components (cf. figure 5.7). This general bias toward larger WET values potentially causes distortions of the actual object geometry and size within the iRADs. Hence, the BPD also helps to preserve the accurate object shape. The reduced amount of inconsistencies in the projection data substantially enhanced the RSP accuracy in tomographic image reconstruction (cf. table 5.3).

The implemented simulation model demonstrated generally very good agreement with experimental results, due to an accurate modeling of the beam properties as well as phantom and detector composition, RSP and geometry. Variations in the obtained WET accuracy between experimental and simulated data for lung tissue originate from neglecting the porous material structure within the MC simulations, thus, not considering the additional Bragg peak degradation [Titt et al., 2015; Magallanes et al., 2019]. The slightly increased WET error observed in the stepped wedge phantom (configuration 2) for the experimental cRAD image compared to the heRAD image, is only attributed to an unfavorable carbon ion Bragg peak position within the range telescope for the WET value of the phantom.

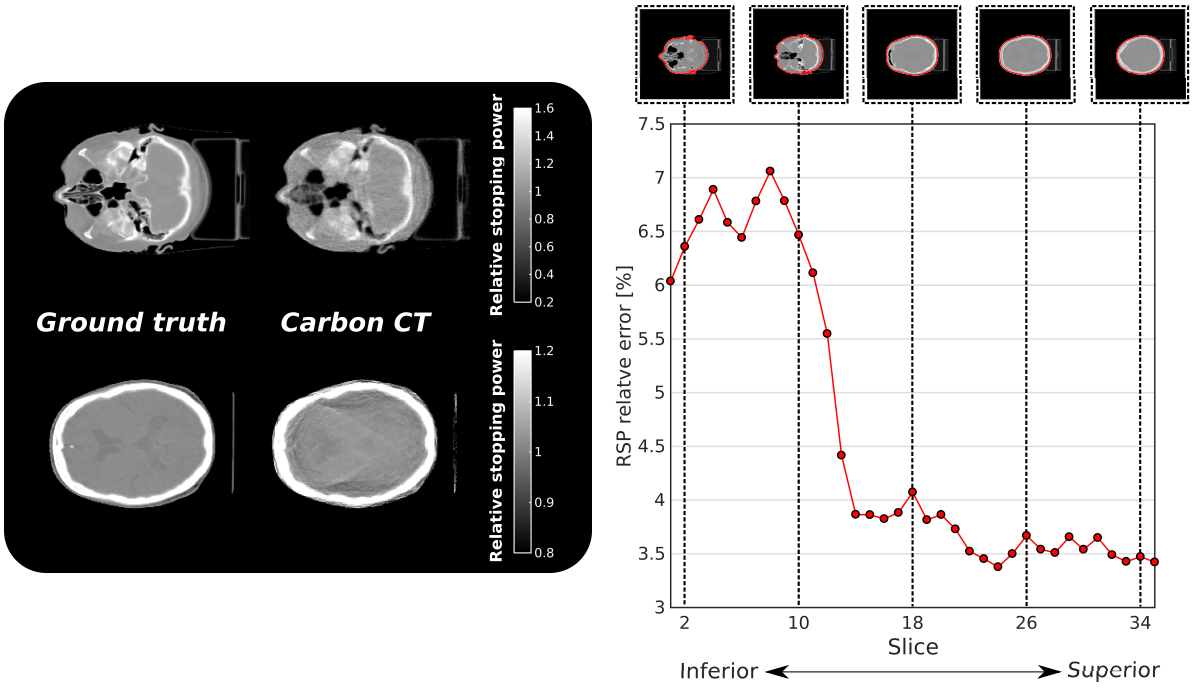

(a) (b)

Figure 5.15: (a) Exemplary reconstructed transaxial cCT slices in comparison to the ground truth images. (b) RSP relative error for the reconstructed images as a function of the transaxial slice location. The corresponding anatomical regions for selected slices are shown above the plot.

Since this is the only WET value within the image other than air, it dominates the error, even though cRAD yields a better geometrical agreement with the reference. For the presented range telescope design, the general WET resolution is limited by the detector granularity of 3 mm PMMA-equivalent thickness. This value exceeds the intrinsic range straggling limit of around 2 mm, 0.9 mm and 0.5 mm (water-equivalent) for the used energies of the simulated clinical-like proton, helium and carbon ion beams, respectively. Since the individual ion beams also have approximately the same range (within less than 2 mm in water), a comparable WET accuracy for the pRADs, heRADs and cRADs was observed.

Due to the comparable WET accuracy at the same imaging dose for all investigated ion species, the superior image quality obtained for carbon ions reflects the reduced MCS and beam spot size (e.g., 3.8 mm FWHM in air at isocenter for around 18.2 cm range in water compared to 6.1 mm and 10.4 mm for the corresponding helium ion and proton beams, respectively). Potential differences in the biological damage between the investigated ions are discussed in chapter 7. Remaining uncertainties at material boundaries or defective (i.e., consistently under- or over-responsive) channels can cause inaccuracies in the projec-

tion data. Those effects are translated into centered ring artifacts in the reconstructed iCT images (cf. figure 5.11) due to the rotational symmetry [Boas and Fleischmann, 2012].

In order to reduce the observed immanent noise issue in experimental acquisitions, the detector signal strength needs to be further improved, either by increasing the thickness of the PPICs active volume or by enhancing the particle collection efficiency. The latter can be potentially achieved by using electronics with adaptive gated trigger capability. This would enable a matching between the integration period and the fluctuating dwell times of individual RPs. Preliminary investigations of adaptive gating using an I4000 multi-channel electrometer (*Pyramid Technical Consultants, Inc., Lexington, MA, USA*) connected to four detector channels indicated a potentially substantial improvement in the measured integrated current [Magallanes et al., 2019].

The proposed BPD method also entails the possibility of supporting the experimental data reconstruction with prior information [Magallanes, 2017]. Using an accurate and experimentally validated MC framework for iCT simulations like the one developed in this thesis and available prior knowledge of the object, e.g., from xCT data, the decomposed simulated detector signal can be used to facilitate the BPD for experimental data. By accounting for a potential misalignment between experimental scenario and MC simulation, this method can further enhance the image quality even in the presence of channel malfunctioning.

While simulated iCTs do not considerably benefited from full angular coverage [Meyer et al., 2017], experimental acquisitions can yield further improved image quality [Magallanes et al., 2019]. The reason is that the additional information from more projections can be used to compensate the noise inherent in the individual radiographies, however, at the cost of an increased dose exposure to the imaged object of interest. Moreover, full angular coverage can be of value for strongly asymmetric cases, i.e., where MCS and nuclear reactions are considerably different for two opposite projections.

In comparison to the currently in-use prototype detector, the performance of a setup with a reduced absorber thickness of 1 mm demonstrated a clear benefit for the RSP accuracy of cCT, due to an improved WET resolution. This quantitatively underlines the usefulness of the envisioned detector upgrade [Meyer et al., 2017]. However, the achievable image quality for the presented integration-mode system lacks of sufficient spatial resolution to be useful for ion therapy treatment planning, as indicated by the the poor image quality for clinical-like data (cf. figure 5.15). While the developed BPD strategy and the proposed system upgrade present promising approaches to enhance the system performance, further

improvement is required.

One potential approach is to fully embed each individual signal component from the BPD into the tomographic image reconstruction [Seller Oria et al., 2018]. Therefore, the integration-lines have to be substituted by cones representing the initial beam spot size convolved with a pre-calculated scattering contribution for the corresponding WET value. Moreover, the iterative image update formula has to be modified accordingly.

Another possibility is to optimize the images in radiographic domain before the tomographic image reconstruction. The inferior spatial resolution limited by the RP spacing can be potentially restored by exploiting the redundant information encoded in the overlap of neighboring beam spots. Such enhancement or reassignment strategies have already been proposed by using additional prior information [Krah et al., 2015] and also without [Gianoli et al., 2016]. These methods yielded an improved image quality for the more challenging proton imaging and could possibly also enable an increased RP spacing and consequently imaging dose reduction.

Due to the statistical distribution of ions within a pencil beam, the presented integration-mode configuration requires certain statistics for obtaining a meaningful representation of the WET distribution for each RP position [Meyer et al., 2017]. This limitation can be eluded with single-particle tracking, since the information available for each particle is processed individually. Therefore, this configuration enables substantially better spatial resolution [Krah et al., 2018a] and lower imaging doses. However, these benefits come at the cost of a more complex detector instrumentation and increased computational time due to the enormous amount of data and the required path estimation.

"All of physics is either impossible or trivial. It is impossible until you understand it, and then it becomes trivial."

Sir Ernest Rutherford

6

Single-Particle Tracking Ion CT for Clinical Treatment Planning

Heavier ions can yield improved image quality by benefiting from reduced MCS in the path estimation for single-particle tracking. However, they also exhibit an increased physical dose (per particle) and suffer from an elevated loss of primaries due to fragmentation, ultimately affecting the noise present in reconstructed images. In this chapter the first comparison of different ion species for iCT, including image quality and range accuracy for proton therapy treatment planning in realistic scenarios is presented. The quality of simulated pCT, heCT and cCT images was assessed for clinical cases of cranial locations. Moreover, the associated range prediction and dose calculation accuracy was quantitatively evaluated using the RayStation TPS. All investigated scenarios were compared to the established clinical practice of deriving RSP maps via a stoichiometric calibration from single energy xCT data. Parts of the results presented in this chapter have been published in Meyer et al. [2019].

6.1 Monte Carlo Model

6.1.1 Simulation of Detection and Data Acquisition

An ideal iCT detector system was simulated, which is represented by solely two scoring planes recording position, direction and energy of each individual ion prior and posterior to the imaged patient volume, 45 cm from the isocenter as in a realistic clinical scenario. Each tracker covered an active area of $30 \times 30\,\mathrm{cm}^2$. The initial beam energy was set to the nominal beam energy E222 available at HIT, which corresponds to 199.44 MeV, 199.03 MeV/u and 385.18 MeV/u for protons, helium and carbon ions, respectively. These energies are equivalent to a range in water of around 26 cm for each ion species, making them hypothetically detectable with the dynamic WEPL range of existing prototype detector systems [Giacometti et al., 2017]. 400 primary protons, 100 helium ions and 20 carbon ions were simulated per RP for a total of 180 projections, resulting in a physical dose of ~ 1.9 mGy for each full tomography. This value is much lower than the typical dose exposure in xCT of 10 to 100 mGy [Murphy et al., 2007]. The individual RP locations were aligned with the voxels of the simulated patient xCT data imported into the FLUKA MC simulation framework, i.e., 1.074 mm and 3 mm spacing in horizontal and vertical direction, respectively. For single-particle tracking, the spacing can in principle be selected independently of the imported xCT data granularity, however, this is useful for a direct comparison with integration-mode, since the sinogram binning is given by the RP spacing.

6.1.2 Clinical Patient Data Sets

The import of the clinical data was implemented in the same way as for the integration-mode study (cf. section 4.1.5). It should be kept in mind that inaccuracies due to the stoichiometric calibration occurring for real patient scenarios are not present when using MC simulations, since the conversion is defined by the user. Thus, simulations allow a consistent and error-free comparison of the reconstructed images with the ground truth. Three representative cranial patient cases were investigated: a left frontobasal anaplastic astrocytoma (patient 1; as used in chapter 5), a nasopharynx cancer (patient 2) and a left sided glioblastoma (patient 3). These patients were originally treated with photons, but also represent common indications for ion therapy. Exemplary xCT slices overlaid with the contours of the PTV and relevant OARs are shown in figure 6.1.

6.2 Treatment Planning

All treatment plan optimizations and dose calculations were performed with a research version of the commercial (analytic) TPS RayStation (*RaySearch Laboratories, Stockholm, Sweden*). Since the current version does not feature a direct import of 3D RSP maps, the reconstructed iCT images were back-converted into HUs prior to the data import using the inverse of the HU-RSP conversion curve applied in the FLUKA MC simulations. Due to the imposed bijectivity of that function, no uncertainty or ambiguity is introduced in this process. The data import into the TPS was performed in the same way for all images, i.e., using the same internal conversion to density and subsequently RSP. This eliminates uncertainties and enables a consistent comparison between the dose distributions calculated on different image sets, independent of the fact that the conversion exploited in the MC simulation is different from the one of the TPS [Meyer et al., 2019].

In order to emulate the typical uncertainties encountered for the HU-RSP conversion based on the stoichiometric calibration approach for single energy xCT data, an additional xCT image set (hereafter referred to as $\mathrm{xCT_{stoi}}$) was imported into the TPS by randomly introducing an error (using a continuous distribution from -3% to +3%) to the RSP values of the conversion curve [Meyer et al., 2019]. In agreement with the findings of Wohlfahrt et al. [2017] for a comparison study between DECT and single energy xCT, the chosen conversion curve resembled a systematic overestimation of the RSP for soft tissue while underestimating it for bony materials.

For each patient case, individual IMPT (cf. figure 6.1) and SFUD proton therapy treatment plans using pencil beam scanning were designed. The reference scenario is given by the dose distribution optimized on the RSP ground truth images obtained from the imported original xCT anatomy (from hereon referred to as $\mathrm{xCT_{GT}}$). Subsequently, the derived treatment plans were recalculated in RayStation on the reconstructed iCTs and the $\mathrm{xCT_{stoi}}$ images without re-optimization of the plan.

For SFUD plans, the recalculated dose distributions were compared to the original (planned) reference by means of beam's-eye view range difference maps. While these plans were not designed to yield clinically optimal results, the field directions were selected to represent cases of large heterogeneities (0°, patient 1) as well as more homogeneous beam paths with long (90°, patient 2) and short penetration depth (90°, patient 3). The beam range was defined as the 80% distal dose falloff along the original field direction. For quantitative comparison with safety margins and range uncertainties in current clinical

practice, the obtained range differences were converted into water-equivalent range. In order to compute the correct scaling, raytracing [Siddon, 1985] was performed on the RSP ground truth between both distal dose falloff locations (evaluated and reference plan) [Wohlfahrt et al., 2017]. To obtain relative range shifts, the results were divided by the corresponding water-equivalent range of the distal falloff location in the reference scenario [Meyer et al., 2019]. Multi-field IMPT plans (shown in figure 6.1) were evaluated based on dose-volume histograms and a global 3D gamma criterion [Podesta et al., 2014] (using a 10% low-dose threshold).

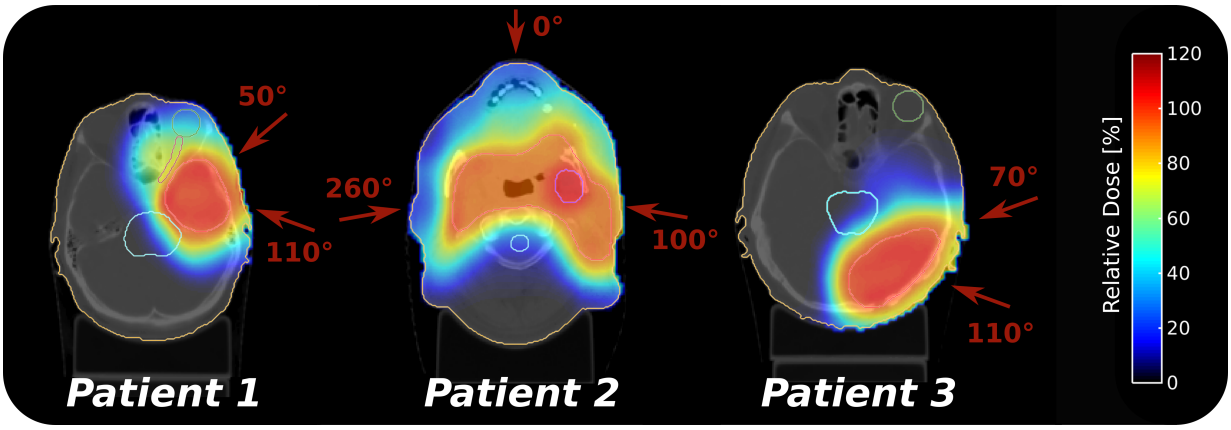

Figure 6.1: PTV and OAR contours for the investigated patient cases. The overlaid (ground truth) relative dose distributions (normalized to the prescribed target dose) are obtained for the indicated beam arrangements of the IMPT plans.

6.3 Results

6.3.1 Comparison of the Path Estimation Models

In order to benchmark the implemented path estimation models, proton, helium and carbon ion beams were simulated in FLUKA to traverse a water phantom of 20 cm, starting from the initial nominal HIT energy E222, corresponding to around 26 cm range in water. The individual ion trajectories were reconstructed by exploiting the information on the ideal particle entrance and exit positions and directions at the surface of the water block available from the MC simulation. This approach enables a quantification of the intrinisc inaccuracies of the employed path estimation models in a homogeneous medium. Exemplary ion trajectories and the corresponding path estimates are shown in figure 6.2 (a, c and e). In all cases, the MLP can be reproduced by the implemented refined CSP model

of Collins-Fekete et al. [2015]. The simple SLP generally provides a less accurate path estimation, however, the differences reduce for heavier particles since MCS is suppressed. Nevertheless, the SLP remains inferior even for carbon ions.

The RMS deviation between the MC particle paths and the estimated SLPs, CSPs and MLPs was calculated for 10^5 events at 201 equally spaced points along the paths. Figure 6.2 (b, d and f) shows the RMS deviation as a function of depth for the three ion types. In agreement with the exemplary ion paths, carbon ions offer the best accuracy. The maximum RMS errors for the CSP observed slightly downstream of the object's center were 0.52 mm, 0.28 mm and 0.17 mm for protons, helium and carbon ions, respectively.

Subsequently, the impact of the observed path estimation variations on the RSP accuracy was evaluated for the tomographic image reconstructions of patient case 1. For all reconstructions presented in this chapter, an ε value of 1×10^{-8}, 1×10^{-7} and 2×10^{-6} was selected as stopping criteria for pCT, heCT and cCT, respectively. The chosen values yield the best compromise between convergence and noise, reflecting the differences in particle statistics. Additionally, the benefit of coupling the TVS scheme (cf. section 4.3.3) to the OS-SART algorithm was quantified. Table 6.1 summarizes the RSP relative errors averaged over all obtained slices for the different reconstruction scenarios. Using the MLP or CSP yielded almost the same image quality in all cases. Compared to the SLP reconstruction, the RSP error was reduced, predominantly for pCT. The implemented TVS scheme enhanced the RSP accuracy substantially for all ion types with an average relative error reduction of 0.42%, 0.49% and 1.02% for pCT, heCT and cCT, respectively. Consequently, from now on all reconstructions are based on the TVS OS-SART algorithm and the CSP model.

	Proton CT			Helium CT			Carbon CT		
	SLP	CSP	MLP	SLP	CSP	MLP	SLP	CSP	MLP
Without TVS	2.25%	1.68%	1.68%	1.73%	1.48%	1.47%	2.66%	2.18%	2.23%
With TVS	1.83%	1.26%	1.26%	1.22%	1.00%	1.00%	1.45%	1.30%	1.30%

Table 6.1: Average RSP relative error for the pCT, heCT and cCT images of patient 1 obtained with different path estimation models and with or without including TVS.

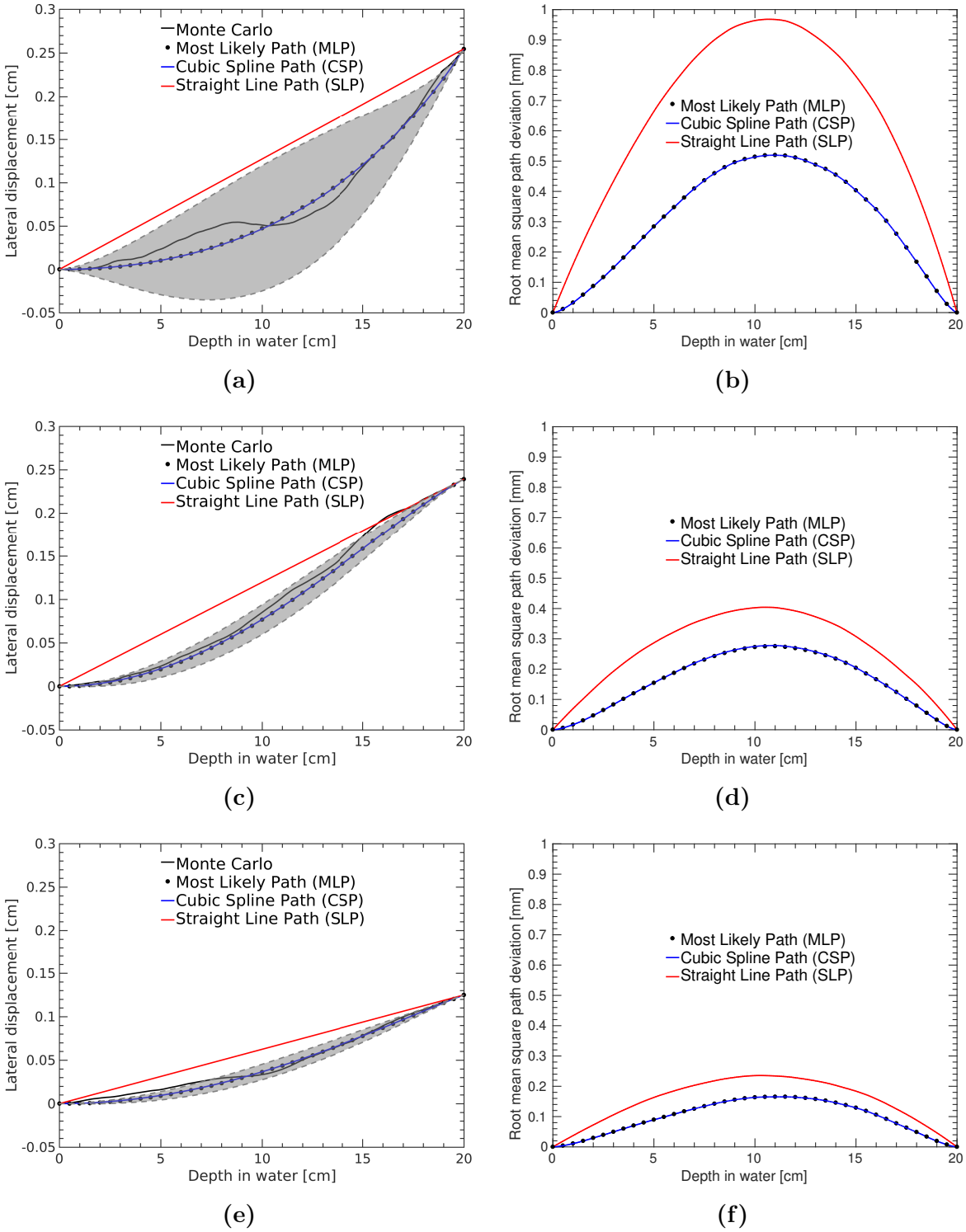

Figure 6.2: Exemplary SLP, CSP and MLP trajectory estimations for simulated (a) ^{1}H, (c) ^{4}He and (e) ^{12}C ions of the initial HIT nominal beam energy E222 along with the corresponding RMS deviation between MC particle trajectories and path estimations (b, d and f) in 20 cm of water. The real path is obtained from the information of the MC simulation. The gray shaded area represents the $\pm 1\sigma$ statistical uncertainty of the MLP model (cf. equation (4.13)).

6.3.2 Image Quality Comparison

Figure 6.3 shows exemplary slices of the reconstructed iCTs. Qualitatively, the displayed cCT images exhibit superior spatial resolution, indicated by an improved visibility of small-sized bony structures. In contrast, brain tissue appears less noisy in the pCT images enhancing the contrast (e.g., for the visibility of the lateral ventricle). The RSP relative errors are plotted in figure 6.4 for all transaxial slices. In general, heCT exhibits superior image quality in terms of a reduced RSP error, being on average 0.2% and 0.3% lower than for pCT and cCT, respectively. In case of highly heterongeous anatomy like the paranasal sinuses or nasal cavities (e.g., figure 6.4: slice 1-10 for patient 1), the relative error is considerably increased. For slices mainly containing homogeneous brain tissue, (e.g., figure 6.4: slice 18-35 for patient 1), the RSP accuracy of pCT surpasses the one of the cCT and yields similar relative error values as heCT. When reducing the particle statistics used in the tomographic image reconstruction for pCT and heCT to match the particle number of 20 ions per RP used for the presented cCT images, the average RSP relative error considering all slices was 6.6%, 1.7% and 1.3% for pCT, heCT and cCT.

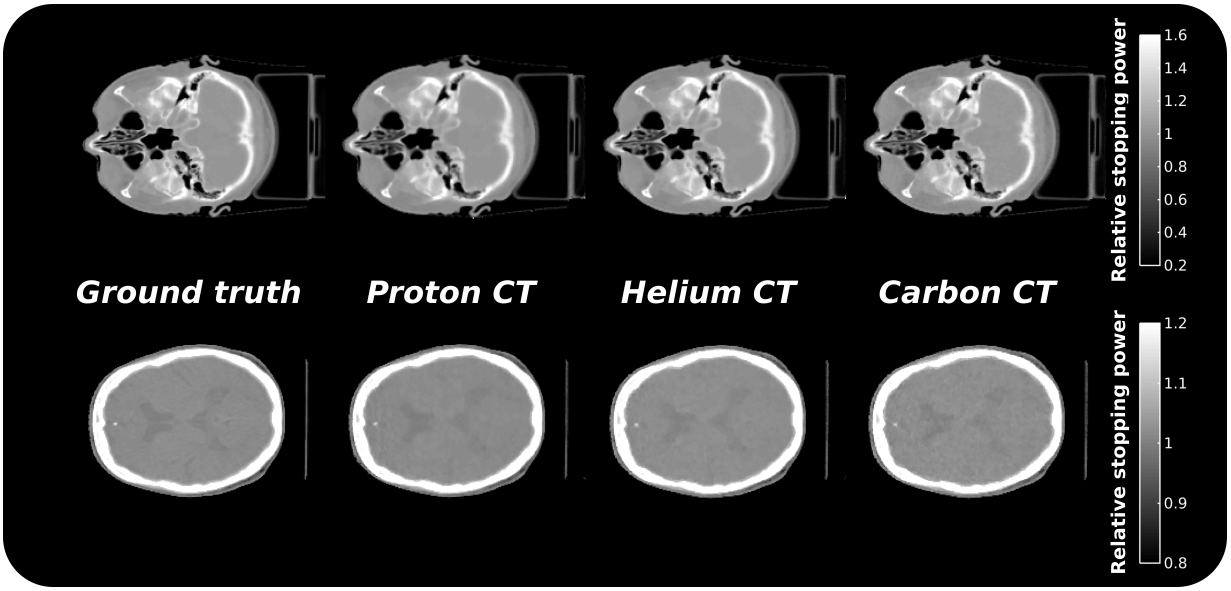

Figure 6.3: Comparison of exemplary reconstructed iCT images at approximately the same imaging dose for patient case 1 and the corresponding ground truth (top row: slice 8; bottom row: slice 25).

The reconstructed RSP distribution for patient 3 is displayed in figure 6.5 as a function of the original HU values, demonstrating good agreement with the ground truth HU-RSP conversion curve used for importing the patient anatomy into the MC simulation. pCT

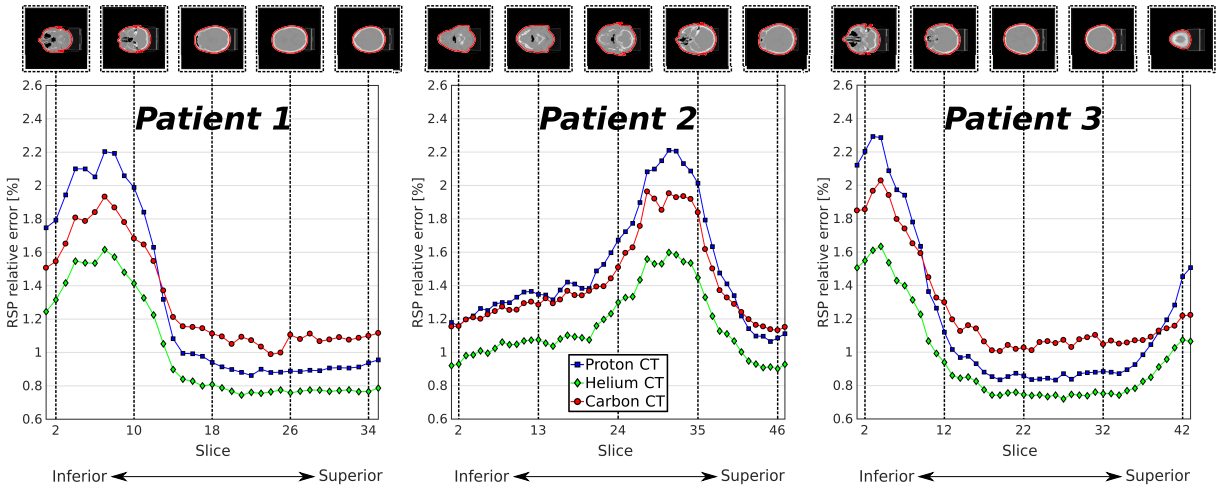

Figure 6.4: Comparison of the RSP relative error for pCT, heCT and cCT at the same imaging dose as a function of the transaxial slice location. The corresponding anatomical regions for selected slices are shown above the plots as reference.

and cCT show worse RSP precision in terms of an increased standard deviation, being 1.3 times higher than for heCT. In the zoom-in plots of figure 6.5, the reconstructed mean RSP underestimates the correct value for bony materials (-2.1%, -1.2% and -0.4% at 1500 HU for pCT, heCT and cCT, respectively) and overestimates it for fat and soft tissue (+0.5%, +0.9% and +1.2% at 0 HU) [Meyer et al., 2019].

6.3.3 Range Calculation Accuracy for SFUD Plans

Figure 6.6 exemplary shows the optimized SFUD dose distribution (i.e., $\mathrm{xCT}_{\mathrm{GT}}$ reference) along with the results for plan recalculations on the reconstructed iCTs and the $\mathrm{xCT}_{\mathrm{stoi}}$ images. In all cases the dose deposition inside the PTV is slightly overestimated, predominantly for cCT and $\mathrm{xCT}_{\mathrm{stoi}}$. This overestimation in turn results in an under-dosage behind the PTV due to a reduced residual range caused by the increased energy loss within the upstream anatomy. Dose differences of up to 0.4%, 1.0% and 2.8% were observed for pCT, heCT and cCT, respectively, compared to 8.5% for the $\mathrm{xCT}_{\mathrm{stoi}}$ data.

Figure 6.7 shows the observed SFUD range variations across the projected target volume, calculated as water-equivalent difference in the position of the 80% distal dose falloff in beam's-eye view between planned (i.e., $\mathrm{xCT}_{\mathrm{GT}}$) and recalculated (i.e., iCTs and $\mathrm{xCT}_{\mathrm{stoi}}$) dose distributions. All iCTs enabled sub-millimeter accuracy with an average ($\pm 1\,\sigma$) relative proton-beam range error of $(+0.09 \pm 0.33)\%$, $(-0.08 \pm 0.24)\%$ and $(-0.35 \pm 0.26)\%$ for pCT, heCT and cCT, respectively. This corresponds to a water-equivalent range error

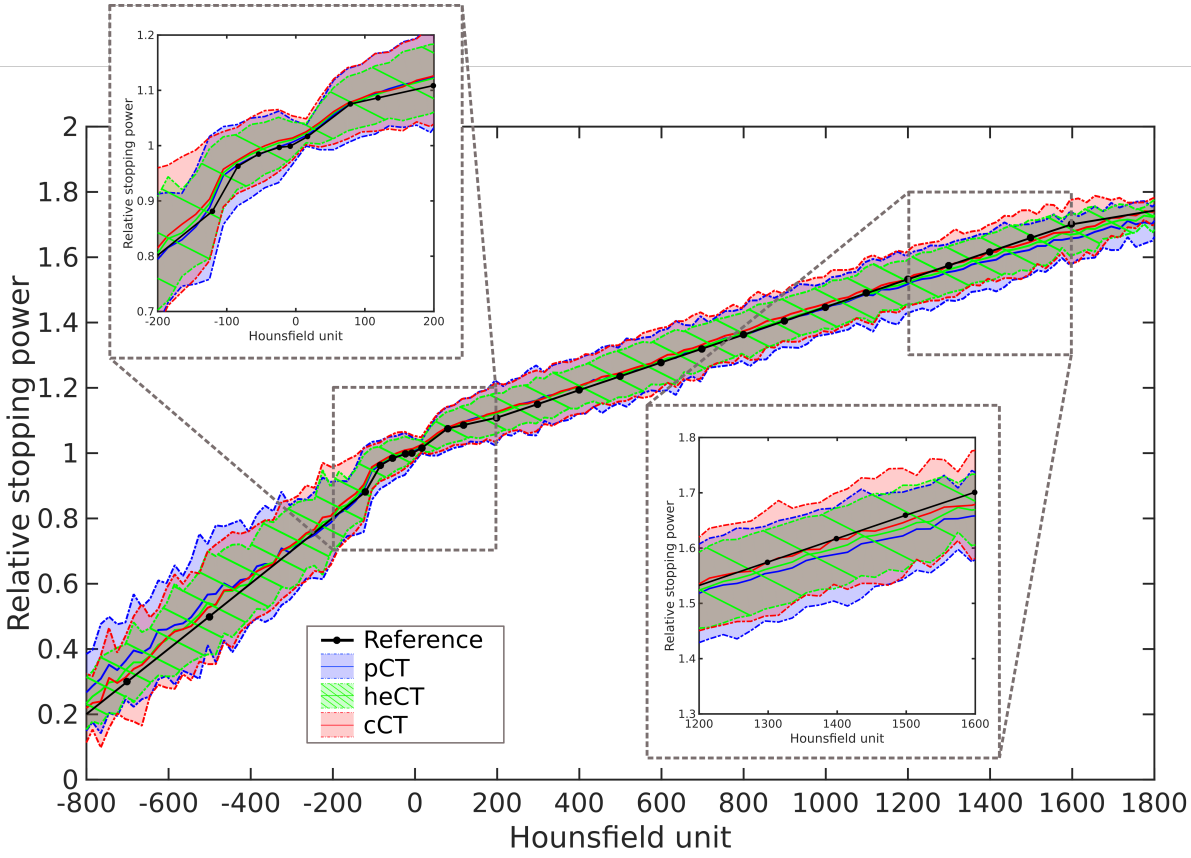

Figure 6.5: Joint histogram of the reconstructed iCTs and the original HU values, shown in steps of 20 HU values. The colored solid lines correspond to the mean value while partially-transparent shaded areas represent the $\pm 3\,\sigma$ interval. An outline is added for improving the visibility of overlapping regions. The black line indicates the ground truth conversion curve being used to import the initial xCT data into the simulation. Figure taken from Meyer et al. [2019].

of $(+0.07 \pm 0.18)$ mm, (-0.08 ± 0.14) mm and (-0.29 ± 0.18) mm. For the pCT data set of patient 2, over-ranging above 1% was observed for pencil beams traversing the nasal cavities. The corresponding range error for the xCT_{stoi} data was $(-1.00 \pm 0.43)\%$ and (-0.84 ± 0.32) mm [Meyer et al., 2019].

6.3.4 Dosimetric Comparison of IMPT Plans

The dosimetric comparison based on clinical multi-field IMPT plans is presented in figure 6.8. The obtained iCT dose-volume histograms were in notable agreement with the reference and variations in $D_{2\%}$ and $D_{98\%}$ (i.e., the dose received by 2% and 98% of contoured volumes, respectively) were not exceeding 15 cGy for OARs. By contrast, variations

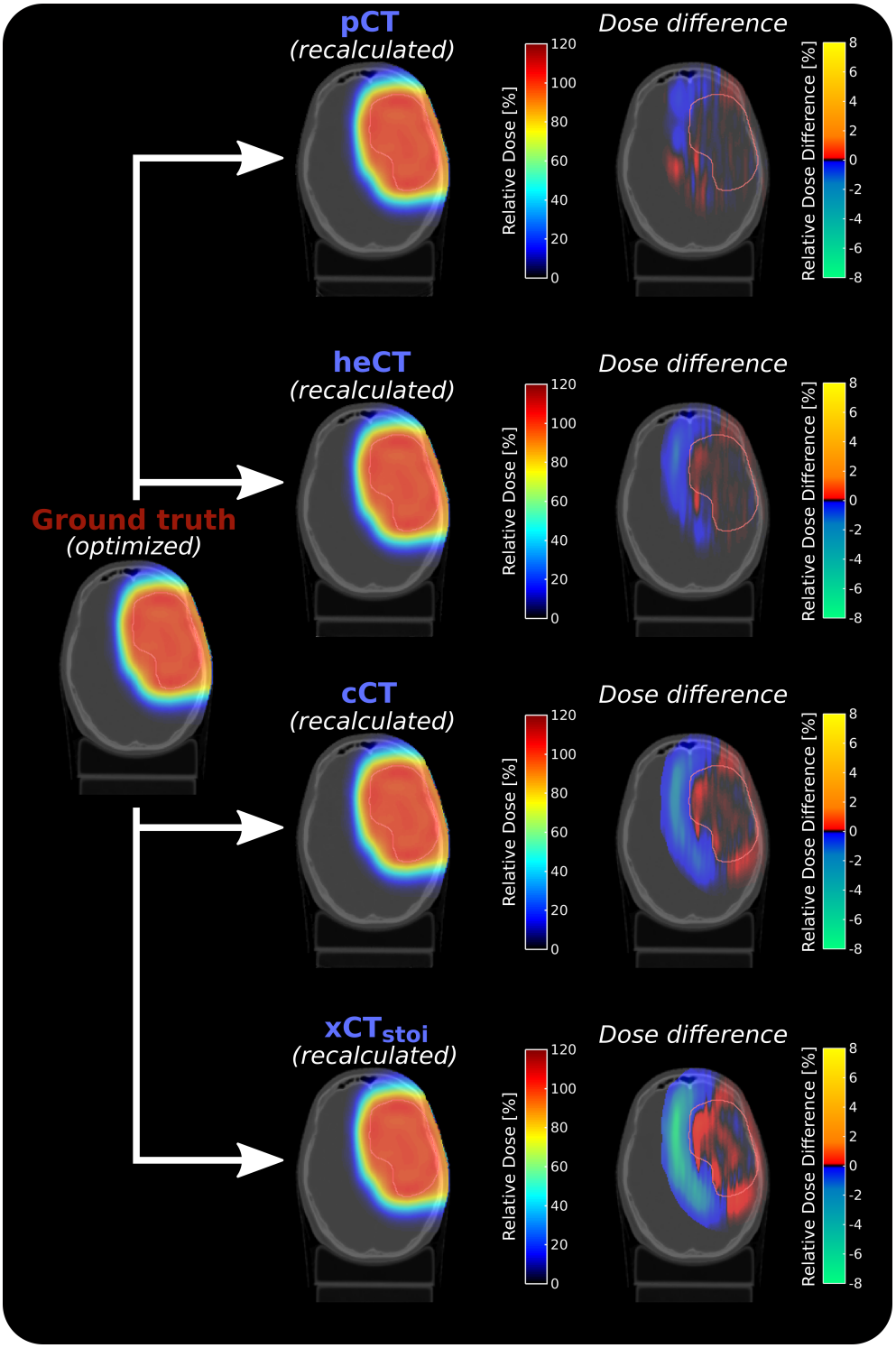

Figure 6.6: Relative dose distributions for patient case 1 (normalized to the prescribed PTV dose) for the optimized reference (xCT_{GT}) plan and the recalculated (iCTs and xCT_{stoi}) plans along with the corresponding relative dose differences. Positive and negative dose difference indicated an over- and under-dosage with respect to the ground truth, respectively.

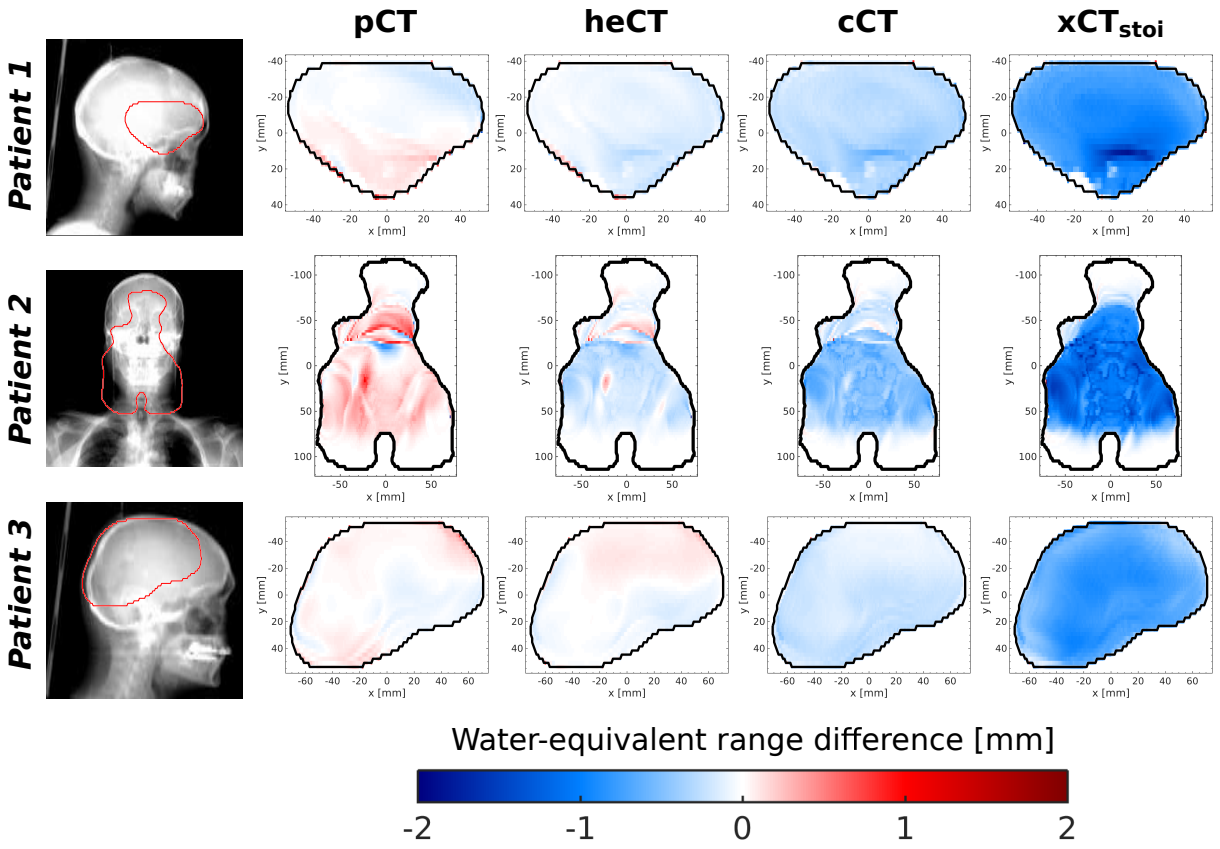

Figure 6.7: Beam's-eye view water-equivalent proton beam range variations for recalculation based on (single-particle tracking) iCTs and xCT_{stoi} with respect to the optimized dose using the reference plan. On the left, the 80% isodose contours are overlaid with the ground truth radiographies. Positive and negative differences indicate an over- and under-ranging, respectively.

of up to 200 cGy were observed for the xCT_{stoi} images [Meyer et al., 2019]. This result was corroborated by an additional global 3D 0.5%/0.5 mm gamma-evaluation, demonstrating excellent dosimetric and spatial agreement between recalculated and reference IMPT dose distributions. The average passing rate for all dose distributions recalculated on iCT images exceeded 99%, whereas xCT_{stoi} only exhibited an average passing rate of 83%.

6.4 Discussion

The implemented CSP offers similar accuracy as the computationally more demanding MLP and is superior to a SLP even for cCT, despite the substantially reduced MCS compared to lighter ions. Furthermore, carbon ions demonstrated the best path estimation accuracy and smallest instrinsic statistical model uncertainty (cf. gray shaded area in fig-

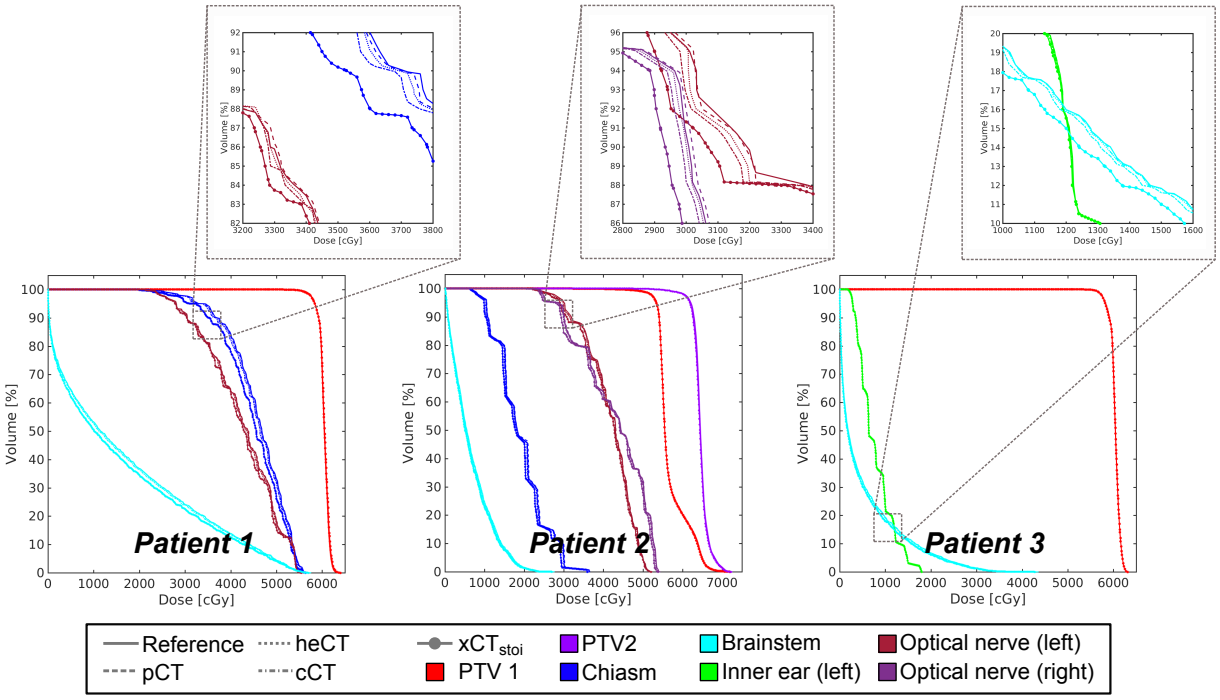

Figure 6.8: Dose-volume histograms for the optimized (ground truth) and recalculated (iCTs and xCT$_{stoi}$) IMPT dose distributions for the three investigated patient cases.

ure 6.2) being in agreement with findings of Collins-Fekete et al. [2017b]. It should be kept in mind that the CSP and MLP formalism are assuming scattering in a homogenous water medium. Collins-Fekete et al. [2017a] demonstrated that an extension of the underlying Fermi-Eyges formalism to the actual material composition and particle energy does not substantially improve the path accuracy. However, the use of a hull contour to restrict the beginning and end of the CSP estimation is of fundamental importance, since the surrounding air is a major contribution to the path uncertainty. Although the selected approach in this work exploited prior knowledge of the patient anatomy, an approximated image based on SLPs [Shrestha et al., 2018] or analytical reconstruction [Giacometti et al., 2017] could be alternatively used. The implemented TVS scheme demonstrated a substantial benefit for the quality of reconstructed iCT images. Largest improvements were obtained for cCT, since the tomographic image reconstruction employed the fewest amount of particle histories (as a consequence of a reduced number of primary particles at the same imaging dose and an increased nuclear fragmentation). Due to the assumed ideal iCT system, the TVS method is expected to be even more useful in realistic noisy scenarios.

While all iCTs provided accurate RSP values (cf. figure 6.4), differences between the three ion species mainly represent variations in the path estimation accuracy and the

number of particles used in the image reconstruction at the investigated dose level. While carbon ions offer the most accurate path estimate (cf. figure 6.2), cCT reconstructions employ reduced statistics due to nuclear fragmentation and less primary ions compared to heCT and pCT in order to match the imaging dose. This results in an increased noise for the reconstructed cCT images as it can be see in figure 6.3.

The reduced RSP accuracy for bony materials and low-HU regions (cf. figure 6.5) results in an increased RSP relative error for slices containing highly heterogeneous anatomy (cf. figure 6.4: slice 1-10 for patient 1). This is caused by partial volume effects during the tomographic image reconstruction and inaccuracies in the path estimation. The latter originates from assuming scattering in a homogeneous water material instead of the actual patient anatomy within the path estimation model and the intrinsic statistical uncertainty of the model itself [Collins-Fekete et al., 2015]. Both effects are enhanced for pCT due to an increased MCS compared to heavier ions.

In contrast, for soft tissue the path estimation is relatively accurate for all investigated ion species since the scattering condition is comparable to water and the anatomy is largely homogeneous. Here, pCT provides superior image quality due to less noise from an increased number of particle histories at the same imaging dose. This is supported by the large RSP error of pCT compared to heCT and cCT observed at the same particle statistics. The remaining RSP inaccuracy introduced by the reconstruction demonstrates the current limitation of iCT even for an ideal detector configuration [Meyer et al., 2019].

Figures 6.6 and 6.7 illustrate the influence of remaining RSP uncertainties in iCT on the dose calculation accuracy for SFUD proton therapy plans for cranial treatment sites. Overall, superior performance was observed for heCT, demonstrating better spatial resolution at heterogeneities than pCT and less RSP uncertainty and noise for soft tissue regions compared to cCT. pCT provides better range accuracy than cCT since brain and soft tissue represent the main penetration medium, thus, limiting the impact of the enhanced spatial resolution of cCT. For the considered anatomical locations, the achieved range agreement with the reference of better than 0.4% for all simulated iCTs substantially surpasses the accuracy of the current clinical practice of deriving RSP maps from single energy xCT data based on a stoichiometric calibration procedure, which is assumed to introduce uncertainties of 1-3% [Yang et al., 2012]. The observed range accuracy of $(-1.00 \pm 0.43)\%$ for the xCT data with artificially added uncertainty (i.e., xCT_{stoi}) is similar to the results of Wohlfahrt et al. [2017] for a comparison between single energy and DECT based RSP estimation. The authors of that study reported mean water-equivalent relative range

shifts significantly larger than 1% for a head-tumor patient cohort. This underlines the plausibility of the artificially added inaccuracies to mimic the uncertainties of the stoichiometric conversion method. The general range underestimation (i.e., negative values in figure 6.7) is expected due to the systematic RSP overestimation in soft and brain tissue compared with the ground truth reference. This effect dominates the range inaccuracies in the considered scenarios since the beam mainly penetrates brain tissue. However, it should be kept in mind that current pCT prototypes are being optimized for cranial indications [Sadrozinski et al., 2013].

Nevertheless, the presented theoretical MC study using an ideal iCT detector system does not address challenges and limitations related to the experimental realization of iCT. A realistic detector configuration potentially deteriorates the estimated gain in treatment planning accuracy due to a degraded image quality in terms of spatial resolution and RSP accuracy. The latter is mainly determined by the WEPL resolution of the residual range/energy detector which is intrinsically restricted by the particles' range straggling limit and the actual detector configuration (e.g., the energy resolution for a calorimeter or the absorber thickness for a range telescope). For the investigated scenarios, the range straggling related to completely stopping protons of 200 MeV initial energy corresponds to around 2.8 mm (water-equivalent), in addition to the initial energy spread of the accelerator. The latter is almost negligible, since the initial momentum spread of the HIT synchroton in the relevant energy range is around 0.05% (FWHM) [Parodi et al., 2012], corresponding to a range straggling (σ) of less than 0.2 mm. Both contributions (except for range straggling within the detector itself) are intrinsically embedded in the MC simulations and therefore also the impact on the RSP accuracy. The range straggling of helium and carbon ions is reduced by approximately 33% and 50%, respectively, corresponding to around 1.0 mm and 1.5 mm. The currently most complete iCT prototype system (based on a five-stage plastic scintillator WEPL detector) achieves an average WEPL resolution of 3 mm for 200 MeV proton beams [Bashkirov et al., 2016]. Since the system is a combination of both energy (i.e., ion type independent) and range detector (i.e., ion type dependent), the WEPL resolution can not be directly translated to other ions species.

The spatial resolution substantially depends on accuracy of the ion trajectories implemented within the tomographic system matrix. The intrinsic statistical uncertainties of the path estimation models are fully accounted for in this study. However, compared to the presented ideal iCT system, a real detector will have limited precision in measuring the individual particle positions due to the employed tracker configuration and its char-

acteristics (i.e., material budget and spatial resolution). For a typical pCT system, the intrinsic uncertainty of the path estimation is around 0.723 mm, while the contribution from the tracking system is 0.356 mm, resulting in a total uncertainty of 0.805 mm [Bopp et al., 2014]. Compared to protons, heavier ions will benefit from reduced MCS in the innermost part of the tracker unit, hence, reducing the uncertainty in the estimated particle direction. This represents a further argument in favor of helium ions compared to protons. Additionally, nuclear fragmentation within the detector material can introduce inaccuracies in the measured WEPL (typically an overestimation) or further degrade the available particle statistics for the tomographic image reconstruction, thus increasing the necessary imaging dose in order to safeguard the same image quality [Meyer et al., 2019].

The observed general range underestimation for SFUD plans is related to an average RSP overestimation (predominantly for soft and brain tissue), which in turn might have two potential underlying causes. First, the conversion of the energy loss of each individual ion into WEPL is based on the Bethe-Bloch formula, neglecting energy loss due to other interaction types (e.g., nuclear reactions). However, the resulting overestimation effect is small, since the applied 3σ data cuts [Schulte et al., 2008] should have removed the vast majority of events with nuclear collisions and large-angle MCS. Secondly, the fit factors of the employed CSP model have some uncertainty and simply assume scattering in uniform homogenous material [Collins-Fekete et al., 2015]. Therefore, the scattering and consequently the path segment length in bony material can be underestimated, causing an RSP overestimation for the considered anatomical location (neglecting partial volume effects). Generally, the RSP overestimation for very small HU values seems to be mostly compensated by the underestimation for bony anatomy [Meyer et al., 2019].

Figure 6.8 demonstrates the very promising dosimetric accuracy for clinical IMPT plans, which is furthermore confirmed by high gamma passing-rates at a very stringent criteria of 0.5%/0.5 mm. The variations between the individual iCTs were not substantial due to a comparable RSP accuracy (cf. figure 6.4). Additionally, the designed treatment plans turned out to be relatively robust, nevertheless, iCT yielded clearly superior outcome compared to xCT_{stoi}. The presented results underline the potential of iCT as a replacement for xCT imaging in order to reduce range uncertainties in ion therapy treatment planning. Moreover, ion imaging can be employed for in-room position verification and to establish adaptive treatment workflows [Cassetta et al., 2019]. However, various clinical studies have already demonstrated that recent developments in X-ray imaging technology like DECT can also provide improved treatment planning accuracy compared to conventional single

energy xCT [Wohlfahrt et al., 2017]. While those devices already exist as commercial clinical products, they are typically not integrated at the treatment room isocenter and the RSP accuracy should still be theoretically inferior to the one enabled by iCT [Hansen et al., 2015].

"Science is not everything, but science is very beautiful."

J. Robert Oppenheimer

7

Radiobiological Implications of Ion CT

While iCT potentially offers improved treatment planning accuracy at lower physical dose exposure, ion beams can have elevated LET spectra compared to sparsely ionizing X-rays. This calls for a careful consideration of potential biological effects. Hence, in this chapter the radiobiological implications encountered at typical iCT acquisition conditions are investigated in a first theoretical study. Changes in the RBE with iCT particle type and spectrum were considered by incorporating the mechanistic RMF model into the FLUKA MC code. The RMF model estimates are based on radiation quality dependent parameters which are calculated as function of particle type and kinetic energy from the independently developed Monte Carlo Damage Simulation (MCDS) algorithm. The derivation of relevant radiobiological quantities within the framework of the RMF model and its implementation in FLUKA are described. The results regarding the RBE for cell death and DSB induction at typical low-dose iCT irradiation scenarios are presented. Parts of the results shown in this chapter have been published in Meyer et al. [2019].

7.1 Biological Damage Prediction Using the RMF Model

The RMF model, developed by Carlson et al. [2008], is a mechanistic radiobiological model. It explicitly links the time-dependent kinetics of DSB induction and processing with reproductive cell death via a coupled system of non-linear ordinary differential equations. Compared to the earlier *lethal and potentially lethal model* of Curtis [1986] and the *repair-misrepair model* of Tobias [1985], the RMF model treats initial DSB formation as a compound Poisson process [Paganetti et al., 2019]. A review on the main concepts of the RMF model and its relation with the LQ formalism will be given. For further details the reader is referred to Carlson et al. [2008] and references therein.

An important physical parameter in the RMF model is the yield of initial DSBs. There is strong theoretical and experimental evidence of a linear relationship between DSB induction and dose between approximately 1 mGy and up to several hundred Gy [Rothkamm and Löbrich, 2003]. Moreover, the induction of DNA damage by ionizing radiation is similar among all eukaryotes [Carlson, 2006]. Therefore, DSB yield represents an ideal measure for the radiation-induced damage as it depends only on the radiation quality and not on the irradiated cell type [Frese, 2011].

Figure 7.1 summarizes the different pathways of cellular DNA DSB processing, which are explicitly considered within the RMF model. Following the original derivation of Carlson [2006], the expected rate of change in the average number of lethal forms of DNA damage per cell at time t ($\mathrm{d}F/\mathrm{d}t$) due to exposure of ionizing radiation is expressed through

$$\frac{\mathrm{d}F(t)}{\mathrm{d}t} = (1 - f_R)\,\Sigma\,\dot{D}(t) + [(1-a)\,\varphi\,\lambda_R + \lambda_F + \gamma\,\eta\,\epsilon]L(t) + \gamma\,\eta\,L^2(t)\,, \tag{7.1}$$

where $\dot{D}(t)$ and $L(t)$ are the time-dependent dose rate and average number of DSBs per cell, respectively. λ_R and λ_F are the rates of first-order repair and damage fixation, respectively.

Out of the nine potential pathways for the removal of radiation-induced DSBs, five cause lethal forms of DNA damage (cf. figure 7.1). The number of intrinsically unrejoinable DSBs (pathway 4 in figure 7.1) is given by $(1 - f_R)\,\Sigma\,\dot{D}(t)$ where f_R is the fraction of potentially rejoinable DSBs and Σ is the initial number of DSBs per Gray and cell or giga base pair. However, the assumption that all DSBs are potentially rejoinable (i.e., $f_R = 1$) demonstrated the best agreement between model predictions and experimental data [Carlson et al., 2008]. The fraction of DSBs that undergoes lethal first-order misrepair (pathway

2 in figure 7.1) is given by $(1-a)\,\varphi\,\lambda_R\,L(t)$, where $(1-a)$ and φ are the probabilities that a single DSB is misrepaired and that a misrepaired DSB is actually lethal, respectively. $\lambda_F\,L(t)$ (pathway 5 in figure 7.1) represents DSB fixation by extrinsic processes.

In addition, there can be misrejoining of break-ends associated with two different DSBs. Lethal misrejoining of two DSBs created by the same radiation track (so-called intra-track binary misrepair; pathway 6 in figure 7.1) is expressed through $\gamma\,\eta\,\epsilon\,L(t)$, where $\epsilon = \bar{z}_F\,f_R\,\Sigma$ is the average number of potentially rejoinable DSBs formed per track and η is the probability that break-ends interact in a pairwise fashion. γ is the fraction of pairwise DSBs being lethal and $\bar{z}_F$ is the frequency-mean specific energy, which can be approximated for a spherical water target of diameter d_{tar}, assumed to be 5 µm, by [Carlson et al., 2008]

$$\bar{z}_F\,[\mathrm{Gy}] = 0.204\,\frac{\mathrm{LET}}{d_{\mathrm{tar}}^2}\,\left[\frac{\mathrm{keV}}{\mu\mathrm{m}^3}\right]\,. \tag{7.2}$$

Finally, lethal misrejoining of DSBs created by two different radiation tracks (so-called inter-track binary misrepair; pathway 8 in figure 7.1) corresponds to the term $\gamma\,\eta\,L^2(t)$.

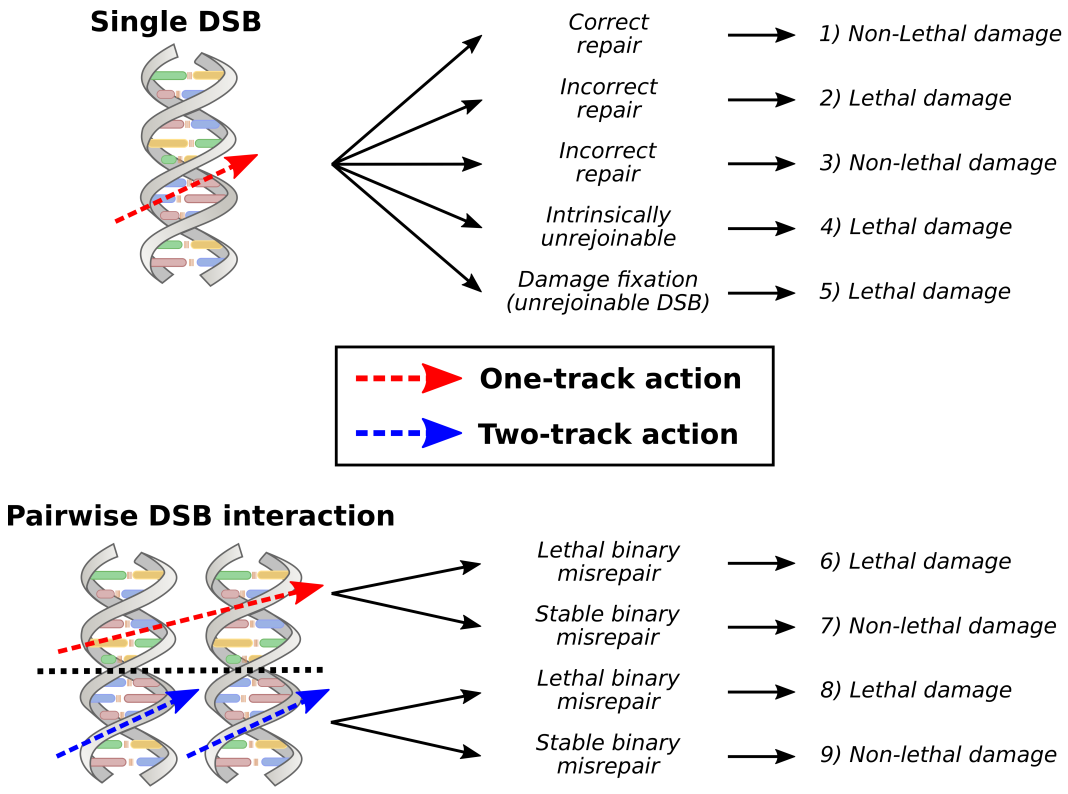

Figure 7.1: Potential pathways for the cellular processing of DSBs by one-track (red arrows) and two-track (blue arrows) mechanisms. Adapted from Carlson [2006] and Frese [2011].

In the limit of small doses and dose-rates, the cell survival according to the widely used LQ model can be obtained as an approximate time-integrated solution of equation (7.1). The detailed derivation can be found in Carlson [2006]. In conclusion, the RMF model predictions for the contributions of one-track (α) and two-track (β) interactions are

$$\alpha = \theta\,\Sigma + \kappa\,\bar{z}_F\,\Sigma^2 \quad \text{and} \quad \beta = \frac{\kappa}{2}\,\Sigma^2\,, \tag{7.3}$$

where the fraction of initial DSBs undergoing first-order misrepair and damage fixation (θ) and pairwise damage interaction (κ) are given by

$$\theta = \frac{(1-a)\,\varphi\,\lambda_R + \lambda_F}{\lambda_R + \lambda_F} \qquad \text{and} \quad \kappa = \frac{\eta}{\lambda_R + \lambda_F}\,(\gamma - \theta)\,. \tag{7.4}$$

Within the framework of the RMF model, the radiation response characteristics of a cell exposed to an ion beam ($\alpha_{\text{ion}}, \beta_{\text{ion}}$) can be calculated from a set of known LQ tissue radiosensitivity parameters of a low-LET reference radiation (α_X, β_X) based on the formalism presented by Frese et al. [2012] and Kamp et al. [2015]:

$$\alpha_{\text{ion}} = \frac{\Sigma}{\Sigma_X}\left[\alpha_X + 2\,\frac{\beta_X}{\Sigma_X}\,(\Sigma\,\bar{z}_F - \Sigma_X\,\bar{z}_{F,X})\right] \quad \text{and} \quad \beta_{\text{ion}} = \left(\frac{\Sigma}{\Sigma_X}\right)^2 \beta_X\,, \tag{7.5}$$

using the DSB induction (Σ) and the frequency-mean specific energy ($\bar{z}_F$) for the considered particle radiation ($\Sigma, \bar{z}_F$) and the reference radiation quality ($\Sigma_X, \bar{z}_{F,X}$). Substituting the LQ radiosensitiviy parameters in the original RBE formula (cf. equation (2.14)) by the derived parameters of equation (7.5), yields the following expression for the RBE for cell death according to the RMF model:

$$\begin{aligned}\text{RBE}_{\text{RMF}}&\left(\left(\frac{\alpha}{\beta}\right)_X, \Sigma_X, \bar{z}_{F,X}, \Sigma, \bar{z}_F, D_{\text{ion}}\right) = \\ &\frac{1}{2\,D_{\text{ion}}}\left[\sqrt{\left[\left(\frac{\alpha}{\beta}\right)_X + 2\,D_{\text{ion}}\,\frac{\Sigma}{\Sigma_X}\right]^2 + \frac{8\,D_{\text{ion}}}{\Sigma_X^2}\,(\bar{z}_F\,\Sigma^2 - \bar{z}_{F,X}\,\Sigma_X\,\Sigma)} - \left(\frac{\alpha}{\beta}\right)_X\right]\,.\end{aligned} \tag{7.6}$$

Moreover, one can directly estimate the RBE for DSB induction defined as the ratio of DSB induction by the ion irradiation and the reference radiation:

$$\text{RBE}_{\text{DSB}} = \frac{\Sigma}{\Sigma_X} = \sqrt{\frac{\beta_{\text{ion}}}{\beta_X}}\,. \tag{7.7}$$

7.1.1 Parameter Estimation Using the MCDS Algorithm

As introduced in the previous section, within the framework of the RMF model the processing of initial DSBs into lethal forms of DNA damage is governed by two cell-specific adjustable biological parameters, θ and κ, which are independent or a weak function of radiation quality. Furthermore, one requires the DSB yield, Σ, which is a strong function of radiation quality but is approximately the same *in vitro* and *in vivo* and among all mammalian cells [Frese et al., 2012], along with the well-defined physical parameter $\bar{z}_{F,X}$, also being the same *in vitro* and *in vivo*.

By using the independently developed MCDS algorithm (available at `http://faculty.washington.edu/trawets/mcds/`) [Semenenko and Stewart, 2004; Stewart et al., 2011] for predicting the impact of changes in radiation quality on DSB induction, the number of *ad hoc* adjustable parameters required to compute the RBE can be reduced. Briefly, the MCDS algorithm simulates damage induction in a small uniformly irradiated segment of a DNA molecule using a two-step approach with four adjustable parameters [Semenenko and Stewart, 2004]. First, the expected number of lesions produced in a cell per Gy of radiation is randomly distributed in the DNA segment of a given length. The length is defined by an *ad hoc* model parameter, which depends on particle type and kinetic energy and should not be considered equivalent to the DNA content of a specific chromosome or cell [Semenenko and Stewart, 2006]. In the second step, the distribution of lesions is subdivided into clusters and grouped into base damages, single-strand breaks and DSBs. Cellular and genetic damage in adjacent or nearby cells with respect to irradiated ones arising from extracellular signals, the so-called bystander effect [Wright, 2010], are not explicitly distinguished from physiochemical mechanisms. However, these effects are implicitly embedded in the values of the selected parameters of the MCDS algorithm [Stewart et al., 2015].

In this work MCDS version 3.10A with default settings [Stewart et al., 2011] was used to predict α_{ion} and β_{ion} (by means of Σ and $\bar{z}_F$) as a function of particle type and energy under normoxic conditions (i.e., O_2 concentration greater than about 21% [Stewart et al., 2011]). The corresponding parameters for the reference radiation were obtained by simulating the secondary electron energy spectrum of a ^{60}Co source [Hsiao and Stewart, 2008] ($\Sigma_X = 8.2706\ \text{Gbp}^{-1}\text{Gy}^{-1}, \bar{z}_{F,X} = 0.0019\,\text{Gy}$). The resulting radiosensitivity parameters as a function of particle type and energy can be seen in figure 7.2. For very low energies the results become inaccurate, since the LET prediction disagreement between FLUKA and MCDS increases. The $\alpha_{\text{ion}}/\beta_{\text{ion}}$ database is the main input for biological dose calculations using FLUKA as it will be presented in the subsequent section.

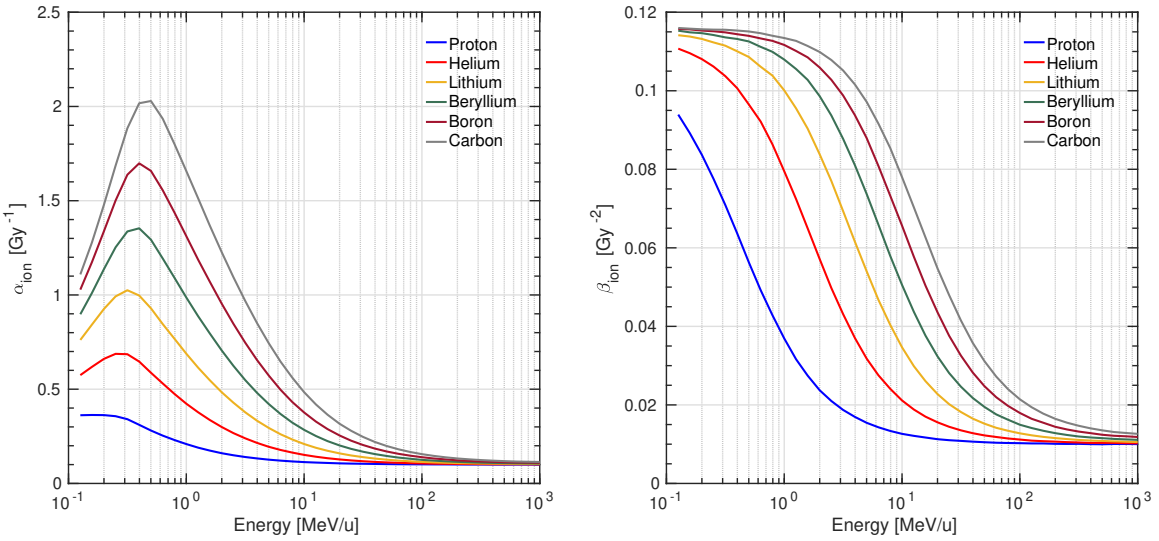

(a) **(b)**

Figure 7.2: MCDS predictions for (a) α_{ion} and (b) β_{ion} for particles from protons up to ^{12}C ions using a reference tissue radiosensitivity of $\alpha_X = 0.1\,\text{Gy}^{-1}$ and $\beta_X = 0.01\,\text{Gy}^{-2}$. The reference radiation quality was ^{60}Co ($\Sigma_X = 8.2706\,\text{Gbp}^{-1}\text{Gy}^{-1}$, $\bar{z}_{F,X} = 0.0019\,\text{Gy}$).

7.1.2 Incorporating the RMF Model in the FLUKA Code

The MCDS algorithm or event-by-event track structure simulations (which reproduce single energy depositions on a nanometer scale) allow to predict the radiation action in biological targets for a given particle type and energy. However, for ion imaging (and the clinical application of particle beams in general) these approaches are not feasible due to strong variations of radiation quality and the unsustainable amount of required computational resources. Hence, a common approach consists in using a combined multiscale model by incorporating radiobiological information (e.g., results of calculations carried out using the MCDS algorithm) in condensed history MC codes such as FLUKA [Mairani et al., 2010].

Energy loss and nuclear fragmentation will generate a complex spectrum of different particles types and energies contributing to the total physical dose deposited at any given point (voxel) inside the patient. According to the theory of dual radiation action [Kellerer and Rossi, 1978], which is applied in the presented implementation, pairwise interplay between sub-lesions produced by different interactions can cause non-linear effects. Hence, the total number of lesions is larger than the sum of the individual lesions produced by each particle. For a biological system irradiated by different radiation types these synergistic effects of radiation can be incorporated into the total effect calculation by computing dose-

weighted average values of α and $\sqrt{\beta}$ [Zaider and Rossi, 1980]. In the case of contributions from n dose depositions originating from different radiation types (each characterized by a certain value of $\alpha_{\text{ion},i}$ and $\sqrt{\beta_{\text{ion},i}}$) the dose-averaged LQ parameters can be calculated as

$$\alpha_D = \frac{\sum_{i=1}^{n} \alpha_{\text{ion},i}\, D_i}{D} \quad \text{and} \quad \sqrt{\beta_D} = \frac{\sum_{i=1}^{n} \sqrt{\beta_{\text{ion},i}}\, D_i}{D}\,, \tag{7.8}$$

where $D = \sum_{i=1}^{n} D_i$ is the total dose of the irradiation in each individual voxel.

The implemented FLUKA-RMF coupling is based on the approach presented by Mairani et al. [2010] for the local effect model. This method relies on previous work by Ballarini et al. [2003] for investigating chromosome aberration induction in human cells by neutrons and in turn was an extension of a method originally developed for dose equivalent calculations [Ferrari and Pelliccioni, 1994]. At the initialization stage, an interface reads the tabulated RMF estimates, i.e., α_{ion} and β_{ion} for the requested cell line and reference radiation quality as a function of particle type and energy (see figure 7.3, panel 1). During the runtime of the simulation FLUKA provides information on the mixed radiation field in terms of particle type (Z and A), kinetic energy and unrestricted LET in water for all primary and secondary ($Z = 1...6$) particles. This enables an *'on-the-fly'* calculation of α_{ion} and β_{ion} (see figure 7.3, panel 2 and 3) by interpolating the radiosensitity parameters of the corresponding RMF tabulation according the actual particle energy. Based on the standard FLUKA scoring capabilities, the physical dose D_i, $\alpha_{\text{ion},i} \times D_i$ and $\sqrt{\beta_{\text{ion},i}} \times D_i$ are stored for each i-th energy deposition (see figure 7.3, panel 3). In a similar manner, the unrestricted LET (in water) is scored. The whole procedure is implemented within the *comscw.f* and *fluscw.f* user routines. The scoring grid is aligned with the xCT voxels and rotated in synchronization with the patient anatomy according to the simulated projection, since the beam direction is fixed. At the end of the simulation, dose-weighted average LQ parameters can be computed according to equation (7.8) (see figure 7.3, panel 4). Inserting these quantities into equations (2.14) and (7.7) finally enables to calculate the RBE for DSB induction and reproductive cell death, respectively.

7.1.3 Decoupling of Biological Modeling and Physical Dose

The presented FLUKA implementation requires a pre-calculated RMF database which in turn depends on the radiosensitivity of the investigated cell line (α_X and β_X) and the reference radiation quality ($\bar{z}_{F,X}$ and Σ_X). Kamp et al. [2017] realized that the RMF

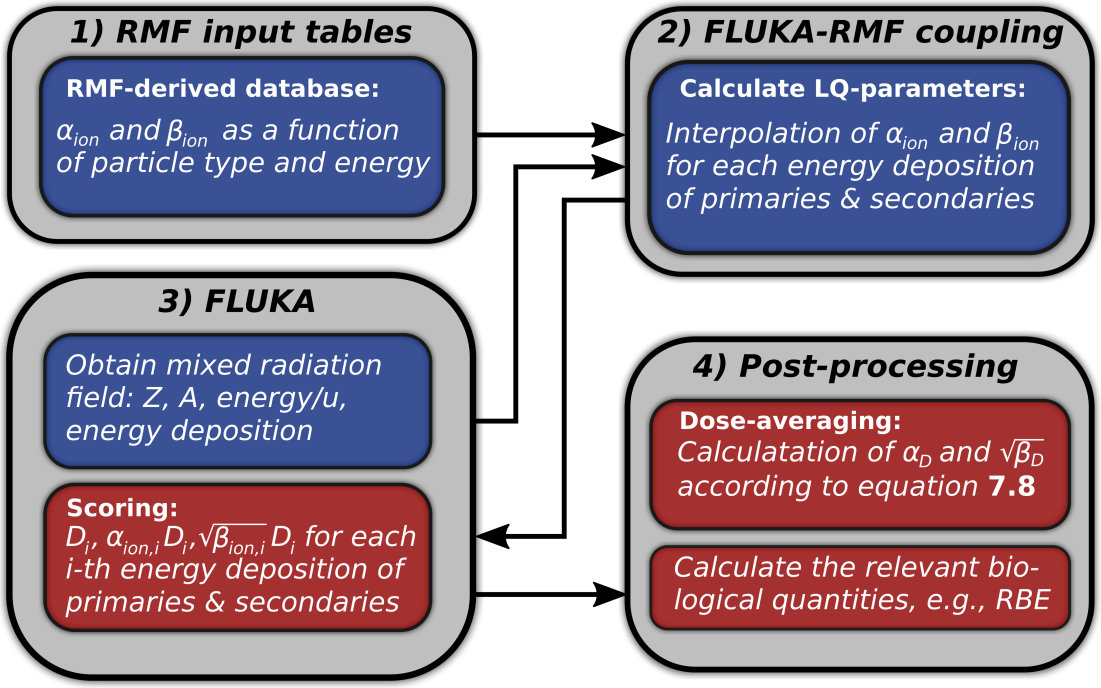

Figure 7.3: Schematic of the coupling between FLUKA MC simulations and the RMF model with MCDS DNA damage estimates for biological dose computation.

model exhibits the favorable property of enabling a complete disentanglement of physical beam properties from biological radiosensitivity parameters. Based on equation (7.5) one can rewrite the dose-weighted tissue radiosensitivity parameters as

$$\alpha_D = \alpha_X \, c_1 + \beta_X \, c_2 \quad \text{and} \quad \beta_D = \beta_X \, (c_1)^2 \,, \tag{7.9}$$

where c_1 and c_2 are the so-called *decoupling parameters* [Kamp et al., 2017]. Hence, α_X and β_X can always be factored out, which enables separating the physical properties of the ion beam irradiation (i.e., the physical dose and averaging of particle and energy spectrum) from the biological tissue radiosensitivity parameters. Two important aspects should be noted. First, those changes can be performed for every voxel independently, for instance allowing to variably adjust the radiosensitivity for different organs. Second, the $c_1 - c_2$ formalism does not require an adjustment of the FLUKA-RMF coupling, since a conversion to α_D and β_D (and back) is possible at any time.

In addition to the aforementioned online adaptation of the radiosensitivity parameters developed by Kamp et al. [2017], it was discovered that a similar formalism can be employed to change the reference radiation quality parameters (i.e., Σ_X and $\bar{z}_{F,X}$). However, the

formalism is not as compact as for the radiosensitivity due to the more complex dependency of α_{ion} on Σ_X and $\bar{z}_{F,X}$. Inserting the dose-averaged LQ parameters in equation (7.5) one can obtain the following expression for the DSB yield:

$$\Sigma = \sqrt{\frac{\beta_D}{\beta_X}}\,\Sigma_X\,. \tag{7.10}$$

The same procedure can be applied to the frequency-mean specific energy:

$$\bar{z}_F = \left(\alpha_D \left(\frac{\Sigma_X}{\Sigma}\right)^2 - \alpha_X \frac{\Sigma_X}{\Sigma}\right) \frac{1}{2\beta_X} + \frac{\Sigma_X}{\Sigma}\,\bar{z}_{F,X}\,, \tag{7.11}$$

which can be further simplified by inserting Σ_X/Σ according to equation (7.10):

$$\bar{z}_F = \frac{\alpha_D}{2\beta_D} - \frac{\alpha_X}{2\sqrt{\beta_X\,\beta_D}} + \sqrt{\frac{\beta_X}{\beta_D}}\,\bar{z}_{F,X}\,. \tag{7.12}$$

Hence, the simulation-derived values of α_D and β_D can be converted at any time into $\bar{z}_F$ and Σ. Consequently, one can re-calculate α_D and β_D according to equation (7.5) for a different reference radiation simply by inserting the new values for $\bar{z}_{F,X}$ and Σ_X. This decoupling feature was exploited to calculate the biological dose response relative to a 200 kVp X-ray energy spectrum ($\Sigma_X = 8.68\,\text{Gbp}^{-1}\text{Gy}^{-1}, \bar{z}_{F,X} = 0.012\,\text{Gy}$) [Frese et al., 2012] for a tungsten anode with 0.5 mm copper and 4 mm aluminum filtration. Moreover, a diagnostic 130 kVp X-ray energy spectrum ($\Sigma_X = 10.4749\,\text{Gbp}^{-1}\text{Gy}^{-1}, \bar{z}_{F,X} = 0.0392\,\text{Gy}$) obtained for a tungsten anode with 0.8 mm beryllium filtration [Stewart et al., 2015] was used as reference radiation. This previously investigated setting can serve as best case reference scenario for xCT treatment planning, yielding slightly reduced biological effects in comparison to the more typically chosen tube voltage of 120 kVp [Meyer et al., 2019].

Theoretically, it is possible to implement both decoupling approaches directly into the MC simulations by adjusting the RMF input tables accordingly. However, this was not pursued in order to keep the format of the user routines in compliance with the structure required by other radiobiological models (which do not offer the RMF-specific decoupling features), as it is also foreseen to be implemented in a future public FLUKA release.

7.2 Results

7.2.1 Verification of the Implementation for a SOBP

The coupling of radiobiological models to general purpose MC codes has been investigated in various studies [Mairani et al., 2010, 2016; Guan et al., 2018]. Furthermore, the combination of RMF model and MCDS algorithm has been previously applied by Kamp et al. [2015] in combination with nuclear fragmentation spectra obtained from FLUKA MC simulations. However, no references, neither simulated nor experimental, for the radiobiological implications at iCT irradiation conditions exist at the moment. Hence, in order to verify the developed implementation of the FLUKA-RMF coupling, a typical 3D carbon ion SOBP ($3 \times 3 \times 3\,\mathrm{cm}^3$ at a depth of 11 cm to 14 cm) in a water phantom was simulated.

Figure 7.4a shows the physical dose profile along the central axis of the SOBP and the corresponding DSB yield. The RBE for cell death according to the RMF model (relative to ^{60}Co for $(\alpha/\beta)_X = 10\,\mathrm{Gy}$) is presented in figure 7.4b. As expected, the yield of DSBs and consequently the RBE rise after the proximal edge where the first Bragg peak is located. Across the width of the SOBP both quantities demonstrate an increasing slope, which results in a sharp peak toward the distal edge of the SOBP, dominated by the most energetic Bragg peak. A similar behavior has been observed by analytical [Frese et al., 2012] and other MC-based studies [Kamp et al., 2015; Guan et al., 2018]. Within the fragmentation tail proximal to the target region, the RBE is dominated by secondary particles and varies only slowly between 1.7 and 1.4, being roughly in agreement with findings for a similar scenario by Guan et al. [2018]. It should be kept in mind that a detailed quantitative comparison is not possible due to differences in irradiation scenario and reference condition. However, the results qualitatively demonstrate the correct implementation of the FLUKA-RMF coupling.

7.2.2 RBE for DNA Double-Strand Break Induction

In the following, the dosimetric results for the imaging scenario presented in chapter 6 will be reported, i.e., a total of 400 protons, 100 helium ions or 20 carbon ions were simulated per RP for 180 projections. The RP spacing was 3 mm in vertical and 1.074 mm in horizontal direction, resulting in a physical dose of $\sim 1.9\,\mathrm{mGy}$ for the full tomography.

Figure 7.5a shows the spatial $\mathrm{RBE}_{\mathrm{DSB}}$ distributions according to the MCDS algorithm obtained for the different iCT scenarios, overlaid with the patient anatomy. The results

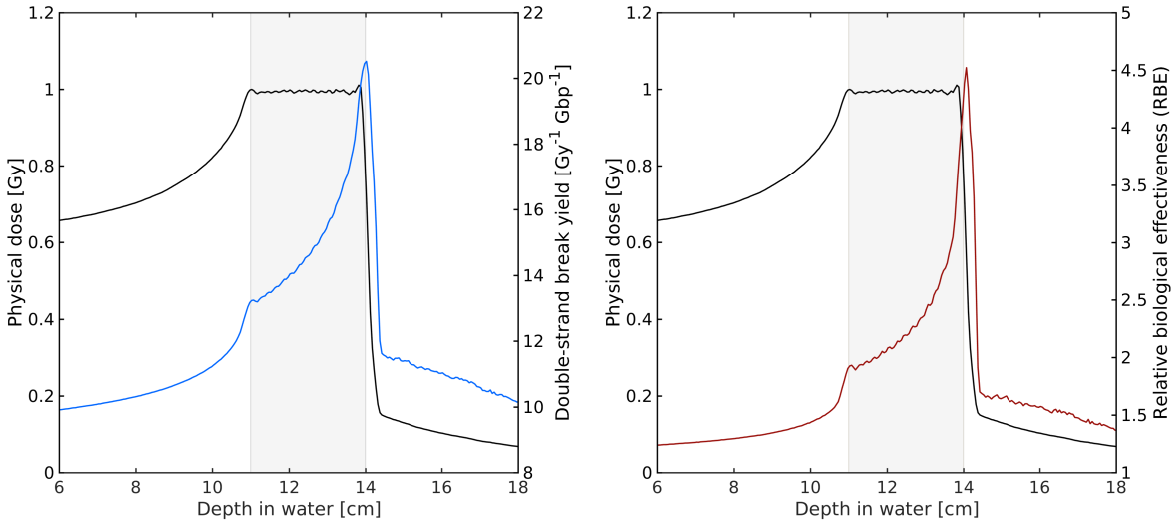

(a) **(b)**

Figure 7.4: Physical and biological properties of a ^{12}C ion SOBP in a water target. The gray shaded area indicates the proximal ($z = 11\,\text{cm}$) and distal ($z = 14\,\text{cm}$) part of the target region. (a) Dose-averaged DSB yield based on DNA damage estimates from the MCDS algorithm. (b) RBE values for reproductive cell death according to the RMF model computed by equation (7.6) using $(\alpha/\beta)_X = 10\,\text{Gy}$ for a ^{60}Co reference radiation.

are expressed relative to the 130 kVp xCT spectrum. Overall, the RBE distributions across the whole patient are largely homogeneous. For the heCT and cCT cases a slightly increased RBE toward the left side of the patient (i.e., bottom part of the image) can be observed. The corresponding RBE histograms for pCT, heCT and cCT simulations are displayed in figure 7.5b. Table 7.1 summarizes the RBE_{DSB} predictions (i.e., mean ± standard deviation) obtained for the different iCT types and reference conditions. On average, the RBE_{DSB} estimations for heCT and cCT simulations exhibited a 3.0% and 16.8% larger mean value compared to pCT, respectively. The corresponding unrestricted dose-averaged LET values (in water) [Bauer et al., 2014] were 2.33 keV/µm, 4.00 keV/µm and 11.85 keV/µm for pCT, heCT and cCT, respectively.

7.2.3 RBE for Reproductive Cell Death

The estimated spatial distributions of RBE for reproductive cell death according to the RMF model are displayed in figure 7.6a relative to 130 kVp X-rays assuming $(\alpha/\beta)_X = 10\,\text{Gy}$, overlaid with the anatomy of patient case 1. Besides slightly larger RBE

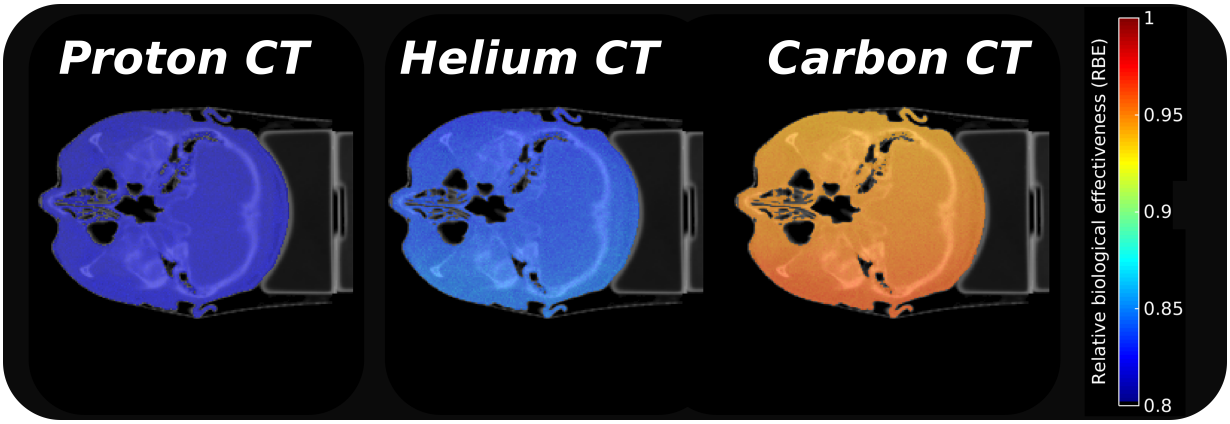

(a)

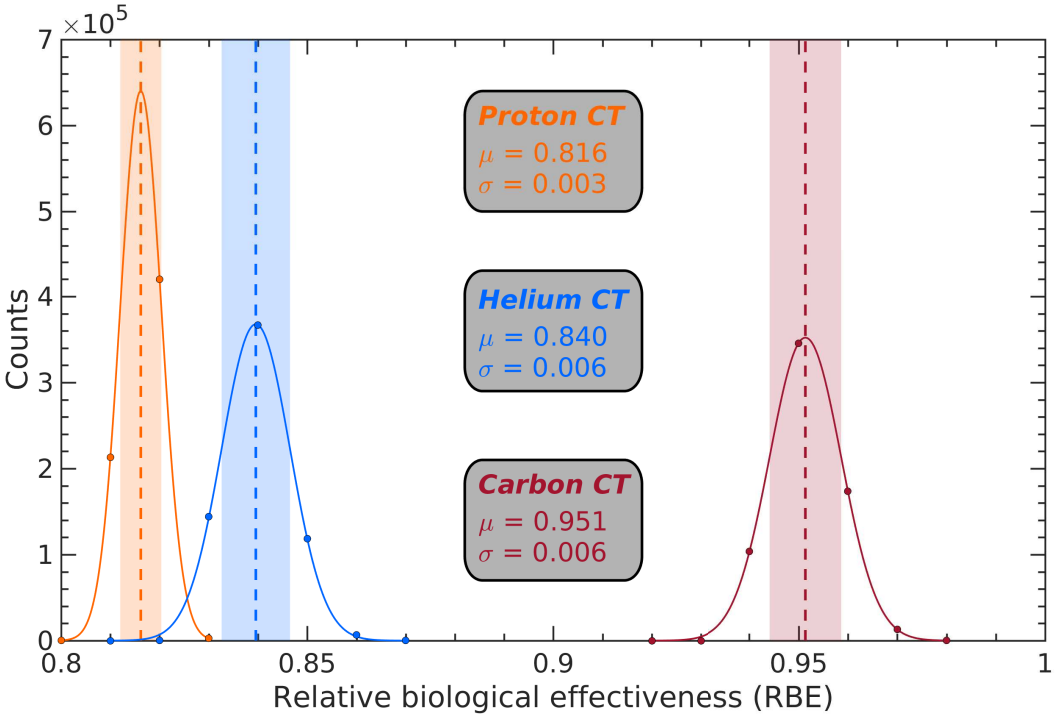

(b)

Figure 7.5: (a) RBE_{DSB} distributions relative to 130 kVp X-rays overlaid with the anatomy of patient case 1. (b) Histogram of the corresponding RBE_{DSB} distributions for pCT, heCT and cCT simulations. The shaded areas represent the ±1 standard deviation interval.

values, the spatial pattern shows strong similarities to the RBE_{DSB} results of the previous section. Figure 7.6b shows the corresponding RBE histograms for the pCT, heCT and cCT scenarios. The RBE_{RMF} predictions (i.e., mean ± standard deviation) obtained for the different iCT types and reference conditions are summarized in table 7.2. The RBE_{RMF}

Patient	Proton CT	Helium CT	Carbon CT
	RBE_{DSB}	RBE_{DSB}	RBE_{DSB}
Reference radiation: ^{60}Co γ-rays			
Patient 1	1.034 ± 0.004	1.064 ± 0.008	1.205 ± 0.008
Patient 2	1.032 ± 0.004	1.065 ± 0.009	1.208 ± 0.011
Patient 3	1.032 ± 0.004	1.063 ± 0.008	1.205 ± 0.009
Reference radiation: 200 kVp X-rays			
Patient 1	0.986 ± 0.004	1.013 ± 0.007	1.148 ± 0.008
Patient 2	0.984 ± 0.004	1.015 ± 0.009	1.151 ± 0.010
Patient 3	0.984 ± 0.004	1.013 ± 0.008	1.148 ± 0.008
Reference radiation: 130 kVp X-rays			
Patient 1	0.816 ± 0.003	0.840 ± 0.006	0.951 ± 0.006
Patient 2	0.815 ± 0.003	0.841 ± 0.008	0.954 ± 0.009
Patient 3	0.815 ± 0.003	0.839 ± 0.007	0.952 ± 0.007

Table 7.1: Summary of the RBE results (i.e., mean ± standard deviation) for different reference conditions, estimated in the total imaging volume of the iCT simulations. RBE_{DSB} is the RBE for DNA DSB induction predicted by the MCDS algorithm.

predictions (i.e., mean value over all investigated reference radiations) for $(\alpha/\beta)_X = 10\,\text{Gy}$ were 1.4%, 1.8% and 2.4% larger than the corresponding RBE_{DSB} estimates for pCT, heCT and cCT, respectively. On average (including all presented biological modeling), the RBE for pCT was 3.8% lower than for heCT and 18.9% lower than for cCT.

7.3 Discussion

Besides the improved RSP accuracy at lower physical dose exposure compared to X-rays, it also has to be considered that ions, in particular heavy charged particles like carbon ions, can potentially have high LET. Hence, in this work variations in the RBE with ion type and spectrum were quantified by coupling the FLUKA MC code to the RMF model.

The used RMF model estimations implicitly included δ-rays since the MCDS algorithm is tuned to experimental data and track structure simulations [Stewart et al., 2011]. There-

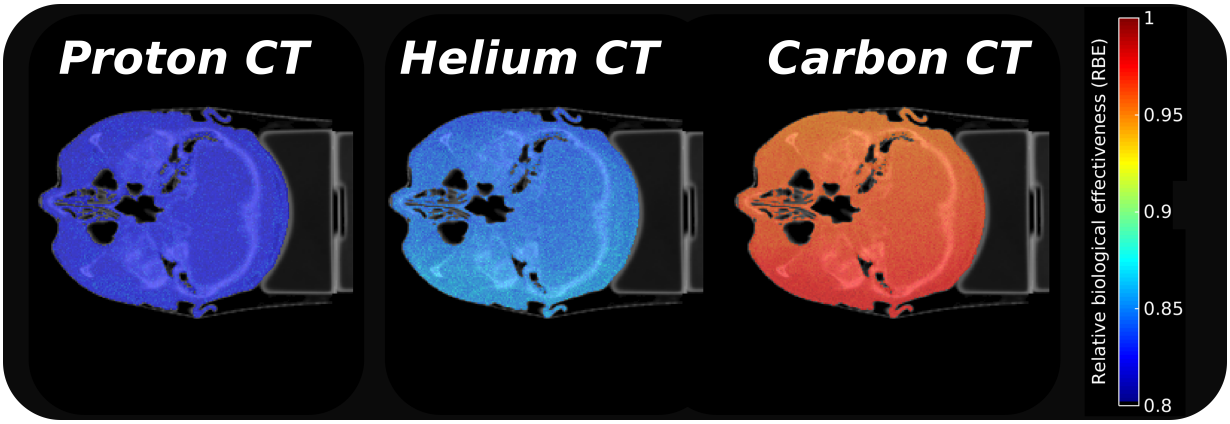

(a)

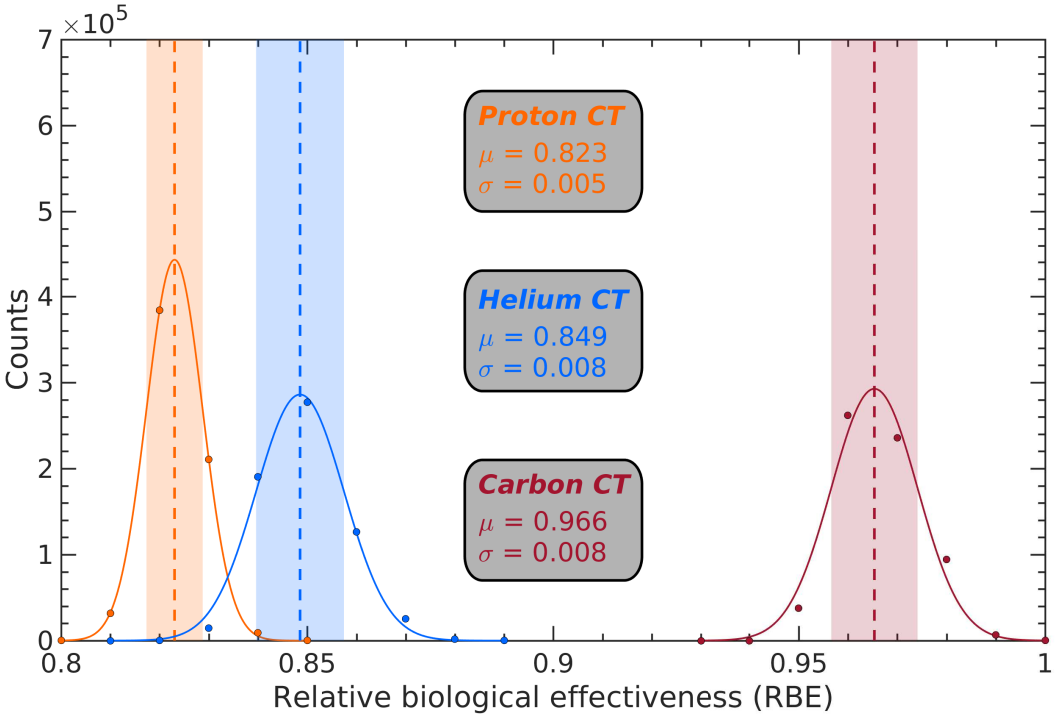

(b)

Figure 7.6: (a) $\mathrm{RBE}_{\mathrm{RMF}}$ distributions relative to 130 kVp X-rays for $(\alpha/\beta)_X = 10\,\mathrm{Gy}$ overlaid with the anatomy of patient case 1. (b) Histogram of the corresponding $\mathrm{RBE}_{\mathrm{RMF}}$ distributions for pCT, heCT and cCT simulations. The shaded areas represent the ±1 standard deviation interval.

fore, a CSDA without explicit δ-ray production (for all energies) was implemented for the conducted MC simulations by using an appropriate production threshold. For typical clinical energies, the presented approach results in dose variations below 0.7% compared to the explicit tracking of secondary electrons above 100 keV [Mairani et al., 2010]. Even though

Patient	Proton CT		Helium CT		Carbon CT	
	$RBE^{2\,Gy}_{RMF}$	$RBE^{10\,Gy}_{RMF}$	$RBE^{2\,Gy}_{RMF}$	$RBE^{10\,Gy}_{RMF}$	$RBE^{2\,Gy}_{RMF}$	$RBE^{10\,Gy}_{RMF}$
Reference radiation: ^{60}Co γ-rays						
Patient 1	1.138 ± 0.021	1.055 ± 0.001	1.192 ± 0.030	1.089 ± 0.011	1.381 ± 0.024	1.240 ± 0.011
Patient 2	1.126 ± 0.020	1.051 ± 0.007	1.188 ± 0.032	1.090 ± 0.013	1.386 ± 0.030	1.243 ± 0.014
Patient 3	1.126 ± 0.020	1.052 ± 0.007	1.182 ± 0.031	1.087 ± 0.012	1.379 ± 0.024	1.240 ± 0.011
Reference radiation: 200 kVp X-rays						
Patient 1	1.070 ± 0.020	1.002 ± 0.007	1.119 ± 0.028	1.035 ± 0.011	1.297 ± 0.022	1.178 ± 0.010
Patient 2	1.059 ± 0.018	0.999 ± 0.006	1.116 ± 0.030	1.035 ± 0.013	1.301 ± 0.027	1.181 ± 0.013
Patient 3	1.059 ± 0.018	0.999 ± 0.006	1.111 ± 0.028	1.032 ± 0.011	1.295 ± 0.022	1.178 ± 0.011
Reference radiation: 130 kVp X-rays						
Patient 1	0.850 ± 0.014	0.823 ± 0.005	0.888 ± 0.020	0.849 ± 0.008	1.026 ± 0.016	0.966 ± 0.008
Patient 2	0.843 ± 0.013	0.821 ± 0.005	0.886 ± 0.021	0.850 ± 0.010	1.029 ± 0.020	0.969 ± 0.011
Patient 3	0.843 ± 0.013	0.821 ± 0.005	0.882 ± 0.020	0.848 ± 0.009	1.024 ± 0.016	0.966 ± 0.008

Table 7.2: Summary of the RBE results (i.e., mean ± standard deviation) for different reference conditions, estimated in the total imaging volume of the iCT simulations. RBE_{RMF} is the RBE for reproductive cell death predicted by the RMF model for an assumed reference tissue radiosensitivity of $(\alpha/\beta)_X$=2 Gy and $(\alpha/\beta)_X$=10 Gy.

the range of δ-rays in the high energy iCT regime can be up to several millimeters, the observed dose discrepancy was still small, with maximum variations of around 0.2 mGy for the cCT case.

Using a diagnostic xCT spectrum as reference radiation enables evaluating the radiobiological implications encountered when replacing conventional xCT for treatment planning imaging with iCT. The considerable changes in RBE_{DSB} with reference radiation are in agreement with a previously reported value of 1.259 for the RBE_{DSB} of 130 kVp X-rays relative to ^{60}Co γ-rays [Stewart et al., 2015]. In general, all reported RBE_{DSB} values (cf. table 7.1) relative to the 130 kVp X-ray spectrum were below 1, indicating reduced radiobiological implications compared to X-ray imaging, since the dose received by the patients solely originates from the low-LET plateau region of the Bragg curve. The processing of DSBs into chromosome aberrations is widely considered a dominant mechanism for radiation induced carcinogenesis [Byrne et al., 2014], which is considered as important biological endpoint for imaging applications [Meyer et al., 2019].

In addition, RBE_{RMF} (cf. table 7.2) directly provides an estimate of the RBE for reproductive cell death based on the RMF and LQ models. However, the LQ formalism is

typically only valid at treatment doses, i.e., from around 1 Gy to 10 Gy (depending on the biological end point), and when fitting α and β to a response curve [Paganetti, 2012a]. At the investigated dose level of ion imaging applications, an underestimation of the radiation effects, the so-called low-dose hyper-radiosensitivity [Marples et al., 2004; Marples and Collis, 2008], may occur. Besides for photons, the hyper-radiosensitivity survival response was experimentally observed after π-meson and proton irradiation [Marples and Joiner, 1993; Marples and Skov, 1996; Marples et al., 1997], as well as for charged-particle microbeams [Schettino et al., 2001], helium ions [Tsoulou et al., 2001] and high-LET neutron exposure at low dose-rate [Dionet et al., 2000]. In contrast, the inflection in the survival curve caused by the induced increased radioradioresistance (following the hyper-radiosensitivity) is considered a phenomenon specific to low-LET radiation injury [Marples et al., 2004]. Therefore, these biological effects might be less important for high-LET particle radiation, even though a LET dependence of hyper-radiosensitivity related parameters can neither be confirmed nor disproved at this time [Heuskin et al., 2013].

The increased spread of RBE values obtained for the heCT and cCT simulations, as indicated by a larger RBE standard deviation compared to the pCT results, is most likely attributed to projectile fragmentation which cannot occur for protons. Nuclear interactions can create low energy (i.e., high LET) fragments of elevated RBE. Since all acquired 180 projections were entering from the right hemisphere of the patients (i.e., the upper halves in figures 7.5b and 7.6b) an increased RBE is visually evident in the left hemisphere due to the increasing LET and build-up of secondary fragments. However, this effect is rather small, since the energies of primary particles are sufficiently high to locate the increasing RBE occurring toward the Bragg peak mostly outside the patient.

The experimental data used for validating the MCDS algorithm indicate that the number of DSBs as measured by the γ-H2AX assay is a linear function of absorbed doses as low as 1 mGy [Stewart et al., 2011; Rothkamm and Löbrich, 2003]. Even though those measurements have not been confirmed for every ion type in this dose regime, there is strong experimental and theoretical evidence that DNA damage is linearly correlated with physical doses from around 1 mGy to 1000 Gy for all types of ions and energies. Under the investigated iCT imaging conditions (i.e., mGy physical doses), the absolute cell survival might be considerably affected by aforementioned low-dose hyper-radiosensitivity which has been observed for low- and high-LET radiation [Marples and Collis, 2008]. However, in this study the particular interest is in relative biological effects between different particles at the same dose level, rather than absolute cell survival. The relative yield of damage

(i.e., RBE_{DSB}) is less sensitive to factors such as low-dose hyper-radiosensitivity, cell proliferation, cycle effects or measurement artifacts. Furthermore, it is the relative DSB yield that plays a significant role in the RMF model rather than the absolute number of DSBs per cell [Meyer et al., 2019].

While this theoretical study provides first insights into the expected radiobiological implications of iCT, further studies are required for future patient application. Nevertheless, these initial investigations and considerations support iCT as promising low-dose modality for treatment planning and frequent isocentric imaging in adaptive ion therapy.

"What we usually consider as impossible are simply engineering problems... there's no law of physics preventing them."

Michio Kaku

8

Toward a Small Animal Proton CT System

In this chapter, a MC-based design optimization and performance study for a single-particle tracking pCT system will be presented. The proposed configuration is based on gaseous Micromegas detectors and a Time-Projection-Chamber (TPC) dedicated to pre-clinical research with small animals. For the envisaged construction of the detector system, a geometrical optimization of the individual detector components is conducted based on a realistic implementation in FLUKA in order to enable an operation close to the intrinsic physical performance limits. The overall image quality in terms of RSP accuracy and spatial resolution is evaluated. Moreover, a first demonstration of pCT for small animal imaging is presented along with a quantitative evaluation of the achievable RSP accuracy and noise. This work has been performed within the European Research Council funded project Small animal proton Irradiator for Research In Molecular Image-guided radiation-Oncology (SIRMIO) (PI: Prof. Katia Parodi).

8.1 The SIRMIO Project

Pre-clinical small animal radiotherapy studies are a crucial component of radiobiological and translational cancer research. This is of paramount importance to unravel the fundamental *in vivo* characteristics of cancer and normal tissue response to radiation exposure. In particular, the orthotopic xenotransplantation of patient-derived tumors can serve as a realistic model for clinical scenarios, since it retains the interplay between tumor cells, normal tissue and the tumor microenvironment [Baumann et al., 2012]. For photon-based pre-clinical irradiation studies, several research groups have developed dedicated platforms over the last years (see Verhaegen et al. [2011, 2018] and references therein). Furthermore, two small animal irradiators with on-board image-guidance are commercially available: the SARRP system [Wong et al., 2008] (*Xstrahl Ltd., Camberley, UK*) and the X-RAD 225Cx [Clarkson et al., 2011] (*Precision X-Ray Inc., North Branford, CT, USA*). Nowadays ion therapy emerges as a state-of-the art treatment modality for humans due to its superior dose conformity, however, most small animal irradiators are not suitable for ion beam irradiations except for rare cases [Ford et al., 2017].

To bridge the gap between ion therapy and pre-clinical research, the SIRMIO project aims to develop an adequate and portable prototype system for high precision small animal proton irradiation based on existing experimental beam lines at clinical facilities [Parodi et al., 2019]. The modular configuration will feature a dedicated passive and active magnetic focusing system to provide enhanced beam quality (in terms of size and transmission) required for the irradiation of small scale structures in orthotopic murine cancer models. The platform will be equipped with novel image-guidance systems including tomographic proton transmission imaging (for treatment planning and position verification) and ionoacoustics (for online range monitoring) in combination with established ultrasound (for real-time morphological imaging) and PET imaging (for functional information).

SIRMIO aims at realizing the first dedicated, compact and cost-effective small animal precision proton irradiator (shown in figure 8.1) for advancing molecular oncology and animal-based proton therapy research. This will provide new possibilities to gain insight in the *in situ* biological response of cancerous and normal tissue to proton irradiation.

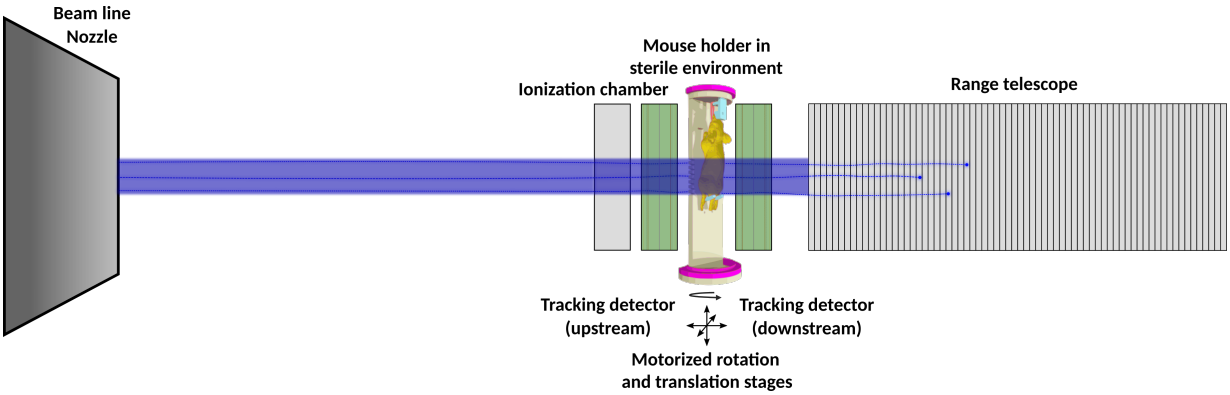

(a)

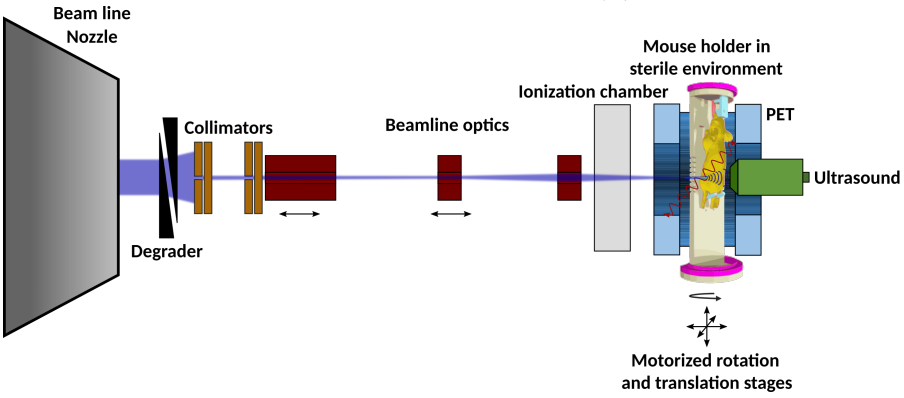

(b)

Figure 8.1: Sketch of the individual components of the SIRMIO platform for image-guided preclinical proton irradiation. The mouse is located at isocenter in a dedicated, sterile and motor-controlled holder (containing temperature control and oxygen/anesthesia supply). (a) Treatment planning imaging configuration: for imaging the clinical proton beam as provided by the accelerator of the facility is used. The single-particle tracking pCT system consists of two tracking detector doublets located upstream and downstream of the imaged object and a range telescope. (b) Irradiation configuration: the clinical proton beam is degraded and collimated before entering the focusing beam line optics (a system of movable magnets). Beam parameters are verified using a permanently installed ionization chamber. Online image-guidance will be provided by a PET and ultrasound system. Adapted from a figure courtesy of Dr. Matthias Würl [Parodi et al., 2019].

8.2 Proton CT Detector System

The proposed pCT system is based on planar gaseous particle detectors of the Micromegas (MICRO-MEsh GASeous) type [Giomataris et al., 1996]. Micromegas are asymmetric parallel plate avalanche chambers with a several millimeter wide drift region and a sub-millimeter amplification region, separated by a thin conductive micro-mesh which is held by supportive pillars. Charged particles traversing the sensitive detector volume ionize the

gas mixture inside the drift region, producing electron-ion pairs. The ionization electrons are separated by the drift field (which is of the order 0.2 kV/cm [Bortfeldt et al., 2017]) and guided within 100 ns into the high-field amplification region between micro-mesh and anode structure [Bortfeldt, 2014]. Here, the electrons are amplified by triggering Townsend avalanches detected at the charge-sensitive readout strips, which are individually connected to high-voltage and capacitively coupled to the electronics (so-called *'floating strips'*).

Due to the finely segmented anode structure and the fast signal generation process, an excellent spatial resolution and a good multi-hit resolution can be achieved [Bortfeldt et al., 2017]. Moreover, Micromegas can reliably detect individual particles at fluxes of up to 60 MHz/cm^2 [Bortfeldt et al., 2016], since positive ions are drained fast thus avoiding the creation of space charge. Efficiency and spatial resolution deterioration originating from nondestructive discharges between micro-mesh and anode strips are massively suppressed by the floating strip design [Bortfeldt et al., 2016]. During a discharge, affected strips will *'float'*, meaning that the potential difference between mesh and strips quickly levels, which will disrupt the discharge [Bortfeldt, 2014]. Since other strips are unaffected by the local discharge, the detector itself remains efficient.

Within this work, Micromegas detectors in two different functionalities are investigated. The tracking systems located upstream and downstream with respect to the imaged object each consist of a doublet of novel 2D position sensitive Micromegas tracking detectors [Bortfeldt et al., 2017; Klitzner, 2019], schematically shown in figure 8.2a. Here, the beam enters perpendicularly to the $x - y$ readout structure, hence, directly providing 2D position information. 10 µm thin Kapton foils are used for the gas window and the drift electrode. The micro-mesh is made from woven stainless steel and consists of 18 µm thick wires, exhibiting around 50% optical transparency. The two sub-detectors are shielded from each other by a 30 µm thin aluminum foil. Since the overall proton scattering within the detectors is dominated by the metallic strips of the readout structure, three different configurations are investigated: two realizations of copper-based floating strip Micromegas and a novel aluminum-based design. In the conventional approach, the anode consists of 33 µm thick copper strips (photo-lithographically etched), of 250 µm width and 500 µm pitch, individually connected to high-voltage. In order to obtain 2D position information, signals are registered via two additional 33 µm thick layers of copper strips (one perpendicular and one parallel with respect to the floating strips), each separated by a 25 µm thin layer of insulating Kapton. While a bipolar signal is directly induced in the perpendicular-oriented strips, the signal on parallel strips is dominantly capacitively coupled from the

anode floating strips [Klitzner, 2019]. In an attempt to reduce the material budget, two modifications of this configuration are proposed. First, the parallel position information can be directly retrieved from the floating strips by photo-lithographically produced capacitors outside the active volume. Consequently, the parallel copper layer can be removed, approximately reducing the total material budget by 30%. Additionally, the copper strips are replaced by 9 µm thick aluminum strips which are glued (12 µm epoxy) onto 10 µm insulating Kapton. Due to the reduced overall thickness and the about six times larger radiation length for aluminum compared to copper (8.897 cm and 1.436 cm respectively [Groom]), MCS is expected to be substantially reduced (cf. equation (2.7)).

The residual range detector functions as a range counter and is based on a TPC with Micromegas readout structure and integrated Mylar field-shaping absorbers placed parallel to the electric field, as schematically shown in figure 8.2b. Protons enter the sensitive gas volume, which has a readout structure located at the bottom of the detector (i.e., $y-z$ plane; cf. figure 8.2b); thus, only the particle position in the horizontal plane (i.e., y and z) is directly measured, whereas the vertical one (i.e., x) is indirectly inferred from the measured drift time relative to a reference signal provided by the rear tracker. In between each absorber pair, the TPC readout structure contains 2×2 readout strips providing redundant position information to reconstruct the proton trajectory within the TPC. Furthermore, small readout pads are placed on both sides in order to identify particles escaping in lateral (i.e., y) direction from the range telescope. The WEPL information is derived from the individual proton's residual range inside the detector system, i.e., the TPC stage (in between two absorbers) in beam (i.e., z) direction where the last energy deposition is detected, based on a dedicated calibration. All detectors contained an 80:20 vol% mixture of Ne:CF_4 at atmospheric pressure.

Both components of the pCT system are currently under development and will be built in-house. The aim of this work is to provide MC simulation support in order to optimize the detector configuration and quantify the expected performance with respect to the requirements for pre-clinical small animal research.

8.3 Monte Carlo Model

The *in silico* model of the Micromegas tracking detector system explicitly considers the used materials and geometries (cf. section 8.2), except for neglecting the optical transparency of the micro-mesh by assuming a homogeneous iron layer. In order to incorporate the

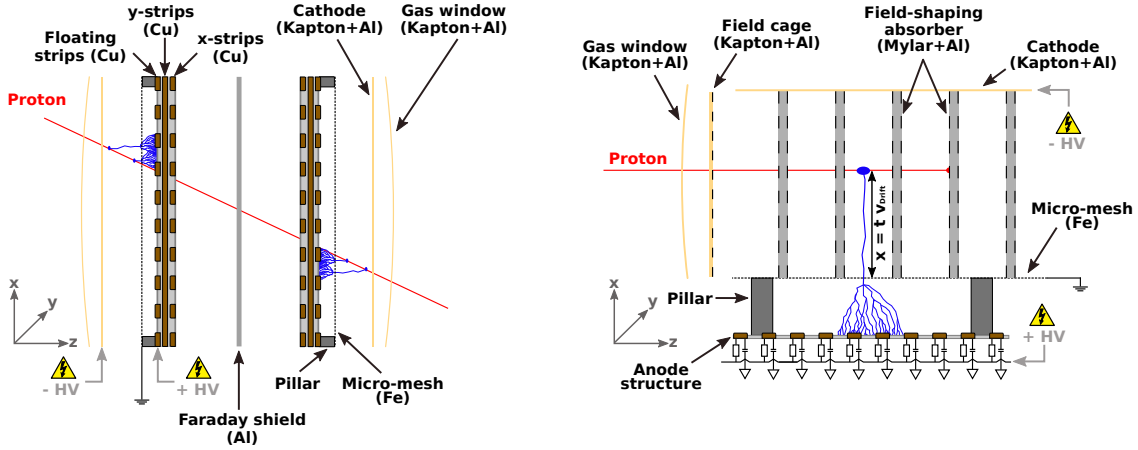

Figure 8.2: (a) Micromegas doublet tracking detectors using copper readout strips (3 layer design). (b) TPC-based range telescope design. Drawings are not to scale.

expected spatial resolution of the tracking detectors, an uncertainty (randomly sampled from a normal distribution with conservatively chosen σ=80 µm) was added to the obtained lateral position values.

The range telescope is modeled as alternating structures of 5 mm wide, gas-filled active regions and homogeneous Mylar absorbers of thickness $d = \{250, 500, 750, 1000\}$ µm. For each proton, the integrated energy deposition within each gas gap in between two absorbers was scored through dedicated FLUKA user routines. It was assumed that the correct track of each event (i.e., the correct sequence of energy depositions within the TPC regions) was recorded and solely the residual range information is later used.

Simulations were performed with scanned proton beams of 75 MeV nominal energy (i.e., a range in water of around 46.2 mm), implemented using the beam model approach introduced in section 4.1.3. All active regions of the detectors contained the 80:20 vol% mixture of Ne:CF_4 as planned for the experimental setup. Additionally, the ionization chamber model was included as it is foreseen to be permanently installed in the SIRMIO system for beam quality assurance and reference measurements. The entire FLUKA simulation geometry is depicted in figure 8.3.

In order to evaluate the imaging performance of the pCT system for typical pre-clinical scenarios, the anatomy of a dead mouse was imported into the MC simulation framework (cf. section 4.1.5). The data was obtained from a high resolution X-ray micro-CT and

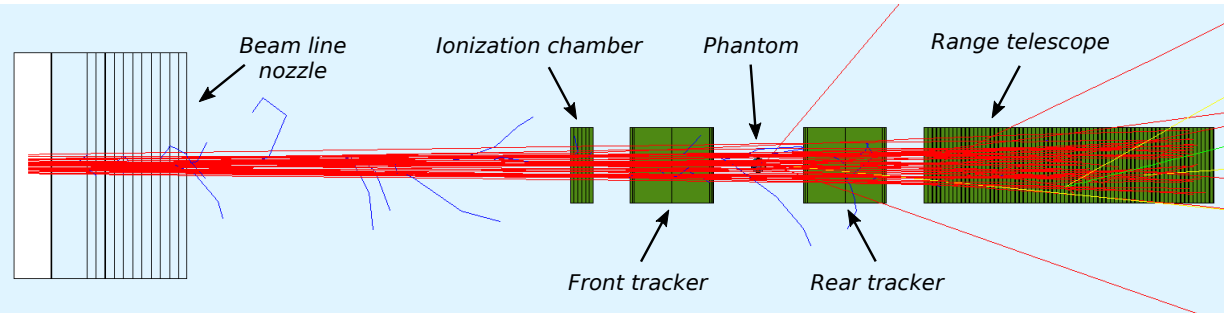

Figure 8.3: Simulation geometry of the SIRMIO pCT system implemented in FLUKA.

down-sampled by cubic-spline interpolation to an isotropic resolution of 0.2 mm (voxel size), comparable to conventional CBCT systems for pre-clinical research.

8.4 System Performance Characterization

The intrinsic performance of an iCT system can be characterized by its image quality, which is determined by the achievable RSP accuracy and spatial resolution of the reconstructed image. The latter is mainly restricted by the path estimation embedded within the tomographic system matrix, which in turn has two main sources of potential inaccuracies. First, the models employed to estimate the ion trajectories within the object of interest (cf. section 4.2) have intrinsic uncertainties due to their statistical nature and the assumption of uniform water as scattering medium. Second, the precision in the measurement of the particle positions as well as the subsequent calculation of their directions is restricted by four extrinsic factors related to the tracker configuration and its characteristics [Bopp et al., 2014]. The latter are given by: (1) the spatial resolution of the tracking system; (2) the material budget x/X_0 (i.e., the ratio between the material thickness and its radiation length; cf. equations (2.7) and (2.8)) of the innermost part of the Micromegas doublet, which determines the amount of scattering a particle undergoes without the possibility to measure it. The limitations due to the tracker configuration can be characterized by: (3) the spacing between the individual planes within one Micromegas doublet; (4) the distance between tracking module and the object of interest. For all studies, the spacing between the tracker frontfaces and the isocenter was 4 cm in order to guarantee sufficient space for the mouse-holder system. As final characterization of the tracker performance, a slanted-edge phantom (i.e., a water phantom with a square insert of 8 mm side length and 2° inclination) was simulated in order to quantify the spatial resolution (cf. section

4.5.2). Due to the symmetry of the phantom, an average composite ESF was obtained by combining the oversampled ESFs from each side of the insert.

The RSP accuracy strongly depends on the WEPL resolution, which for the presented range counter configuration is determined by the detector granularity, i.e., the thickness of the Mylar absorber foils. However, the achievable accuracy is intrinsically limited by the total range straggling, causing particles of the same nominal beam energy to stop at different depth inside the detector. The range straggling of a mono-energetic proton beam due to energy loss fluctuations (σ_R; cf. equation (2.6)) is roughly 1.1% of the mean range. Based on the analytical relationship between initial energy E_0 and the range R according to Bortfeld [1997] ($R = \alpha\ E_0^p$ with $\alpha = 0.0022\,\mathrm{cm/MeV^p}$, $p = 1.77$), the additional range straggling due to the initial Gaussian momentum spread of around 1% FWHM [Englbrecht, 2014] (which corresponds to σ_E=0.61 MeV) can be derived through error propagation. Thus, the total range straggling $\sigma_{R,\mathrm{tot}}$ is given by combining both uncertainties in quadrature:

$$\begin{aligned}\sigma_{R,\mathrm{tot}} &= \sqrt{\sigma_R^2 + (\partial R/\partial E)^2\,\sigma_E^2} \\ &= \sqrt{(1.1\%\ R)^2 + \left(\alpha\ p\ E_0^{p-1}\right)^2\ \sigma_E^2} \\ &= \sqrt{(0.50\,\mathrm{mm})^2 + (0.66\,\mathrm{mm})^2} \\ &= 0.83\,\mathrm{mm}\,.\end{aligned} \tag{8.1}$$

In order to quantitatively evaluate the achievable RSP accuracy, the pCT acquisition of a cylindrical water phantom (⌀ 30 mm) with five tissue-equivalent insert rods (⌀ 6 mm; muscle, liver, adipose, trabecular bone 200 and bone 400 from *CIRS*; cf. table 5.1) was simulated. The results were assessed on a ROI-basis as explained in section 4.5.1.

8.5 Contrast Enhancement

In order to exploit the potentially improved dose calculation accuracy enabled by pCT, a crucial prerequisite is the visibility of the target volume within the images to perform the structure delineation for treatment planning. For this purpose, current practice in clinical and pre-clinical radiation therapy relies on contrast enhanced xCT images (possibly supported by magnetic resonance imaging or PET). However, due to the weak dependence of stopping power on the material atomic number (cf. equation (2.1)) in comparison to X-ray attenuation (cf. equation (3.4)) conventional diagnostic contrast agents will be less

effective for iCT imaging. Since stopping power scales linearly with mass density a very dense contrast agent containing heavy elements would be favorable. Hence, gold (particularly in the form of Gold-Nanoparticles (GNPs) [Hainfeld et al., 2006]) is a very promising candidate due to the high mean density compared to common contrast agents based on iodine or barium. GNPs have diameters in the range of 2 nm to 100 nm [Cole et al., 2015] and can be functionalized by conjugating them with cancer-specific antibodies to enhance the targeting efficacy and tumor uptake [Nakagawa et al., 2016].

The feasibility of using GNPs to enhance the visibility of features in pCT images was investigated for a cylindrical water phantom (⌀ 30 mm) with eight circular inserts (⌀ 4 mm) containing a varying additional amount of homogeneously distributed gold to approximate a uniform distribution of GNPs. The concentration of gold within the inserts (specified as mass percentage $100\,\mathrm{wt\%} \times m_{\mathrm{gold}}/m_{\mathrm{total}}$) was ranging from 1 wt% to 8 wt%. In order to reflect the added weight of gold inside each gold-loaded insert, the density of the gold-water mixture in the MC simulation was increased with respect to the unity density of water (e.g., $1.05\,\mathrm{g\,cm^{-3}}$ for a concentration of 5 wt%) [Cho et al., 2009]. pCT acquisitions were simulated at 50 mGy and 100 mGy dose exposure. RSP images were reconstructed on a $0.2 \times 0.2 \times 0.2\,\mathrm{mm^3}$ voxel grid as it will be required for pre-clinical investigations. Moreover, simulations were conducted with an additional 2 mg Au/g background concentration, i.e., within the phantom volume surrounding the insert regions, in order to investigate the potential effect of GNPs present in tissue surrounding a tumor [Cho et al., 2009].

The impact of the gold-enrichment on the inserts' visibility was quantitatively assessed based on the Contrast-to-Noise Ratio (CNR) being defined as

$$CNR = \frac{|\mu_{\mathrm{ROI}} - \mu_{\mathrm{BG}}|}{\sqrt{\sigma^2_{\mathrm{ROI}} + \sigma^2_{\mathrm{BG}}}} \tag{8.2}$$

where μ_{ROI} and μ_{BG} are the mean RSP values of the ROI (i.e., within the inserts) and background, respectively, and σ_{ROI} and σ_{BG} are the corresponding standard deviations. According to the Rose criterion [Burgess, 1999], the CNR should be at least $3 \sim 5$ in order to guarantee a reliably differentiation between the background and the feature of interest. In the following, the (quite strict) requirement of CNR≥ 5 will be employed as a measure for 100% detectability.

8.6 Optimization and Results

8.6.1 Tracking System Optimization

For all investigations regarding the tracker optimization, the range telescope was neglected and the ideal WEPL was directly computed from the particles' kinetic energy loss in between the trackers as in chapter 6. The path estimation accuracy enabled by the proposed detector configurations was investigated in simulations of a 2 cm thick water phantom. The RMS deviation between the MC proton trajectories and the estimated paths was calculated for 10^5 events at 41 equally spaced points along the paths.

Figure 8.4a shows the different contributions of uncertainty sources for the RMS path deviation of a SLP and CSP estimation for the case of a three-layer copper configuration. The overall path error is largely dominated by uncertainties originating from the tracking detector system (i.e., finite spatial resolution and MCS within the material). While the intrinsic model uncertainty is smaller for the CSP compared to the SLP (maximum RMS path deviation of 0.04 mm and 0.07 mm respectively), the overall contribution is rather small considering an object of 2 cm water. As expected, the error due to the straight projection through air onto the object surface is almost identical for the SLP and CSP, since it does not depend on the path model. The current detector performance at the investigated proton beam energy of 75 MeV resulted in a worse performance of the CSP compared to the SLP (average RMS path deviation of 0.44 mm and 0.39 mm respectively). For 3 cm water the mean path accuracy for the SLP and CSP was almost identical. Since the most dominant WEPL values for imaging of pre-clinical data (except for the surrounding air) are in the range of 2 cm to 3 cm, in the following only SLP reconstructions are considered. The total RMS path estimation deviation for the three different readout structure configurations is shown in figure 8.4b as a function of depth. The average RMS path deviation for the configuration with aluminum strips was 0.29 mm, and thus 0.07 mm and 0.10 mm smaller than for the copper-based designs with two and three layers of strips in the readout structure, respectively.

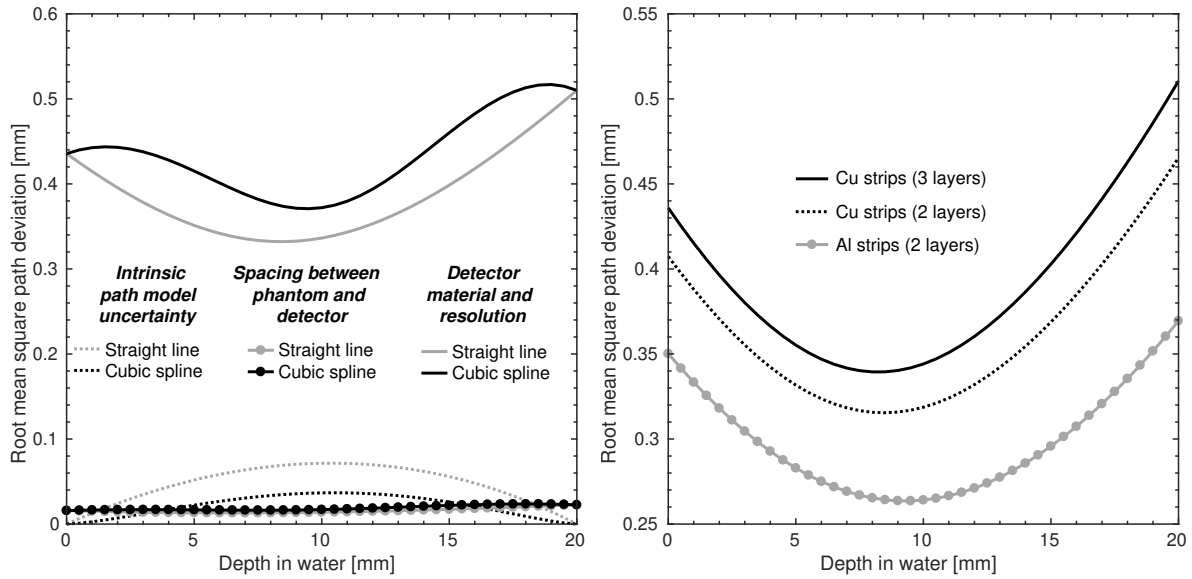

(a) (b)

Figure 8.4: (a) Uncertainty sources contributing to the total RMS path error for a SLP and CSP estimation for the case of a three-layer copper configuration. (b) Comparison of the total RMS SLP estimation error for the three different readout structure designs.

The distance between the inner and outer detector of each Micromegas doublets influences the precision of the track angle measurement. Hence, the distance between the layers in the upstream and downstream tracker doublets was varied from 1 cm to 10 cm in 0.5 cm increments independent of one another. For the detector system with aluminum strip readout, the resulting surface plot of the average RMS path estimation error is shown in figure 8.5a and exemplary profiles are displayed in figure 8.5b. Increasing upstream and downstream tracker spacing to more than 7 cm did not considerably improve the path accuracy. This configuration yielded an average RMS path deviation of 0.18 mm. The corresponding ideal separation for the two-layer copper-based configuration was around 6 cm for the upstream and downstream tracker. It is important to note that the value for the separation of the upstream tracker planes will depend on the absolute angular value (i.e., the divergence of the incident proton beam) since the angular uncertainty decreases with increasing absolute angular value. Furthermore, the downstream value will vary according to the particles' residual energy (i.e., shape and WET of the object). As a cautious choice to avoid potential spatial resolution degradation, 10 cm spacing of tracker sub-systems will be used for both detectors.

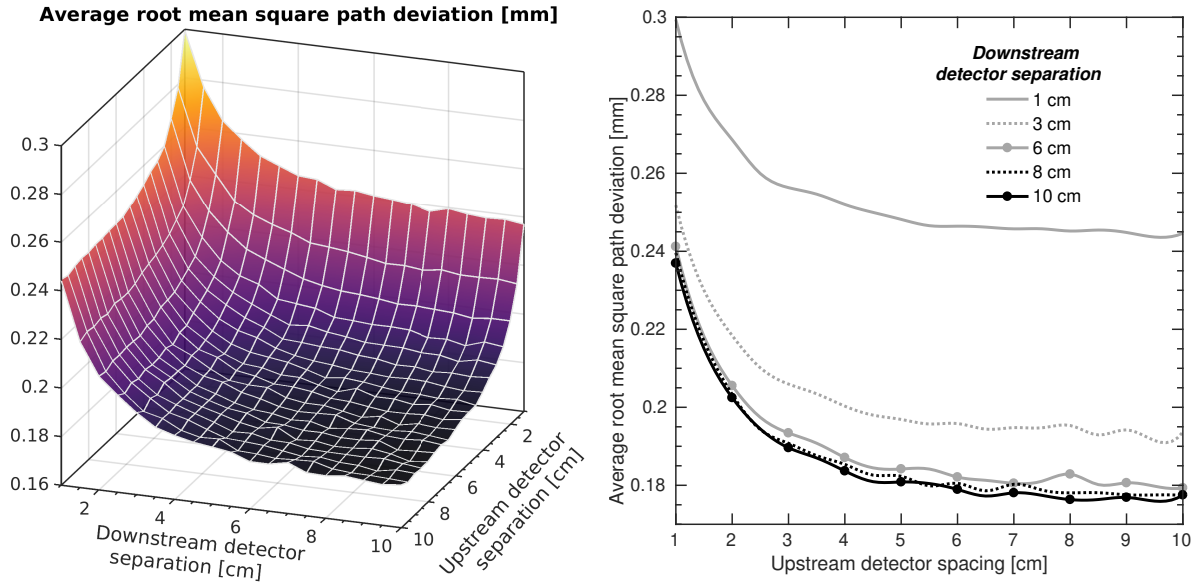

(a) (b)

Figure 8.5: (a) Surface plot of the average RMS path estimation error for the aluminum-based readout structure configuration as a function of upstream and downstream detector separation. (b) Corresponding RMS path deviation profiles for exemplary downstream tracker separations.

For the aluminum-based design, the reconstructed pCT image of the slanted-edge phantom and the ROIs used for the construction of the oversampled ESF can be seen in figure 8.6a. The resulting MTF curves for the different tracker configurations are shown in figure 8.6b. The obtained spatial resolution (at 10% MTF) was $1.9\,\mathrm{mm}^{-1}$, $2.2\,\mathrm{mm}^{-1}$ and $2.8\,\mathrm{mm}^{-1}$ for the copper-based designs with three and two layers, and the aluminum strips configuration. The results are close to the performance of an ideal tracker system (obtained by using the MC information on the particles' position and direction at the entrance/exit of the tracking detectors), which enabled a spatial resolution of $3.4\,\mathrm{mm}^{-1}$. Additional simulation studies with an incorporated range telescope model confirmed that the spatial resolution is not substantially affected by the performance of the WEPL detector.

8.6.2 Range Telescope Optimization

For the range telescope performance investigation, the optimized model of the aluminum-based tracking detectors was employed in the simulation framework. In order to enable a direct correlation between the proton range inside the TPC and the corresponding WEPL, configuration-specific calibration simulations were conducted in a similar way as proposed

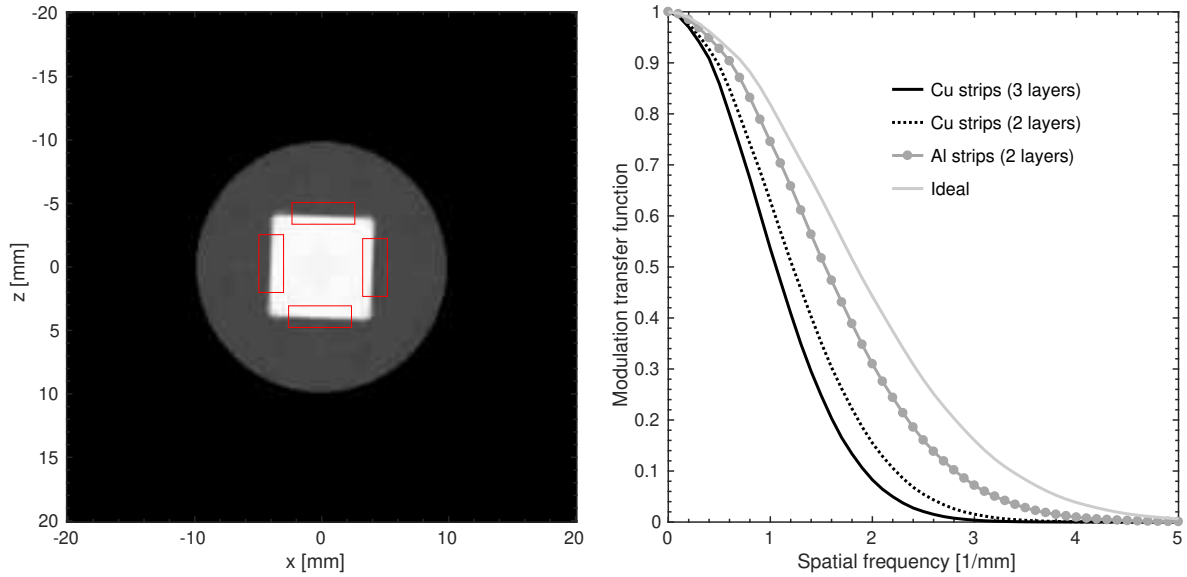

(a) **(b)**

Figure 8.6: (a) Reconstructed pCT image of the slanted-edge phantom using an optimized aluminum-based tracker system. The red rectangles are the ROIs used for the ESF construction and the viewing window is set between RSP values of 0.7 (black) and 1.7 (white). (b) Comparison of the corresponding MTF curves for the different tracker configurations along with an ideal system.

by Bashkirov et al. [2016]. A series of MC simulations was performed for a water column phantom of varying length and the response of the complete detector system was recorded. The water thickness was varied from 0 mm to 45 mm. In order to establish the calibration function, the data are processed in a three-step procedure: (1) the path length of each individual proton within the water phantom and surrounding air is computed based on the tracker information; (2) the WEPL of each recorded proton is calculated by multiplying the material RSP (known from the MC simulation) with the corresponding intersection lengths; (3) the estimated WEPL is stored together with the response of the range telescope (i.e., the range within the TPC (R_{TPC}) in terms of the stage where the last energy deposition is detected). This procedure was conducted for detector configurations with Mylar absorber thicknesses of 250 µm, 500 µm, 750 µm and 1000 µm.

The pre-processed data were used to generate the R_{TPC} distribution for each WEPL value, which was fitted with a Gaussian function. To obtain the R_{TPC} to WEPL conversion

in analytical form, the mean values in turn are fitted with a simple first order polynomial:

$$\mathrm{WEPL} = p_0 + p_1 \; R_{\mathrm{TPC}} \,, \tag{8.3}$$

where p_0 and p_1 are fit parameters (similar to the integration-mode calibration in chapter 5). p_0 represents the energy-dependent maximum WEPL that can be resolved (i.e., traversed by the beam), while p_1 corresponds to the configuration-dependent inverse of the water-equivalent absorber foil thickness. The calibration curves are shown in figure 8.7a. Based on the established calibration function, the standard deviation of the detector response can be converted into WEPL resolution by using Gaussian error propagation. The resulting WEPL resolutions as a function of WEPL being imaged are shown in figure 8.7b. As expected, the WEPL resolution improves for thinner absorbers and is mostly constant except for statistical fluctuations. For increasing absorber thicknesses a systematically deteriorated performance toward lower WEPL values can be observed.

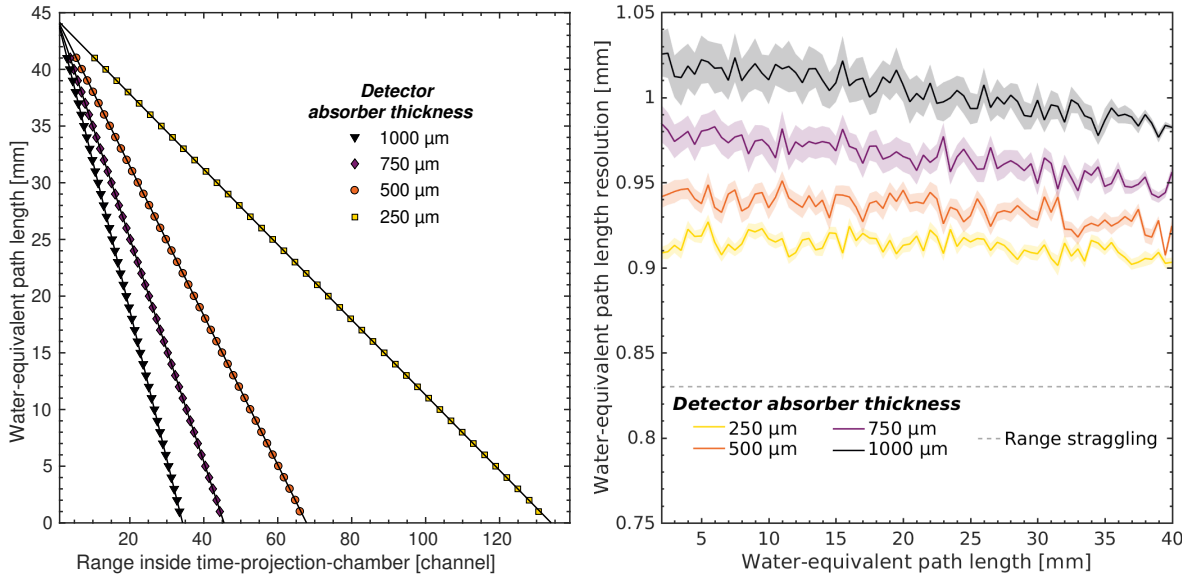

(a) **(b)**

Figure 8.7: (a) Simulated calibration plot for the different TPC-based range telescope configurations: WEPL value versus range inside the detector obtained as mean value of the Gaussian fit. The 95% confidence level is within $\pm$<0.01 channels and thus not shown. The black lines are first order polynomial fits used to extract the calibration functions. (b) WEPL resolution for the different TPC-based range telescope configurations as a function of WEPL being imaged: the total range straggling limit indicated by the dashed gray line is given by equation (8.1) and the shaded area represents the 95% confidence interval obtained from the Gaussian fits.

An exemplary reconstructed pCT slice of the rod phantom for the TPC with 500 µm thick Mylar absorbers is shown in figure 8.8a. The corresponding RSP accuracy for the insert materials achieved for different absorber thicknesses is displayed as bar plot in figure 8.8b, reflecting the improved WEPL resolution for thinner absorber slabs. Overall, sub-1% RSP accuracy was demonstrated; however, results for 1000 µm absorber thickness resulted in image artifacts of slightly distorted insert geometries. The mean RSP accuracy was 0.53%, 0.27%, 0.24% and 0.22% for the designs with a granularity of 1000 µm, 750 µm, 500 µm and 250 µm Mylar slabs, respectively. Hence, an absorber thickness between 500 µm and 750 µm represents the best compromise between achievable RSP accuracy and detector complexity, since an increased amount of thinner absorbers (and readout channels) is required to safeguard the same dynamic WEPL range.

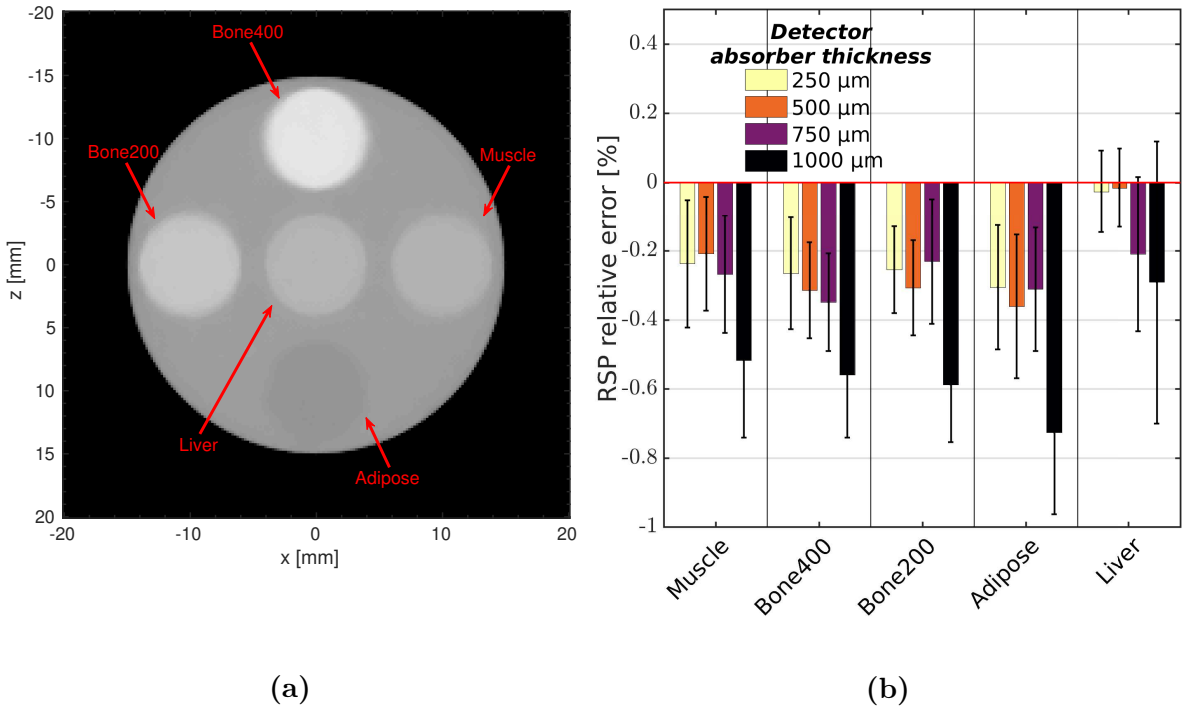

(a) (b)

Figure 8.8: (a) Reconstructed pCT image of the cylindrical water phantom used for RSP accuracy evaluation obtained with a range telescope of 500 µm thick Mylar absorbers. The viewing window is set between RSP values of 0.7 (black) and 1.7 (white). (b) RSP relative error distributions for different absorber thicknesses displayed as bar plot. The bars correspond to the mean relative error values and whiskers represent the $\pm 1\sigma$ intervals.

8.6.3 Contrast Enhancement

For the optimized detector configuration with aluminum-based trackers and the TPC with 500 µm absorber thickness, the reconstructed pCT images at 50 mGy and 100 mGy physical dose (without background concentration) are presented in figure 8.9a and 8.9c, respectively. The corresponding CNR values are shown in figure 8.9b and 8.9d as a function of gold concentration along with the linear regression (using a fixed intercept at zero CNR). Qualitatively, inserts of more than 7 wt% start to become visually recognizable. Based on the linear regression model, concentrations of 10.4 wt% and 7.8 wt% are required to effectively distinguish the insert from the background (i.e., CNR$\geq$ 5) at 50 mGy and 100 mGy, respectively. The corresponding values for simulations with the additional 2 mg Au/g background concentration were 10.8 wt% and 8.0 wt%.

8.6.4 Imaging of Pre-Clinical Data

Figure 8.10 shows the reconstructed pCT images of a cranial mouse anatomy for detector systems with 500 µm and 750 µm absorbers along with the ground truth and the result for an ideal detector as used in chapter 6. The images were obtained for (93 ± 5) mGy dose exposure and using the aluminum-based tracking detectors. The mouse ears were excluded from the FBP-derived contour since they would incorrectly enlarge the mask, which is required to be convex in order to avoid ambiguities. Since the ears are rather thin, it is reasonable to neglect the scattering and assume a straight proton path. For both absorber thicknesses, the images accurately represent the reference anatomy at a low noise level. However, the limited spatial resolution causes a blurring of the small bony anatomy. The corresponding RSP relative errors were 2.6%, 4.6% and 4.8% for the ideal detector and the TPC with 500 µm and 750 µm absorber thickness, respectively. The corresponding RSP distributions are displayed as joint histogram in figure 8.11. In particular for the reconstruction with the real detector model, the mean RSP for bone-like materials (HU$>$1200) and soft tissue-tissue (-500$<$HU$<$0) is underestimated by up to 0.15.

8.7 Discussion

The observed superiority of the SLP over the CSP is at first glance contradictory to previous findings; however, this result reflects differences in the irradiation condition and detector modeling. Compared to the ideal detector system employed in chapter 6, the pre-clinical

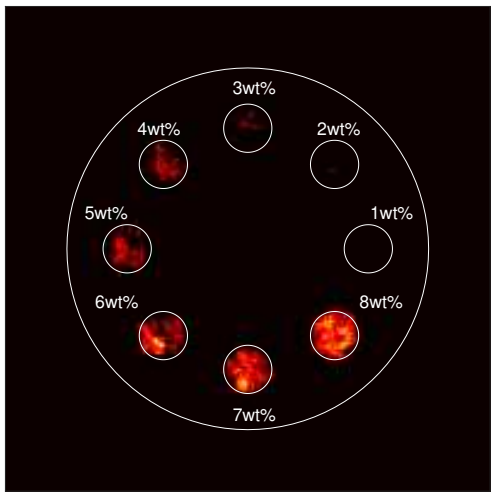

(a)

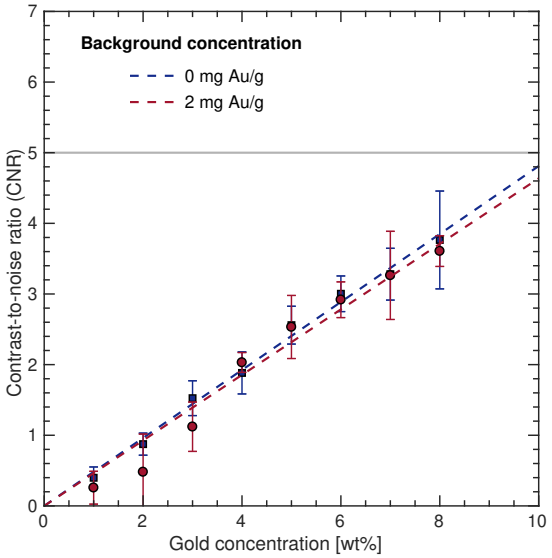

(b)

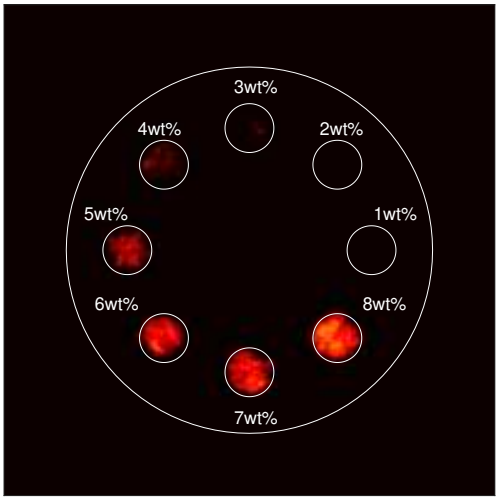

(c)

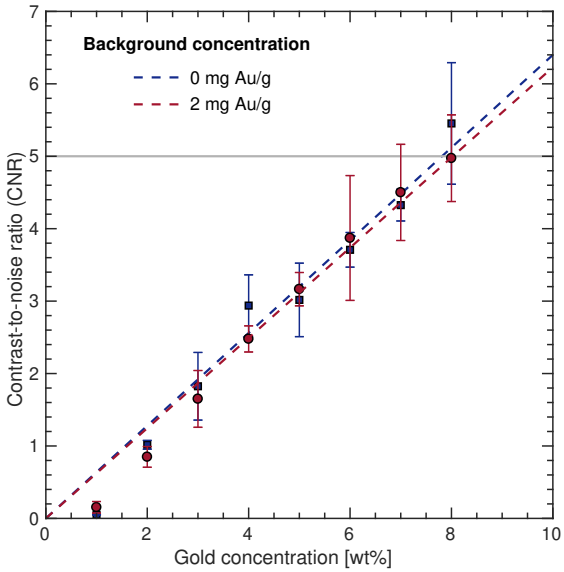

(d)

Figure 8.9: (a)/(c) Reconstructed pCT images for the cylindrical phantom with gold-loaded inserts obtained at 50 mGy and 100 mGy dose exposure, respectively. The viewing window is set between RSP values of 1.01 (black) and 1.05 (yellow). (b)/(d) Mean (markers) and standard deviation (whiskers) of computed CNR values for three slices (0.2 mm thickness) obtained at 50 mGy and 100 mGy dose exposure respectively. The dashed lines represent the corresponding linear regressions of the original data and the solid gray line indicates the Rose criterion.

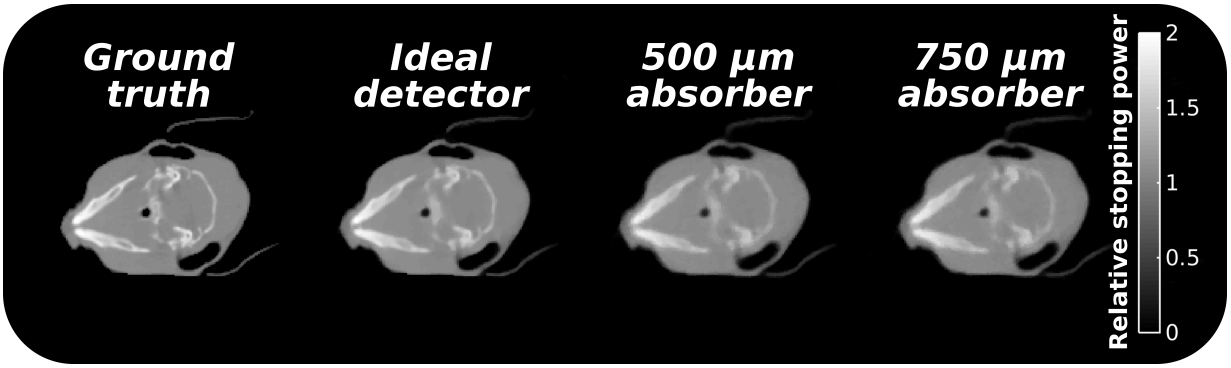

Figure 8.10: Comparison of exemplary reconstructed pCT images obtained with different detector configurations for the mouse xCT data along with the corresponding ground truth.

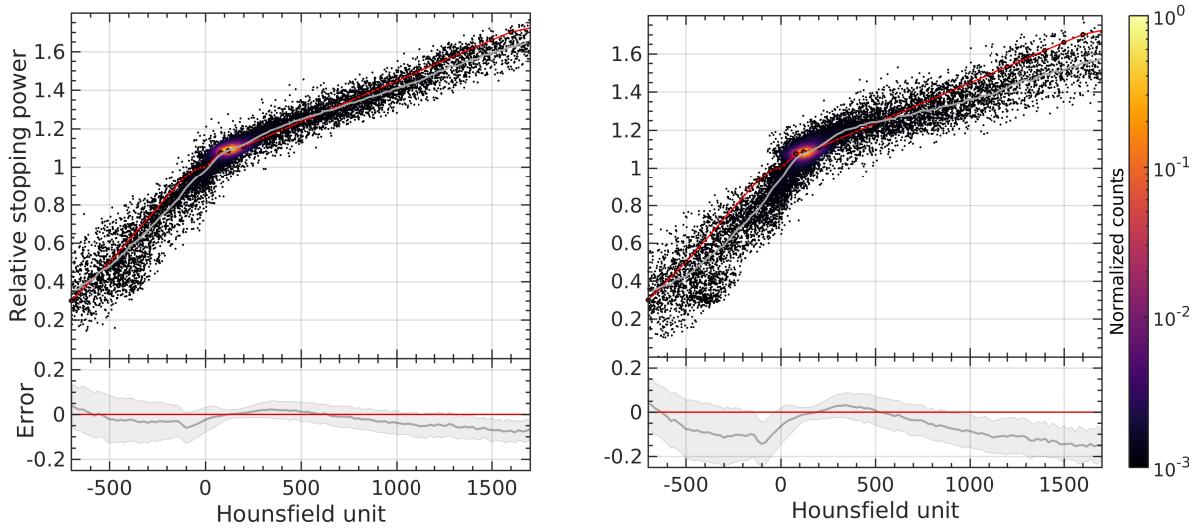

Figure 8.11: Joint histogram of the reconstructed pCTs (for an (a) ideal detector and (b) an aluminum-based tracker and TPC with 500 µm thick absorber slabs) and the original HU values. The red line indicates the ground truth conversion curve being used to import the initial xCT data into the MC simulation. The curve below shows the corresponding RSP error (mean$\pm 1\sigma$).

investigation differs in two points: first, the realistic modeling of the complete tracker system reveals inaccuracies in the proton direction estimation, particularly due to the MCS in the readout strips. Second, the shallow penetration depth of 2 cm substantially limits the amount of MCS within the object, which reduces the impact of the intrinsic path uncertainty. Consequently, uncertainties introduced into the CSP formalism by inaccurate direction vectors are mitigating the theoretically reduced intrinsic path uncertainties,

causing an overall superior accuracy for the SLP.

Theoretical investigations regarding the path estimation accuracy at clinical energies typically evaluate the maximum RMS path deviation (e.g., in chapter 6), occurring slightly downstream the object center due to the intrinsic path model uncertainty [Schulte et al., 2008]. However, for tomographic imaging it is more appropriate to use the center of the imaged object, since it is the expected location of poorest spatial resolution due to the intersection of multiple projection angles [Penfold et al., 2011]. For the pre-clinical system investigated in this chapter, slightly better resolution is expected in the center of the object. Nevertheless, this might be misleading for the general performance quantification since murine tumors are typically shallow-seated or superficial; hence, the mean RMS error was chosen as a conservative measure to reflect the overall path estimation accuracy.

The obtained spatial resolution of around 2-3 mm^{-1} for the optimized pCT system is comparable to the performance of CBCT systems commonly used in pre-clinical research [Song et al., 2010]. However, the level of detail visible in the presented pCT reconstructions for realistic small animal data (cf. figure 8.10) appears slightly inferior to the estimated spatial resolution based on phantom simulations. This in turn can have two reasons: first, the slanted-edge method is highly sensitive to noise (due to the differentiation operation; cf. equation (4.28)), possibly introducing some uncertainty. Second, the mouse data contain highly heterogeneous 3D anatomy, which creates additional path uncertainties compared to the rotationally symmetric homogeneous 2D phantom case. On the other hand, pCT is expected to provide considerably better RSP accuracy than xCT systems. In particular, the elemental composition of murine tissues is substantially different from human tissue [Schyns et al., 2019], demonstrating a large intra-tissue variability. This fact might introduce further uncertainties in the stoichiometric calibration method, which is based on a limited number of reference tissues. In contrast, pCT represents the most intuitive solution in order to ideally completely elude those uncertainties.

The degraded WEPL resolution toward smaller WEPL values (cf. figure 8.7b) might be a consequence of the large residual range within the TPC of the corresponding protons. MCS and the initial particle direction could accumulate to a detectable difference between the CSDA range within the detector and the actually measured projected range in z-direction, resulting in an increased standard deviation of the Gaussian fit, particularly for configurations with thicker absorbers. This effect can potentially be compensated by exploiting the available proton track information within the TPC, even though the contribution is of minor impact. The RSP underestimation observed for phantom simulations

(cf. figure 8.8b) is also reflected in the reconstructions for pre-clinical data (cf. figure 8.11b). Since this effect persists even for an ideal tracker system, it must be intrinsically related to the range telescope performance. Future work should investigate more elaborated calibration procedures embedding the available proton track and energy deposition information in order to enhance the achievable RSP accuracy.

The implemented macroscopic modeling of GNPs as a homogeneous gold concentration for computational purposes is a reasonable assumption and has been previously applied to estimate the physical dose enhancement for γ- and X-rays [Cho et al., 2009], as well as the contrast enhancement in fluorescence CT [Jones and Cho, 2011], spectral xCT [Müllner et al., 2015] and pCT [Schulte et al., 2004b]. The feasibility of the estimated gold concentrations in real pre-clinical scenarios can be gauged with the following back-of-the-envelope calculation: a 1% density enhancement requires 10 mg of gold within 1 g of tumor with unity density, which corresponds to around 3×10^{19} gold atoms. Since gold forms an *fcc* structure (i.e., 4 gold atoms per unit cell of volume) with a lattice constant of 0.408 nm, the total number of gold atoms in a spherical GNP of 50 nm radius can be approximated by $4 \times \frac{4/3\ \pi\ (50\ \mathrm{nm})^3}{(0.408\,\mathrm{nm})^3} \approx 3 \times 10^7$. Consequently, one would require 10^{12} GNPs per gram of tumor (with unity density). Assuming that 1 g of tumor tissue contains around 10^9 cells [Monte, 2009], 8 wt% of gold therefore corresponds to 8×10^3 GNPs per cell. Considering data available in current literature (see Cole et al. [2015] and references therein), the required concentration seems rather high, but feasible.

While the Rose criterion is based on the assumption of white noise, noise in tomographic imaging is typically correlated due to the reconstruction [Toth, 2012]. Nevertheless, the performed CNR quantification still represents an adequate measure as demonstrated by the good agreement with the visual perception of the inserts. In comparison to pCT, DECT enables imaging of substantially lower GNP concentrations, e.g., Badea et al. [2011] report a limit of detectability at around 15 mg/ml (i.e., 1.5 wt%), while Clark et al. [2013] even state values ranging from 4 mg/ml down to 1 mg/ml. It should be noted that in pCT imaging the total amount of gold per unit volume (voxel) is the only important parameter regardless of the actual particle shape (as it is also the case for xCT [Popovtzer et al., 2008]). However, high GNP concentration can cause cytotoxicity due to necrosis and apoptosis. Pan et al. [2007] observed that particularly large GNPs are nontoxic up to relatively high concentrations, which is beneficial for imaging applications since the maximum gold mass delivered per cell increases with the size of GNPs [Cole et al., 2015].

GNPs typically exhibit a long retention in blood [Nakagawa et al., 2016] and can be de-

tected up to several hours after injection. Furthermore, work by Lin et al. [2015] based on dedicated microscopic TOPAS MC simulations demonstrated that the radio-enhancement (using the dose response predicted by the local effect model) of GNPs depends on the radiation quality. Hence, GNPs might compromise comparison studies between photon and proton irradiations as foreseen within the SIRMIO project. Furthermore, one also needs to consider that contrast agents can introduce ion beam range shifts. While this effect was found to be negligible for iodine-based agents in humans [Wertz and Jäkel, 2004], the impact for GNPs in small animals might be more critical since generally higher precision is demanded. An alternative approach to GNPs for tumor localization is the use of an in-house developed pre-clinical ultrasound system [Lascaud et al., 2019] in conjunction with a short-lived micro bubbles [Stride and Saffari, 2003]. However, this requires a precise co-registration between pCT and non-Cartesian ultrasound images, currently under investigation.

For the study of pre-clinical small animal data, the in-house developed mouse holder was not included in the simulation. It consists of a rigid fixation system, heating and connections for air and anesthesia supply. In order to guarantee a sterile environment for immunodeficient mice, the chamber is sealed with a 150 µm thin Kapton foil. To further reduce MCS for ultra-precise irradiation, the support layer on the backside will contain cutouts (sealed with a 50 µm thin Kapton foil) at irradiation locations of foreseen applications. In order to compensate the potential deterioration of the pCT spatial resolution due to additional material budget, the tracking system could be moved slightly closer to the holder.

Finally, all presented simulations employed the implemented active pencil beam scanning, which might not be available at every proton therapy facility. However, the use of scattering foils in order to create a broad proton beam for imaging is not expected to substantially alter the image quality if the divergence is limited, since the image formation is based on the measurement of individual protons. Moreover, the use of a double-scattering system could be required to match the MHz detector readout in facilities with too high instantaneous beam intensity.

"You know how some people fuss about the high cost of CT-scanners, so you can imagine what they would say if one suggested that the X-ray tube in the scanner should be replaced by a much more expensive cyclotron!"

Allan M. Cormack

9

Conclusions and Perspectives

In the following, the most important conclusions of this work are summarized and the future perspectives are discussed. This thesis is divided in four main parts. The first part is focused on the performance of integration-mode ion imaging. In the second and third part, the achievable gain in treatment planning accuracy for single-particle tracking iCT and the associated radiobiological implications expected in clinical scenarios are studied. In the last part, a novel pCT system for pre-clinical research with small animals is investigated and the performance is optimized.

The performance of integration-mode ion imaging using a range telescope prototype under investigation at HIT is presented in chapter 5. Both, simulated and experimental phantom studies demonstrate a good image quality and an accurate WET and RSP retrieval. Particularly carbon ions yield superior performance in integration-mode imaging compared to protons or helium ions, reflecting the reduced sensitivity to MCS and the smaller pencil beam size. While the developed BPD strategy enables a clear benefit for integration-mode imaging, the image quality for highly heterogeneous clinical-like data remains limited, due to prevailing signal ambiguities from range dilution effects.

In order to address the observed shortcomings, future work needs to aim at developing advanced computational strategies for fully utilizing the sparse amount of information retrieved with integration-mode data. In this context, two different directions can be pursued. First, improvements within the tomographic image reconstruction could incorporate the entire WET histogram obtained from the BPD along with information on MCS and the finite beam spot size [Seller Oria et al., 2018]. Alternatively, the redundant information encoded in the overlap of neighboring pencil beams could be exploited, since the RP separation is typically smaller than the pencil beam size. Based on a dedicated optimization procedure, it is possible to redistribute the individual WET components in radiography domain to improve the spatial resolution [Krah et al., 2015; Gianoli et al., 2016].

The improvements compared to previous work [Rinaldi et al., 2013; Magallanes, 2017] obtained within this thesis and the observed limitations will bolster the future development of integration-mode transmission ion imaging. Since an implementation can be obtained with rather unsophisticated detector instrumentation, commercial and cost-effective imaging systems may be employed, which will facilitate the transition of ion imaging (in particular using iRADs for position verification [Farace et al., 2016; Hammi et al., 2018]) toward clinical routine.

The clinical potential of single-particle tracking iCT was studied in chapter 6. Compared to integration-mode imaging, a substantially better image quality is achieved, since blurring induced by ambiguities from MCS and the finite beam spot size are compensated. At the investigated dose level of around 2 mGy and for the considered ideal detector, heCT offers superior RSP accuracy for clinical-like data compared to pCT and cCT. In addition, the associated treatment planning comparison demonstrates improved range accuracy for all ions with respect to uncertainties inherent in the stoichiometric HU-RSP conversion employed in current clinical practice. For the investigated cranial sites, in particular pCT and heCT demonstrate very good dosimetic agreement with the ground truth reference.

Future work needs to assess to which extent realistic detector instrumentation can enable results close to the presented intrinsic capabilities. Furthermore, the dosimetric impact of possibly reduced tumor safety margins stemming from the reduced range uncertainties as enabled by iCT needs to be investigated. In order to integrate iCT into clinical practice, a dedicated treatment workflow must be developed. If fast solutions for image reconstruction (e.g., GPU-based implementations of iterative algorithms [Karonis et al., 2013]), as well as for delineation and treatment planning (e.g., based on machine learning techniques

[Feng et al., 2018]) are available, iCT will potentially enable performing treatment planning, delivery and verification inside the treatment room without requiring repositioning of the patient or additional imaging technologies.

This work underlines the usefulness of iCT for potentially reducing range uncertainties in ion therapy treatment (re-)planning with respect to single energy xCT. The reduction of the related tumor safety margins will ultimately limit normal tissue damage, improving the dose conformality for patient receiving ion therapy treatments.

The radiobiological implications related to iCT are estimated in chapter 7. To this end, the mechanistic RMF model with MCDS DNA damage predictions was integrated into the FLUKA MC simulation framework. As expected, the RBE of pCT for the irradiation scenario of chapter 6 (i.e., for the same physical dose) is generally lower than for heCT and cCT. The RBE predictions for all considered biological endpoints indicate that iCT generates potentially reduced radiobiological effects compared to typical xCT spectra used for treatment planning imaging.

An important limitation for the presented radiobiological investigation is the sparse availability of experimental data on biological effects for typical iCT irradiation conditions, i.e., ion beams of very high energy delivering imaging doses of a few mGy. Clinical applications of iCT for human patients demand a careful experimental investigation and validation. Future work should aim at dedicated cell line experiments in order to quantitatively evaluate the potentially unfavorable radiobiological implications and relevant effects like low-dose hyper-radiosensitivity.

The performed theoretical analysis of this study represents an important step to gain first insights into the biological effects of low-dose iCT imaging. Besides the improved RSP accuracy and the reduced physical imaging dose, the results potentially provide a further argument in favor of iCT over conventional xCT; not only for treatment planning and adaptive strategies but also for daily isocentric image guidance for patient positioning.

The optimization of a pCT system for small animal imaging is the aim of chapter 8. The system consists of planar Micromegas detectors as tracker system and a segmented TPC with vertical absorber foils functioning as a range telescope. Based on MC simulations of a realistic detector implementation, a novel readout structure with aluminum electrodes promises superior performance due to the reduced material budget. For the

range telescope, a Mylar absorber thickness between 500 µm and 750 µm is found to yield the best compromise between WEPL resolution and complexity of the detector instrumentation. In the subsequent *in silico* study of pCT, the optimized detector system enabled accurate imaging for pre-clinical data. Relying on this pCT system, an investigation on the use of GNPs as pCT contrast agent for improving tumor visibility for target delineation determined a required concentration of around 8 mg gold per gram of imaged tissue to provide a detectable contrast enhancement.

The next task will be to investigate the treatment planning accuracy enabled by the reconstructed pCT images, as it has been done for clinical-like data in chapter 6. Due to the required high resolution for small animal irradiation, a dedicated MC dose engine is necessary. Therefore, the prototype TPS μ-RayStation (*RaySearch Laboratories, Stockholm, Sweden*), which was developed particularly for pre-clinical small animal irradiation, will be used within a license (signed) and research collaboration (under negotiation) agreement within the SIRMIO project. The general functioning principle of the proposed TPC configuration for a reliable electron extraction over wide drift distances has been already demonstrated using a small-scale prototype [Lämmer, 2019]. The investigation of an optimal experimental realization is currently ongoing. The photo-lithographic structuring of the aluminum-based 2D Micromegas tracking detector has been mastered in-house and future work will investigate the capabilities and aging characteristics of this novel design.

The pCT system thoroughly characterized and optimized *in silico* within this thesis might not only enable a deeper investigation of ion imaging but also provide an in-room image-guidance system for position verification and treatment planning, potentially improving the range accuracy in pre-clinical research. This opens new pathways for high-precision proton irradiation studies of tumor-bearing small animal models in a controlled and well defined environment.

~

The development of ion imaging has come a long way since the days of Cormack and Koehler. Due to great advances in methodology, hardware and image reconstruction, iCT has evolved from an obscure activity at physics laboratories into the potentially most intuitive solution for eliminating range uncertainties in ion therapy. The findings of this thesis underline that iCT could indeed hold the promise of providing superior treatment planning accuracy at lower patient dose exposure compared to current clinical practice. This also makes it an attractive modality for emerging small animal precision ion irradiation platforms. Thus, ion imaging can play an important role in the ongoing fight against cancer.

Acknowledgments

There are never enough words to acknowledge all the people, who supported me during the last three and a half years. However, I will try to do my best to extend my heartfelt thanks to everyone who helped and supported me in accomplishing this Ph.D. thesis, since this might be my only opportunity to thank these individuals in writing.

My deepest gratitude goes first and foremost to my supervisor Prof. Katia Parodi. Dear Katia, you deserve thanks for so many things. Primarily, for creating the research environment in which I have performed my dissertation work. Thank you for encouraging my research and scientific growth in every possible way. You always provided guidance and support, while also giving me the freedom to work independently and pursue my own ideas. Your inspiring commitment and expertise were invaluable to develop myself as a researcher in the best possible way. I also can't thank you enough for giving me the opportunity to present my work at various national and international conferences.

I want to express my sincere appreciation for my friend and co-supervisor Dr. Chiara Gianoli for her continuous guidance and encouragement. Chiara, thank you for all your advice not only concerning my work or science, but also life in general. I am indebted to you for sharing your inestimable important knowledge on image reconstruction. Above all, I want to thank you for your kindness and all the things you taught me in the five years we were sharing an office! I wish you, Leo and little Margherita all the best for the future.

I am extremely gratefully to acknowledge the support and advice of Prof. David J. Carlson. Dear Dave, thank you for sharing with me your scientific expertise and immense knowledge on radiation biology. The work with you was a great pleasure and added a valuable (and rather different) piece of research to my dissertation.

Special thanks goes to Dr. Florian Kamp for all his help and the extensive support, in

particular for providing the clinical data and the Monte Carlo damage simulations.

I would like to thank Prof. Otmar Biebel for reviewing this thesis as second referee and Prof. Barbara Ercolano, Prof. Joachim Rädler, Prof. Thomas Kuhr and Prof. Bernhard Mayer for accepting my invitation to be members of my dissertation committee.

I have to kindly acknowledge support with the treatment planning software by Prof. Guillaume Landry and Dr. Marco Pinto. Furthermore, I want to thank Prof. Kirsten Lauber and Prof. Frank Verhaegen for providing the mouse CT data, which were used for investigating the feasibility of proton computed tomography in pre-clinical scenarios.

Throughout the last years I crossed paths with many graduate students who have influenced my research. Lorena, thank you for guiding me during the beginning of my Ph.D. and for your continuous support. I know you will find your way. Thank you Ben, Max and Carmen for the enjoyable working atmosphere and the enriching scientific discussions. I wish you all the best for the future, especially for your own Ph.D. journeys.

In want to thank all members of the SIRMIO project for scientifically insightful (even though sometimes rather long) group meetings, where I could learn various new things. In particular, many thanks to Dr. Matthias Würl and Katrin Schnürle for very enriching scientific discussions about ion imaging. Moreover, I would like to extend my sincere thanks Dr. Jona Bortfeldt for sharing his expertise in detector technology and giving helpful general advice. In this context I also must acknowledge Dr. Felix Klitzner for providing me valuable insight into the signal formation of Micromegas detectors.

Completing this work would have been all the more difficult were it not for the support and friendship of many people. I owe a very big thanks to my good friends Franz, Juliana, Silvia, Thomas, Matthias and Katrin for a great time at work and even more enjoyable after work hours and weekends. I also want to thank my former classmates Thomas and Flo for all the good time we spend together since starting our physics career. We have come a long way since the days of solving exercise sheets of undergraduate courses; and now we all work toward our dissertation. Moreover, a big thanks to my friend Ludovica for her advice and always finding the time to enjoy a good coffee or pizza; but foremost I want to thank her for her never ending and contagious positive attitude.

Furthermore, a very big thanks also to all other colleagues at the department for exchanging scientific ideas and restorative lunch and coffee breaks, and so many nice cakes.

I am unbelievably happy that during my Ph.D. journey I made not only scientific discover-

ies, but also found my soulmate. Ingrid, there are times when words are simply not enough to express appreciation. Even though things were not always easy, first sharing the same office and now being 6000 km apart, I could always rely on your unfailing support. Thank you for your constant love, enduring my (mostly unfounded) worries, always motivating me and also proof reading this work. You are more than my partner, more like a part of me, thank you for being in my life.

Last but not least, I want to gratefully thank my family, in particular my parents, my sister Anka and my aunt Moni for all the support and continuous encouragement. I could always rely on you and spend some relaxing days at home during the weekends. I do not know how to thank you enough for providing me with the opportunity to be where I am today. This accomplishment would not have been possible without you. Thank you!

Bibliography

S. Abe et al. Heavy ion CT system based on measurement of residual range distribution. *Jpn J Med Phys*, 22(1):39–47, 2002.

M. H. Albrecht et al. Dual-energy CT of the heart current and future status. *European Journal of Radiology*, 105:110–118, 2018.

R. E. Alvarez and A. Macovski. Energy-selective reconstructions in X-ray computerised tomography. *Physics in Medicine & Biology*, 21(5):733–744, 1976.

U. Amaldi and G. Kraft. Radiotherapy with beams of carbon ions. *Reports on Progress in Physics*, 68(8):1861, 2005.

A. Andersen and A. C. Kak. Simultaneous algebraic reconstruction technique (SART): a superior implementation of the ART algorithm. *Ultrasonic imaging*, 6(1):81–94, 1984.

N. Arbor et al. Monte Carlo comparison of x-ray and proton CT for range calculations of proton therapy beams. *Physics in Medicine & Biology*, 60(19):7585–7599, 2015.

C. T. Badea et al. Dual-energy micro-CT imaging for differentiation of iodine- and gold-based nanoparticles. In *Proc. SPIE 7961 Medical Imaging 2011: Physics of Medical Imaging*, 2011.

F. Ballarini et al. Estimating mixed field effects: An application supporting the lack of a non-linear component for chromosome aberration induction by neutrons. *Radiation Protection Dosimetry*, 103(1):19–27, 2003.

W. H. Barkas. *Nuclear research emulsions. Vol.1: Techniques and theory.* Academic Press, 1963.

W. H. Barkas, J. N. Dyer, and H. H. Heckman. Resolution of the Σ^--mass anomaly. *Phys. Rev. Lett.*, 11:26–28, 1963.

V. A. Bashkirov et al. Novel scintillation detector design and performance for proton radiography and computed tomography. *Med. Phys.*, 43(2):664–674, 2016.

G. Battistoni et al. The FLUKA code: An accurate simulation tool for particle therapy. *Frontiers in Oncology*, 6:116, 2016.

J. Bauer et al. Integration and evaluation of automated Monte Carlo simulations in the clinical practice of scanned proton and carbon ion beam therapy. *Physics in Medicine & Biology*, 59(16):4635, 2014.

M. Baumann, D. Zips, and M. Krause. Experimentelle Tumortherapie. *Strahlentherapie und Onkologie*, 188(S3):291–294, 2012.

M. Beister, D. Kolditz, and W. A. Kalender. Iterative reconstruction methods in X-ray CT. *Physica Medica*, 28(2):94–108, 2012.

M. Belli et al. Direct Comparison of Biological Effectiveness of Protons and Alpha-particles of the Same LET. II. Mutation Induction at the HPRT Locus in V79 Cells. *International Journal of Radiation Biology*, 61(5):625–629, 1992.

E. H. Bentefour, R. Schnuerer, and H.-M. Lu. Concept of proton radiography using energy resolved dose measurement. *Physics in Medicine & Biology*, 61(16):N386, 2016.

E. V. Benton, H. R. P., and C. A. Tobias. Heavy-particle radiography. *Science*, 182(4111): 474–476, 1973.

M. J. Berger et al. Stopping Powers and Ranges for Protons and Alpha Particles (Report 49). *Journal of the International Commission on Radiation Units and Measurements*, os25(2), 1993.

M. J. Berger, J. Coursey, M. Zucker, and J. Chang. ESTAR, PSTAR, and ASTAR: Computer Programs for Calculating Stopping-Power and Range Tables for Electrons, Protons, and Helium Ions (version 1.2.3). Technical report, NIST, Gaithersburg, MD, 2005.

H. Bethe. Zur Theorie des Durchgangs schneller Korpuskularstrahlen durch Materie. *Annalen der Physik*, 397:325–400, 1930.

J. Bian et al. Investigation of iterative image reconstruction in low-dose breast CT. *Physics in Medicine & Biology*, 59(11):2659, 2014.

F. Bloch. Bremsvermögen von Atomen mit mehreren Elektronen. *Zeitschrift für Physik*, 81(5-6):363–376, 1933a.

F. Bloch. Zur Bremsung rasch bewegter Teilchen beim Durchgang durch Materie. *Annalen der Physik*, 408:285–320, 1933b.

F. E. Boas and D. Fleischmann. CT artifacts: causes and reduction techniques. *Imaging in Medicine*, 4(2):229–240, 2012.

T. T. Böhlen et al. Benchmarking nuclear models of FLUKA and GEANT4 for carbon ion therapy. *Physics in Medicine & Biology*, 55(19):5833, 2010.

T. Böhlen et al. The FLUKA Code: Developments and Challenges for High Energy and Medical Applications. *Nuclear Data Sheets*, 120:211–214, 2014.

N. Bohr. On the decrease of velocity of swiftly moving electrified particles in passing through matter. *The London, Edinburgh, and Dublin Philosophical Magazine and Journal of Science*, 30(178):581–612, 1915.

N. Bohr. The penetration of atomic particles through matter. *K. Dan. Vidensk. Selsk. Mat. Fys. Medd.*, 18(8):1–144, 1948.

C. Bopp et al. Proton computed tomography from multiple physics processes. *Physics in Medicine & Biology*, 58(20):7261, 2013.

C. Bopp, R. Rescigno, M. Rousseau, and D. Brasse. The impact of tracking system properties on the most likely path estimation in proton CT. *Physics in Medicine & Biology*, 59(23):N197–N210, 2014.

T. Bortfeld. An analytical approximation of the bragg curve for therapeutic proton beams. *Medical Physics*, 24(12):2024–2033, 1997.

J. Bortfeldt et al. Low material budget floating strip micromegas for ion transmission radiography. *Nuclear Instruments and Methods in Physics Research Section A: Accelerators, Spectrometers, Detectors and Associated Equipment*, 845:210–214, 2017.

J. Bortfeldt. *Development of Floating Strip Micromegas Detectors*. PhD thesis, Ludwig-Maximilians-Universität München, 2014.

J. Bortfeldt et al. High-Rate Capable Floating Strip Micromegas. *Nuclear and Particle Physics Proceedings*, 273:1173–1179, 2016.

H. L. Bradt and B. Peters. The Heavy Nuclei of the Primary Cosmic Radiation. *Phys. Rev.*, 77:54–70, 1950.

W. H. Bragg and R. Kleeman. On the α particles of radium, and their loss of range in passing through various atoms and molecules. *Philosophical Magazine Series 6*, 10(57): 318–340, 1905.

F. Bray et al. Global cancer statistics 2018: Globocan estimates of incidence and mortality worldwide for 36 cancers in 185 countries. *CA: A Cancer Journal for Clinicians*, 68(6): 394–424, 2018.

J. H. Breasted. *The Edwin Smith surgical papyrus*, volume III. 1930.

C. Brusasco et al. A dosimetry system for fast measurement of 3D depth-dose profiles in charged-particle tumor therapy with scanning techniques. *Nuclear Instruments and Methods in Physics Research Section B: Beam Interactions with Materials and Atoms*, 168(4):578–592, 2000.

M. Bueno, H. Paganetti, M. A. Duch, and J. Schuemann. An algorithm to assess the need for clinical Monte Carlo dose calculation for small proton therapy fields based on quantification of tissue heterogeneity. *Medical Physics*, 40(8):081704, 2013.

A. E. Burgess. The Rose model, revisited. *Journal of the Optical Society of America A*, 16(3):633, 1999.

M. Byrne et al. Mechanisms of oncogenic chromosomal translocations. *Annals of the New York Academy of Sciences*, 1310(1):89–97, 2014.

A. Cárabe-Fernández, R. G. Dale, and B. Jones. The incorporation of the concept of minimum RBE (RBE_{min}) into the linear-quadratic model and the potential for improved radiobiological analysis of high-LET treatments. *International journal of radiation biology*, 83(1):27–39, 2007.

D. J. Carlson. *Mechanisms of Intrinsic Radiation Sensitivity: The effects of DNA damage repair, oxygen, and radiation quality.* PhD thesis, Purdue University, 2006.

D. J. Carlson, R. D. Stewart, V. A. Semenenko, and G. A. Sandison. Combined Use of Monte Carlo DNA Damage Simulations and Deterministic Repair Models to Examine Putative Mechanisms of Cell Killing. *Radiation Research*, 169(4):447–459, 2008.

R. Cassetta et al. Accuracy of low-dose proton CT image registration for pretreatment alignment verification in reference to planning proton CT. *Journal of Applied Clinical Medical Physics*, 20(4):83–90, 2019.

M. Cavinato et al. Monte Carlo calculations using the Boltzmann Master Equation theory of nuclear reactions. *Physics Letters B*, 382(1-2):1–5, 1996.

Y. Censor, R. Davidi, and G. T. Herman. Perturbation resilience and superiorization of iterative algorithms. *Inverse Problems*, 26(6):065008, 2010.

Y. Censor. Weak and Strong Superiorization: Between Feasibility-Seeking and Minimization. *Analele Universitatii Ovidius Constanta - Seria Matematica*, 23(3):41–54, 2015.

Y. Censor et al. On the effectiveness of projection methods for convex feasibility problems with linear inequality constraints. *Computational Optimization and Applications*, 51(3): 1065–1088, 2012.

G. T. Chen et al. Treatment planning for heavy ion radiotherapy. *International Journal of Radiation Oncology*Biology*Physics*, 5(10):1809–1819, 1979.

S. H. Cho, B. L. Jones, and S. Krishnan. The dosimetric feasibility of gold nanoparticle-aided radiation therapy (GNRT) via brachytherapy using low-energy gamma-/x-ray sources. *Physics in Medicine & Biology*, 54(16):4889–4905, 2009.

D. P. Clark et al. In vivo characterization of tumor vasculature using iodine and gold nanoparticles and dual energy micro-CT. *Physics in Medicine & Biology*, 58(6):1683–1704, 2013.

R. Clarkson et al. Characterization of image quality and image-guidance performance of a preclinical microirradiator. *Medical Physics*, 38(2):845–856, 2011.

B. Clasie, H. Paganetti, and H. M. Kooy. Dose calculation algorithms. In *Proton Therapy Physics*, chapter 12, pages 381–412. CRC Press, 2012.

L. E. Cole et al. Gold nanoparticles as contrast agents in x-ray imaging and computed tomography. *Nanomedicine*, 10(2):321–341, 2015.

C.-A. Collins-Fekete. *On particle imaging with application to particle radiotherapy*. PhD thesis, Université Laval, 2017.

C.-A. Collins-Fekete et al. Developing a phenomenological model of the proton trajectory within a heterogeneous medium required for proton imaging. *Physics in Medicine & Biology*, 60(13):5071, 2015.

C.-A. Collins-Fekete et al. Extension of the fermi-eyges most-likely path in heterogeneous medium with prior knowledge information. *Physics in Medicine & Biology*, 62(24):9207, 2017a.

C.-A. Collins-Fekete et al. A theoretical framework to predict the most likely ion path in particle imaging. *Physics in Medicine & Biology*, 62(5):1777, 2017b.

P. L. Combettes and J. Luo. An adaptive level set method for nondifferentiable constrained image recovery. *IEEE Transactions on Image Processing*, 11(11):1295–1304, 2002.

A. M. Cormack. Representation of a Function by Its Line Integrals, with Some Radiological Applications. *Journal of Applied Physics*, 34(9):2722–2727, 1963.

A. M. Cormack. Representation of a Function by Its Line Integrals, with Some Radiological Applications. II. *Journal of Applied Physics*, 35(10):2908–2913, 1964.

S. B. Curtis. Lethal and Potentially Lethal Lesions Induced by Radiation - A Unified Repair Model. *Radiation Research*, 106(2):252–270, 1986.

I. J. Das and H. Paganetti. Introduction and History of Proton Therapy. In *Principles and Practice of Proton Beam Therapy*, chapter 1, pages 1–20. Medical Physics Publishing. Inc., 2015.

R. Davidi, G. Herman, and Y. Censor. Perturbation-resilient block-iterative projection methods with application to image reconstruction from projections. *International Transactions in Operational Research*, 16(4):505–524, 2009.

J. Debus et al. Bestrahlung von Schädelbasistumoren mit Kohlenstoffionen bei der GSI. Erste klinische Ergebnisse und zukünftige Perspektiven. *Strahlentherapie und Onkologie*, 176(5):211–216, 2000.

C. Dionet et al. Effects of Low-Dose Neutrons Applied at Reduced Dose Rate on Human Melanoma Cells. *Radiation Research*, 154(4):406–411, 2000.

M. Durante and H. Paganetti. Nuclear physics in particle therapy: a review. *Reports on Progress in Physics*, 79(9):096702, 2016.

D. Emfietzoglou et al. A dielectric response study of the electronic stopping power of liquid water for energetic protons and a new I-value for water. *Physics in Medicine & Biology*, 54(11):3451–3472, 2009.

M. Engelsmann and C. Bert. Precision and Uncertainties in Proton Therapy for Moving Targets. In *Proton Therapy Physics*, chapter 14, pages 435–460. CRC Press, 2012.

F. S. Englbrecht. Experimental based Monte Carlo modeling of a clinical proton beam. Master's thesis, Ludwig-Maximilians-Universität München, 2014.

M. Esposito et al. PRaVDA: The first solid-state system for proton computed tomography. *Physica Medica*, 55:149–154, 2018.

L. Eyges. Multiple Scattering with Energy Loss. *Phys. Rev.*, 74:1534–1535, 1948.

U. Fano. Penetration of Protons, Alpha Particles, and Mesons. *Annual Review of Nuclear and Particle Science*, 13:1–66, 1963.

P. Farace, R. Righetto, and A. Meijers. Pencil beam proton radiography using a multilayer ionization chamber. *Physics in Medicine & Biology*, 61(11):4078, 2016.

A. Fassò, A. Ferrari, J. Ranft, and P. R. Sala. An update about FLUKA, 1995. Proc. 2nd Workshop on Simulating Accelerator Radiation Environments (SARE 2), CERN, Geneva, Switzerland 9-11 Oct, 1995. Ed. G.R. Stevenson, CERN Report TIS-RP/97-05 (1997), p. 158-170.

M. Feng, G. Valdes, N. Dixit, and T. D. Solberg. Machine Learning in Radiation Oncology: Opportunities, Requirements, and Needs. *Frontiers in Oncology*, 8:110, 2018.

A. Ferrari and M. Pelliccioni. On the Conversion Coefficients from Fluence to Ambient Dose Equivalent. *Radiation Protection Dosimetry*, 54(4):251–255, 1994.

A. Ferrari and P. Sala. A new model for hadronic interactions at intermediate energies for the FLUKA code. In *Int. Conference on Monte Carlo Simulation in High Energy and*

Nuclear Physics (MC93), Tallahassee (Florida) 22-26 February 1993, pages 277–288, 1993.

A. Ferrari, P. Sala, R. Guaraldi, and F. Padoani. An improved multiple scattering model for charged particle transport. *Nuclear Instruments and Methods in Physics Research Section B: Beam Interactions with Materials and Atoms*, 71(4):412–426, 1992.

A. Ferrari, P. Sala, A. Fassò, and J. Ranft. FLUKA: a multi-particle transport code. Technical report, CERN-2005-10 (2005), INFN/TC 05/11, SLAC-R-773, 2005.

E. Fokas, G. Kraft, H. An, and R. Engenhart-Cabillic. Ion beam radiobiology and cancer: Time to update ourselves. *Biochimica et Biophysica Acta (BBA) - Reviews on Cancer*, 1796(2):216–229, 2009.

E. Ford et al. An image-guided precision proton radiation platform for preclinical *in vivo* research. *Physics in Medicine & Biology*, 62(1):43–58, 2017.

M. C. Frese, V. K. Yu, R. D. Stewart, and D. J. Carlson. A Mechanism-Based Approach to Predict the Relative Biological Effectiveness of Protons and Carbon Ions in Radiation Therapy. *International Journal of Radiation Oncology*Biology*Physics*, 83(1):442 – 450, 2012.

M. C. Frese. *Potentials and Risks of Advanced Radiobiological Treatment Planning for Proton and Carbon Ion Therapy.* PhD thesis, Ruperto-Carola University of Heidelberg, 2011.

T. Friedrich et al. Calculation of the biological effects of ion beams based on the microscopic spatial damage distribution pattern. *International Journal of Radiation Biology*, 88(1-2): 103–107, 2012.

H. Fujita et al. A simple method for determining the modulation transfer function in digital radiography. *Medical Imaging, IEEE Transactions on*, 11(1):34–39, 1992.

Y. Furusawa et al. Inactivation of Aerobic and Hypoxic Cells from Three Different Cell Lines by Accelerated ^{3}He,- ^{12}C- and ^{20}Ne-Ion Beams. *Radiation Research*, 154(5):485–496, 2000.

T. Gehrke, C. Amato, S. Berke, and M. Martišíková. Theoretical and experimental comparison of proton and helium-beam radiography using silicon pixel detectors. *Physics in Medicine & Biology*, 63(3):035037, 2018a.

T. Gehrke, R. Gallas, O. Jäkel, and M. Martišíková. Proof of principle of helium-beam radiography using silicon pixel detectors for energy deposition measurement, identification, and tracking of single ions. *Medical Physics*, 45(2):817–829, 2018b.

V. Giacometti et al. Software platform for simulation of a prototype proton CT scanner. *Medical Physics*, 44(3):1002–1016, 2017.

C. Gianoli et al. Spatial Resolution Enhancement in Integration-Mode Detectors for Proton Radiography and Tomography. *Radiotherapy and Oncology*, 118:S46–S47, 2016.

C. Gianoli et al. Analytical simulator of proton radiography and tomography for different detector configurations. *Physica Medica*, 59:92–99, 2019.

Y. Giomataris, P. Rebourgeard, J. Robert, and G. Charpak. Micromegas: a high-granularity position-sensitive gaseous detector for high particle-flux environments. *Nuclear Instruments and Methods in Physics Research Section A: Accelerators, Spectrometers, Detectors and Associated Equipment*, 376(1):29–35, 1996.

P. Giubilato et al. iMPACT: Innovative pCT scanner. In *2015 IEEE Nuclear Science Symposium and Medical Imaging Conference (NSS/MIC)*, 2015.

M. Goitein. Three-dimensional density reconstruction from a series of two-dimensional projections. *Nuclear Instruments and Methods*, 101(3):509–518, 1972.

M. Goitein. *Radiation Oncology: A Physicist's-Eye View*. Springer-Verlag New York, 2008.

M. Goitein, A. J. Lomax, and E. S. Pedroni. Treating Cancer with Protons. *Physics Today*, 55(9):45–50, 2002.

B. Gottschalk et al. Multiple Coulomb scattering of 160 MeV protons. *Nuclear Instruments and Methods in Physics Research Section B: Beam Interactions with Materials and Atoms*, 74(4):467–490, 1993.

B. Gottschalk. Physics of Proton Interactions in Matter. In *Proton Therapy Physics*, chapter 1, pages 19–60. CRC Press, 2012.

D. E. Greiner et al. Momentum Distributions of Isotopes Produced by Fragmentation of Relativistic ^{12}C and ^{16}O Projectiles. *Phys. Rev. Lett.*, 35:152–155, 1975.

D. E. Groom. http://pdg.lbl.gov/2018/atomicnuclearproperties/index.html. Accessed: 2019-05-17.

F. Guan et al. A mechanistic relative biological effectiveness model-based biological dose optimization for charged particle radiobiology studies. *Physics in Medicine & Biology*, 64(1):015008, dec 2018.

K. Gunzert-Marx, H. Iwase, D. Schardt, and R. S. Simon. Secondary beam fragments produced by 200 MeV u^{-1} ^{12}C ions in water and their dose contributions in carbon ion radiotherapy. *New Journal of Physics*, 10(7):075003, 2008.

T. Haberer, W. Becher, D. Schardt, and G. Kraft. Magnetic scanning system for heavy ion therapy. *Nuclear Instruments and Methods in Physics Research Section A: Accelerators, Spectrometers, Detectors and Associated Equipment*, 330(1-2):296–305, 1993.

T. Haberer et al. The Heidelberg Ion Therapy Center. *Radiotherapy and Oncology*, 73, Supplement 2:S186–S190, 2004.

J. F. Hainfeld, D. N. Slatkin, T. M. Focella, and H. M. Smilowitz. Gold nanoparticles: a new X-ray contrast agent. *The British Journal of Radiology*, 79(939):248–253, 2006.

S. I. Hajdu. A note from history: Landmarks in history of cancer, part 1. *Cancer*, 117(5): 1097–1102, 2011.

A. Hammi et al. Patient positioning verification for proton therapy using proton radiography. *Physics in Medicine & Biology*, 63(24):245009, 2018.

D. C. Hansen, J. B. B. Petersen, N. Bassler, and T. S. Sørensen. Improved proton computed tomography by dual modality image reconstruction. *Medical Physics*, 41(3):031904, 2014.

D. C. Hansen et al. A simulation study on proton computed tomography (CT) stopping power accuracy using dual energy CT scans as benchmark. *Acta Oncologica*, 54(9): 1638–1642, 2015.

K. M. Hanson et al. Computed tomography using proton energy loss. *Physics in Medicine & Biology*, 26(6):965, 1981.

K. M. Hanson et al. Proton computed tomography of human specimens. *Physics in Medicine & Biology*, 27(1):25, 1982.

R. B. Hawkins. A microdosimetric-kinetic theory of the dependence of the RBE for cell death on LET. *Medical Physics*, 25(7):1157–1170, 1998.

B. J. Heismann, J. Leppert, and K. Stierstorfer. Density and atomic number measurements with spectral x-ray attenuation method. *Journal of Applied Physics*, 94(3):2073–2079, 2003.

J. S. Hendricks. A Monte Carlo Code for Particle Transport. *Los Alamos Science*, 1994.

P. Henriquet et al. Interaction vertex imaging (IVI) for carbon ion therapy monitoring: a feasibility study. *Physics in Medicine & Biology*, 57(14):4655, 2012.

G. T. Herman. *Fundamentals of Computerized Tomography*. Springer-Verlag GmbH, 2009.

G. T. Herman, E. Garduño, R. Davidi, and Y. Censor. Superiorization: An optimization heuristic for medical physics. *Medical Physics*, 39(9):5532–5546, 2012.

D. Herring and D. Compton. The degree of precision required in the radiation dose delivered in cancer radiotherapy. *Computers in radiotherapy. Br J Radiol Special Report*, 5(10): 51–58, 1971.

A.-C. Heuskin, C. Michiels, and S. Lucas. Low dose hypersensitivity following in vitro cell irradiation with charged particles: Is the mechanism the same as with X-ray radiation? *International Journal of Radiation Biology*, 90(1):81–89, 2013.

V. L. Highland. Some practical remarks on multiple scattering. *Nuclear Instruments and Methods*, 129(2):497–499, 1975.

Y. Hsiao and R. D. Stewart. Monte Carlo simulation of DNA damage induction by x-rays and selected radioisotopes. *Physics in Medicine & Biology*, 53(1):233–244, 2008.

N. Hudobivnik et al. Comparison of proton therapy treatment planning for head tumors with a pencil beam algorithm on dual and single energy CT images. *Medical Physics*, 43(1):495–504, 2016.

J. Hüfner, K. Schäfer, and B. Schürmann. Abrasion-ablation in reactions between relativistic heavy ions. *Phys. Rev. C*, 12:1888–1898, 1975.

N. Hünemohr et al. Tissue decomposition from dual energy CT data for MC based dose calculation in particle therapy. *Medical Physics*, 41(6):061714, 2014.

ICRU. Fundamental quantities and units for ionizing radiation (ICRU report 85). *Journal of the International Commission on Radiation Units and Measurements*, 11(1), 2011.

D. F. Jackson and D. Hawkes. X-ray attenuation coefficients of elements and mixtures. *Physics Reports*, 70(3):169 – 233, 1981.

F. Jacobs et al. A Fast Algorithm to Calculate the Exact Radiological Path Through a Pixel Or Voxel Space. *Journal of Computing and Information Technology*, 6, 12 1998.

O. Jäkel et al. Relation between carbon ion ranges and x-ray CT numbers. *Medical Physics*, 28(4):701–703, 2001.

O. Jäkel. Ranges of ions in metals for use in particle treatment planning. *Physics in Medicine & Biology*, 51(9):N173, 2006.

O. Jäkel and P. Reiss. The influence of metal artefacts on the range of ion beams. *Physics in Medicine & Biology*, 52(3):635, 2007.

X. Jia, J. Schümann, H. Paganetti, and S. B. Jiang. GPU-based fast Monte Carlo dose calculation for proton therapy. *Physics in Medicine & Biology*, 57(23):7783–7797, 2012.

X. Jia, P. Ziegenhein, and S. B. Jiang. GPU-based high-performance computing for radiation therapy. *Physics in Medicine & Biology*, 59(4):R151–R182, 2014.

H. Jiang and H. Paganetti. Adaptation of GEANT4 to Monte Carlo dose calculations based on CT data. *Medical Physics*, 31(10):2811–2818, 2004.

R. P. Johnson et al. A Fast Experimental Scanner for Proton CT: Technical Performance and First Experience With Phantom Scans. *IEEE Transactions on Nuclear Science*, 63 (1):52–60, 2016.

R. P. Johnson. Review of medical radiography and tomography with proton beams. *Reports on Progress in Physics*, 81(1):016701, 2018.

B. L. Jones and S. H. Cho. The feasibility of polychromatic cone-beam x-ray fluorescence computed tomography (XFCT) imaging of gold nanoparticle-loaded objects: a Monte Carlo study. *Physics in Medicine & Biology*, 56(12):3719–3730, 2011.

A. C. Kak and M. Slaney. *Principles of Computerized Tomographic Imaging*. IEEE Press, 1988.

F. Kamp, D. J. Carlson, and J. J. Wilkens. Rapid implementation of the repair-misrepair-fixation (RMF) model facilitating online adaption of radiosensitivity parameters in ion therapy. *Physics in Medicine & Biology*, 62(13):N285, 2017.

F. Kamp et al. Fast Biological Modeling for Voxel-based Heavy Ion Treatment Planning Using the Mechanistic Repair-Misrepair-Fixation Model and Nuclear Fragment Spectra. *International Journal of Radiation Oncology*Biology*Physics*, 93(3):557–568, 2015.

T. Kanai et al. Spot scanning system for proton radiotherapy. *Medical Physics*, 7(4): 365–369, 1980.

C. P. Karger and P. Peschke. RBE and related modeling in carbon-ion therapy. *Physics in Medicine & Biology*, 63(1):01TR02, 2018.

N. T. Karonis et al. Distributed and hardware accelerated computing for clinical medical imaging using proton computed tomography (pCT). *Journal of Parallel and Distributed Computing*, 73(12):1605–1612, 2013.

A. M. Kellerer and H. H. Rossi. A Generalized Formulation of Dual Radiation Action. *Radiation Research*, 75(3):471, 1978.

L. Kelleter et al. Spectroscopic study of prompt-gamma emission for range verification in proton therapy. *Physica Medica*, 34:7–17, 2017.

R. N. Kjellberg, W. H. Sweet, W. M. Preston, and A. M. Koehler. The bragg peak of a proton beam in intracranial therapy of tumors. *Transactions of the American Neurological Association*, 87:216–218, 1962.

F. Klitzner. *Research and Development of Two-Dimensional Floating Strip Micromegas Detectors*. PhD thesis, Ludwig-Maximilians-Universität München, 2019.

A.-C. Knopf and A. Lomax. In vivo proton range verification: a review. *Physics in Medicine & Biology*, 58(15):R131, 2013.

A. M. Koehler. Proton Radiography. *Science*, 160:303–304, 1968.

B. M. G. Kopp. Ion Imaging with Protons, Helium- and Carbon Ions - An experimental study. Master's thesis, Ludwig-Maximilians-Universität München, 2017.

A. C. Kraan. Range Verification Methods in Particle Therapy: Underlying Physics and Monte Carlo Modeling. *Frontiers in Oncology*, 5:150, 2015.

N. Krah et al. An advanced image processing method to improve the spatial resolution of ion radiographies. *Physics in Medicine & Biology*, 60(21):8525, 2015.

N. Krah et al. A comprehensive theoretical comparison of proton imaging set-ups in terms of spatial resolution. *Physics in Medicine & Biology*, 63(13):135013, 2018a.

N. Krah et al. Proton radiography with a commercial range telescope detector using dedicated post processing methods. *Physics in Medicine & Biology*, 63(20):205016, 2018b.

M. Krämer. http://bio.gsi.de/docs/trax.html.

M. Krämer and M. Durante. Ion beam transport calculations and treatment plans in particle therapy. *The European Physical Journal D*, 60(1):195–202, 2010.

J. J. Kruse. Immobilization and Simulation. In *Principles and Practice of Proton Beam Therapy*, chapter 18, pages 521–540. Medical Physics Publishing. Inc., 2015.

P. Lämmer. Studies on an ionization chamber and time projection chamber for beam position monitoring and ion transmission imaging. Master's thesis, Ludwig-Maximilians-Universität München, 2019.

G. Landry and C.-h. Hua. Current state and future applications of radiological image guidance for particle therapy. *Medical Physics*, 45(11):e1086–e1095, 2018.

G. Landry, J. Seco, M. Gaudreault, and F. Verhaegen. Deriving effective atomic numbers from DECT based on a parameterization of the ratio of high and low linear attenuation coefficients. *Physics in Medicine & Biology*, 58(19):6851–6866, 2013.

G. Landry et al. Phantom based evaluation of CT to CBCT image registration for proton therapy dose recalculation. *Physics in Medicine & Biology*, 60(2):595, 2015.

K. Langen, J. Polf, and R. Schulte. Imaging for Proton Therapy. In *Principles and Practice of Proton Beam Therapy*, chapter 7, pages 165–190. Medical Physics Publishing. Inc., 2015.

B. Larsson. Pre-therapeutic Physical Experiments with High Energy Protons. *The British Journal of Radiology*, 34(399):143–151, 1961.

J. Lascaud et al. Applicability of Capacitive Micromachined Ultrasonic Transducers for the detection of proton-induced thermoacoustic waves. In *submitted to IEEE IUS 2019*, 2019.

T. Li et al. Reconstruction for proton computed tomography by tracing proton trajectories: A Monte Carlo study. *Medical Physics*, 33(3):699–706, 2006.

J. Liebl, H. Paganetti, M. Zhu, and B. A. Winey. The influence of patient positioning uncertainties in proton radiotherapy on proton range and dose distributions. *Medical Physics*, 41(9):091711, 2014.

Y. Lin, S. J. McMahon, H. Paganetti, and J. Schuemann. Biological modeling of gold nanoparticle enhanced radiotherapy for proton therapy. *Physics in Medicine & Biology*, 60(10):4149–4168, 2015.

U. Linz. Physical and Biological Rationale for Using Ions in Therapy. In *Ion Beam Therapy: Fundamentals, Technology, Clinical Applications*, chapter 4, pages 45–60. Springer Berlin Heidelberg, 2012.

A. Lomax. What will the medical physics of proton therapy look like 10 yr from now? A personal view. *Medical Physics*, 45(11):e984–e993, 2018.

M. Lomax, L. Folkes, and P. O'Neill. Biological Consequences of Radiation-induced DNA Damage: Relevance to Radiotherapy. *Clinical Oncology*, 25(10):578–585, 2013.

T. Lomax, A. Bolsi, F. Albertini, and D. Weber. Treatment Planning for Pencil Beam Scanning. In *Principles and Practice of Proton Beam Therapy*, chapter 24, pages 667–708. Medical Physics Publishing. Inc., 2015.

G. R. Lynch and O. I. Dahl. Approximations to multiple coulomb scattering. *Nuclear Instruments and Methods in Physics Research Section B: Beam Interactions with Materials and Atoms*, 58(1):6–10, 1991.

L. Magallanes et al. Upgrading an Integrating Carbon Ion Transmission Imaging System with Active Scanning Beam Delivery towards Low Dose Ion Imaging. *Submitted to IEEE Transactions on Radiation and Plasma Medical Sciences*, 2019.

L. Magallanes. *Low-dose ion-based transmissionradiography and tomography foroptimization of carbon ion-beamtherapy.* PhD thesis, Ludwig-Maximilians-Universität München, 2017.

A. Mairani et al. The FLUKA Monte Carlo code coupled with the local effect model for biological calculations in carbon ion therapy. *Physics in Medicine & Biology*, 55(15): 4273–4289, 2010.

A. Mairani et al. A Monte Carlo-based treatment planning tool for proton therapy. *Physics in Medicine & Biology*, 58(8):2471, 2013.

A. Mairani et al. Biologically optimized helium ion plans: calculation approach and its in vitro validation. *Physics in Medicine & Biology*, 61(11):4283, 2016.

A. Mairani. *Nucleus-Nucleus Interaction Modelling and Applications in Ion Therapy Treatment Planning*. PhD thesis, Università degli studi di Pavia, 2007.

T. Marcelos. Carbon ion radiography and tomography: a Monte Carlo study. Master's thesis, Universidade de Lisboa Faculdade de Ciências Departamento de Física, 2014.

B. Marples and M. C. Joiner. The Response of Chinese Hamster V79 Cells to Low Radiation Doses: Evidence of Enhanced Sensitivity of the Whole Cell Population. *Radiation Research*, 133(1):41, 1993.

B. Marples and K. A. Skov. Small Doses of High-Linear Energy Transfer Radiation Increase the Radioresistance of Chinese Hamster V79 Cells to Subsequent X Irradiation. *Radiation Research*, 146(4):382, 1996.

B. Marples, P. Lambin, K. A. Skov, and M. C. Joiner. Low dose hyper-radiosensitivity and increased radioresistance in mammalian cells. *International Journal of Radiation Biology*, 71(6):721–735, 1997.

B. Marples et al. Low-Dose Hyper-radiosensitivity: A Consequence of Ineffective Cell Cycle Arrest of Radiation-Damaged G2-Phase Cells. *Radiation Research*, 161(3):247–255, 2004.

B. Marples and S. J. Collis. Low-Dose Hyper-Radiosensitivity: Past, Present, and Future. *International Journal of Radiation Oncology*Biology*Physics*, 70(5):1310–1318, 2008.

S. Mattiazzo et al. The iMPACT project tracker and calorimeter. *Nuclear Instruments and Methods in Physics Research Section A: Accelerators, Spectrometers, Detectors and Associated Equipment*, 845:664–667, 2017.

S. Mattiazzo et al. iMPACT: An Innovative Tracker and Calorimeter for Proton Computed Tomography. *IEEE Transactions on Radiation and Plasma Medical Sciences*, 2(4):345–352, 2018.

S. Meyer et al. Tomographic imaging with carbon ion beams. In *2016 IEEE Nuclear Science Symposium, Medical Imaging Conference and Room-Temperature Semiconductor Detector Workshop (NSS/MIC/RTSD)*, pages 1–5, 2016.

S. Meyer et al. Dosimetric accuracy and radiobiological implications of ion computed tomography for proton therapy treatment planning. *Physics in Medicine & Biology*, 64 (12):125008, 2019.

S. Meyer. A systematic Monte Carlo study of the influence of different acquisition and detector parameters on theimage quality of carbon ion radiography andtomography using a range telescope. Master's thesis, Ludwig-Maximilians-Universität München, 2015.

S. Meyer et al. Comparative Monte Carlo study on the performance of integration- and list-mode detector configurations for carbon ion computed tomography. *Physics in Medicine & Biology*, 62(3):1096, 2017.

B. J. Mijnheer, J. J. Battermann, and A. Wambersie. What degree of accuracy is required and can be achieved in photon and neutron therapy? *Radiotherapy and Oncology*, 8(3): 237–252, 1987.

R. Mohan, X. R. Zhu, and H. Paganetti. Dose Calculations for Proton Beam Therapy: Semi-empirical Analytical Methods. In *Principles and Practice of Proton Beam Therapy*, chapter 19, pages 541–570. Medical Physics Publishing. Inc., 2015.

Moliére. Theorie der Streuung schneller geladener Teilchen II. Mehrfach-und Vielfachstreuung. *Z. Naturforsch. A*, 3:78–97, 1948.

U. D. Monte. Does the cell number 10^9 still really fit one gram of tumor tissue? *Cell Cycle*, 8(3):505–506, 2009.

I. Mori and Y. Machida. Deriving the modulation transfer function of CT from extremely noisy edge profiles. *Radiological physics and technology*, 2(1):22, 2009.

S. Mori, A.-C. Knopf, and K. Umegaki. Motion management in particle therapy. *Medical Physics*, 45(11):e994–e1010, 2018.

M. Müllner, H. Schlattl, C. Hoeschen, and O. Dietrich. Feasibility of spectral CT imaging for the detection of liver lesions with gold-based contrast agents – a simulation study. *Physica Medica*, 31(8):875–881, 2015.

H. Muraishi et al. Evaluation of spatial resolution for heavy ion CT system based on the measurement of residual range distribution with HIMAC. *IEEE Transactions on Nuclear Science*, 56(5):2714–2721, 2009.

H. Muraishi et al. Experimental study of heavy-ion computed tomography using a scintillation screen and an electron-multiplying charged coupled device camera for human head imaging. *Japanese Journal of Applied Physics*, 55(3):036401, 2016.

M. J. Murphy et al. The management of imaging dose during image-guided radiotherapy: Report of the AAPM task group 75. *Medical Physics*, 34(10):4041–4063, 2007.

T. Nakagawa et al. X-ray computed tomography imaging of a tumor with high sensitivity using gold nanoparticles conjugated to a cancer-specific antibody via polyethylene glycol chains on their surface. *Science and Technology of Advanced Materials*, 17(1):387–397, 2016.

W. D. Newhauser and R. Zhang. The physics of proton therapy. *Physics in Medicine & Biology*, 60(8):R155, 2015.

H. Nikjoo et al. Track structure in radiation biology: theory and applications. *International Journal of Radiation Biology*, 73(4):355–364, 1998.

C. Oancea et al. PO-0888: Comparison of x-ray CT and proton based CT planning in the presence of titanium dental implants. *Radiotherapy and Oncology*, 127:S470–S471, 2018.

D. Ondreka and U. Weinrich. The Heidelberg Ion Therapy (HIT) Accelerator Coming into Operation. *Proc. EPAC08 Genoa*, pages 979–981, 2008.

H. Owen, A. Lomax, and S. Jolly. Current and future accelerator technologies for charged particle therapy. *Nuclear Instruments and Methods in Physics Research Section A: Accelerators, Spectrometers, Detectors and Associated Equipment*, 809:96–104, 2016.

H. Paganetti. Nuclear interactions in proton therapy: dose and relative biological effect distributions originating from primary and secondary particles. *Physics in Medicine & Biology*, 47(5):747, 2002.

H. Paganetti. The Physics of Proton Biology. In *Proton Therapy Physics*, chapter 19, pages 593–627. CRC Press, 2012a.

H. Paganetti. Range uncertainties in proton therapy and the role of Monte Carlo simulations. *Physics in Medicine & Biology*, 57(11):R99, 2012b.

H. Paganetti. Proton Relative Biological Effectiveness. In *Principles and Practice of Proton Beam Therapy*, chapter 5, pages 109–128. Medical Physics Publishing. Inc., 2015.

H. Paganetti, J. Schuemann, and R. Mohan. Dose Calculations for Proton Beam Therapy: Monte Carlo. In *Principles and Practice of Proton Beam Therapy*, chapter 20, pages 571–594. Medical Physics Publishing. Inc., 2015.

H. Paganetti et al. Report of the AAPM TG-256 on the relative biological effectiveness of proton beams in radiation therapy. *Medical Physics*, 46(3):e53–e78, 2019.

J. R. Palta and D. K. Yeung. Precision and Uncertainties in Proton Therapy for Nonmoving Targets. In *Proton Therapy Physics*, chapter 13, pages 413–434. CRC Press, 2012.

Y. Pan et al. Size-Dependent Cytotoxicity of Gold Nanoparticles. *Small*, 3(11):1941–1949, 2007.

Y.-K. Park, G. C. Sharp, J. Phillips, and B. A. Winey. Proton dose calculation on scatter-corrected CBCT image: Feasibility study for adaptive proton therapy. *Medical Physics*, 42(8):4449–4459, 2015.

K. Parodi, A. Ferrari, F. Sommerer, and H. Paganetti. Clinical CT-based calculations of dose and positron emitter distributions in proton therapy using the FLUKA Monte Carlo code. *Physics in Medicine & Biology*, 52(12):3369, 2007.

K. Parodi et al. Monte Carlo simulations to support start-up and treatment planning of scanned proton and carbon ion therapy at a synchrotron-based facility. *Physics in Medicine & Biology*, 57(12):3759, 2012.

K. Parodi et al. Towards a novel small animal proton irradiation platform - the SIRMIO project. *Accepted for publication in Acta Oncologica*, 2019.

K. Parodi. *On the feasibility of dose quantification with in-beam PET data in radiotherapy with ^{12}C and proton beams.* PhD thesis, Technische Universität Dresden, Germany, 2004.

K. Parodi and J. C. Polf. In vivo range verification in particle therapy. *Medical Physics*, 45(11):e1036–e1050, 2018.

K. Parodi et al. PET imaging for treatment verification of ion therapy: Implementation and experience at GSI Darmstadt and MGH Boston. *Nuclear Instruments and Methods in Physics Research Section A: Accelerators, Spectrometers, Detectors and Associated Equipment*, 591(1):282–286, 2008.

A. Peeters et al. How costly is particle therapy? Cost analysis of external beam radiotherapy with carbon-ions, protons and photons. *Radiotherapy and Oncology*, 95(1):45–53, 2010.

S. N. Penfold, A. B. Rosenfeld, R. W. Schulte, and K. E. Schubert. A more accurate reconstruction system matrix for quantitative proton computed tomography. *Medical Physics*, 36(10):4511–4518, 2009.

S. N. Penfold, R. W. Schulte, Y. Censor, and A. B. Rosenfeld. Total variation superiorization schemes in proton computed tomography image reconstruction. *Medical Physics*, 37(11):5887–5895, 2010.

S. N. Penfold, A. B. Rosenfeld, R. W. Schulte, and H.-F. W. Sadrozinksi. Geometrical optimization of a particle tracking system for proton computed tomography. *Radiation Measurements*, 46(12):2069–2072, 2011.

S. Penfold and Y. Censor. Techniques in Iterative Proton CT Image Reconstruction. *Sensing and Imaging*, 16(1):19, 2015. ISSN 1557-2072.

S. N. Penfold. *Image reconstruction and Monte Carlo simulations in the development ofproton computed tomography for applications in proton radiation therapy*. PhD thesis, University of Wollongong, 2010.

H. E. S. Pettersen. *A Digital Tracking Calorimeter for Proton Computed Tomography*. PhD thesis, University of Bergen, 2018.

P. Piersimoni et al. Helium CT: Monte Carlo simulation results for an ideal source and detector with comparison to proton CT. *Medical Physics*, 45(7):3264–3274, 2018.

M. Podesta, L. C. Persoon, and F. Verhaegen. A novel time dependent gamma evaluation function for dynamic 2D and 3D dose distributions. *Physics in Medicine & Biology*, 59 (20):5973, 2014.

J. C. Polf et al. Measurement and calculation of characteristic prompt gamma ray spectra emitted during proton irradiation. *Physics in Medicine & Biology*, 54(22):N519, 2009.

G. Poludniowski, N. M. Allinson, and P. M. Evans. Proton computed tomography reconstruction using a backprojection-then-filtering approach. *Physics in Medicine & Biology*, 59(24):7905–7918, 2014.

R. Popovtzer et al. Targeted gold nanoparticles enable molecular CT imaging of cancer. *Nano letters*, 8(12):4593–4596, 2008.

PTCOG. http://www.ptcog.ch. Accessed: 2018-11-01.

C. T. Quinones. *Proton computed tomography*. PhD thesis, Université de Lyon, 2016.

M. Rädler. Noise Reconstruction in Proton Computed Tomography. Master's thesis, Ludwig-Maximilians-Universität München, 2017.

I. Rinaldi et al. Experimental characterization of a prototype detector system for carbon ion radiography and tomography. *Physics in Medicine & Biology*, 58(3):413, 2013.

I. Rinaldi et al. Experimental investigations on carbon ion scanning radiography using a range telescope. *Physics in Medicine & Biology*, 59(12):3041, 2014.

I. Rinaldi. *Investigation of novel imaging methods using therapeutic ion beams*. PhD thesis, Combined Faculties for the Natural Sciences and for Mathematics of the Ruperto-Carola University of Heidelberg, 2011.

S. Rit et al. Filtered backprojection proton CT reconstruction along most likely paths. *Medical Physics*, 40(3):031103, 2013.

O. Rodrigues. Des lois géometriques qui regissent les déplacements d'un systéme solide dans l'espace, et de la variation des coordonnées provenant de ces déplacement considérées indépendent des causes qui peuvent les produire. *J. Math. Pures Appl.*, 5:380–440, 1840.

S. Roesler, R. Engel, and J. Ranft. The Monte Carlo event generator DPMJET-III. In *Advanced Monte Carlo for radiation physics, particle transport simulation and applications. Proceedings, Conference, MC2000, Lisbon, Portugal, October 23-26, 2000*, pages 1033–1038, 2000.

B. Rossi. *High-Energy Particles*. Prentice-Hall Physics Series. Prentice-Hall, Englewood Cliffs, NJ, 1952.

K. Rothkamm and M. Löbrich. Evidence for a lack of DNA double-strand break repair in human cells exposed to very low x-ray doses. *Proceedings of the National Academy of Sciences of the United States of America*, 100(9):5057–5062, 2003.

H.-W. Sadrozinski et al. Development of a head scanner for proton CT. *Nuclear Instruments and Methods in Physics Research Section A: Accelerators, Spectrometers, Detectors and Associated Equipment*, 699:205–210, 2013.

M. Saito. Potential of dual-energy subtraction for converting CT numbers to electron density based on a single linear relationship. *Medical Physics*, 39(4):2021–2030, 2012.

B. Schaffner and E. Pedroni. The precision of proton range calculations in proton radiotherapy treatment planning: experimental verification of the relation between CT-HU and proton stopping power. *Physics in Medicine & Biology*, 43(6):1579, 1998.

B. Schaffner, E. Pedroni, and A. Lomax. Dose calculation models for proton treatment planning using a dynamic beam delivery system: an attempt to include density heterogeneity effects in the analytical dose calculation. *Physics in Medicine & Biology*, 44(1): 27, 1999.

D. Schardt, T. Elsässer, and D. Schulz-Ertner. Heavy-ion tumor therapy: Physical and radiobiological benefits. *Rev. Mod. Phys.*, 82:383–425, 2010.

C. Scheidenberger et al. Energy-Loss-Straggling Experiments with Relativistic Heavy Ions in Solids. *Phys. Rev. Lett.*, 77:3987–3990, 1996.

G. Schettino et al. Low-Dose Hypersensitivity in Chinese Hamster V79 Cells Targeted with Counted Protons Using a Charged-Particle Microbeam. *Radiation Research*, 156 (5):526–534, 2001.

J. M. Schippers. Beam Delivery Systems for Particle Radiation Therapy: Current Status and Recent Developments. *Reviews of Accelerator Science and Technology*, 02(01):179–200, 2009.

J. M. Schippers and A. J. Lomax. Emerging technologies in proton therapy. *Acta Oncologica*, 50(6):838–850, 2011.

M. Schippers. Proton Beam Production and Dose Delivery Techniques. In *Principles and Practice of Proton Beam Therapy*, chapter 6, pages 129–164. Medical Physics Publishing. Inc., 2015.

C. D. Schlaff et al. Bringing the heavy: carbon ion therapy in the radiobiological and clinical context. *Radiation Oncology*, 9(1):88, 2014.

U. Schneider and E. Pedroni. Proton radiography as a tool for quality control in proton therapy. *Medical physics*, 22(4):353–363, 1995.

U. Schneider and E. Pedroni. Multiple Coulomb scattering and spatial resolution in proton radiography. *Medical Physics*, 21(11):1657–1663, 1994.

U. Schneider, E. Pedroni, and A. Lomax. The calibration of CT Hounsfield units for radiotherapy treatment planning. *Physics in Medicine & Biology*, 41(1):111, 1996.

U. Schneider et al. First proton radiography of an animal patient. *Medical Physics*, 31(5): 1046–1051, 2004.

U. Schneider et al. Patient specific optimization of the relation between CT-Hounsfield units and proton stopping power with proton radiography. *Medical Physics*, 32(1):195–199, 2005.

W. Schneider, T. Bortfeld, and W. Schlegel. Correlation between CT numbers and tissue parameters needed for Monte Carlo simulations of clinical dose distributions. *Physics in Medicine & Biology*, 45(2):459, 2000.

C. Schoemers et al. The intensity feedback system at Heidelberg Ion-Beam Therapy Centre. *Nuclear Instruments and Methods in Physics Research Section A: Accelerators, Spectrometers, Detectors and Associated Equipment*, 795:92–99, 2015.

R. Schulte et al. Conceptual design of a proton computed tomography system for applications in proton radiation therapy. *IEEE Transactions on Nuclear Science*, 51(3): 866–872, 2004a.

R. Schulte et al. Nanoparticle-enhanced proton computed tomography: A Monte Carlo simulation study. In *2004 2nd IEEE International Symposium on Biomedical Imaging: Macro to Nano*. IEEE, 2004b.

R. W. Schulte, S. N. Penfold, J. T. Tafas, and K. E. Schubert. A maximum likelihood proton path formalism for application in proton computed tomography. *Medical Physics*, 35(11):4849–4856, 2008.

R. W. Schulte and A. J. Wroe. New developments in treatment planning and verification of particle beam therapy. *Translational Cancer Research*, 1(3), 2012.

R. W. Schulte et al. Density resolution of proton computed tomography. *Medical Physics*, 32(4):1035–1046, 2005.

B. Schultze et al. An Improved Method of Total Variation Superiorization Applied to Reconstruction in Proton Computed Tomography. *arXiv e-prints*, art. arXiv:1803.01112, 2018.

D. Schulz-Ertner and H. Tsujii. Particle Radiation Therapy Using Proton and Heavier Ion Beams. *Journal of Clinical Oncology*, 25(8):953–964, 2007.

M. Schwarz. Treatment planning in proton therapy. *The European Physical Journal Plus*, 126(7), 2011.

L. E. J. R. Schyns et al. Murine vs human tissue compositions: implications of using human tissue compositions for photon energy absorption in mice. *The British Journal of Radiology*, 92(1095), 2019.

C. Seller Oria et al. A Dedicated Tomographic Image Reconstruction Algorithm for Integration-Mode Detector Configuration in Ion Imaging. In *IEEE Nuclear Science Symposium and Medical Imaging Conference (NSS/MIC)*, 2018.

V. A. Semenenko and R. D. Stewart. A Fast Monte Carlo Algorithm to Simulate the Spectrum of DNA Damages Formed by Ionizing Radiation. 161(4):451–457, 2004.

V. A. Semenenko and R. D. Stewart. Fast Monte Carlo simulation of DNA damage formed by electrons and light ions. *Physics in Medicine & Biology*, 51(7):1693–1706, 2006.

D. Shrestha et al. Iterative reconstruction with boundary detection for carbon ion computed tomography. *Physics in Medicine & Biology*, 63(5):055002, 2018.

R. L. Siddon. Fast calculation of the exact radiological path for a three-dimensional CT array. *Medical Physics*, 12(2):252–255, 1985.

E. Y. Sidky and X. Pan. Image reconstruction in circular cone-beam computed tomography by constrained, total-variation minimization. *Physics in Medicine & Biology*, 53(17): 4777, 2008.

M. J. Siegel et al. White Paper of the Society of Computed Body Tomography and Magnetic Resonance on Dual-Energy CT, Part 1: Technology and Terminology. *Journal of Computer Assisted Tomography*, 40(6):841–845, 2016.

J. M. Slater et al. The proton treatment center at Loma Linda University Medical Center: Rationale for and description of its development. *International Journal of Radiation Oncology*Biology*Physics*, 22(2):383–389, 1992.

A. R. Smith. Vision 20/20: Proton therapy. *Medical Physics*, 36(2):556–568, 2009.

F. G. Sommer et al. Heavy-Ion Radiography: Density Resolution and Specimen Radiography. *Investigative Radiology*, 13(2), 1978.

K. H. Song et al. An x-ray image guidance system for small animal stereotactic irradiation. *Physics in Medicine and Biology*, 55(23):7345–7362, 2010.

H. Sorge, H. Stöcker, and W. Greiner. Relativistic quantum molecular dynamics approach to nuclear collisions at ultrarelativistic energies. *Nuclear Physics A*, 498:567–576, 1989.

M. Soukup, M. Fippel, and M. Alber. A pencil beam algorithm for intensity modulated proton therapy derived from Monte Carlo simulations. *Physics in Medicine & Biology*, 50(21):5089–5104, 2005.

V. W. Steward and A. M. Koehler. Proton Beam Radiography in Tumor Detection. *Science*, 179(76):913–914, 1973.

R. D. Stewart et al. Effects of Radiation Quality and Oxygen on Clustered DNA Lesions and Cell Death. *Radiation Research*, 176(5):587–602, 2011.

R. D. Stewart et al. Rapid MCNP simulation of DNA double strand break (DSB) relative biological effectiveness (RBE) for photons, neutrons, and light ions. *Physics in Medicine & Biology*, 60(21):8249–8274, 2015.

E. Stride and N. Saffari. Microbubble ultrasound contrast agents: A review. *Proceedings of the Institution of Mechanical Engineers, Part H: Journal of Engineering in Medicine*, 217(6):429–447, 2003.

J. T. Taylor et al. An experimental demonstration of a new type of proton computed tomography using a novel silicon tracking detector. *Medical Physics*, 43(11):6129–6136, 2016.

J. Telsemeyer. *Investigation of an Amorphous Silicon Flat-Panel Detector for Ion Radiography*. PhD thesis, Combined Faculties for the Natural Sciences and for Mathematics of the Ruperto-Carola University of Heidelberg, 2012.

J. Telsemeyer, O. Jäkel, and M. Martišíková. Quantitative carbon ion beam radiography and tomography with a flat-panel detector. *Physics in Medicine & Biology*, 57(23):7957, 2012.

T. Tessonnier et al. Experimental dosimetric comparison of ^{1}H, ^{4}He, ^{12}C and ^{16}O scanned ion beams. *Physics in Medicine & Biology*, 62(10):3958, 2017.

T. Tessonnier et al. Phase space generation for proton and carbon ion beams for external users' applications at the Heidelberg Ion Therapy Center. *Frontiers in Oncology*, 5(297), 2016.

M. Testa et al. Proton radiography and proton computed tomography based on time-resolved dose measurements. *Physics in Medicine & Biology*, 58(22):8215, 2013.

U. Titt et al. Degradation of proton depth dose distributions attributable to microstructures in lung-equivalent material. *Medical Physics*, 42(11):6425–6432, 2015.

C. A. Tobias, H. O. Anger, and J. H. Lawrence. Radiological use of high energy deuterons and alpha particles. *Am J Roentgenol Radium Ther Nucl Med.*, 67:1, 1952.

C. A. Tobias et al. Pituitary Irradiation with High-Energy Proton Beams A Preliminary Report. *Cancer Research*, 18:121–134, 1958.

C. A. Tobias et al. Particle radiography and autoactivation. *International Journal of Radiation Oncology*Biology*Physics*, 3:35–44, 1977.

C. A. Tobias. The Repair-Misrepair Model in Radiobiology: Comparison to Other Models. *Radiation Research*, 104(2):S77, 1985.

T. L. Toth. Image Quality in CT: Challenges and Perspectives. In *Radiation Dose from Multidetector CT*, chapter 4, pages 81–100. Springer-Verlag Berlin Heidelberg, 2012.

A. Trofimov et al. Radiotherapy Treatment of Early-Stage Prostate Cancer with IMRT and Protons: A Treatment Planning Comparison. *International Journal of Radiation Oncology*Biology*Physics*, 69(2):444–453, 2007.

A. V. Trofimov, J. H. Unkelbach, and D. Craft. Treatment-Planning Optimization. In *Proton Therapy Physics*, chapter 15, pages 462–488. CRC Press, 2012.

C. Tschalär and H. D. Maccabee. Energy-Straggling Measurements of Heavy Charged Particles in Thick Absorbers. *Phys. Rev. B*, 1:2863–2869, 1970.

E. Tsoulou, L. Baggio, R. Cherubini, and C. A. Kalfas. Low-dose hypersensitivity of V79 cells under exposure to γ-rays and ^{4}He ions of different energies: survival and chromosome aberrations. *International Journal of Radiation Biology*, 77(11):1133–1139, 2001.

J. Unkelbach, D. Craft, B. L. Gorissen, and T. Bortfeld. Treatment Plan Optimization in Proton Therapy. In *Principles and Practice of Proton Beam Therapy*, chapter 22, pages 623–646. Medical Physics Publishing. Inc., 2015.

F. Verhaegen, P. Granton, and E. Tryggestad. Small animal radiotherapy research platforms. *Physics in Medicine & Biology*, 56(12):R55–R83, 2011.

F. Verhaegen et al. ESTRO ACROP: Technology for precision small animal radiotherapy research: Optimal use and challenges. *Radiotherapy and Oncology*, 126(3):471–478, 2018.

V. Vlachoudis. FLAIR: a powerful but user friendly graphical interface for FLUKA. In *Proc. Int. Conf. on Mathematics, Computational Methods & Reactor Physics (M&C 2009), Saratoga Springs, New York*, 2009.

B. Voss et al. GSI Scientific Report 2011-1. page 484, 2010.

G. Wang and M. Jiang. Ordered-subset simultaneous algebraic reconstruction techniques (OS-SART). *Journal of X-Ray Science and Technology*, 12:169–177, 2004.

M. Wedenberg, B. K. Lind, and B. Hårdemark. A model for the relative biological effectiveness of protons: The tissue specific parameter α/β of photons is a predictor for the sensitivity to LET changes. *Acta Oncologica*, 52(3):580–588, 2013.

M. Wedenberg, C. Beltran, A. Mairani, and M. Alber. Advanced Treatment Planning. *Medical Physics*, 45(11):e1011–e1023, 2018.

H. Wertz and O. Jäkel. Influence of iodine contrast agent on the range of ion beams for radiotherapy. *Medical Physics*, 31(4):767–773, 2004.

WHO. *World Cancer Report 2014*. International Agency for Research on Cancer, 2014.

J. J. Wilkens and U. Oelfke. A phenomenological model for the relative biological effectiveness in therapeutic proton beams. *Physics in Medicine & Biology*, 49(13):2811, 2004.

D. C. Williams. The most likely path of an energetic charged particle through a uniform medium. *Physics in Medicine & Biology*, 49(13):2899, 2004.

R. Wilson. Radiological use of fast protons. *Radiology*, 47(5):487–491, 1946.

P. Wohlfahrt et al. Dual-energy CT based proton range prediction in head and pelvic tumor patients. *Radiotherapy and Oncology*, 125(3):526–533, 2017.

J. Wong et al. High-Resolution, Small Animal Radiation Research Platform With X-Ray Tomographic Guidance Capabilities. *International Journal of Radiation Oncology*Biology*Physics*, 71(5):1591–1599, 2008.

E. G. Wright. Manifestations and mechanisms of non-targeted effects of ionizing radiation. *Mutation Research/Fundamental and Molecular Mechanisms of Mutagenesis*, 687(1):28–33, 2010.

A. J. Wroe, D. A. Bush, R. W. Schulte, and J. D. Slater. Clinical Immobilization Techniques for Proton Therapy. *Technology in Cancer Research & Treatment*, 14(1):71–79, 2015.

Würl. PET activation studies at a cyclotron-basedproton therapy facility. Master's thesis, Ludwig-Maximilians-Universität München, 2014.

M. Würl, F. Englbrecht, K. Parodi, and M. Hillbrand. Dosimetric impact of the low-dose envelope of scanned proton beams at a ProBeam facility: comparison of measurements with TPS and MC calculations. *Physics in Medicine & Biology*, 61(2):958, 2016.

M. Yang et al. Theoretical variance analysis of single- and dual-energy computed tomography methods for calculating proton stopping power ratios of biological tissues. *Physics in Medicine & Biology*, 55(5):1343, 2010.

M. Yang et al. Comprehensive analysis of proton range uncertainties related to patient stopping-power-ratio estimation using the stoichiometric calibration. *Physics in Medicine & Biology*, 57(13):4095–4115, 2012.

M. Zaider and H. H. Rossi. The synergistic effects of different radiations. *Radiation Research*, 83(3):732–739, 1980.

R. Zhang et al. Improvement of single detector proton radiography by incorporating intensity of time-resolved dose rate functions. *Physics in Medicine & Biology*, 63(1):015030, 2018.

J. F. Ziegler. Stopping of energetic light ions in elemental matter. *Journal of Applied Physics*, 85(3):1249–1272, 1999.

A. Zietman. The Practicing Clinician's Perspective on Proton Beam Therapy. In *Principles and Practice of Proton Beam Therapy*, chapter 3, pages 43–80. Medical Physics Publishing. Inc., 2015.

P. Zygmanski, K. P. Gall, M. S. Z. Rabin, and S. J. Rosenthal. The measurement of proton stopping power using proton-cone-beam computed tomography. *Physics in Medicine & Biology*, 45(2):511, 2000.